

Cover Page



Universiteit Leiden



The handle <http://hdl.handle.net/1887/43359> holds various files of this Leiden University dissertation.

Author: Köhlinger, F.

Title: Weighing the dark : cosmological applications of gravitational lensing

Issue Date: 2016-09-28

Weighing the Dark:
Cosmological Applications of Gravitational Lensing

ISBN: 978-94-6233-384-0

Weighing the Dark: Cosmological Applications of Gravitational Lensing

Proefschrift

ter verkrijging van
de graad van Doctor aan de Universiteit Leiden,
op gezag van Rector Magnificus prof. mr. C.J.J.M. Stolker,
volgens besluit van het College voor Promoties
te verdedigen op woensdag 28 september 2016
klokke 13.45 uur

door

Fabian Köhlinger

geboren te Gießen, Duitsland
in 1985

Promotiecommissie

Promotor: Prof. dr. Koenraad Kuijken
Co-promotor: Dr. Henk Hoekstra

Overige leden: Prof. dr. Sarah Bridle (University of Manchester)
Prof. dr. Huub Röttgering
Prof. dr. Joop Schaye
Prof. dr. Masahiro Takada (The University of Tokyo)
Dr. Alessandra Silvestri

Cover: graphics designed by Robert Salewsky and the author. Based on an image of the strongly lensed ‘horseshoe’ Einstein ring observed with the *Hubble Space Telescope* (Image credit: ESA/Hubble & NASA).

Für meine Frau und Familie

Contents

1	Introduction	1
1.1	A brief history of the Universe	1
1.2	Gravitational lensing	5
1.3	Cosmic large-scale structure	7
1.4	This thesis	8
2	Strong lensing in RX J1347.5–1145 revisited	13
2.1	Introduction	14
2.1.1	RX J1347.5–1145	14
2.2	Data	16
2.2.1	Multiple image systems in RX J1347.5–1145	17
2.3	Methods	21
2.3.1	Parametric – GLAFIC	21
2.3.2	Non-parametric – PIXELENS	24
2.4	Analysis	25
2.4.1	Parametric – GLAFIC	25
2.4.2	Non-parametric – PIXELENS	29
2.4.3	Mass estimates – PIXELENS and GLAFIC	30
2.5	Conclusions	33
2.A	Additional table	36
3	Statistical uncertainties and systematic errors	39
3.1	Introduction	40
3.2	Statistical uncertainties	42
3.2.1	Halo abundance	42
3.2.2	Mass model	43
3.2.3	Weak-lensing formalism	44
3.2.4	Results	46
3.3	Systematic errors	49
3.3.1	Photometric redshift bias	50
3.3.2	Miscentring bias	53
3.4	Conclusions	58
4	The CFHTLenS shear power spectrum	63
4.1	Introduction	64
4.2	Theory	65
4.3	Quadratic estimator	66
4.4	CFHTLenS measurements	68
4.5	Method validation and covariances	71
4.5.1	Signal extraction validation	72
4.5.2	Band-power covariance	73
4.5.3	Computing resources	75
4.6	The CFHTLenS shear power spectrum	75
4.7	Cosmological inference	78
4.7.1	Theoretical power spectrum	78

4.7.2	The shear likelihood	79
4.7.3	Models and discussion	79
4.8	Conclusions	88
4.A	Indices and derivatives	93
4.B	Additional figures	95
5	The KiDS-450 shear power spectrum	99
5.1	Introduction	100
5.2	Theory	102
5.3	Quadratic estimator	103
5.4	KiDS-450 measurements	105
5.5	Multiplicative bias correction and sensitivity to large-scale additive bias . . .	109
5.6	Covariance	110
5.7	The KiDS-450 shear power spectrum	112
5.7.1	Qualitative comparison to correlation functions	113
5.8	Cosmological inference	115
5.8.1	Theoretical power spectrum	117
5.8.2	Models	120
5.8.3	Results and discussion	122
5.9	Conclusions	124
5.A	Updated derivation of the window function matrix	130
5.B	Additional figures	130
6	Samenvatting	133
6.1	Modern kosmologisch onderzoek	133
6.2	Zwaartekrachtlenzen	134
6.3	Dit proefschrift	135
7	Zusammenfassung	137
7.1	Moderne Kosmologie	137
7.2	Der Gravitationslinseneffekt	138
7.3	Der Inhalt dieser Doktorarbeit	139
	Publications	141
	Curriculum Vitae	143
	Acknowledgements	145

1.1 A brief history of the Universe

The questions concerning the origin, evolution, and fate of the Universe are probably as old as conscious mankind. For millennia the attempts to answer these questions were fundamentally connected to the religious narratives emerging throughout all human cultures. Just a few centuries ago with the rise of modern natural sciences based on observations and experiments, with which predictive mathematical theories can be falsified, the task of answering these cosmological questions moved beyond religious belief and physical cosmology started to emerge.

Just about a century ago Albert Einstein presented his field equations of gravity, the key equations of his theory of general relativity, to the Prussian Academy of Science in Berlin ([Einstein 1915b](#)). Within two years, in 1917, Einstein applied these field equations to the whole Universe and established the field of relativistic cosmology ([Einstein 1917](#)), which until today is at the very roots of our view on the cosmos.

Nowadays the theory of general relativity is regarded as a triumph of human mind, but at the time there was really no observational evidence supporting such a major revision of the prevalent gravity theory of Newtonian mechanics. Only the tiny precession of Mercury's perihelion hinted already in 1859 at an inconsistency in Newtonian mechanics ([Le Verrier 1859](#)), although astronomical zeitgeist favoured explaining the discrepancy rather with a never-to-be-detected planet 'Volcano'.

General relativity could naturally explain the precession of Mercury's perihelion ([Einstein 1915a](#)) and further observational evidence for it became available in 1919. During a solar eclipse Arthur S. Eddington observed the deflection angles of stars in close projected vicinity on the sky to the Sun ([Eddington 1920](#)). The observations employed the gravitational lensing effect, the phenomenon that light from a background source is deflected due to the mass of a foreground lens. In this particular case, the mass of the Sun deflects the light of stars in close projected vicinity to it on the sky. The observations convincingly showed that the stars visible during the eclipse did not appear at positions deflected by an angle predicted by Newtonian gravity. These results made Einstein world famous over night and contributed to the general acceptance of his new theory of gravity in the scientific community. This triggered rich theoretical research in this new field by Willem de Sitter (e.g. [de Sitter 1917](#)), Alexander Friedmann (e.g. [Friedmann 1922](#)), and Georges Lemaître (e.g. [Lemaître 1927](#)), and many others.

Around the same time, in 1920, the 'Great Debate' between astronomers Harlow Shapley and Heber Curtis was in full progress about what the actual size of the Universe is ([Shapley & Curtis 1921](#)). Shapley argued that the Milky Way represents the entirety of the Universe. Thus, he was convinced that the peculiar 'spiral nebulae', of which more and more were being observed as bigger and bigger telescopes became available, were contained in the Milky Way. Curtis, however, believed the nebulae to be 'island universes' arguing that they are

extragalactic and galaxies just like the Milky Way. Eventually, the debate was settled by the work of Edwin Hubble (Hubble 1925) and others who showed that the ‘spiral nebulae’ were indeed galaxies of their own. Spectral data of these nebulae taken by Slipher and interpreted by Lemaître and Hubble showed that almost all galaxies also seemed to be moving away from us (Slipher 1917; Lemaître 1927; Hubble 1929). This cosmic recession, however, was already interpreted by Lemaître in a cosmological sense as actually being the effect of an expanding Universe rather than the Doppler shifted peculiar motions of galaxies. The discovery of the expansion of the Universe made Einstein admit his ‘greatest blunder’ by which he referred to the introduction of the cosmological constant in his field equations in order to make the Universe eternal and static.

Tracing the evolution of an expanding Universe backwards in time leads to the conclusion that there must have been a point in space-time from which the Universe started its expansion, the ‘Big Bang’, estimated to have happened about 13.8 billion years ago. The Big Bang cosmology also predicts that the Universe was very dense and hot in its beginning and became cooler and less dense while expanding. When the Universe cooled down to a temperature that allowed for creating the first neutral hydrogen atoms out of the hot particle and radiation plasma, the Universe became transparent to radiation (around 380 000 years after the Big Bang). Even today we are able to observe the relics of this thermal radiation, the afterglow released right after the formation of the first neutral atoms, redshifted to very long (radio) wavelengths. In 1964, Arno Penzias and Robert Wilson discovered this cosmic microwave background (CMB) radiation by chance (Penzias & Wilson 1965). Today ever more precise and accurate measurements of the tiny temperature fluctuations in the CMB, for example by the *Wilkinson Microwave Anisotropy Probe* (WMAP; Hinshaw et al. 2013) or the *Planck* satellite (Planck Collaboration XIII 2015a), led to a detailed view on the Universe and its constituents expressed in terms of just a handful of cosmological parameters. The tiny temperature fluctuations, the seeds for all subsequent cosmic large-scale structure, are interpreted to be due to quantum fluctuations in the primordial plasma present directly after the Big Bang. These fluctuations are believed to be magnified to cosmic size during inflation, the extremely short period of exponential expansion of the Universe just 10^{-36} seconds after the Big Bang. Moreover, inflation theories whose development started in the early 1980s (Guth 1981; Linde 1982; Steinhardt 1982) also address and solve major problems of Big Bang cosmology:

- (i) the horizon problem – the distribution of the tiny temperature fluctuations in CMB maps are extremely isotropic and homogeneous even for regions of space that must have been causally disconnected, i.e. behind an observational horizon, due to expansion and the finiteness of the speed of light by the time the CMB radiation was released.
- (ii) the flatness problem – the observed flatness of space today presents a fine-tuning problem because in the past space must have been even ‘flatter’ in the sense that today’s measured tiny curvature parameter must have been orders of magnitude tinier in the past.
- (iii) the magnetic-monopole problem – in the extreme temperature and density conditions just after the Big Bang the weak, strong, and electromagnetic forces are believed to be unified, which is commonly referred to as the grand unification theory (GUT). However, as soon as the conditions become less extreme the GUT force is expected to undergo a spontaneous symmetry breaking into the three forces we know today during which magnetic monopoles are predicted to have been produced in large abundances. However, these have not been observed yet.

An extremely short inflationary period right after the Big Bang for about 10^{-35} to 10^{-34} seconds solves all three problems: a flat region of space sufficiently small to be isotropic and homogeneous is magnified to cosmic size which solves the horizon and flatness problems. If inflation also happened before the density and temperature conditions allowed for the

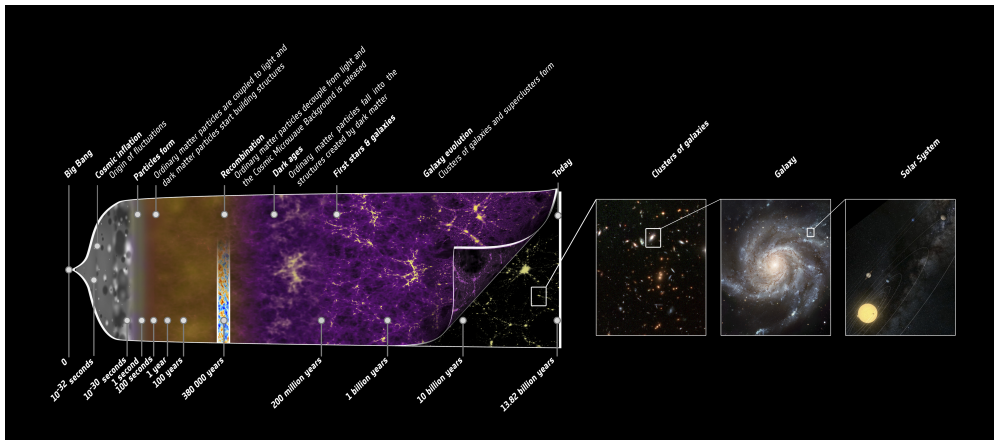


Figure 1.1: A brief history of the Universe from the Big Bang to today (Credit: ESA, C. Carreau).

production of magnetic monopoles, then these would form later already separated by cosmic distances while the Universe continues to expand. Hence, their observable density would be reduced by many orders of magnitude. Although inflation solves the problems of Big Bang cosmology, its physical nature is not at all understood yet. Moreover, no direct evidence for inflation, such as primordial gravitational waves, has been detected yet either ([BICEP2 Collaboration 2014](#)), but instruments becoming increasingly more sensitive might change this already in the very near future.

A major revelation of the modern cosmological concordance model is that all atoms and particles, which we and all the matter interacting with us in daily-life consist of, contribute only about 20 per cent to the total matter in the Universe. The remaining 80 per cent consists of something that we refer to as ‘dark matter’ (so that at least we have a name for it). However, the total matter of the Universe represents only about 30 per cent of its total energy density. The remaining 70 per cent of the energy density is usually attributed to the even more mysterious ‘dark energy’. This cosmological ingredient is required to explain the accelerated expansion of the Universe as indicated by the observations of supernovae in the late 1990s ([Riess et al. 1998](#); [Perlmutter et al. 1999](#)). The source of the accelerated expansion is counteracting the tendency of matter to cluster on cosmologically large scales due to gravity. An attempt of connecting the accelerated expansion of space to the standard model of particle physics interprets Einstein’s ‘greatest blunder’, the cosmological constant, as the energy density of the vacuum. The standard model of particle physics predicts that the vacuum possesses energy due to the constant production and annihilation of particles and antiparticles within the limits of Heisenberg’s uncertainty principle. Unfortunately, quantitative predictions for this vacuum energy are off by about 100 orders of magnitude. In principle, this discrepancy can be explained by postulating an additional symmetry which cancels the effect of vacuum energy up to the small amount we measure today and attribute to the cosmological constant. Therefore, alternative explanations for the accelerated expansion are explored (for example it might be time-dependent) and in order to combine them into a common framework, we call the physical cause just ‘dark energy’ (a term that is also liked better by funding agencies). However, any dark energy theory must still explain why the cosmological constant can be set to zero. [Lovell \(1972\)](#) showed that the cosmological constant is a fundamental ingredient to Einstein’s field equations under general mathematical assumptions: Einstein’s field equations explicitly including the cosmological constant are the only unique formulation of tensor

equations depending only on the metric up to its second-order derivatives in four dimensional space-time.

In that regard, explaining the physical nature of dark matter is considered to be a slightly easier task: although no particle of the standard model possesses the properties of dark matter one can think of extensions, such as super-symmetry, that predict a stable Weakly Interacting Massive Particle (WIMP), whose properties match the ones of dark matter. However, even at the currently most powerful particle collider experiment, the Large Hadron Collider (LHC), super-symmetric particles have not been detected yet. This is either a sign that super-symmetry is not the correct extension or that the energies reached by the LHC are still just too low.

Neutrinos, particles that interact only via gravity and the weak force, were once a candidate for hot dark matter. Measurements and simulations of the cosmic large-scale structure formation have shown though, that dark matter must be cold in the sense that their velocity dispersion is small. Hence, their free streaming length, the distance indicating how far dark matter particles could move in the early Universe before being affected by gravitational collapse, sets the minimum length scale for subsequent structure formation. Density fluctuations within this minimum length scale are washed out due to the free streaming of dark matter particles. In order to explain the observationally established bottom-up scenario of cosmic structure formation then, potential dark matter particles must be cold. The bottom-up scenario of structure formation implies that large structures such as galaxy clusters build up from smaller structures like galaxies and hence they formed later. Despite not being a viable dark matter candidate anymore, neutrinos are still required as an ingredient for our cosmological model since they affect the growth of cosmic large-scale structure (cf. [Lesgourgues & Pastor 2006](#) for a review). Large ground experiments such as *Super-Kamiokande* and the Sudbury Neutrino Observatory (SNO) measured neutrino oscillations, i.e. the mixture of neutrino flavour eigenstates (electron, muon, and tau neutrino) with their mass eigenstates (m_1 , m_2 , and m_3), for the first time around the year 2000 ([Super-Kamiokande Collaboration 1998](#); [SNO Collaboration 2001, 2002](#)). These flavour oscillations imply that neutrinos possess a (tiny) mass, which is in contradiction with fiducial standard model predictions implying massless neutrinos. However, with this kind of experiments it is only possible to measure (squared) mass differences. The absolute mass scale of neutrinos, however, determines the mass-hierarchy between the three neutrinos: in the normal hierarchy scenario one mass eigenstate is the lowest and the other two are increasingly more massive. In contrast to that, the inverted hierarchy predicts three degenerate mass eigenstates. The lower mass bound is set at $\Sigma m_\nu \geq 0.06 \text{ eV}$ by the lowest measured mass difference. The most stringent upper mass bounds come, however, from cosmological probes. For example, CMB constraints from *Planck* set an upper bound of $\Sigma m_\nu < 0.72 \text{ eV}$ ([Planck Collaboration XIII 2015a](#)), whereas a combination of $\text{Ly}\alpha$ power spectrum measurements with constraints from baryon acoustic oscillations (BAO) yields an upper bound of $\Sigma m_\nu < 0.14 \text{ eV}$ ([Palanque-Delabrouille et al. 2015](#)). Pushing this boundary to values lower than $\sim 0.1 \text{ eV}$ in combination with the measured (squared) mass differences will enable us to determine the absolute values of the three mass eigenstates. Hence, neutrino masses are yet another current research topic linking once more the cosmological concordance model and the standard model of particle physics.

In summary, a host of observations can be reconciled within a cosmological concordance model. It is based on general relativity, and we have very precise and accurate measurements of the energy densities for the constituents of the Universe. However, we do not at all understand what the physical nature of the two dominant species, dark matter and dark energy, is. Revealing that is the major motivation behind current cosmological research. An advance in that direction is also naturally linked to new insights regarding the standard model of particle

physics and its inevitable extension.

1.2 Gravitational lensing

Already Newtonian gravity predicts the perpendicular deflection of light from a source behind a mass distribution, a lens, along the line-of-sight towards an observer (assuming a corpuscular theory of light though). However, general relativity predicts the effect to be twice as large, which was confirmed by the larger deflection angles observed by [Eddington \(1920\)](#).

Treating the propagation of light in the full framework of general relativity employing arbitrarily curved space-times is challenging. Employing the space-time of the cosmological concordance model, which encodes the observationally established isotropy and homogeneity of the Universe when averaged over sufficiently large scales, reduces the complexity of the equations substantially. Furthermore, we can assume for a typical configuration of observer, lens, and source that the diameter of the lens is negligible compared to the distances from source to lens, from source to observer, and from lens to observer. Moreover, the peculiar motion of the lens is usually also negligible compared to the speed of light. Then the complexity of the equations simplifies to the level of geometrical optics: the deflection of light rays from a background source due to a mass in its foreground can be described by an effective refraction index, altering the propagation speed of the emitted light in the vicinity of the lens.

The geometrical configuration of the observer-lens-source system and the mass distribution of the lens determine whether we observe strong image distortions and/or multiple image systems or only weak but coherent deflections in the lensed image(s) of the background source. We refer to these two regimes as strong and weak lensing, respectively. Mathematically the image distortions due to gravitational lensing can be described in terms of a mapping from the plane of each background source to the plane of the lens (or image plane). Curves in the lens plane along which this mapping becomes singular (and hence where it is locally not invertible) are called ‘critical curves’. Mapping these critical curves back into the source plane yields ‘caustic curves’ (following the nomenclature of mathematical singularity theory). When a source crosses a caustic curve towards the lens a pair of strongly magnified images is created in the lens plane, which can be observed as a pair of multiple images of the same source. In general, caustic curves are not smooth and hence more than two images of the same source can occur in the lens plane. Critical curves and correspondingly strong lensing phenomena only occur in close vicinity to the lens, whereas weak lensing can still be observed at large distances from the lens. Fig. 1.2a shows an example of a strongly lensed and highly distorted multiple image system forming a ‘horseshoe’ of one and the same background galaxy. When the mass distribution of the lens is axis-symmetric and the source, observer, and lens are aligned along the line-of-sight a perfectly circular ‘Einstein ring’ of multiple images can be observed.

Already in the 1930s when dark matter entered the scientific discussion, Fritz Zwicky pointed out that clusters of galaxies must contain much more mass than estimated from their light alone. He reached this conclusion by applying the virial theorem to the Coma and Virgo clusters of galaxies assuming that the systems are in hydrostatic equilibrium ([Zwicky 1937b](#)). Back of the envelope calculations further show that galaxies or entire clusters of galaxies are due to their high masses ideal objects to target for observing strong lensing phenomena (e.g. [Zwicky 1937a](#)). It still took until 1979, however, before the first strong lensing object, a doubly lensed quasar, was discovered ([Walsh et al. 1979](#)). The first luminous arcs, i.e. highly distorted images of background galaxies, were found in galaxy clusters and also attributed to strong gravitational lensing in 1987 ([Lynds & Petrosian 1986](#); [Soucail et al. 1987](#); [Paczynski 1987](#)). Today strong lensing has developed into a major tool for estimating the mass of a



Figure 1.2: (a) Horseshoe ‘Einstein ring’ observed with the *Hubble Space Telescope*. The ‘horseshoe’ is actually the strongly lensed image of a galaxy in the background of the lens, the massive elliptical galaxy in the centre of the horseshoe (Credit: ESA/Hubble & NASA). (b) Composite image of the merging Bullet cluster. The hot intra-cluster gas observed through its thermal Bremsstrahlung in X-rays (red contours) lags behind the dark matter dominated mass component (blue contours) as inferred from weak lensing (Credit: NASA/CXC/M. Weiss).

lens (e.g. [Johnson et al. 2014](#); [Zitrin et al. 2015](#)), which is possible if one can model very accurately and precisely the lensing geometry including, for example, the positions of where multiple images or luminous arcs are expected to occur. Moreover, the most massive lenses, i.e. galaxy clusters, are used as dedicated ‘natural telescopes’ in the search for the light of the oldest galaxies in the Universe (e.g. [Coe et al. 2013](#); [Bouwens et al. 2014](#)). Just like in regular optics, lensed images are also magnified and thus allow for detailed spectral studies of objects that are too far away to be resolved even with our current best telescopes.

The effects due to weak lensing are not visible by eye and can only be studied statistically. Images of objects in the outskirts of lenses, for example, are only very weakly distorted by the gradient of the lens’ gravitational potential. Assuming that the intrinsic shapes of galaxies are randomly distributed in the Universe, averaging the shapes of a statistically large sample of background galaxies around a lens yields the gravitational shear contribution, i.e. the coherent image distortions due to the lens, since the signal of the randomly distributed intrinsic shapes averages out. Again this technique can be used to study the mass scale and distribution within objects such as galaxy clusters very accurately and precisely. However, instead of looking at single lenses, we can also look at the weak-lensing effect due to the entire cosmic large-scale structure along the line-of-sight and study its mass distribution, in that sense we use the entire Universe as a lens. This approach is referred to as ‘cosmic shear’. Cosmic shear signals were detected for the first time in 2000 ([Bacon et al. 2000](#); [Van Waerbeke et al. 2000](#); [Wittman et al. 2000](#); [Kaiser et al. 2000](#)). Studying it also as a function of redshift, for example in tomographic redshift slices, allows us to infer the growth rate of structures in and the geometry of the Universe (cf. [Kilbinger 2015](#) for a recent review). Apart from measuring shapes for millions of galaxies very accurately and precisely this also requires to estimate their redshifts. In order to measure shapes and (photometric) redshifts at the same time, large dedicated optical multi-band imaging surveys such as the Kilo-Degree Survey (KiDS; [Jong et al. 2012](#); [de Jong et al. 2015](#); [Kuijken et al. 2015](#)), the Subaru Hyper SuprimeCam survey (HSC), and the Dark Energy Survey (DES; [Flaugher 2005](#); [Jarvis et al. 2015](#)) are carried out right now. They are expected to cover several 1000 square degrees in the next few years, which presents an improvement by an order of magnitude compared to weak-lensing surveys that are currently

available. Within the next decade this development will culminate in nearly all-sky surveys carried out by spaceborne observatories such as the *Euclid* satellite (Laureijs et al. 2011).

1.3 Cosmic large-scale structure

The largest gravitationally bound objects in the Universe are clusters of galaxies. The time it takes for a member galaxy to cross a cluster once is an order of magnitude shorter than a Hubble time. Therefore, cluster member galaxies had enough time to cross low-redshift galaxy clusters several times and hence virialized galaxy clusters can be observed in the local Universe. The application of equilibrium physics to such virialized clusters by Fritz Zwicky in 1937 showed already that the stellar, i.e. light emitting mass, was not enough to explain why clusters are gravitationally bound (Zwicky 1937b). Today it is an observationally well-established fact that indeed galaxy clusters are dominated by dark matter, and intra-cluster gas together with the stellar mass of the constituent member galaxies make up only a small fraction of the total mass in a cluster. This makes galaxy clusters ideal objects to study properties of dark matter, as for example the famous merging ‘Bullet cluster’ in Fig. 1.2b shows: whereas the baryons of the smaller ‘Bullet cluster’, i.e. mainly the intra-cluster gas as observed in X-rays (red contours), lag behind due to colliding with the baryons of the bigger cluster, the dominant dark matter of both clusters (blue contours) passed right through (Markevitch et al. 2002; Clowe et al. 2006), also implying that the cross-section of potential dark matter particles must be tiny (e.g. Markevitch et al. 2004).

The cosmological concordance model also predicts a universal density profile for an ensemble of galaxy clusters (Navarro et al. 1997). Although the physical principles behind such a profile are not fully understood yet, studying the mass distribution of galaxy clusters is an important cosmological test and strong lensing, for example, can be used to produce very accurate and precise measurements of the mass distribution in the core region of a cluster. Moreover, the number of clusters per cosmic volume of a given mass at a given redshift is strongly dependent on parameters of the cosmological model influencing the growth of structure. Hence, with the detection of hundreds of massive clusters over recent years mainly due to applying new observation techniques such as the Sunyaev–Zel’dovich (SZ) effect (Sunyaev & Zeldovich 1972), cluster counts have become an important independent cosmological probe (e.g. Planck Collaboration XXIV 2015b). The SZ effect describes the average energy boost a low-energy CMB photon gains due to inverse Compton scattering with high-energy electrons of the hot intra-cluster gas when passing through a galaxy cluster. This effect is independent of the redshift of the cluster and although many massive clusters have already been discovered employing the SZ effect, it has one shortcoming: in order to estimate the actual mass of the cluster, which is an essential ingredient for the cluster counts, from the measured strength of the SZ effect, one has to rely on scaling relations calibrated with other mass measurement techniques such as weak lensing. The level of uncertainty of the mass estimates for clusters is fundamentally limited by the accuracy and precision of these scaling relations. Investigating the statistical uncertainties and systematic errors of different mass calibration methods is hence an important topic of current research in order to improve the precision and accuracy of cluster counts as a competitive cosmological probe.

In the big picture of cosmic large-scale structure galaxy clusters are the nodes of the ‘cosmic web’: filaments of dark matter, gas, and galaxies extend through space-time in a web-like structure and the ‘empty’, i.e. extremely under-dense, regions in between are referred to as ‘cosmic voids’. The evolution of the large-scale structure over cosmic time is very sensitive to the clustering properties of dark and luminous matter. Hence, studying its evolution, for example by means of measuring the cosmic shear signal as a function of redshift, is a very

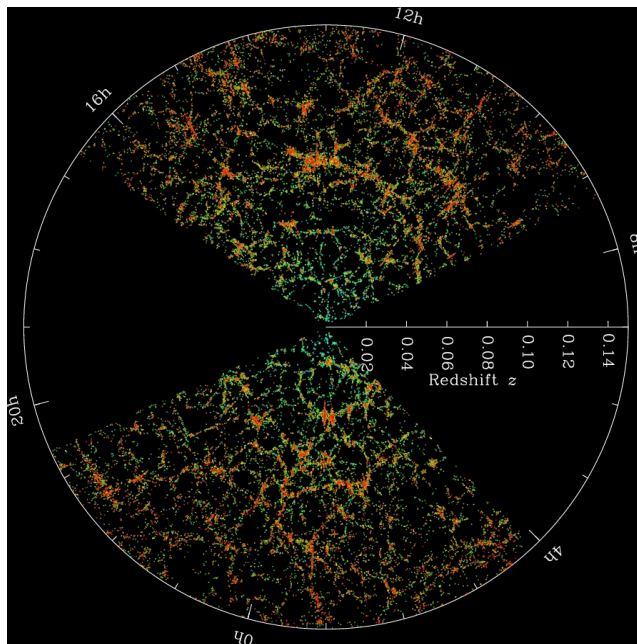


Figure 1.3: A map of the cosmic large-scale structure as seen in the Sloan Digital Sky Survey. Every dot in this picture represents an entire galaxy (Credit: M. Blanton and the Sloan Digital Sky Survey).

promising cosmological probe, especially in the current era of dedicated large-area imaging surveys serving as pathfinder missions in anticipation of the close to all-sky surveys of the next decade.

1.4 This thesis

In the following chapters we present applications of strong and weak gravitational lensing in a cosmological context.

We start in **Chapter 2** with the very detailed study of the strong lens model required to explain the occurrences of giant luminous arcs and multiple image systems based on high-quality data from the Cluster Lensing And Supernova survey with Hubble (CLASH; [Postman et al. 2012](#)) in the massive and very X-ray luminous merging cluster RX J1347.5–1145. In addition to presenting a consistent lens model derived with two independent modelling approaches, we finally measure the mass profile of and the mass distribution in the cluster core.

In **Chapter 3** we look at ensembles of galaxy clusters and address the limitations of weak lensing in deriving mass estimates for ensembles of clusters. We study this with a focus on the future *Euclid* mission ([Laureijs et al. 2011](#)) and derive the level of statistical uncertainties on the mass estimates for this mission and study the impact of various sources of bias. In particular, we investigate the bias due to cluster member galaxies that due to erroneously assigned photometric redshifts are scattered into the galaxy source sample. For stacks of galaxy clusters this effect is severe and must be properly accounted for. Finally, we investigate the bias due to miscentring, the displacement between the true position of the minimum of the gravitational potential of the galaxy cluster and any observationally defined cluster centre. With respect to the expected low level of statistical uncertainties this bias is significant. However, complementary future missions such as the X-ray survey *eROSITA* ([Merloni et al. 2012](#)) will allow us

to put very informative priors on miscentring parameters, making it possible to mitigate this bias.

In the final two chapters we take the leap from studying galaxy clusters to studying the entire cosmic large-scale structure using cosmic shear. Significant advances in computer technology allow us also to employ a computationally demanding maximum-likelihood algorithm to extract the power spectrum of cosmic shear in terms of band powers instead of following the standard approach in the literature of using shear-shear correlation-functions to measure the cosmic shear signal in real-space. A major advantage of the power-spectrum estimator is that scale-dependent features such as those caused by massive neutrinos or baryon feedback can be studied much more cleanly in the cosmic shear power spectrum. In order to improve cosmological parameter constraints, in **Chapter 4** we extend the technique to include redshift bins and test it extensively on mock data before applying it to shear catalogues from the lensing analysis of the Canada–France–Hawaii Telescope Legacy Survey (CFHTLenS; [Erben et al. 2013](#); [Heymans et al. 2012](#)).

Finally, in **Chapter 5** we use state-of-the-art shear data based on 450 square degrees of imaging data from an intermediate data release from KiDS. Again, we apply the cosmic shear power spectrum estimator to it and derive cosmological parameter constraints. The se results are in tension with latest CMB results from [Planck Collaboration XIII \(2015a\)](#) but agree well with other low-redshift probes.

Bibliography

BICEP2 Collaboration, 2014, [Phys. Rev. Lett.](#), 112, 241101

Bacon D. J., Refregier A. R., Ellis R. S., 2000, [MNRAS](#), 318, 625

Bartelmann M., Schneider P., 2001, [Phys. Rep.](#), 340, 291

Bouwens R. J., et al., 2014, [ApJ](#), 795, 126

Clowe D., Bradač M., Gonzalez A. H., Markevitch M., Randall S. W., Jones C., Zaritsky D., 2006, [ApJL](#), 648, L109

Coe D., et al., 2013, [ApJ](#), 762, 32

Eddington A. S., 1920, *Space, time and gravitation*. Cambridge University Press

Einstein A., 1915a, *Sitzungsber. Königl. Preuß. Akad. Wiss. (Berlin)*, pp 831–839

Einstein A., 1915b, *Sitzungsber. Königl. Preuß. Akad. Wiss. (Berlin)*, pp 844–847

Einstein A., 1917, *Sitzungsber. Königl. Preuß. Akad. Wiss. (Berlin)*, pp 142–152

Erben T., et al., 2013, [MNRAS](#), 433, 2545

Flaugher B., 2005, [Int. J. Mod. Phys. A](#), 20, 3121

Friedmann A., 1922, [Z. Phys.](#), 10, 377

Guth A. H., 1981, [Phys. Rev. D](#), 23, 347

Heymans C., et al., 2012, [MNRAS](#), 427, 146

Hinshaw G., et al., 2013, [ApJS](#), 208, 19

- Hubble E. P., 1925, *Obs.*, 48, 139
- Hubble E., 1929, *Proc. Natl. Acad. Sci.*, 15, 168
- Jarvis M., et al., 2015, preprint (arXiv:1507.05603)
- Johnson T. L., Sharon K., Bayliss M. B., Gladders M. D., Coe D., Ebeling H., 2014, *ApJ*, 797, 48
- Jong J. T. A. d., Kleijn G. A. V., Kuijken K. H., Valentijn E. A., Consortiums K. a. A.-W., 2012, *Exp. Astron.*, 35, 25
- Kaiser N., Wilson G., Luppino G. A., 2000, preprints (arXiv:astro-ph/0003338)
- Kilbinger M., 2015, *Rep. Prog. Phys.*, 78, 086901
- Kuijken K., et al., 2015, *MNRAS*, 454, 3500
- Laureijs R., et al., 2011, preprint (arXiv:1110.3193)
- Le Verrier U. J., 1859, *Ann. Obser. Paris*, 5
- Lemaître G., 1927, *Ann. Soc. Sci. Bruxelles*, 47, 49
- Lesgourgues J., Pastor S., 2006, *Phys. Rep.*, 429, 307
- Linde A. D., 1982, *Phys. Lett. B*, 108, 389
- Lovelock D., 1972, *J. Math. Phys.*, 13, 874
- Lynds R., Petrosian V., 1986, in *BAAS*. p. 1014
- Markevitch M., Gonzalez A. H., David L., Vikhlinin A., Murray S., Forman W., Jones C., Tucker W., 2002, *ApJL*, 567, L27
- Markevitch M., Gonzalez A. H., Clowe D., Vikhlinin A., Forman W., Jones C., Murray S., Tucker W., 2004, *ApJ*, 606, 819
- Merloni A., et al., 2012, preprint (arXiv:1209.3114)
- Navarro J. F., Frenk C. S., White S. D. M., 1997, *ApJ*, 490, 493
- Paczynski B., 1987, *Nature*, 325, 572
- Palanque-Delabrouille N., et al., 2015, *J. Cosmology Astropart. Phys.*, 2015, 045
- Penzias A. A., Wilson R. W., 1965, *ApJ*, 142, 419
- Perlmutter S., et al., 1999, *ApJ*, 517, 565
- Planck Collaboration XIII, 2015a, preprint (arXiv:1502.01589)
- Planck Collaboration XXIV, 2015b, preprints (arXiv:1502.01597)
- Postman M., et al., 2012, *ApJS*, 199, 25
- Riess A. G., et al., 1998, *AJ*, 116, 1009
- SNO Collaboration, 2001, *Phys. Rev. Lett.*, 87, 071301

- SNO Collaboration, 2002, [Phys. Rev. Lett.](#), 89, 011301
- Shapley H., Curtis H. D., 1921, *Bull. Natl. Res. Council.*, Vol. 2, Part 3, No. 11, pp 171–217
- Slipher V. M., 1917, *Proc. Americ. Philos. Soc.*, 56, 403
- Soucail G., Fort B., Mellier Y., Picat J. P., 1987, *A&A*, 172, L14
- Steinhardt P. J., 1982, [Phys. Rev. D](#), 25, 2074
- Sunyaev R. A., Zeldovich Y. B., 1972, *Comm. Astrophys. Space Phys.*, 4, 173
- Super-Kamiokande Collaboration, 1998, [Phys. Rev. Lett.](#), 81, 1562
- Van Waerbeke L., et al., 2000, *A&A*, 358, 30
- Walsh D., Carswell R. F., Weymann R. J., 1979, [Nature](#), 279, 381
- Wittman D. M., Tyson J. A., Kirkman D., Dell’Antonio I., Bernstein G., 2000, *Nature*, 405, 143
- Zitrin A., et al., 2015, [ApJ](#), 801, 44
- Zwicky F., 1937a, [Phys. Rev.](#), 51, 290
- Zwicky F., 1937b, [ApJ](#), 86, 217
- de Jong J. T. A., et al., 2015, [A&A](#), 582, A62
- de Sitter W., 1917, [MNRAS](#), 78, 3

Strong lensing in RX J1347.5–1145

revisited*

We present a revised strong lensing mass reconstruction of the galaxy cluster RX J1347.5–1145. The X-ray luminous cluster at redshift $z = 0.451$ has already been studied intensively in the past. Based on information of two such previous (strong-)lensing studies by Halkola et al. and Bradač et al., as well as by incorporating newly available data from the Cluster Lensing And Supernova survey with Hubble, we identified four systems of multiply lensed images (anew) in the redshift range $1.75 \leq z \leq 4.19$. One multiple image system consists of in total eight multiply lensed images of the same source. The analysis based on a parametric mass model derived with the software GLAFIC suggests that the high image multiplicity is due to the source ($z_{\text{phot}} = 4.19$) being located on a so-called ‘swallowtail’ caustic. In addition to the parametric mass model, we also employed a non-parametric approach using the software PIXELENs in order to reconstruct the projected mass of the cluster using the same strong lensing data input. Both reconstructed mass models agree in revealing several mass components and a highly elliptical shape of the mass distribution. Furthermore, the projected mass inside, for example, a radius $R \sim 35 \text{ arcsec} \sim 200 \text{ kpc}$ of the cluster for a source at redshift $z = 1.75$ is $M(< R) \approx (2.19^{+0.01}_{-0.02}) \times 10^{14} M_{\odot}$ as estimated by GLAFIC. Within the same radius PIXELENs predicts a mass of $M(< R) \approx (2.47 \pm 0.01) \times 10^{14} M_{\odot}$ which exceeds the GLAFIC estimate by ≈ 13 per cent. The difference could be related to the fundamental degeneracy involved when constraining dark matter substructures with gravitationally lensed arcs.

F. Köhlinger and R. W. Schmidt
2014, *MNRAS*, **Volume 437**, Issue 2, pp 1858–1871

*Based on observations made with the NASA/ESA *Hubble Space Telescope*, and obtained from the Hubble Legacy Archive, which is a collaboration between the Space Telescope Science Institute (STScI/NASA), the Space Telescope European Coordinating Facility (ST-EFC/ESA) and the Canadian Astronomy Data Centre (CADC/NRC/CSA).

2.1 Introduction

In resolving the nature of the two exotic ingredients of current standard Λ -cold dark matter (Λ CDM) cosmology – dark matter and dark energy – the determination of accurate masses and mass profiles plays an important role: the mass distribution in galaxy clusters, for example, is a direct test for predictions of the CDM paradigm (e.g. Bartelmann et al. 2013) since numerical simulations in the scope of Λ CDM predict a universal mass profile for mass haloes covering scales from galaxies to clusters of galaxies (Navarro et al. 1997, 2010).

Once the mass and its distribution are determined, dark energy models can be constrained with various techniques either from using mass-calibrated number counts or scaling relations (e.g. Allen et al. 2011; Giardini et al. 2013; Planck Collaboration XX 2013 and references therein) or even using the systems on their own (e.g. Golse et al. 2002, Jullo et al. 2010). Therefore, mass profiles of galaxy clusters are a valuable probe for putting further constraints on cosmological parameters such as Ω_m , σ_8 or the equation-of-state parameter for dark energy w .

In this paper we scrutinize the evidence for multiple images of background systems and its implication for the central mass distribution in the system RX J1347.5–1145.

2.1.1 RX J1347.5–1145

The galaxy cluster RX J1347.5–1145 at redshift $z = 0.451$ is among the most luminous X-ray clusters known to date (Schindler et al. 1995) and has already been studied intensively in the past.

Various data sets are available for this cluster ranging from X-ray (Schindler et al. 1995, 1997; Allen et al. 2002; Ettori et al. 2004; Gitti & Schindler 2004; Gitti et al. 2007; Mahdavi et al. 2013) to optical (Fischer & Tyson 1997; Sahu et al. 1998; Cohen & Kneib 2002; Ravindranath & Ho 2002; Verdugo et al. 2012) and radio observations of the Sunyaev–Zel’dovich (SZ) effect (Komatsu et al. 2001; Pointecouteau et al. 2001; Kitayama et al. 2004; Plagge et al. 2013). Mass estimates from various studies using different techniques like strong-lensing, weak-lensing, a combined strong and weak lensing analysis, X-ray measurements, velocity dispersion measurements from spectroscopic data or the SZ effect often yielded discrepant results. Particularly, the dynamical mass estimate (Cohen & Kneib 2002), early X-ray measurements (Schindler et al. 1997) and gravitational lensing estimates (Fischer & Tyson 1997) yielded a discrepancy of factor ~ 3 .

Possible reasons for the discrepancy between the results of the different mass reconstruction approaches might be due to the shape of the cluster potential, projection effects or more complicated gas physics in the cluster which have not been fully taken into account. Moreover, the different mass reconstruction techniques are also affected by various systematic effects such as cluster member contamination, unknown or uncertain redshifts for multiply lensed images, ambiguous identification of multiple image systems and temperature calibrations, and it is very challenging to quantify the effects of these systematics correctly on the uncertainties of the respective analysis.

A specific proposal for resolving the discrepancy between the mass estimates in RX J1347.5–1145 was suggested by Cohen & Kneib (2002) stating that the cluster is likely to be ongoing a major merger. This would bias the velocity dispersion measurements and also affect the X-ray results due to special merger dynamics and thus might be the key to reconciling the low velocity dispersion mass estimate with the higher estimates from lensing and X-ray measurements.

The peculiarity of the cluster RX J1347.5–1145 to contain *two* bright cD galaxies (cf. Fig. 2.1; throughout this work we will refer to the western cD galaxy as brightest cluster

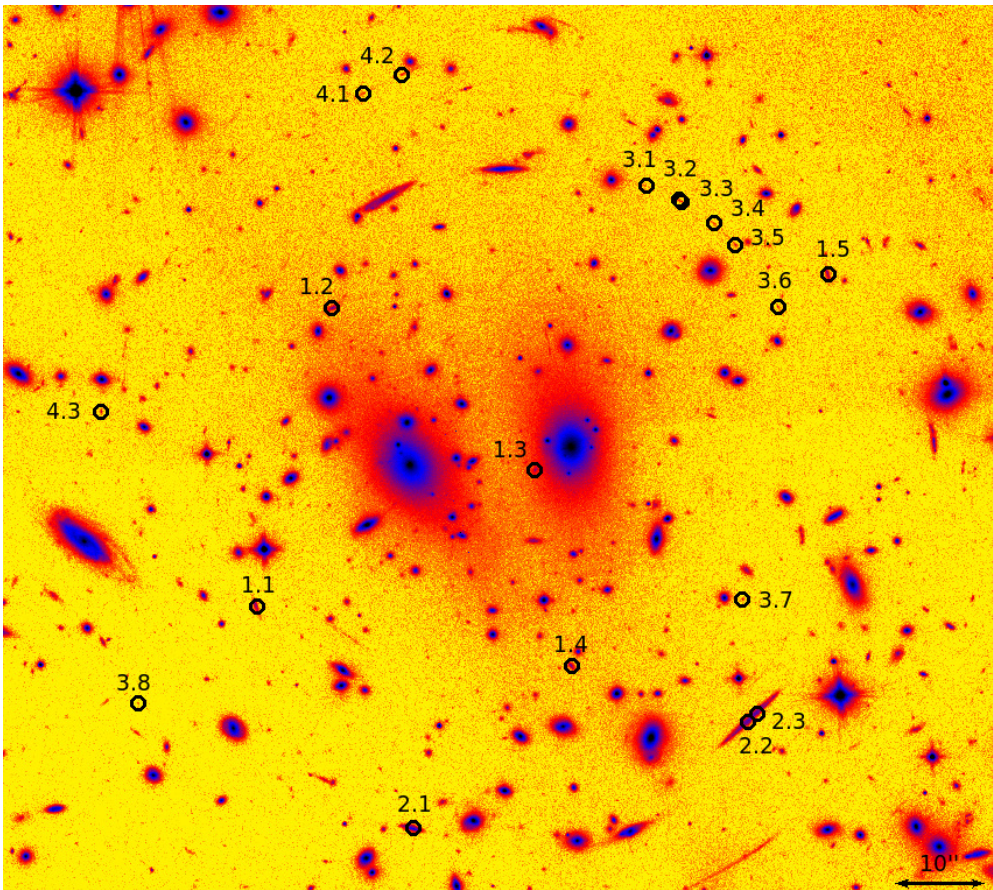


Figure 2.1: The CLASH ACS-IR detection image (cf. Section 2.2). North is up and east is left. For better visibility of faint multiply lensed images, this image is presented in false colours which encode brightness information. Denoted are identified multiple image system candidates as used in this work for the best-fitting models discussed in Section 2.4. Also compare with identifications of multiple image systems from Bradač et al. (2008) and Halkola et al. (2008) in Table 2.1.

galaxy (BCG) while calling the other just second cD galaxy) at its centre can be taken as further support for this merger scenario. Moreover, a region of shocked gas in the south-east of the cluster was observed by Komatsu et al. (2001) using the SZ effect and by Allen et al. (2002) in X-ray data from *Chandra* (cf. Fig. 2.6).

All these peculiarities and especially the discrepancies in the mass reconstruction of those early papers were revised when new deep data from the Advanced Camera for Surveys (ACS) from the *Hubble Space Telescope* (*HST*) became available in 2008. Bradač et al. (2008) presented a mass reconstruction based on a combined strong and weak lensing analysis and found their results in accordance to results obtained from an X-ray analysis, also presented in their paper (cf. Fig. 2.11). Halkola et al. (2008) obtained results solely based on a strong lensing analysis, but also found their mass results to agree with other results presented in the literature (cf. Fig. 2.11).

Despite the consistent mass estimates, both studies did not quite present a consistent description of the cluster with respect to its strong lensing features. First of all, there is a somewhat ambiguous and sometimes even contradictory identification of multiple image systems

between both papers (cf. Table 2.1). Moreover, in some of the identified multiple image systems, there are some missing but necessarily expected counter images which will be discussed in more detail in Section 2.2.1.

Another point was, that there was only one spectroscopically confirmed redshift for only one multiple image system available at the time of their analyses. The redshifts of other multiple image systems were either fixed using lower precision photometric redshifts or left free for fitting then. Therefore, as soon as high quality data from the Cluster Lensing And Supernova survey with Hubble (CLASH; Postman et al. 2012) became available, we started to investigate the cluster again with strong lensing in order to present a more consistent high detail strong lensing model. As mentioned before crucial ingredients for a strong lensing mass reconstruction are fixed redshifts of a multiple image system and the unambiguous identification of such systems. With the high quality of the provided CLASH data including robust photometry and reliable photometric redshifts and by having improved the multiple image identification with this data, we present here a high detail strong lensing model of the cluster RX J1347.5–1145. This entails a thorough discussion of the known multiply imaged systems, but fortunately does not alter the consistency with X-ray mass models when allowing for substructure in the core.

The paper is structured as follows. In Section 2.2 we describe the input data used for our analysis and explain the data fitting further in Section 2.3. The analysis and results are presented in Section 2.4 and conclusions are finally drawn in Section 2.5.

For comparison of results obtained here with previous work we also adopt a Λ CDM cosmology with $\Omega_m = 0.3$, $\Omega_\Lambda = 0.7$ and Hubble constant $H_0 = 70 \text{ km s}^{-1} \text{ Mpc}^{-1}$. At the redshift of the cluster, $z_{\text{lens}} = 0.451$, one arcsecond then corresponds to 5.77 kpc.

2.2 Data

The galaxy cluster RX J1347.5–1145 was re-observed as one out of 25 galaxy cluster targets of the CLASH programme (cf. Postman et al. 2012 for full details on this survey).

The images were taken in 16 broadband filters of the Wide Field Camera 3 (WFC3)/UVIS¹, WFC3/IR² and ACS/WFC³ of *HST* comprising a total spectral range from near-UV to near-IR, yielding highly reliable photometry. The filters were especially selected for that purpose based on tests with simulated photometric data in order to achieve a precision on photometric redshifts of $\sigma_z \sim 0.02(1+z)$ using the software BPZ (Benítez 2000; Benítez et al. 2004; Coe et al. 2006).

In addition to images, catalogues including the photometry from all 16 bands and photometric redshifts for identified sources are also made available to the public. For the creation of these public catalogues one detection image consisting of the weighted sum of all ACS/WFC and WFC3/IR images was used in order to run the software SExtractor (Bertin & Arnouts 1996) on it for detecting objects and measuring their photometry. A second detection image was created solely from the WFC3/IR images for the search for highly redshifted objects, also resulting in a respective second catalogue. Both catalogues are based on the lower-resolution (i.e. 1 pix = 65 mas) detection images. We will refer to the first catalogue based on ACS/WFC and WFC3/IR images as ‘CLASH ACS-IR catalogue’ and to the second one based on WFC3/IR images only as ‘CLASH IR catalogue’. The detection images are denoted as ‘CLASH ACS-IR detection image’ and ‘CLASH IR detection image’, respectively.

In the following analysis we primarily consulted the CLASH ACS-IR catalogue due to the more rigid criteria on object detections. Just for objects not already contained in there (chiefly

¹ F225W, F275W, F336W and F390W

² F105W, F110W, F125W, F140W and F160W

³ F435W, F475W, F606W, F625W, F775W, F814W and F850LP

multiple image system 1), we used the CLASH IR catalogue.

2.2.1 Multiple image systems in RX J1347.5–1145

As mentioned in Section 2.1, there are already candidates for multiple image systems published in the literature (Bradač et al. 2008; Halkola et al. 2008). These served as initial data input for our early models and we usually followed the identifications and image affiliations by Halkola et al. (2008).

However, the CLASH data and catalogues and also predictions from early models led to a new interpretation of some of the multiple image systems. Moreover, we could also include additional images that were not yet included in previous studies.

We do not consider single image systems of previous studies, because these do not impose any new constraints on the strong lensing model. We show an overview of all images used during our final analysis in Fig. 2.1. In Table 2.1 we summarize the properties of these systems and also indicate for ease of comparison their nomenclature in the studies of Halkola et al. (2008) and Bradač et al. (2008), if applicable.

The cluster centre is set on the BCG at position $RA = 206^{\circ}8775$, $Dec = -11^{\circ}7526$ (J2000). Furthermore, all photometric redshift estimates for the multiple image systems are derived as an average over the individual redshifts (cf. Table 2.1) of the images affiliated to the respective multiple image system. Additionally, we checked colours and surface brightnesses based on the 16 band photometry of all multiple image systems to be consistent. Exemplarily, we list one colour ($M_{F475W} - M_{F814W}$) and the surface brightness in one filter (S_{F814W}) in Table 2.1 for each multiply lensed image.

Table 2.1: Positions (Δ RA, Δ Dec), colour ($M_{F475W} - M_{F814W}$), surface brightness (S_{F814W}) and photometric redshifts (z_{phot}) with 95 per cent confidence intervals for each image of the multiple image systems from the indicated CLASH catalogues. Note that image 1.3 is apparently a drop out (very closely located to BCG) and could not be identified in the CLASH ACS-IR catalogue either. Therefore, we did not consider it for the calculation of the redshift of the whole system. All coordinates are given relative to the cluster centre at position RA = 206:8775, Dec = $-11^{\circ}7526$ (J2000). Please refer also to Fig. 2.1. For convenience we also give the nomenclature from Halkola et al. (2008) (Ha08) and Bradač et al. (2008) (Br08).

Multiple Images			Δ RA (arcsec)	Δ Dec (arcsec)	$M_{F475W} - M_{F814W}$	S_{F814W} (mag arcsec $^{-2}$)	z_{phot}	z_{spec}	Catalogue	Comments
This work	Ha08	Br08								
1.1	1a	I	-35.61	-17.70	0.20 ± 0.05	24.42 ± 0.03	$2.39^{+0.03}_{-0.08}$	-	IR	(a)
1.2	1b	I	-26.96	15.34	0.06 ± 0.05	24.55 ± 0.03	$2.19^{+0.01}_{-0.13}$	-	IR	(a)
1.3	1c	I	-4.02	-2.54	1.53 ± 0.17	24.71 ± 0.03	$0.55^{+0.01}_{-0.06}$	-	IR	(a), (b)
1.4	1d	I	0.01	-24.24	0.29 ± 0.06	24.35 ± 0.03	$1.92^{+0.14}_{-0.04}$	-	IR	(a)
1.5	1e	I	28.97	19.06	0.15 ± 0.06	24.54 ± 0.03	$2.39^{+0.03}_{-0.24}$	-	IR	(a)
2.1	2a	A	-18.00	-42.19	0.20 ± 0.02	23.48 ± 0.01	$1.78^{+0.01}_{-0.01}$	1.75	ACS-IR	
2.2	-	-	19.55	-30.46	-	-	-	-	-	(c)
2.3	2b	A	20.57	-29.46	0.18 ± 0.01	23.47 ± 0.01	$1.78^{+0.01}_{-0.01}$	1.75	ACS-IR	(c)
3.1	12a	B	8.27	28.92	1.62 ± 0.40	23.57 ± 0.09	$4.01^{+0.18}_{-0.19}$	-	ACS-IR	
3.2	-	-	12.15	27.32	1.51 ± 0.33	23.75 ± 0.08	$4.11^{+0.13}_{-0.17}$	-	ACS-IR	
3.3	-	-	12.45	27.14	3.01 ± 0.74	23.41 ± 0.06	$4.36^{+0.08}_{-0.10}$	-	ACS-IR	(d)
3.4	12b	B	16.13	24.72	2.23 ± 0.47	23.34 ± 0.07	$4.14^{+0.11}_{-0.12}$	-	ACS-IR	
3.5	11a	B	18.51	22.36	2.00 ± 0.34	23.42 ± 0.06	$4.23^{+0.11}_{-0.05}$	-	ACS-IR	
3.6	11b	B	23.35	15.51	1.76 ± 0.26	23.52 ± 0.05	$4.15^{+0.08}_{-0.08}$	-	ACS-IR	
3.7	11c?	-	19.38	-16.84	2.06 ± 0.39	23.50 ± 0.07	$4.39^{+0.10}_{-0.11}$	-	ACS-IR	
3.8	11d?	-	-48.95	-28.36	2.44 ± 0.81	23.49 ± 0.11	$4.16^{+0.14}_{-0.31}$	-	ACS-IR	
4.1	8a	C	-23.56	39.08	0.98 ± 0.17	23.59 ± 0.06	$3.57^{+0.14}_{-0.06}$	-	ACS-IR	
4.2	8b	C	-19.05	41.27	1.00 ± 0.14	23.87 ± 0.05	$3.62^{+0.12}_{-0.06}$	-	ACS-IR	
4.3	8c?	-	-53.14	3.95	1.01 ± 0.18	23.76 ± 0.07	$3.71^{+0.07}_{-0.12}$	-	ACS-IR	

(a) The error bars of the faint IR catalogue magnitudes appear somewhat underestimated.

(b) Affected by BCG.

(c) The object appears as a single source in the catalogue at position 2.3. Due to basic lensing geometry, we decided to split the object up into two components (cf. Section 2.2.1).

(d) SEXTRACTOR may not split the object correctly.

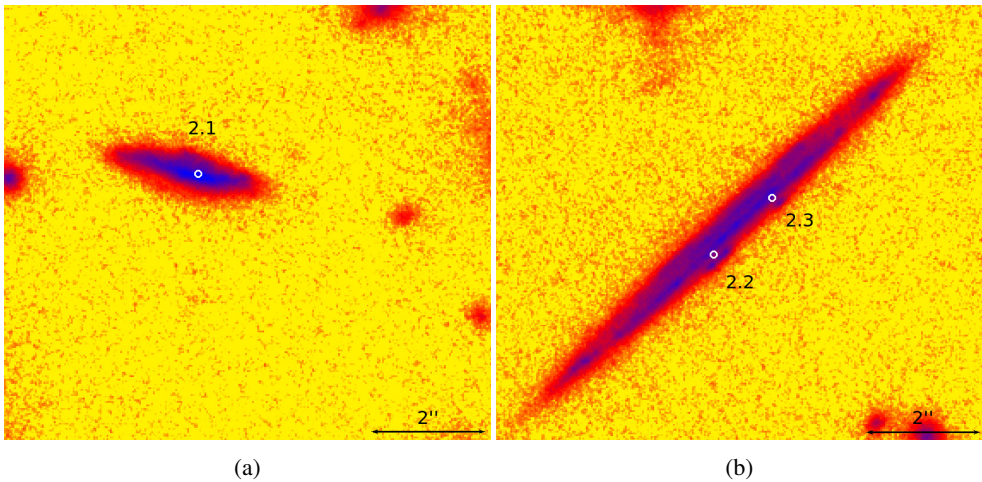


Figure 2.2: Zoom-in on multiply lensed images of multiple image system 2. (a) Image 2.1. (b) Images 2.2 and 2.3. Due to the faintness of the arcs we show a false colour version of the CLASH ACS-IR detection image (cf. Section 2.2).

Multiple image system 1 (five images)

This system consists of five images on four sides of the cluster and one central image (cf. Fig. 2.1). It was already identified in Bradač et al. (2008) and Halkola et al. (2008), and the photometric redshift of this system estimated from the CLASH IR catalogue yields $z_{\text{phot}} = 2.22^{+0.05}_{-0.12}$ which is consistent with the redshift estimates for images ‘1d’ and ‘1e’ by Halkola et al. (2008) with $z_{\text{phot}}^{\text{1d}} = 2.19 \pm 0.05$ and $z_{\text{phot}}^{\text{1e}} = 2.19 \pm 0.15$, respectively (cf. Table 2.1 for nomenclature). The redshift estimate by Bradač et al. (2008) from fitting strong-lensed data yields $z_{\text{fit}}^{\text{1}} = 1.7 \pm 0.2$ though (cf. Table 2.1 for nomenclature).

Note that we did not include image 1.3 in the redshift average, though being a likely member of the multiple image system, the corresponding photometry seems to be affected by the BCG (cf. Fig 2.1).

Multiple image system 2 (three images)

In Fig. 2.2 we show multiple image system 2 which was already identified in Bradač et al. (2008) and Halkola et al. (2008) as well. It consists of one bright arc south-west of the cluster centre and one fainter arc south-east of the centre. However, we interpret the brighter arc to consist of two directly merging images on a tangential critical line due to the general straight elongated shape and especially due to substructures that seem to be exactly mirrored (cf. Fig. 2.2). This new interpretation has significant consequences for the entire mass distribution of the cluster and will be discussed further in Section 2.3.1. Halkola et al. (2008) determined the spectroscopic redshift of this system to be $z_{\text{spec}} = 1.75$. This is also consistent with the photometric redshift estimate from the CLASH ACS-IR catalogue ($z_{\text{phot}} = 1.78^{+0.01}_{-0.01}$).

Multiple image system 3 (eight images + 1)

The main part of this system (cf. Fig. 2.3) is located in the north-west of the cluster centre and is identified in Halkola et al. (2008) as image systems 11 and 12, respectively. However, we interpret the system to originate from just one single source due to the consistent photometric

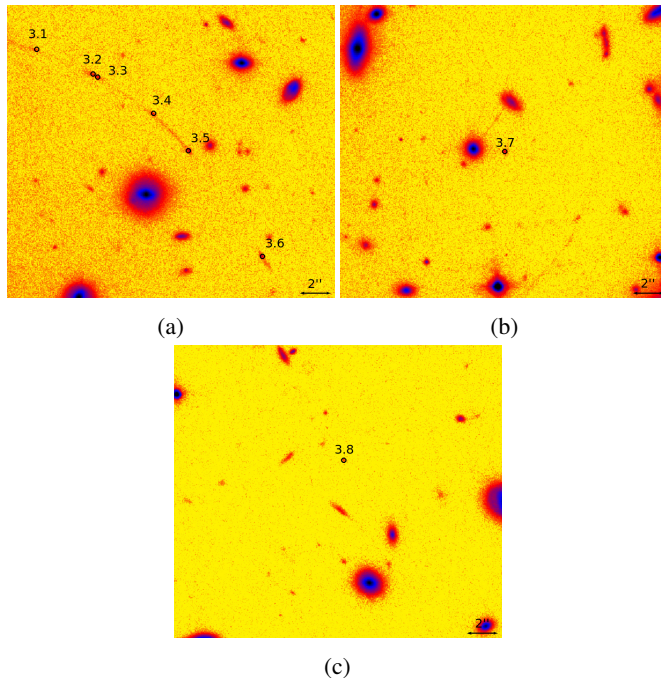


Figure 2.3: Zoom-in on multiply lensed images of multiple image system 3. (a) Images 3.1 to 3.6. (b) Image 3.7. (c) Image 3.8. Due to the faintness of the arcs we show a false colour version of the CLASH ACS-IR detection image (cf. Section 2.2).

redshifts of the images (cf. Table 2.1). Furthermore, we also include the two merging images (cf. images 3.2 and 3.3 in Fig. 2.3) that were not yet considered in previous studies. Nevertheless, their redshifts and location suggest their affiliation to the system, and we interpret them as two merging images on a tangential critical line. Altogether, this part of the system (cf. Fig. 2.7) resembles strongly the massive arc structure in A370 (cf. Richard et al. 2009).

Additionally to the north-western arc structure, there are two more images (cf. Fig. 2.3): one in the south-west and one in the south-east with respect to the cluster centre. Our model predicts further a ninth image directly in the cluster centre, which we were not able to detect yet due to confusion with the BCG.

The photometric redshift of the image system is derived from the CLASH ACS-IR catalogue to be $z_{\text{phot}} = 4.19^{+0.12}_{-0.14}$. This redshift estimate is neither consistent with the photometric redshift estimates presented in Halkola et al. (2008) ($z_{\text{phot}}^{11a} = 2.94 \pm 0.23$, $z_{\text{phot}}^{11b} = 3.61 \pm 0.20$, $z_{\text{phot}}^{11c?} = 2.80 \pm 0.73$ and $z_{\text{phot}}^{12a} = 2.79 \pm 0.75$, $z_{\text{phot}}^{12c?} = 1.75 \pm 1.09$; cf. Table 2.1 for nomenclature) nor with the estimates from fitting strong-lensed data ($z_{\text{fit}}^{\text{B}} = 1.2 \pm 0.1$; cf. Table 2.1 for nomenclature) by Bradač et al. (2008).

Further implications of this system will be discussed in Section 2.4.1.

Multiple image system 4 (three images)

This system (cf. Fig. 2.4) is identified in Halkola et al. (2008) as system 8 consisting of a two-image system merging on a tangential critical line, and we confirm the third image (image 4.3) of this system predicted by Halkola et al. (2008) as ‘8c?’. In Bradač et al. (2008) the two merging images are identified as well. All images are located in the north-east with respect

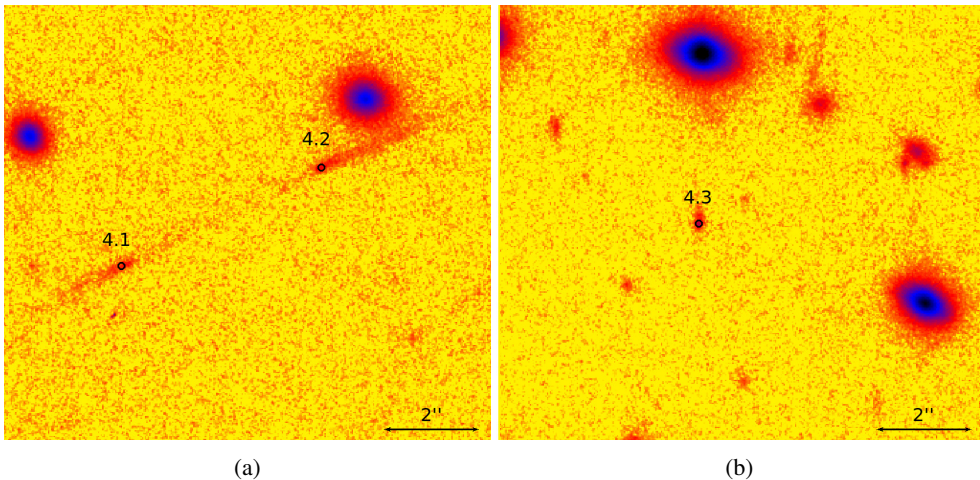


Figure 2.4: Zoom-in on multiply lensed images of multiple image system 4. (a) Image 4.1. (b) Images 4.2 and 4.3. Due to the faintness of the arcs we show a false colour version of the CLASH ACS-IR detection image (cf. Section 2.2).

to the centre of the cluster. Our model predicts the position of the third image (image 4.3) as well. We checked the redshifts of all images in the CLASH ACS-IR catalogue, and found them to be consistently around $z_{\text{phot}} = 3.63^{+0.11}_{-0.08}$, which is also consistent with the photometric redshift estimate of image ‘8c?’ ($z_{\text{phot}}^{8c?} = 3.68 \pm 0.11$; cf. Table 2.1 for nomenclature), but not consistent with the redshift of image ‘8a’ ($z_{\text{phot}}^{8a} = 1.88 \pm 0.19$; cf. Table 2.1 for nomenclature) both estimated by [Halkola et al. \(2008\)](#). Neither is it consistent with the redshift estimate from fitting strong-lensed data ($z_{\text{fit}}^C = 2.0 \pm 1.0$; cf. Table 2.1 for nomenclature) by [Bradač et al. \(2008\)](#).

2.3 Methods

The analysis of strong lensing data can be performed either with parametric or non-parametric modelling software. For the parametric approach a certain (physically or observationally motivated) mass distribution has to be assumed already a priori. The analysis then consists of finding appropriate values for the parameters of the initially assumed mass model. In contrast to that, non-parametric approaches do not require any initial assumptions about the mass distribution. Note, however, the regularization is done as described below.

2.3.1 Parametric – GLAFIC

For the parametric mass reconstruction we have used the publicly available software GLAFIC⁴ ([Oguri 2010](#)). Similar to other parametric software packages like LENSTOOL ([Kneib et al. 1996](#); [Jullo et al. 2007](#); [Jullo & Kneib 2009](#)), GLAFIC offers to set up a multiple component mass model where each component can be described by a large variety of different density profiles. These profiles are usually defined by six to seven parameters (e.g. velocity dispersion, orientation angle and so on).

⁴We have used version 1.1.5 for our analysis. The software can be downloaded from: <http://www.slac.stanford.edu/~oguri/glafic/>

The final parametric model we used to obtain the mass estimates presented further below consists of two smooth mass components for the dark matter including the mass of the ICM, two profiles for the cD galaxies, profiles for further cluster members and finally two additional perturbers (cf. Section 2.4.1). In the following we will discuss the particular types of profiles used for each component in more detail.

Cluster galaxies and perturbers

For modelling the mass distribution of cluster member galaxies we employ a pseudo-Jaffe ellipsoid (‘Jaffe’ in GLAFIC) whose three-dimensional radial density profile is given by

$$\rho(r) \propto \frac{\sigma}{(r^2 + r_{\text{core}}^2)(r^2 + r_{\text{trunc}}^2)}, \quad (2.1)$$

with velocity dispersion σ , core radius r_{core} and truncation radius r_{trunc} . We apply this profile in particular for modelling both cD galaxies individually, as well as both perturbers. In contrast to that the parameters of the other remaining cluster member galaxies are linked according to the following scaling relations

$$\frac{\sigma_i}{\sigma_*} = \left(\frac{L_i}{L_*}\right)^{\frac{1}{4}} \quad \text{and} \quad \frac{r_{\text{trunc},i}}{r_{\text{trunc},*}} = \left(\frac{L_i}{L_*}\right)^{\frac{1}{2}}, \quad (2.2)$$

thus yielding a constant mass-to-light ratio M/L (Natarajan & Kneib 1997). This approach was also performed by Bradač et al. (2008) and Halkola et al. (2008).

The luminosities L_i were derived from the $F814W$ magnitudes taken from the provided CLASH ACS-IR catalogue as well as the other parameters needed. Only the position angles θ_i are not provided in the catalogue, but can be easily estimated from a SExtractor (Bertin & Arnouts 1996) run on one of the respective detection images. The reference values for L_* , σ_* and $r_{\text{trunc},*}$ were chosen such that a galaxy with $\text{mag}_{AB}^{F814W} = 20.5$ has a velocity dispersion $\sigma = 260 \text{ km s}^{-1}$ and a truncation radius $r_{\text{trunc}} = 5 \text{ kpc}$ which is the same normalization as given in Bradač et al. (2008).

This catalogue of cluster member galaxies contains 24 out of the 48 spectroscopically confirmed cluster members from Lu et al. (2010) that are within radius $R \leq 75 \text{ arcsec}$ from the cluster centre. Additionally, we also included the brightest galaxies that are also within radius $R \leq 75 \text{ arcsec}$ from the cluster centre with redshifts in the range $0.4 \leq z_{\text{gal}} \leq 0.5$ and that are not already contained in the previous sample of 24 galaxies. In total, we compiled a catalogue (cf. Table 2.2) of 101 cluster member galaxies.

Smooth mass component

Considering the merger history of the cluster as mentioned in Section 2.1 and the studies from Halkola et al. (2008) and Bradač et al. (2008), we introduced two smooth cluster components in our parametric model right from the beginning as well. Although the topic is still under discussion, one of the most appropriate types of profiles for the dark matter dominated smooth cluster component seems to be the Navarro–Frenk–White (NFW) profile (Navarro et al. 1997). This form of universal mass halo is predicted by cosmological dark matter simulations. Its three-dimensional radial density profile is given as

$$\rho_{\text{nfw}}(r) = \frac{\rho_s}{(r/r_s)(1 + r/r_s)^2}, \quad (2.3)$$

with the characteristic density ρ_s and the scale radius r_s .

Table 2.2: Cluster member galaxies as used for our analysis in GLAFIC. Positions are given with respect to the cluster centre at position RA = 206°8775, Dec = −11°7526 (J2000). Spectroscopically confirmed cluster members by Lu et al. (2010) are marked with ‘asterisk (*)’. The complete Table 2.6 is listed in Appendix 2.A.

Δ RA (arcsec)	Δ Dec (arcsec)	L_i^{F814W}/L_*^{F814W}	e	θ (°)	Lu et al. (2010)
−39.7217	48.1187	3.53737	0.288	76.6772	
17.8258	−53.1457	2.94307	0.251	20.6834	
41.5544	−44.2282	2.53396	0.206	−42.7160	*
50.8514	−33.4127	2.46740	0.275	−87.0736	*
−27.2336	79.3580	2.24430	0.362	24.1564	*
...

The *concentration parameter* c is defined as the ratio of the virial radius r_{vir} to the scale radius r_s ,

$$c = \frac{r_{\text{vir}}}{r_s}. \quad (2.4)$$

Oguri (2010) defines the virial mass M in GLAFIC as

$$M = \frac{4\pi}{3} r_{\text{vir}}^3 \Delta(z) \bar{\rho}(z) = \int_0^{r_{\text{vir}}} 4\pi r^2 \rho_{\text{nfw}}(r) dr, \quad (2.5)$$

where the expression $\Delta(z)\bar{\rho}(z)$ describes the mean overdensity inside a sphere with radius r_{vir} . The non-linear overdensity $\Delta(z)$ is evaluated by adopting the fitting formula of Nakamura & Suto (1997).

Optimization and uncertainties

The optimization of the parameters of the assumed mass profiles is based on a χ^2 -minimization with a *downhill-simplex* algorithm (Nelder & Mead 1965), described in more detail in Oguri (2010). Due to the complexity of the mass model we restrict all calculations to the source plane, where we approximate the χ^2 of the i th image per multiple image system as (Oguri 2010)

$$\chi_{\text{pos}}^2 \approx \chi_{\text{pos,src}}^2 = \sum_i \frac{(\mathbf{u}_{i,\text{obs}} - \mathbf{u})^T \mathbf{M}_i^2 (\mathbf{u}_{i,\text{obs}} - \mathbf{u})}{\sigma_{i,\text{pos}}^2}. \quad (2.6)$$

This ‘corrected’ source-plane χ^2 follows from the assumption that the fitted image plane position is close to the observed image position. Then, the magnification tensor $\mathbf{M}_i = d\mathbf{x}_i/d\mathbf{u}$ can be used to approximately relate the image positions \mathbf{x} to the source-plane positions \mathbf{u} (Kochanek 1991), i.e.

$$\mathbf{x}_{i,\text{obs}} - \mathbf{x}_i \approx \mathbf{M}_i (\mathbf{u}_{i,\text{obs}} - \mathbf{u}). \quad (2.7)$$

We set the positional uncertainties $\sigma_{i,\text{pos}}$ of multiply lensed images to 0.5 arcsec which is higher than the typically observed value of ~ 0.1 arcsec for measurements by *HST* (e.g. Golse et al. 2002). However, setting the uncertainties that low during the optimization process was too restrictive for the optimization routine. This is in fact necessary because of the unknown matter distribution along the line-of-sight, which may change positions by this amount on the scale of galaxy clusters (M. Bartelmann, private communication).

For the estimation of uncertainties of model parameters, GLAFIC provides built-in functions in order to perform a Bayesian likelihood interpretation employing a Monte Carlo Markov Chain (MCMC) approach. However, a non-trivial complication arises, due to the limitation of all calculations to the source plane. Although GLAFIC also provides routines in order to perform MCMC calculations in the source plane in general, a test run of the built-in MCMC routine of GLAFIC in the source plane revealed that a fair fraction of the models did not correspond to the observations, for example, predicting an incorrect amount of images per multiple image system or incorrect image positions. The reason is that equation (2.7) is not valid in the direct vicinity of a caustic. In regions of strongly clustered caustics this leads sometimes to wrong models, which we needed to discard.

Since a direct inversion for each single χ^2 -calculation is too time consuming (e.g. one sequence of χ^2 -minimizations of the mass model presented in Section 2.4.1 in the image plane takes about one month on a typical work station⁵), we employed a Monte Carlo approach, i.e. we varied the input data within the given uncertainties in order to derive uncertainties for the model parameters including a check for the correct amount and positions of images at the end of a full χ^2 -minimization run. In particular, the input data for GLAFIC consists of the positions of the images in the multiple image systems (cf. Table 2.1). So, the initial positions were varied by drawing random positions from a Gaussian distribution centred on the observed position with width $\sigma = 0.5$ arcsec corresponding to the assumed positional uncertainties of the images. Furthermore, the positions of merging images were linked to each other, so that they were always shifted by the same amount in the same direction in order to avoid shifts of the images against each other (positional fluctuations due to large scale structure affect larger scales).

For each set of varied input data we performed a χ^2 -minimization run of the mass model in the source plane based on the initial best-fitting parameters. The photometric redshifts for multiple image systems 1, 3 and 4 were also free to vary within the given errors. In total 500 models were calculated. Finally, the prediction of the correct amount of images per multiple image system and their positions were checked visually for each such model by performing a full inversion of the lens equation. This resulted in 366 accepted models (i.e. ≈ 73 per cent) from which the 68 per cent confidence intervals for the results obtained with GLAFIC were calculated.

Since the optimization for a set of varied input data started always from the best-fitting model parameters, this sampling method is rather insensitive to possibly existing, entirely different solutions for the mass model, and assumes implicitly that the best-fitting model is the global minimum in solution space.

2.3.2 Non-parametric – PIXELENS

Detailed information about the functionality of PIXELENS⁶ is presented in Saha & Williams (1997, 2004). The non-parametric approach in PIXELENS employs a formulation of the lens equation in terms of the arrival-time surface. Introducing square mass pixels allows it then to express the effective lensing potential in terms of the convergence κ such that the lens equation becomes linear in the unknowns, κ and source plane positions β . Observations of image positions of multiply lensed systems, and in general also time delay information, then impose constraints on the linear equation system.

In addition to restricting all calculations again to the source plane, such an equation system

⁵Four CPUs with 2.66 GHz each and 8 GB RAM. Note that GLAFIC is not parallelized yet.

⁶We have used version 2.17 for our analysis. The software can be downloaded from: <http://www.qgd.uzh.ch/projects/pixelens/>

remains under-determined which results in a whole family of best-fitting models for a given image configuration.

In order to deal with this situation, `PIXELENS` employs a built-in MCMC approach and creates an ensemble of 100 lens models per given image configuration. Since all equations are linear in the unknowns, the best-fitting model and its uncertainties are obtained by finally averaging over the ensemble.

Note that in addition to the standard regularization assumptions of `PIXELENS` (‘the prior’, cf. Saha & Williams 2004), we demand further that the tilt of iso-contours is $\leq 60^\circ$.

2.4 Analysis

2.4.1 Parametric – GLAFIC

For the parametric modelling, we did not include all image systems available and all their respective images at once. Instead, we included them iteratively. Thus, deriving the best-fitting model in `GLAFIC` was a sequence of including a multiple image system with subsequent source plane optimization of the proposed mass distribution, and then checking the predictions via a full inversion of the lens equation in order to calculate predicted images. If additional images are predicted by the mass model, these have to be checked carefully by comparing their position, morphology, colour, surface brightness and redshift with all other confirmed images of the multiple image system. Here especially, the `CLASH` catalogues constitute an invaluable data source and facilitate the decision whether or not to include or refuse such an additionally predicted image, and hence improve the whole mass model significantly.

Based on the $F814W$ filter, we define a limiting magnitude for a 5σ source detection as $m_{\text{lim}}^{F814W} = ZP^{F814W} - 2.5 \log_{10}(5 \sqrt{N_{\text{pix}}} \sigma_{\text{bkg}})$ (e.g. Erben et al. 2009), where ZP is the extinction-corrected magnitude zeropoint in $F814W$, N_{pix} the minimal number of continuous pixels that define a source in the catalogue (i.e. $N_{\text{pix}} = 9$) and σ_{bkg} the sky background noise estimation. The values for the limiting magnitude and surface brightness are then $m_{\text{lim}}^{F814W} \approx 28.4$ mag and $S_{\text{lim}}^{F814W} \approx 24.9$ mag arcsec $^{-2}$, respectively.

If the additional image is indeed a correct prediction (with a candidate source) with respect to the limits defined above, it will be included as a new constraint for the next optimization step in addition to the next multiple image system. If the additional image is a false prediction (no candidate source available), one will vary the input model parameters and start with those a new optimization run.

Eventually, this whole process converged to a best-fitting model including all four multiple image systems presented in Section 2.2.1. These provide in total 38 constraints from observed image positions with which the 28 free model parameters were fit, yielding a reduced χ_{red}^2 of 0.68 (9 degrees of freedom). We did not include further constraints from fluxes as a measure for the magnification ratio, since the systematic errors for flux constraints are still under discussion (e.g. Kochanek 1991, Liesenborgs & De Rijcke 2012).

The critical curves and caustics with observed and predicted image positions for all multiple image systems included in the best-fitting model are presented in Fig. 2.5.

In Tables 2.3, 2.4 and 2.5 we present an overview of the fitted values of parameters of the best-fitting model in `GLAFIC` including the 68 per cent confidence intervals estimated from the Monte Carlo sampling as described in Section 2.3.1.

Finally, we show in Fig. 2.6 the convergence contours obtained from the best-fitting model. The contours are very elliptical and resemble the contours obtained with `PIXELENS` (cf. Fig. 2.8) in general.

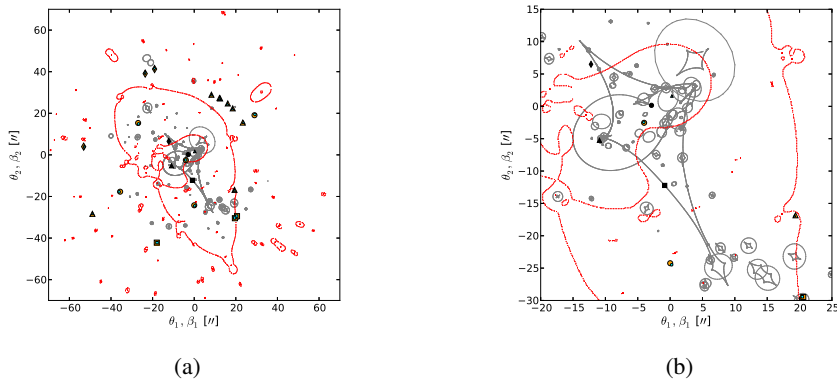


Figure 2.5: Critical curves (red, dotted lines) and caustics (grey, solid lines) in RX J1347.5–1145 obtained from the best-fitting model in GLAFIC. The critical curves and caustics are plotted for the redshift of multiple image system 2 at $z = 1.75$. Furthermore, we show observed images (orange), predicted images (cyan) and the respective sources (black) for all four multiple image systems. Different symbols denote different multiple image systems (system 1: \circ ; system 2: \square ; system 3: \triangle ; system 4: \diamond). (a) Total area used for the strong lensing analysis. (b) Zoom-in on central part.

Table 2.3: Parameters for the smooth mass components described by NFW profiles from the best-fitting model in GLAFIC, the uncertainties are estimated as described in Section 2.3.1. ‘NFW1’ is located close to the BCG and ‘NFW2’ is in the south-east of the cluster (cf. Fig. 2.6). For a detailed explanation of the parameters and model please refer to Section 2.3.1.

Model	$M (M_{\odot} h^{-1})$	ΔRA (arcsec)	ΔDec (arcsec)	e	θ ($^{\circ}$)	c
NFW1	$(5.75^{+0.72}_{-0.35}) \times 10^{14}$	$0.14^{+0.36}_{-0.45}$	$5.15^{+0.59}_{-0.34}$	$0.15^{+0.04}_{-0.02}$	$-144.91^{+2.11}_{-4.63}$	$6.08^{+0.18}_{-1.15}$
NFW2	$(5.23^{+0.39}_{-0.56}) \times 10^{14}$	$-8.26^{+0.41}_{-0.50}$	$-12.84^{+0.43}_{-0.68}$	$0.66^{+0.02}_{-0.03}$	$-145.80^{+0.70}_{-0.74}$	$4.72^{+0.24}_{-0.24}$

Table 2.4: Parameters for the two cD galaxies in the cluster each modelled separately with a pseudo-Jaffe profile (cf. Section 2.3.1 also for a detailed explanation of the parameters) from the best-fitting model obtained in GLAFIC.

Object	σ (km s^{-1})	ΔRA (arcsec)	ΔDec (arcsec)	e	θ ($^{\circ}$)	r_{trunc} (arcsec)	r_{core} (arcsec)
BCG	593.59	0.00	0.00	0.32	2.16	4.89	0.95
2 nd cD	344.00	-18.27	-1.95	0.26	44.37	3.87	0.79

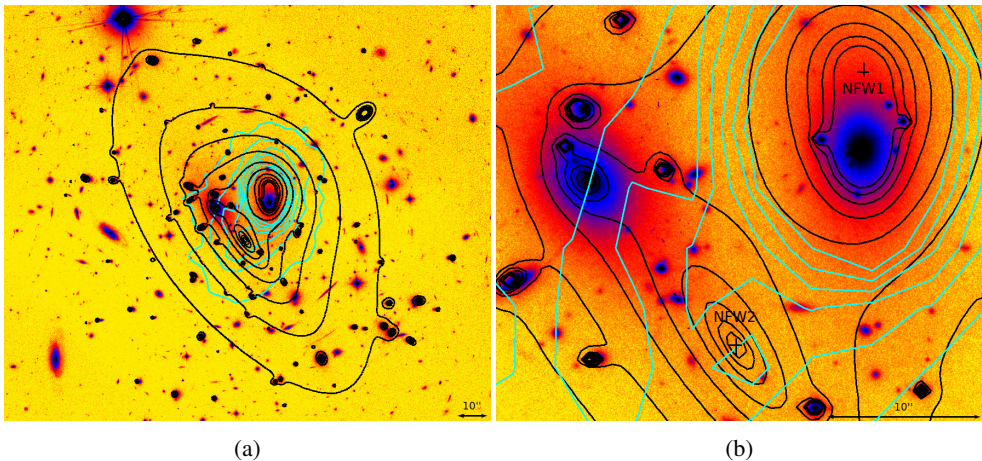


Figure 2.6: (a) Surface mass density contours (solid, black lines) in units of the critical surface mass density obtained from the best-fitting parametric model in GLAFIC for redshift $z = 1.75$. Furthermore, we show X-ray brightness contours (solid, cyan lines) from *Chandra*. The contours of the second NFW profile (NFW2) coincide with the centre of the south-eastern extension of the X-ray surface brightness contours. (b) Zoom-in on the positions of the NFW profiles (black crosses, showing the 68 per cent confidence interval for the position), mass and X-ray contours.

The distinct ellipticity may be caused by the new interpretation of the prominent, elongated arc feature (images 2.2 and 2.3) of multiple image system 2 (cf. Fig. 2.2 and Section 2.2.1) to count as two merging images, and not just as one image constraint, as it was described in both Bradač et al. (2008) and Halkola et al. (2008).⁷ However, when counting this elongated arc as the result of two merging images, the course of the critical curve in this region must necessarily change such that it must go straight through the symmetry axis of this arc (cf. Fig. 2.5). This in turn requires an adjustment of the mass profile accordingly, and this was achieved using GLAFIC by shifting the second NFW profile away from the position of the second cD galaxy (where we had placed the second NFW halo initially) towards the south-west. It was necessary to keep the position of the second NFW profile free [not fixed at the position of the second cD galaxy], as we already mentioned in Section 2.3.1.

Multiple image system 3 in detail

Apart from the new interpretation of the elongated arc in multiple image system 2 and its consequences for the mass distribution, another new interpretation was to count images 3.1 to 3.8 as only one multiple image system. This interpretation was not at all clear from the beginning due to differing interpretations of the affiliation of these images in Bradač et al. (2008) and Halkola et al. (2008). Initially, we followed the image affiliations presented in the latter study, since their definitions appeared to be more consistent. This means in particular that we also affiliated images 3.1 to 3.8 with two different multiple image systems (we want to emphasize again, that images 3.2 and 3.3 were not at all considered in both studies, although they were visible in earlier data sets) in the beginning of our analysis.

However, whenever models were employed with system 3 split into two systems, GLAFIC predicted additional images in the vicinity of images 3.7 (‘11c?’ in Halkola et al. 2008; also

⁷Halkola et al. (2008) present a simulated image of images 2.2 and 2.3 based on their best-fitting model which does suggest they also modelled it as two merging images.

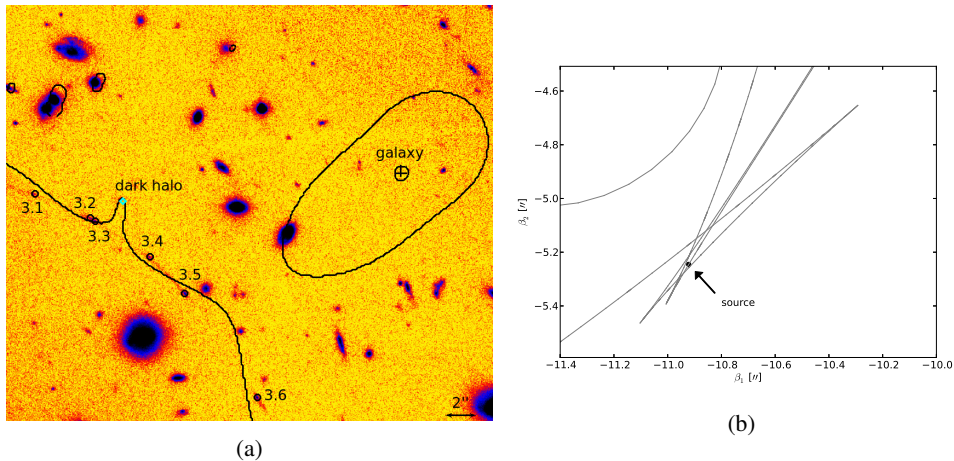


Figure 2.7: (a) Critical curves (solid, black lines) close to images 3.1 to 3.6 at redshift $z = 4.19$ in RX J1347.5–1145. Furthermore, the positions of the perturbers necessary for this course of the critical curves are shown. Very close to the position of the object ‘dark halo’ (cyan) is a very faint source visible, whereas the object ‘galaxy’ (black cross) represents a massive model of a possible overdensity in this region. Due to the faintness of images 3.1 to 3.6 we use a high contrast, false colour version of the CLASH ACS-IR detection image. (b) Multiply folded ‘swallowtail’ caustics (solid, grey lines) and position of the ‘source’ (black) for image system 3 within these. Compare to similar arc feature in A370 (Richard et al. 2009).

cf. Table 2.1 for nomenclature) and 3.8 (‘11d?’ in Halkola et al. 2008), respectively. This is indeed expected from the small separation of images 3.1 to 3.6.

A search in the CLASH catalogues revealed no second image with appropriate redshift in the vicinity of image 3.8 (‘11d?’ in Halkola et al. 2008) and the proposed candidate image (‘12c?’) from Halkola et al. (2008) is included in the CLASH ACS-IR catalogue with a too low redshift of $z_{\text{phot}} = 0.87^{+0.18}_{-0.36}$.

Therefore and further because of the redshifts of all images later found to be consistent due to the then available CLASH catalogues, we finally interpreted all images to originate from one source only.

Moreover, the north-western arc structures (images 3.1 to 3.6 in Fig. 2.7) of image system 3 strongly resemble the prominent arc feature of A370 (cf. Richard et al. 2009), as mentioned in Section 2.2.1. The special arc configuration in A370 is caused by the source being located on a doubly folded caustic (a so-called ‘swallowtail’).

Guided by this resemblance between multiple image system 3 and the multiple image system in A370, we adopted this swallowtail folding by at first modelling one of the more luminous neighbouring galaxies separately at a fixed position, making use again of the pseudo-Jaffe profile (cf. Section 2.3.1). Later the coordinates were left free for fitting as well, because during the optimization high masses were assigned to this object (i.e. ‘galaxy’ in Table 2.5). Thus, we rather tend to interpret the object ‘galaxy’ to represent an overdensity in the whole north-western part of the cluster than just to count it as an individual massive object.

In addition to that, we further included another perturber (i.e. ‘dark halo’ in Table 2.5) in close vicinity to the two merging images 3.2 and 3.3 modelled again with a pseudo-Jaffe profile (cf. Section 2.3.1 and Table 2.5) in order to force the critical line to bend exactly through the merging images (cf. Section 2.2.1). All seven parameters of this additional mass halo were left free for fitting (of course providing appropriate initial values, especially for

Table 2.5: Model parameters for the additionally predicted perturbers which were both modelled with the pseudo-Jaffe profile (cf. Section 2.3.1 also for a detailed explanation of the parameters). In case the parameters were free for optimization during the error estimation process (cf. Section 2.3.1) the respective 68 per cent confidence intervals are noted as well.

Object	σ (km s ⁻¹)	Δ RA (arcsec)	Δ Dec (arcsec)	e	θ (°)	r_{trunc} (arcsec)	r_{core} (arcsec)
galaxy	762.85 ^{+40.45} _{-94.09}	32.29 ^{+0.46} _{-0.33}	30.29 ^{+0.54} _{-0.26}	0.35	-49.16	1.51 ^{+0.20} _{-0.19}	0.19 ^{+0.09} _{-0.86}
dark halo	290.28 ^{+87.71} _{-66.78}	14.04	28.42	0.49	10.94	1.25 ^{+0.05} _{-0.53}	1.10 ^{+0.69} _{-0.05}

its position). Interestingly, the fitted position for the additional profile coincides with the position of a very small and faint object (cf. Fig. 2.7). A search for this object in both CLASH catalogues revealed a redshift limit of $z_{\text{phot}} > 0.7$ and a very high upper limit of $z \approx 3$. Although an unambiguous determination of its photometric redshift is not possible at the moment, the data rather suggest to assign the object to the background of the cluster ($z_{\text{cluster}} = 0.451$). Whether this really means that this additional mass halo is not physically related to the respective faint object at all and thus rather another dark matter overdensity, is hard to assess at the moment. See also [Liesenborgs & De Rijcke \(2012\)](#) on the degeneracies involved in modelling cluster lens components.

2.4.2 Non-parametric – PIXELENS

The resolution for the pixel map radius in PIXELENS is limited only by computational power and time. The highest, still feasible resolution comprised ~ 22 mass pixels corresponding to a physical size of ~ 3.2 arcsec \times 3.2 arcsec per pixel.

Furthermore and in analogy to the parametric approach, we did not include all four multiple image systems available in our modelling at once. Instead, we included them again sequentially in order to check for additional predicted images.

Finally, we included multiple image systems 1 (images 1.1 to 1.5), 2 (images 2.1 to 2.3) and 4 (images 4.1 to 4.3) in full detail. The very complicated eightfold lensed image system 3, however, had to be approximated: the north-western part of image system 3 with the sixfold image (images 3.1 to 3.6) seems to arise due to a complicated caustic folding caused by a local disturbance in the mass distribution, as discussed in Section 2.4.1. Thus, we decided to include only the ‘main’ images of this north-western part (i.e. images 3.1, 3.4, 3.5 and 3.6) and images 3.7 and 3.8 in our PIXELENS analysis.

In Fig. 2.8 we show contours of the convergence in logarithmic spacing derived from this mass model. From that already a highly elliptical and irregular mass distribution is visible.

It is apparent that PIXELENS finds significant substructure in the south-eastern part of the cluster. This is coinciding very well with the second NFW component of the GLAFIC model and the X-ray observations from *Chandra* (cf. Fig. 2.6). As we have noticed in Section 2.1, an irregular extension to the south-east of the cluster is visible in X-ray images as well. Thus, this lensing analysis also provides further support for RX J1347.5–1145 being in a merger between two subclusters.

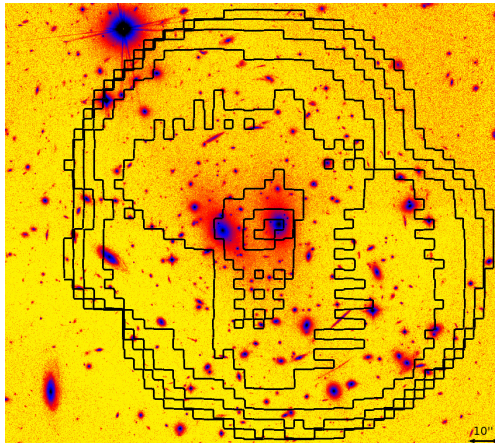


Figure 2.8: Surface mass density contours (solid, black lines) in units of the critical surface mass density obtained from the best-fitting, non-parametric model in `PIXELEN`s for the total mass. The spacing between contour levels is logarithmic and the difference between contour levels is 0.5 mag in surface density. The sixth contour from the outside corresponds to the critical density. Contours are overlaid on a composite false colour image of RX J1347.5–1145. North is up and east is left.

2.4.3 Mass estimates – `PIXELEN`s and `GLAFIC`

From the best-fitting models obtained both with `PIXELEN`s and `GLAFIC` we derived estimates for the projected mass enclosed by a cylinder of radius R centred on the BCG:

$$M(< R_n) = \sum_{i=1}^n \kappa(R_i, z) \Sigma_{\text{crit}}(z) \pi (R_i - R_{i-1})^2, \quad (2.8)$$

where the convergence κ is circularly symmetric and $R_0 = 0$.

Apart from deriving a best-fitting model, we also investigated with `PIXELEN`s additional mass models derived with different image configurations, i.e. less images per image system and less image systems in total. The results support our simplification regarding image system 3 in the `PIXELEN`s analysis (i.e. not including images 3.2 and 3.3; cf. Section 2.4.2) since different image configurations do not affect the enclosed mass estimates as shown in Fig. 2.9: all mass estimates are statistically consistent within their 68 per cent confidence intervals. Hence, we conclude that the image systems provide enough constraints for deriving consistent mass estimates with `PIXELEN`s; as expected, the uncertainties become larger for models with less constraints. We also want to emphasize that nine out of in total sixteen images are located in a distance range of $150 \text{ kpc} \leq R_{\text{img}} \leq 200 \text{ kpc}$ from the cluster centre, thus, the most robust estimates for the enclosed mass of the cluster can only be obtained within this range. This argument holds also for the `GLAFIC` analysis.

In Fig. 2.10(a) we show the enclosed mass estimates from the best-fitting models of `GLAFIC` and `PIXELEN`s, respectively. The errors for the `GLAFIC` mass estimates were derived using the Monte Carlo approach described in Section 2.3.1. It is apparent that both estimates are consistent within radii $R \lesssim 170 \text{ kpc}$ best constrained by multiple image systems, but start to deviate for larger radii where less strong lensing constraints are available.

Additionally, we show in Fig. 2.10b the differential mass dM/dR plotted against the radius R for the best-fitting models in `PIXELEN`s and `GLAFIC`, respectively. Note, how well the profiles agree overall, just in the central region and for larger radii (less strong lensing constraints) does `PIXELEN`s overestimate the mass as compared to `GLAFIC`.

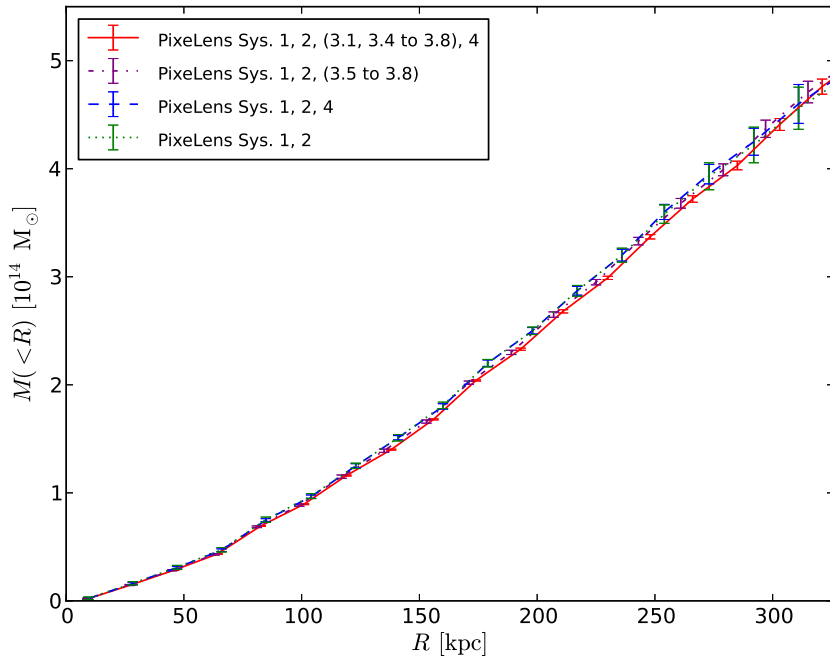


Figure 2.9: Plots of enclosed mass estimates derived from different PIXELENS models. The models differ by including less and less images per multiple image system and less and less multiple image systems in total as indicated in the legend. All mass estimates are statistically consistent within their 68 per cent confidence intervals.

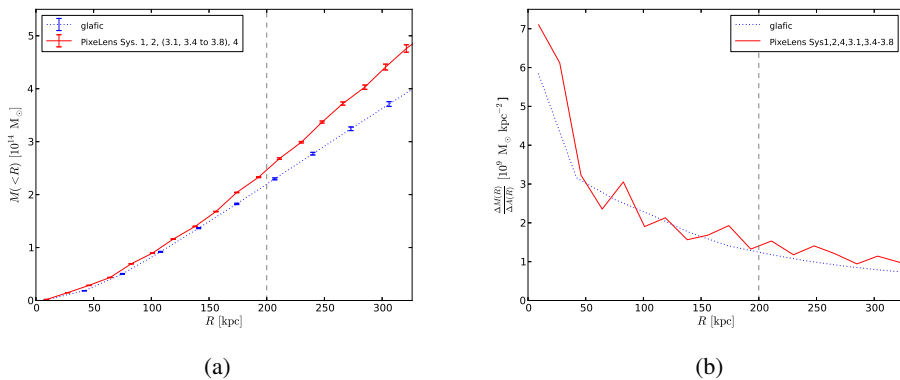


Figure 2.10: (a) Plots of enclosed mass estimates derived from PIXELENS (red, solid line) and GLAFIC (blue, dotted line) best-fitting models, respectively. The dashed, vertical line marks the radius $R = 200$ kpc (i.e. distance from cluster centre of multiple image system 2) where deviations in the profiles between PIXELENS and GLAFIC arise. (b) Differential mass plots for the best-fitting models of PIXELENS (red, solid line) and GLAFIC (dotted, blue line), respectively. The central regions seem to be systematically overestimated by PIXELENS, and in addition PIXELENS assigns also more mass to larger radii. Both combined results in the observed discrepancy between the enclosed mass estimates of PIXELENS and GLAFIC, respectively.

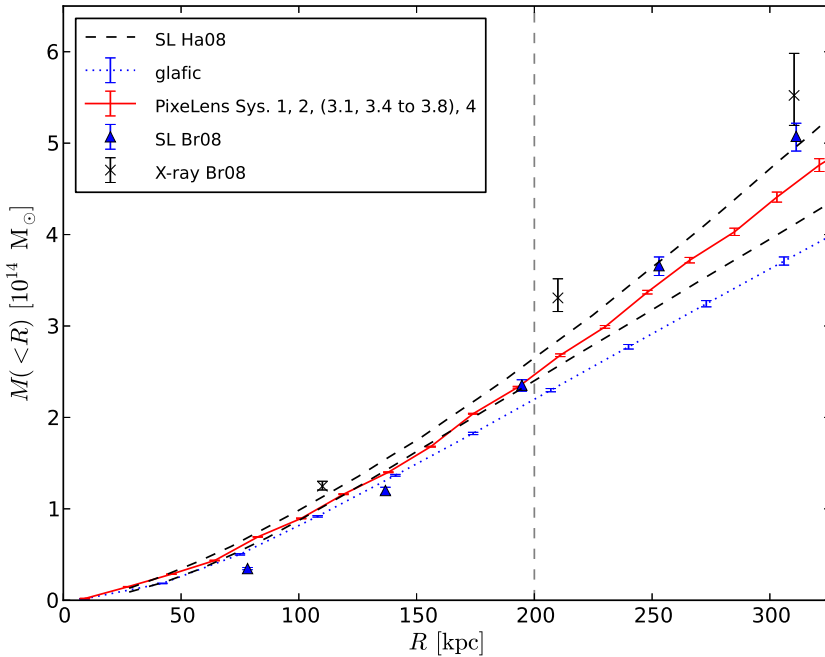


Figure 2.11: Enclosed mass estimates from strong lensing analyses using the non-parametric approach of `PIXELENS` (solid, red line), the parametric approach of `GLAFIC` (blue, dashed line), a parametrized model (blue, filled triangles) by [Bradač et al. \(2008\)](#) (Br08) and the 68 per cent confidence interval obtained by [Halkola et al. \(2008\)](#) (Ha08) by using strong lensing data only (black, dashed lines). Additionally, we show a mass estimate from X-ray data obtained by [Bradač et al. \(2008\)](#) (Br08). The dashed, vertical line marks the position of images 2.2 and 2.3 at a radius $R \sim 200$ kpc from the cluster centre.

Finally, we compare the best-fitting mass estimates from `GLAFIC` and `PIXELENS` with the results presented in [Bradač et al. \(2008\)](#) and [Halkola et al. \(2008\)](#) in Fig. 2.11. Among these results are projected mass estimates from an X-ray data analysis, a parametric strong lensing analysis both obtained by [Bradač et al. \(2008\)](#)⁸ and the 68 per cent confidence interval based on strong lensing data from [Halkola et al. \(2008\)](#). While the estimates from strong lensing analyses by [Bradač et al. \(2008\)](#) and by [Halkola et al. \(2008\)](#) and from `PIXELENS` agree well within their uncertainties, the estimates from `GLAFIC` appear to be significantly lower, especially for radii $R \gtrsim 150$ kpc. The estimates based on X-ray measurements performed by [Bradač et al. \(2008\)](#) are somewhat high compared to the strong lensing analyses.

In order to give a quantitative example, we use the distance $R_{\text{arc}} \sim 35$ arcsec ~ 200 kpc from the prominent, elongated arc (images 2.2 and 2.3 at redshift $z = 1.75$) to the cluster centre for an estimate of the enclosed, projected mass $M(< R_{\text{arc}})$ within that radius. The best fit from `GLAFIC` yields a mass $M(< R_{\text{arc}}) \approx (2.19^{+0.01}_{-0.02}) \times 10^{14} M_{\odot}$, whereas the `PIXELENS` estimate exceeds this by ≈ 13 per cent with a mass of $M(< R_{\text{arc}}) \approx (2.47 \pm 0.01) \times 10^{14} M_{\odot}$. The `PIXELENS` estimate is statistically consistent with the estimates by [Halkola et al. \(2008\)](#) $M(< R_{\text{arc}}) \approx (2.56 \pm 0.12) \times 10^{14} M_{\odot}$ and [Bradač et al. \(2008\)](#) $M(< R_{\text{arc}}) \approx (2.47^{+0.06}_{-0.07}) \times 10^{14} M_{\odot}$.

⁸We want to emphasize that we are only comparing to their parametrized strong lensing model and not to their combined (non-parametric) strong and weak lensing model, since our focus is on the cluster core only.

However, the X-ray mass estimate $M(< R_{\text{arc}}) \approx (3.10^{+0.19}_{-0.14}) \times 10^{14} M_{\odot}$ within this radius as estimated by Bradač et al. (2008) is higher by ≈ 26 per cent compared to the values from `PIXELENS` and Halkola et al. (2008) and it exceeds the result from `GLAFIC` by ≈ 42 per cent. Note, however, that the strong lensing analyses by Bradač et al. (2008) and Halkola et al. (2008) make different assumptions about the lensing data (cf. Table 2.1).

2.5 Conclusions

Based on image identifications and strong lensing analyses in Bradač et al. (2008) and Halkola et al. (2008), as well as by interpreting some of the multiple image systems anew and including new images in the analysis, we present a consistent strong lensing analysis of the cluster RX J1347.5–1145.

We have reconstructed its mass distribution by employing the parametric software `GLAFIC` (Oguri 2010) and the non-parametric software `PIXELENS` (Saha & Williams 1997, 2004).

The results from these two analyses present further support for the merger scenario and produced mass maps of the cluster which agree well with each other in revealing several mass components and a highly elliptical mass distribution. Furthermore, the fitted position of the second NFW profile from our parametric `GLAFIC` model coincides very well with a region of shocked gas visible in X-ray data (Komatsu et al. 2001). Also the non-parametric best-fitting model obtained with `PIXELENS` assigns a high amount of substructure to this cluster region. We find that the mass estimates of `PIXELENS` and `GLAFIC` are consistent within ≈ 13 per cent at radii best constrained by our data, but deviate stronger for larger radii with less constraints.

This difference inside the arc radii could be due to on the one hand, that the parametric model used in `GLAFIC` could be inaccurate in the sense of not assigning sufficient mass to the profiles in use in this model (or just not containing sufficient additional profiles). This would imply that this model is not finding physically existent mass in the outer regions of the cluster which is in contrast well-captured by the other analyses (cf. Fig 2.11).

On the other hand, the mass model in `GLAFIC` is the only one among all these analyses that explains the images 3.1 to 3.8 as resulting from only one source. Considering the consistent redshifts of these images according to CLASH data supports this approach strongly. The eightfold occurrence of the same image is consistent with being caused by a complicated swallowtail caustic folding. Such a complicated folding can be caused by two additional mass components in the vicinity of images 3.1 to 3.6. One of these represents a mass overdensity in the north-western part of the cluster which is coinciding with a higher concentration of cluster galaxies in this region. The other perturbing profile is less massive and might be physically connected to a very faint background object. Hence, introducing these additional components which leads to the corresponding caustic folding, might be the reason for this particular mass model to require less mass than the other models.

Note, however, that Schneider & Sluse (2013) have shown that strong lensing observables (except time delays) are invariant under the so-called ‘source-plane transformation’ which leads to a certain arbitrariness in the choice of mass models. This invariance is only an approximate one for asymmetric lenses such as clusters and the comparison of our findings to previous results obtained with less well-constrained data (e.g. redshifts) and different assumptions about the mass profile shows that all these mass profiles are consistent albeit within a larger scatter not accounted for by the estimated uncertainties (cf. Fig 2.11). This degeneracy in mass profiles might thus be another hint towards such a fundamental level of systematic uncertainties immanent in strong lensing due to the source-plane transformation.

To measure cluster masses beyond the arc regime, X-ray masses or weak lensing estimates are required. In this respect it is also important to note that the weak lensing studies at larger

radii by Fischer & Tyson (1997) and the one included in Bradač et al. (2008) are consistent with X-ray measurements by Allen et al. (2002) and Bradač et al. (2008), respectively.

Acknowledgements

We would like to thank the anonymous referee for detailed comments which helped to further improve this work and its presentation.

This work profits immensely from the high-quality data made available by CLASH. We thank the whole CLASH team for their amazing effort and their community-friendly data release policy. We are deeply grateful to P. Saha and M. Oguri for making their software available to the public and especially for their helpful suggestions and correspondence. We also thank J. Wambsgans and H. Hoekstra for fruitful comments on this work.

Some/all of the data presented in this paper were obtained from the Mikulski Archive for Space Telescopes (MAST). STScI is operated by the Association of Universities for Research in Astronomy, Inc., under NASA contract NAS5-26555. Support for MAST for non-HST data is provided by the NASA Office of Space Science via grant NNX13AC07G and by other grants and contracts.

Bibliography

- Allen S. W., Schmidt R. W., Fabian A. C., 2002, *MNRAS*, 335, 256
- Allen S. W., Evrard A. E., Mantz A. B., 2011, *ARA&A*, 49, 409
- Bartelmann M., Limousin M., Meneghetti M., Schmidt R., 2013, *Space Sci. Rev.*, 177, 3
- Benítez N., 2000, *ApJ*, 536, 571
- Benítez N., et al., 2004, *ApJS*, 150, 1
- Bertin E., Arnouts S., 1996, *A&AS*, 117, 393
- Bradač M., et al., 2008, *ApJ*, 681, 187
- Coe D., Benítez N., Sánchez S. F., Jee M., Bouwens R., Ford H., 2006, *AJ*, 132, 926
- Cohen J. G., Kneib J.-P., 2002, *ApJ*, 573, 524
- Erben T., et al., 2009, *A&A*, 493, 1197
- Ettori S., Tozzi P., Borgani S., Rosati P., 2004, *A&A*, 417, 13
- Fischer P., Tyson J. A., 1997, *AJ*, 114, 14
- Giodini S., Lovisari L., Pointecouteau E., Ettori S., Reiprich T. H., Hoekstra H., 2013, *Space Sci. Rev.*, 177, 247
- Gitti M., Schindler S., 2004, *A&A*, 427, L9
- Gitti M., Piffaretti R., Schindler S., 2007, *A&A*, 472, 383
- Golse G., Kneib J.-P., Soucail G., 2002, *A&A*, 387, 788

- Halkola A., Hildebrandt H., Schrabback T., Lombardi M., Bradač M., Erben T., Schneider P., Wuttke D., 2008, *A&A*, 481, 65
- Jullo E., Kneib J.-P., 2009, *MNRAS*, 395, 1319
- Jullo E., Kneib J.-P., Limousin M., Elíasdóttir A., Marshall P. J., Verdugo T., 2007, *New J.Phys.*, 9, 447
- Jullo E., Natarajan P., Kneib J.-P., D’Aloisio A., Limousin M., Richard J., Schimd C., 2010, *Science*, 329, 924
- Kitayama T., Komatsu E., Ota N., Kuwabara T., Suto Y., Yoshikawa K., Hattori M., Matsuo H., 2004, *PASJ*, 56, 17
- Kneib J.-P., Ellis R. S., Smail I., Couch W. J., Sharples R. M., 1996, *ApJ*, 471, 643
- Kochanek C. S., 1991, *ApJ*, 373, 354
- Komatsu E., et al., 2001, *PASJ*, 53, 57
- Liesenborgs J., De Rijcke S., 2012, *MNRAS*, 425, 1772
- Lu T., et al., 2010, *MNRAS*, 403, 1787
- Mahdavi A., Hoekstra H., Babul A., Bildfell C., Jeltema T., Henry J. P., 2013, *ApJ*, 767, 116
- Nakamura T. T., Suto Y., 1997, *Prog. Theor. Phys.*, 97, 49
- Natarajan P., Kneib J.-P., 1997, *MNRAS*, 287, 833
- Navarro J. F., Frenk C. S., White S. D. M., 1997, *ApJ*, 490, 493
- Navarro J. F., et al., 2010, *MNRAS*, 402, 21
- Nelder J. A., Mead R., 1965, *Comput. J.*, 7, 308
- Oguri M., 2010, *PASJ*, 62, 1017
- Plagge T. J., et al., 2013, *ApJ*, 770, 112
- Planck Collaboration XX, 2013, preprint (arXiv:1303.5080)
- Pointecouteau E., Giard M., Benoit A., Désert F. X., Bernard J. P., Coron N., Lamarre J. M., 2001, *ApJ*, 552, 42
- Postman M., et al., 2012, *ApJS*, 199, 25
- Ravindranath S., Ho L. C., 2002, *ApJ*, 577, 133
- Richard J., Kneib J. P., Limousin M., Edge A., Jullo E., 2009, *MNRASL*, 402, L44
- Saha P., Williams L. L. R., 1997, *MNRAS*, 292, 148
- Saha P., Williams L. L. R., 2004, *AJ*, 127, 2604
- Sahu K. C., et al., 1998, *ApJL*, 492, L125
- Schindler S., et al., 1995, *A&A*, 299, L9

Schindler S., Hattori M., Neumann D. M., Böhringer H., 1997, *A&A*, 317, 646

Schneider P., Sluse D., 2013, preprint (arXiv:1306.4675)

Verdugo M., Lerchster M., Böhringer H., Hildebrandt H., Ziegler B. L., Erben T., Finoguenov A., Chon G., 2012, *MNRAS*, 421, 1949

2.A Additional table

In the following we show all entries of Table 2.2.

Table 2.6: Cluster member galaxies as used for our analysis in GLAFIC. Positions are given with respect to the cluster centre at position RA = 206°8775, Dec = −11°7526 (J2000). Spectroscopically confirmed cluster members by [Lu et al. \(2010\)](#) are marked with ‘asterisk (*)’.

Δ RA (arcsec)	Δ Dec (arcsec)	L_i^{F814W}/L_*^{F814W}	e	θ (°)	Lu et al. (2010)
−39.7217	48.1187	3.53737	0.288	76.6772	
17.8258	−53.1457	2.94307	0.251	20.6834	
41.5544	−44.2282	2.53396	0.206	−42.7160	*
50.8514	−33.4127	2.46740	0.275	−87.0736	*
−27.2336	79.3580	2.24430	0.362	24.1564	*
−27.2876	5.4396	2.12051	0.503	68.8246	*
38.9794	−42.0250	1.71759	0.041	7.2478	*
−18.6095	2.6698	1.64847	0.270	82.6778	*
−23.0746	−8.5878	1.49927	0.458	−62.4015	*
−22.9846	77.2931	1.48977	0.244	80.3499	*
−62.4737	8.0971	1.18424	0.362	55.7281	*
48.2256	−47.0963	1.17274	0.484	53.5377	*
9.6149	−10.1434	1.17090	0.499	−6.3700	*
−32.0951	−65.1452	1.15910	0.058	−5.4457	
−26.7350	0.7272	1.07567	0.680	−59.2898	
40.8006	−34.2792	1.06033	0.036	−40.7785	
62.1922	−18.8874	0.85373	0.074	−82.5937	*
13.9342	68.6970	0.75977	0.324	−84.1649	
−75.8858	7.5272	0.75900	0.080	44.2637	*
−23.1970	−45.5094	0.73228	0.213	−34.2751	*
−3.1057	−16.9722	0.59189	0.258	80.0946	
5.1408	−27.2938	0.54215	0.339	30.0499	
−25.8224	−24.7194	0.54095	0.474	61.7621	
3.8887	−60.0559	0.50896	0.253	18.7992	
−5.7607	−32.0206	0.50573	0.207	54.1367	*
28.9566	−42.3590	0.48856	0.339	−79.5943	
−53.0543	7.4660	0.48453	0.240	81.2871	
−47.2295	−36.3085	0.46868	0.072	56.5533	*
−15.9278	8.4848	0.46860	0.416	−74.2166	
−13.0075	−1.2845	0.46187	0.344	23.7418	*
−18.6862	−66.6648	0.45541	0.182	4.6530	*
−7.5478	−38.0369	0.43160	0.094	74.3849	
−31.6991	−3.4474	0.42760	0.243	−55.9427	*

Table 2.6: continued

ΔRA (arcsec)	ΔDec (arcsec)	L_i^{F814W}/L_*^{F814W}	e	θ ($^\circ$)	Lu et al. (2010)
-44.8387	-60.8540	0.40513	0.222	3.6020	*
-26.0035	-26.3999	0.40216	0.102	-61.3636	
-19.5642	0.2246	0.38765	0.111	43.2441	
1.9955	-60.8836	0.38655	0.378	-67.2284	
-17.7185	-13.6811	0.38191	0.549	84.9119	
-52.5830	16.9200	0.33309	0.085	-33.2646	*
29.7619	-7.6406	0.32982	0.505	-60.7757	
-58.3528	-40.0529	0.31880	0.531	-82.0882	
8.9842	-54.9277	0.30300	0.065	-45.5450	
32.1199	51.3749	0.29739	0.284	9.0851	*
-24.6413	54.6966	0.29363	0.464	80.4998	
-0.3146	35.7246	0.29078	0.041	75.7230	*
-14.0767	16.9405	0.28912	0.094	47.2299	
18.8204	7.3458	0.28655	0.254	-75.9544	
17.3351	8.2289	0.28447	0.125	-68.1228	
-34.4671	-5.4950	0.25740	0.167	41.4702	
3.9514	-15.7673	0.25340	0.247	65.0552	
-2.6658	0.6980	0.25082	0.075	87.1044	*
32.6365	-42.9257	0.24783	0.090	57.7627	
10.8637	-7.9333	0.23997	0.103	-59.4769	
-8.8783	-20.7349	0.23072	0.112	-80.4163	
17.2854	-16.6738	0.21380	0.042	-18.4828	
2.7256	1.9094	0.21016	0.051	75.8719	
22.1011	-62.2321	0.19803	0.136	22.9194	
57.2216	-36.4100	0.19252	0.136	89.5199	
37.9386	-20.3072	0.18835	0.044	-76.2698	
-54.7258	-20.0372	0.18535	0.113	47.8401	
-24.1916	25.5038	0.17072	0.372	-21.7318	
9.7229	35.1166	0.15801	0.301	48.3972	
2.5528	20.3393	0.15474	0.099	-5.8698	
1.7910	2.9520	0.13709	0.050	-64.0061	
22.9975	-70.2680	0.13250	0.121	-50.8443	
-39.5417	-39.1147	0.11678	0.175	-59.3118	
10.9807	-37.1243	0.10986	0.406	14.2908	
-14.9234	24.3425	0.10463	0.431	-85.2151	
-14.9328	-30.8290	0.10425	0.015	11.1597	
-35.2274	26.9813	0.08856	0.061	17.4453	
-69.1319	2.3112	0.07864	0.547	63.6670	
12.4600	36.2452	0.07686	0.079	46.7527	
39.4042	22.2937	0.07577	0.502	59.9982	
-62.1860	-41.0461	0.07261	0.419	-72.9015	
0.7589	-22.6274	0.06982	0.156	85.2696	
5.2020	-68.8057	0.05878	0.597	-59.1124	
-2.3281	45.8604	0.05568	0.284	5.9754	
-56.8631	31.1900	0.05509	0.135	63.2858	
-19.8497	33.0401	0.05491	0.024	-58.9078	

Table 2.6: continued

ΔRA (arcsec)	ΔDec (arcsec)	L_i^{F814W}/L_*^{F814W}	e	θ ($^\circ$)	Lu et al. (2010)
-39.5248	-19.5721	0.04921	0.078	-11.8005	
-0.3427	53.2843	0.04693	0.376	49.9376	
29.5290	-13.4928	0.04544	0.347	8.9301	
-7.2450	-28.8295	0.03917	0.174	49.6536	
15.0674	-49.0504	0.03284	0.270	-83.0496	
-13.3826	50.3690	0.03279	0.254	38.7964	
14.7866	67.4824	0.03002	0.072	-9.1470	
13.5407	44.1558	0.02587	0.053	-89.7780	
21.2461	38.5002	0.02559	0.079	-49.9459	
-0.3931	-42.9325	0.02498	0.103	7.0096	
10.1135	-22.9244	0.02323	0.199	75.2114	
15.7316	3.4700	0.02205	0.636	67.8657	
6.7050	35.8884	0.02072	0.662	64.8444	
-50.1448	12.9622	0.02056	0.042	-84.3996	
-66.1730	19.5286	0.02019	0.177	-19.5957	
-41.2027	-25.6763	0.01996	0.288	74.7811	
-23.2420	-20.2432	0.01929	0.159	-86.2468	
-57.6760	-20.0243	0.01855	0.180	64.3086	
48.2353	48.0218	0.01829	0.535	-69.3042	
-17.4762	-50.7308	0.01779	0.301	-15.2939	
-67.1695	7.2493	0.01704	0.280	-5.9881	
71.1990	-11.0092	0.01592	0.574	-2.1017	

Statistical uncertainties and systematic errors in weak lensing mass estimates of galaxy clusters

Upcoming and ongoing large area weak lensing surveys will also discover large samples of galaxy clusters. Accurate and precise masses of galaxy clusters are of major importance for cosmology, for example, in establishing well-calibrated observational halo mass functions for comparison with cosmological predictions. We investigate the level of statistical uncertainties and sources of systematic errors expected for weak lensing mass estimates. Future surveys that will cover large areas on the sky, such as *Euclid* or LSST and to lesser extent DES, will provide the largest weak lensing cluster samples with the lowest level of statistical noise regarding ensembles of galaxy clusters. However, the expected low level of statistical uncertainties requires us to scrutinize various sources of systematic errors. In particular, we investigate the bias due to cluster member galaxies which are erroneously treated as background source galaxies due to wrongly assigned photometric redshifts. We find that this effect is significant when referring to stacks of galaxy clusters. Finally, we study the bias due to miscentring, i.e. the displacement between any observationally defined cluster centre and the true minimum of its gravitational potential. The impact of this bias might be significant with respect to the statistical uncertainties. However, complementary future missions such as *eROSITA* will allow us to define stringent priors on miscentring parameters which will mitigate this bias significantly.

F. Köhlinger, H. Hoekstra and M. Eriksen
2015, *MNRAS*, **Volume 453**, Issue 3, pp 3107–3119

3.1 Introduction

Galaxy clusters play an important role in testing cosmological models, for example, by confronting the observed number of galaxy clusters with predictions of the halo mass function (e.g. Tinker et al. 2008, 2010 and references therein). This test is especially sensitive to the values of the matter content of the Universe, Ω_m , and the normalization of the primordial power spectrum of matter density fluctuations, σ_8 . Values for both parameters obtained from recent Sunyaev–Zel’dovich cluster counts by Planck Collaboration XX (2014b); Planck Collaboration XXIV (2015a) are in tension with other independent measurements (e.g. Planck Collaboration XVI 2014a; Planck Collaboration XIII 2015b). To relate the observed cluster counts to predictions for the mass function a conditional scaling relation was used. The analysis in Planck Collaboration XX (2014b) was based on X-ray mass proxies. The uncertainty in the absolute cluster mass scale remains the largest source of uncertainty in the *Planck* cluster count analyses and is quantified by the mass bias. New priors on this mass bias were incorporated in Planck Collaboration XXIV (2015a) based on small overlapping cluster samples with masses measured by employing gravitational lensing (von der Linden et al. 2014; Hoekstra et al. 2015), the deflection of light due to mass as a consequence of Einstein’s equivalence principle. Although these improved priors do not fully lift the observed tension yet, scaling relations entirely based on and not only gauged by gravitational lensing measurements are advantageous. This is due to lensing masses being unaffected by the dynamical state of matter or its physical properties (e.g. being dark or baryonic) in general. One disadvantage though is that lensing only yields estimates for a two-dimensional surface mass density, but with simulations it is possible to propagate these reliably into three-dimensional mass estimates in order to compare them with results from other probes (e.g. Becker & Kravtsov 2011; Meneghetti et al. 2014).

In the strong limit gravitational lensing is characterised by the occurrence of multiply lensed images or arcs of background sources behind the cluster. Employing these lensed images allows a very detailed determination of the mass and mass profile of the cluster core (e.g. Chapter 2, Medezinski et al. 2013, ; Bartelmann et al. 2013 and references therein). In the weak limit small differential deflections of background galaxies are used in a statistical sense to infer the mass of the cluster (e.g. Hoekstra et al. 2013 and references therein).

The primary source of statistical uncertainty in weak lensing based cluster mass estimates is shape noise because galaxies are not intrinsically round. For weak lensing it is necessary to measure shapes accurately from observed images in order to derive ellipticity components which serve as shear estimators (cf. Section 3.2.3). The accumulated errors arising from measuring shapes eventually propagate into weak lensing analyses as shape noise.

Another source of statistical uncertainty is arising from the fact that mass as measured from gravitational lensing is always weighted by the lensing kernel along the line-of-sight and projected into the plane on the sky of the deflecting mass. The effect of this projected foreground and background mass – or cosmic noise – on the accuracy of weak lensing masses has already been studied extensively in the past (e.g. Hoekstra 2001, 2003; Dodelson 2004; Hoekstra et al. 2011). However and in particular for the cosmological test described above, one is interested in a stack of clusters within a given mass (and redshift) range, thus, statistical uncertainties on properties of the stack will scale inversely with the square root of the total number of clusters within these bins.

In the next decade data from a multitude of ground-based weak lensing surveys, for example, the Kilo-Degree Survey (KiDS;¹ de Jong et al. 2012), the Dark Energy Survey (DES;²

¹<http://kids.strw.leidenuniv.nl>

²www.darkenergysurvey.org

Flaugher 2005), and the Subaru Hyper SuprimeCam lensing survey (HSC³) will become available and eventually culminate in the surveys carried out by the Large Synoptic Survey Telescope (LSST;⁴ Ivezić et al. 2008) and the spaceborne *Euclid*⁵ mission (Laureijs et al. 2011). Although the major focus of these surveys will be cosmic shear – the much weaker weak lensing due to cosmological large-scale structure – they will also produce large cluster surveys as ‘by-products’ and allow mass estimates employing shear measurements (cf. Sartoris et al. 2015). Since all of these weak lensing surveys will provide superior statistics in terms of the expected number of clusters to be found due to an orders of magnitude increase in survey area, it is important to scrutinize sources of statistical and systematic uncertainties in the determination of cluster masses using weak gravitational lensing.

In this paper, we will be especially focusing on the *Euclid* survey because it will yield one of the largest cluster samples with a very low level of statistical uncertainties based on weak lensing. This allows us to scrutinize the impact of major sources of uncertainties and biases, eventually answering whether these large cluster surveys will be more affected by statistical uncertainties or systematic errors. Note, however, that the survey design for LSST is very similar to *Euclid* so that our results will also be applicable to this survey and to lesser extent to smaller surveys such as, for example, DES.

Due to the large increase in survey area, we expect *large* samples of clusters to be detected in ongoing and upcoming weak lensing surveys and hence the statistical uncertainties are expected to decrease to levels on which systematic errors will no longer be negligible but instead might even dominate over statistical uncertainties. As we have mentioned already, gravitational lensing always yields a projected mass due to the line-of-sight integration over the lensing kernel. Preferably, the redshifts of (all) background source galaxies should be used in the integration over the lensing kernel (cf. Section 3.2.3) which thus requires to take redshifts of even larger samples of galaxies. In the ongoing and upcoming surveys this will be achieved by employing photometric redshift estimates based on multiband observations since spectroscopy is not feasible anymore given the typical survey areas (at least several thousand square degrees).

However, photometric redshift estimates are less precise and accurate and photometric misidentifications, for example in the cluster member galaxy assignment, will propagate into a biased mass estimate via the lensing kernel. Similarly, the effect of miscentring – the displacement between any observationally defined cluster centre and the minimum of the gravitational potential of the cluster – can also be propagated into a bias of weak lensing mass estimates. On the scale of a single cluster these biases are negligible but this might not be anymore the case once we turn to studying the masses of large ensembles of clusters.

In this paper, we will determine the level of expected statistical uncertainties first and then continue to study possibly important sources of bias. Eventually, these biases will have to be assessed much more rigorously through extensive (numerical) simulations, the aim of this paper is, however, to provide a guideline for the design of these simulations by identifying the most significant sources of bias with respect to the expected level of statistical uncertainties for stacks of galaxy clusters.

The structure of the paper is as follows: in Section 3.2 we establish the level of expected statistical uncertainties on the mass estimates of stacks of galaxy clusters from the *Euclid* survey while describing the weak lensing formalism used in this study at the same time. In Section 3.3 we scrutinize various sources of bias, most importantly the effect of photometric redshift outliers as well as miscentring and compare them to the level of statistical uncertain-

³www.naoj.org/Projects/HSC/

⁴www.lsst.org

⁵www.euclid-ec.org

ties derived in the previous section. Finally, we present our conclusions in Section 3.4.

Throughout this paper we employ a spatially flat Λ CDM cosmology with $\Omega_m = 0.308$, $\Omega_\Lambda = 0.692$, $H_0 = 100 h \text{ km s}^{-1} \text{ Mpc}^{-1}$ with $h = 0.678$, $\sigma_8 = 0.826$ and $n_s = 0.961$ following results from [Planck Collaboration XVI \(2014a\)](#).

3.2 Statistical uncertainties

Estimating the total number of haloes in redshift and cluster mass bins is the first step in answering the question of whether a *Euclid* cluster survey will be limited by statistics or systematics since the statistical uncertainty on a stack of clusters scales inversely with the square root of the total number of haloes in the stack. In a real data analysis one has to stack the clusters according to an observational proxy (e.g. luminosity). This will introduce an Eddington bias ([Eddington 1913](#)) in the stacked quantity as a function of decreasing number density. Hence, the average halo masses on the high mass end will be lowered. This in turn reduces the signal-to-noise ratio of the weak lensing measurement. However, this would only weaken the constraints on systematic errors we derive below. Therefore, we do not assume a proxy for the stacking but stack the clusters directly in mass in order to derive the tightest constraints on systematic errors.

The *Euclid* survey will cover an area of $15\,000 \text{ deg}^2$ on the sky and is expected to detect 30 galaxies per square arcminute ([Laureijs et al. 2011](#)) for which accurate shapes can be determined. For the subsequent analysis we will assume that all clusters within this area will be detected down to redshifts of $z = 1.5$ spanning masses between $6.78 \times 10^{13} h^{-1} M_\odot$ and $2.70 \times 10^{15} h^{-1} M_\odot$. This assumption is deliberately optimistic because it leads to the tightest constraints on systematic errors. Note, however, that for example [Gladders et al. \(2007\)](#) have found their high-redshift sample of clusters from the Red-Sequence Cluster Survey (RCS) to be complete to ≈ 88 per cent.

3.2.1 Halo abundance

The halo abundance can be expressed in the functional form ([Tinker et al. 2008, 2010](#))

$$n(M, z) = \frac{dn}{dM} = \frac{\bar{\rho}_{m,0}}{M} f(\nu) \frac{d\nu}{dM}. \quad (3.1)$$

The function $f(\nu)$ is motivated from extended Press-Schechter theory and can explicitly be written as ([Tinker et al. 2008, 2010](#))

$$f(\nu) = \alpha [1 + (\beta\nu)^{-2\phi}] \nu^{2\eta} e^{-\gamma\nu^{1/2}}, \quad (3.2)$$

where the parameters $\alpha, \beta, \gamma, \eta$, and ϕ are redshift-dependent and have to be calibrated against numerical simulations for the corresponding overdensity $\Delta = 200$ with respect to $\bar{\rho}_m$ (cf. [Tinker et al. 2008, 2010](#) for explicit values of these parameters).

The halo abundance is predicted as a function describing the mass fraction of matter in peaks of a given height, $\nu \equiv \delta_c / \sigma(M, z)$, in the linear density field smoothed at a scale $R = (3M / (4\pi\bar{\rho}_{m,0}))^{1/3}$ ([Press & Schechter 1974](#)), where M and z refer to the cluster mass and redshift, respectively, and $\bar{\rho}_{m,0}$ is the mean matter density of the Universe today. The constant $\delta_c = 1.686$ denotes the critical overdensity for collapse in linear theory and $\sigma(M, z)$ is the root-mean-square (rms) variance of the linear density field smoothed on a scale $R(M)$, which is defined as

$$\sigma^2 = \int_0^\infty P(k) |\hat{W}(kR)|^2 k^2 dk. \quad (3.3)$$

Here, $P(k)$ is the linear matter power spectrum, which we calculate with the fitting formulas provided by Eisenstein & Hu (1999) and \hat{W} is the Fourier transform of the top-hat filter with radius R in real space.

Using equation (3.1) we can now predict the (expected) abundance of haloes per redshift bin i and mass bin j by evaluating

$$N_{ij} = \int_{z_{\text{low},i}}^{z_{\text{high},i}} \int_{M_{\text{low},j}}^{M_{\text{high},j}} \int_V n(M_j, z_i) dz dM dV_{\text{com}}, \quad (3.4)$$

where we integrate over the expected comoving volume of the *Euclid* survey. The subscripts ‘low’ and ‘high’ refer to the lower and upper bounds of the bin, respectively.

3.2.2 Mass model

Next we have to specify a mass model for galaxy clusters from which we will derive shears that can then be compared to the measured shear around galaxy clusters. Numerical simulations of cosmological volumes show that the Navarro–Frenk–White (NFW)-profile (Navarro et al. 1997, 2010) is a good description of the average density profile of an ensemble of haloes over several orders of magnitude in mass when adjusting the halo concentration accordingly.

In the following analysis we assume only a single halo component and a spherically symmetric distribution of the cluster mass. In general, this assumption is over-simplifying and especially for unrelaxed single haloes far from correct (e.g. Shaw et al. 2006). However, since we focus in our analysis on a stacked signal from an ensemble of clusters, this simplification holds, because non-spherical symmetric cluster geometries will average out in the stacking process provided that the selection of the cluster sample is unbiased. An unbiased cluster sample is an important assumption here in order to derive upper limits on systematic errors, but in a real data analysis the cluster selection function has to be fully taken into account, e.g. in a subsequent cosmological analysis.

In this case the radial profile of such an idealized halo can then be expressed as an NFW-profile:

$$\rho(r) = \frac{\delta \bar{\rho}_m(z)}{r/r_s(1+r/r_s)^2}, \quad (3.5)$$

where $\bar{\rho}_m(z)$ is the *mean matter density* of the Universe at the redshift z of the halo. The parameter δ describes the overdensity of the halo and is related to the concentration parameter c through

$$\delta = \frac{200}{3} \frac{c^3}{\ln(1+c) - c/(1+c)}. \quad (3.6)$$

The scale radius r_s is a characteristic radius of a cluster and can be related to the virial radius r_{200} and concentration parameter c via $r_s = r_{200}/c$. We define the virial radius here as the radius of a sphere which contains a mass overdensity of $200\bar{\rho}_m(z)$. Thus, the corresponding mass M_{200} within this sphere is given by

$$M_{200} = \frac{800\pi}{3} \bar{\rho}_m(z) r_{200}^3. \quad (3.7)$$

Furthermore, numerical simulations hint at a (noisy) relation between halo concentration and mass. By applying such a concentration–mass relation, we can reduce the free parameters of the model to only one: the mass M_{200} .

For the concentration–mass relation we use the results of Dutton & Macciò (2014), i.e.

$$\log_{10}(\hat{c}_{200}(\hat{M}_{200})) = a + b \log_{10}(\hat{M}_{200}/(10^{12} h^{-1} M_{\odot})) \quad (3.8)$$

with the redshift-dependent functions $a = 0.520 + (0.905 - 0.520)\exp(-0.617z^{1.21})$ and $b = -0.101 + 0.026z$. The concentration \hat{c}_{200} and mass \hat{M}_{200} are defined with respect to the *critical density* of the Universe. We convert between this definition and our definition of mass and concentration given with respect to the *mean matter density* employing the algorithm from [Hu & Kravtsov \(2003\)](#). Note that at an earlier stage of the subsequent analysis we employed the concentration–mass relation from [Duffy et al. \(2008\)](#) which qualitatively did not affect any of our subsequent results or conclusions. That is expected because the weak lensing signal depends to first order on mass only. Moreover, we do not assume any scatter in the concentration–mass relation, because scatter will mainly affect the shape of the profile at small scales. However, our analysis always assumes that we measure the weak lensing signal of a stack and that these small-scale fluctuations from halo to halo due to scatter in the concentration–mass relation average out.

3.2.3 Weak-lensing formalism

Analytical formulas for the calculation of the weak lensing convergence and shear signal from a spherically symmetric NFW-profile were derived in [Bartelmann \(1996\)](#) and are conveniently re-expressed in [Wright & Brainerd \(2000\)](#). Following these references, we write the convergence as

$$\kappa_{\text{NFW}}(x) = \frac{\Sigma_{\text{NFW}}(x)}{\Sigma_{\text{crit}}}, \quad (3.9)$$

which is thus the ratio of the surface density $\Sigma_{\text{NFW}}(x)$ at projected position $x = R/r_s$ scaled by the critical surface density

$$\Sigma_{\text{crit}} = \frac{c^2}{4\pi G D_l(z_l)} \beta^{-1}(z), \quad (3.10)$$

where $\beta(z)^{-1} = D_s(z)/D_{ls}(z, z_l)$ is the inverse of the lensing efficiency $\beta(z)$. Here D_s , D_l , and D_{ls} denote the angular diameter distances between observer and source, observer and lens, and lens and source, respectively. The constants c and G are the speed of light and gravitational constant, respectively. For explicit formulas of the surface density $\Sigma_{\text{NFW}}(x)$ of an NFW-profile we refer the reader to the original literature ([Bartelmann 1996](#); [Wright & Brainerd 2000](#)).

As we have hinted at already in Section 3.1, weak lensing requires the knowledge of the redshift of the lens and every background source which are entering as variables in the corresponding angular diameter distances. However, instead of considering a redshift for every single background galaxy one assumes or measures a source redshift distribution:

$$p_{\text{src}}(z) = \frac{\beta}{z_0 \Gamma(\frac{1+\alpha}{\beta})} \left(\frac{z}{z_0}\right)^\alpha \exp(-(z/z_0)^\beta), \quad (3.11)$$

where we have adopted the functional form presented in [Vafaei et al. \(2010\)](#) and use $\alpha = 0.96$, $\beta = 1.70$, and $z_0 = 1.07$ corresponding to a median redshift of $z_{\text{med}} = 0.91$ to simulate the *Euclid* survey. Employing this source redshift distribution lets us rewrite the critical surface density as

$$\Sigma_{\text{crit}} = \frac{c^2}{4\pi G D_l(z_l)} \int_{z_{\text{min}}}^{z_{\text{max}}} dz \beta_{\text{eff}}^{-1}(z), \quad (3.12)$$

with the inverse of an effective lensing efficiency $\beta_{\text{eff}} = p(z)\beta(z)$. Note that the source distribution $p(z)$ has now to be renormalized over the range $z_{\text{min}} \leq z \leq z_{\text{max}}$.

In case of *Euclid* and all other ongoing and upcoming lensing surveys, photometric redshifts will also be available. Hence, we will only consider galaxies as sources for the lensing signal with redshifts $z_{\text{min}} = z_{\text{phot}} > z_{\text{cluster}} + 0.15$ where we choose an offset of 0.15 because

the lensing contribution of sources close to the cluster redshift is negligible and for low redshifts the offset of 0.15 corresponds to the expected 3σ uncertainty in photometric redshift $\sigma_z = 0.05(1+z)$.

The tangential shear due to an NFW-profile can be expressed as

$$\gamma_T^{\text{NFW}}(x) = \frac{\bar{\Sigma}_{\text{NFW}}(x) - \Sigma_{\text{NFW}}(x)}{\Sigma_{\text{crit}}}, \quad (3.13)$$

i.e. as a scaled density contrast between the average surface density inside projected radius x and the surface density at radius x . However, observationally, it is only possible to measure the reduced tangential shear g_T , i.e.

$$g_T = \frac{\gamma_T}{1 - \kappa}. \quad (3.14)$$

A parametrized model based on the equations above can then be used to derive the mass of the halo from the measured shear signal. Here, we will also include the effect of cosmic noise. This is important in order to derive more realistic uncertainties on the mass estimates (Hoekstra 2001, 2003; Dodelson 2004; Hoekstra et al. 2011). The most straightforward implementation in order to achieve that is fitting the parametric model directly to a pixelized map of the two Cartesian projections of the reduced shear g_T in the lens plane. These are related to g_T through

$$g_1 = g_T \cos(2\phi) \quad (3.15)$$

$$g_2 = g_T \sin(2\phi). \quad (3.16)$$

For the implementation of cosmic noise contributions we follow Oguri et al. (2010) and calculate the χ^2 as

$$\chi^2 = \sum_{\alpha,\beta=1}^2 \sum_{k,l=1}^{N_{\text{pixel}}} [g_{\alpha}(\theta_k) - g_{\alpha}^m(\theta_k; \mathbf{p})][\mathbf{C}^{-1}]_{\alpha\beta,kl} [g_{\beta}(\theta_l) - g_{\beta}^m(\theta_l; \mathbf{p})], \quad (3.17)$$

where Greek indices run over the two components of the reduced shear g and Roman indices run over the pixel positions ($k, l = 1, \dots, N_{\text{pixel}}$). The matrix \mathbf{C} denotes the covariance matrix and \mathbf{C}^{-1} is its inverse.

By minimizing the χ^2 -value given the distortion ‘data’, we find the best-fitting model parameters. Of course, with data we are referring to the shear components derived from a fiducial parametric model.

We consider now two contributions in the covariance matrix: the dominating intrinsic ellipticity noise, i.e. shape noise, and cosmic noise due to large-scale structure along the line-of-sight. Thus, we write the covariance matrix as

$$\mathbf{C} = \mathbf{C}^{\text{shape}} + \mathbf{C}^{\text{LSS}}. \quad (3.18)$$

The intrinsic ellipticity noise between different galaxies is uncorrelated, thus, the shape noise covariance matrix consists only of diagonal terms

$$[\mathbf{C}^{\text{shape}}]_{\alpha\beta,kl} = \delta_{\alpha\beta} \delta_{kl} \sigma_{\text{shape}}^2, \quad (3.19)$$

where δ_{ij} denotes the Kronecker delta and $\sigma_{\text{shape}}^2 = \sigma_{\text{int}}^2 / N_k$ is the shape noise in pixel k . We estimate the number N_k of background galaxies per pixel as:

$$N_k = A_{\text{pix}} n \int_{z_{\text{min}}}^{z_{\text{max}}} dz p_{\text{src}}(z), \quad (3.20)$$

where A_{pix} stands for the area of one pixel and the source redshift distribution $p_{\text{src}}(z)$ is the one given in equation (3.11). We employ a number density of background sources of $n = 30 \text{ arcmin}^{-2}$ which is expected for the *Euclid* survey (Laureijs et al. 2011). Furthermore, we assume an intrinsic ellipticity noise per galaxy of $\sigma_{\text{int}} = 0.25$ per component.

In contrast to that, large-scale structure along the line-of-sight introduces correlated noise which can be expressed as (Hoekstra 2003; Dodelson 2004)

$$[\mathbf{C}^{\text{LSS}}]_{\alpha\beta,kl} = \xi_{\alpha\beta}(r = |\boldsymbol{\theta}_k - \boldsymbol{\theta}_l|), \quad (3.21)$$

where $\xi_{\alpha\beta}$ denote the cosmic shear correlation functions. Since the universe is statistically isotropic, we express ξ as a function of the length r of the vector connecting the two positions $\boldsymbol{\theta}_k$ and $\boldsymbol{\theta}_l$. In particular, the shear correlation functions constructed from the two shear components are given by

$$\xi_{11}(r) = \cos^2(2\phi)\xi_{++}(r) + \sin^2(2\phi)\xi_{\times\times}(r), \quad (3.22)$$

$$\xi_{22}(r) = \sin^2(2\phi)\xi_{++}(r) + \cos^2(2\phi)\xi_{\times\times}(r), \quad (3.23)$$

$$\xi_{12}(r) = \xi_{21}(r) = \cos(2\phi)\sin(2\phi)[\xi_{++}(r) - \xi_{\times\times}(r)], \quad (3.24)$$

where ϕ is the position angle between the coordinate x -axis and the vector $\mathbf{r} = \boldsymbol{\theta}_k - \boldsymbol{\theta}_l$. ξ_{++} and $\xi_{\times\times}$ denote the tangential and cross-component shear correlation functions (e.g. Bartelmann & Schneider 2001), respectively. For the calculation of these shear correlation functions we have to calculate the non-linear matter power spectrum $P_\delta(k)$ folding in the source redshift distribution defined in equation (3.11). We calculate the non-linear matter power spectrum with the publicly available Boltzmann-code CLASS⁶ (Blas et al. 2011; Audren & Lesgourgues 2011).

In all of our subsequent analyses, we fit the shear signal on a regular grid with constant side length $N_{\text{pixel}} = 20$ which is set to correspond to a square with side length $2 \times 2 R_{\text{vir}}$. Furthermore, we cut out the cluster centre in a square of side length $2 \times 0.2 R_{\text{vir}}$ (we will refer to that more conveniently as fitting ‘from $0.2 R_{\text{vir}}$ to $2 R_{\text{vir}}$ ’ from now on). Larger scales than $2 R_{\text{vir}}$ are avoided since these are completely dominated by cosmic noise due to the smallness of the cluster signal there. In addition to that, two-halo contributions will also bias the NFW-fit on these scales (Becker & Kravtsov 2011). Smaller scales than $0.2 R_{\text{vir}}$ are omitted since this is usually done for practical purposes when dealing with real data in order to minimize the residual contamination by cluster members. Furthermore, the accuracy of shape measurements in high-density and hence high-shear regions is also an issue one tries to circumvent in practice. Finally, we also do expect deviations from the simple NFW-profile on these scales due to effects of substructure (Becker & Kravtsov 2011).

3.2.4 Results

With the formalism outlined above we can now turn to determining the statistical precision of mass estimates from weak lensing measurements. Most importantly, we emphasize that realistic estimates of the statistical uncertainties must include cosmic noise (cf. equation 3.18).

This is demonstrated by Fig. 3.1a and Fig. 3.1b which show the likelihoods $P(M)$ and $P(c)$ as functions of the halo mass M and concentration c , respectively, resulting from the fitting procedure described above for three halo masses in the range $0.87 \leq M/(10^{14} h^{-1} M_\odot) \leq 8.76$, all at the same redshift $z = 0.1875$. In the derivation of $P(M)$ we use the concentration–mass relation given in equation (3.8). In the derivation of $P(c)$ the mass was fixed at the fiducial

⁶Version 2.4.0 from www.class-code.net

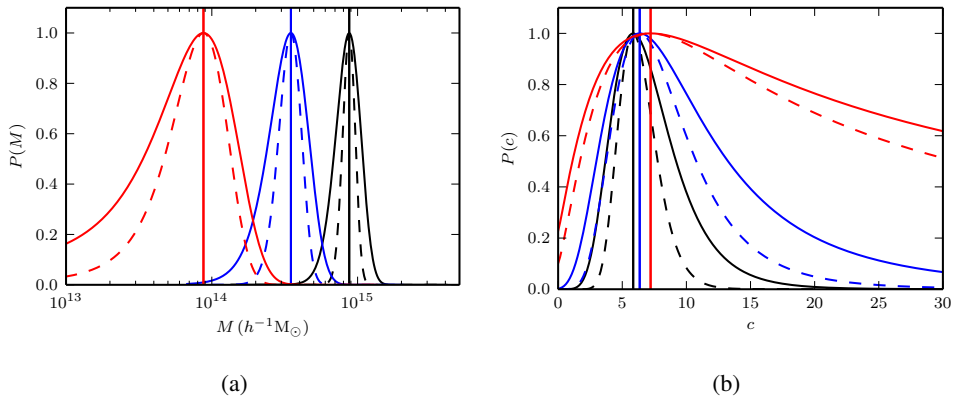


Figure 3.1: (a) Likelihood as a function of halo mass M and concentrations derived through the concentration–mass relation of equation (3.8) for single haloes of masses $M_1 = 0.87 \times 10^{14} h^{-1}M_{\odot}$ (red), $M_2 = 3.50 \times 10^{14} h^{-1}M_{\odot}$ (blue) and $M_3 = 0.87 \times 10^{15} h^{-1}M_{\odot}$ (black). (b) Likelihood as a function of concentration c at fixed fiducial mass M for the same three haloes as in panel (a) (fiducial concentrations are set by employing the concentration–mass relation of equation 3.8). In both panels vertical lines indicate the fiducial values of mass and concentration, respectively. Dashed lines do not include, and solid lines do include large-scale structure contributions in the covariance (cf. equation 3.18).

value for each cluster and the fiducial concentration again derived through employing equation (3.8). We then fit for the concentration c and demonstrate the importance of accounting for large-scale structure contributions in the data covariance.

The dashed lines show the distributions only taking into account shape noise, whereas for the solid lines the effect of large-scale structure is additionally taken into account (cf. equations 3.18, 3.19, 3.21). This results in a significant broadening of the corresponding distributions $P(M)$ and $P(c)$, which in turn increases the uncertainties in the halo mass and concentration significantly. This effect is expected because large-scale structure contributions reduce the weight of large scales on the weak lensing signal. Therefore, it is more pronounced for lower mass haloes since there the lensing signal is much weaker on larger scales compared to high mass haloes.

We continue the analysis by looking further at the stacked weak lensing signal of clusters in eight mass bins from $6.78 \times 10^{13} h^{-1}M_{\odot}$ to $2.70 \times 10^{15} h^{-1}M_{\odot}$ and in four different redshift bins in the range $0 < z < 1.5$.

The relative error of the stacked lensing signal of a halo in each redshift bin $i \in 0, \dots, 3$ and mass bin $j \in 0, \dots, 7$ is estimated by

$$\Delta M_{ij}^{\text{left/right}} = |M(\Delta\chi^2 = 1)^{\text{left/right}} - M_j(z_i)|, \quad (3.25)$$

$$\sigma_{ij} = \frac{1}{2} \frac{(\Delta M_{ij}^{\text{left}} + \Delta M_{ij}^{\text{right}})}{M_j(z_i)}, \quad (3.26)$$

where the χ^2 is calculated again as defined in equation (3.17). The minimal χ^2 is centred on the central value of each mass and redshift bin, respectively.

In Fig. 3.2 we show the expected statistical relative uncertainty on the mass for a stacked weak lensing signal from galaxy clusters in each of the mass and redshift bins specified above. The solid lines correspond to the total relative error including also large-scale structure contributions in the error budget. These are most important for clusters at low redshifts $z \leq 0.75$ and

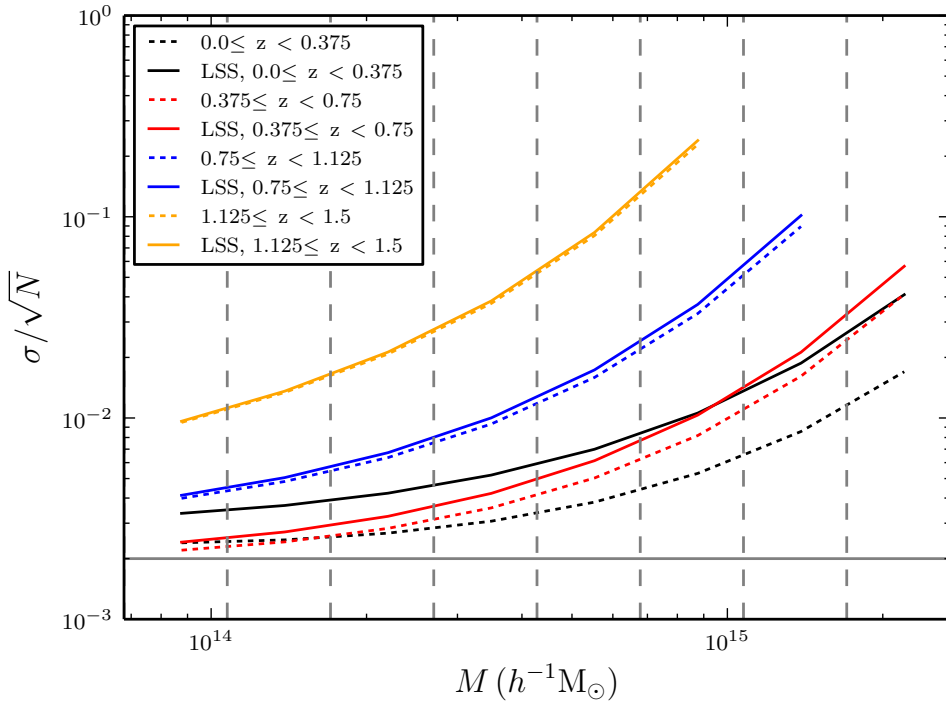


Figure 3.2: Relative uncertainties for masses of galaxy clusters as estimated from a stacked weak lensing signal for different mass and redshift bins. The solid lines take large-scale structure contributions into account whereas the dashed lines only include shot noise contributions (cf. Section 3.2.3). The eight mass bins (vertical, dashed lines) span a range from $6.78 \times 10^{13} h^{-1} M_{\odot}$ to $2.70 \times 10^{15} h^{-1} M_{\odot}$ and the four redshift bins are in the range $0 < z < 1.5$. The horizontal grey line indicates the required upper bound on the multiplicative bias m for *Euclid* (cf. Section 3.3).

Table 3.1: Relative uncertainties in mass.

$M_{\text{low}} (\times 10^{14} h^{-1} M_{\odot})$	$M_{\text{high}} (\times 10^{14} h^{-1} M_{\odot})$	σ_{stat}	$\sigma_{\text{stat}} / \sqrt{N}$	σ	σ / \sqrt{N}	N
0.678	1.075	0.432	0.0024	0.605	0.0034	32509
1.075	1.703	0.322	0.0025	0.477	0.0037	16861
1.703	2.699	0.239	0.0027	0.378	0.0042	7999
2.699	4.278	0.178	0.0031	0.302	0.0052	3363
4.278	6.780	0.132	0.0038	0.242	0.0070	1200
6.780	10.75	0.098	0.0053	0.196	0.0106	342
1.075	17.03	0.073	0.0086	0.159	0.0187	72
17.03	26.99	0.054	0.0170	0.130	0.0410	10

Notes. The relative errors σ / \sqrt{N} for each mass bin of Fig. 3.2 are given for the lowest redshift bin (i.e. $z_{\text{mean}} = 0.1875$). N refers to the number of haloes in each mass bin and M_{low} and M_{high} denote the lower and upper value of each mass bin, respectively.

increase with increasing halo mass driven mainly by the lower abundances of these high-mass clusters.

In Table 3.1 we provide the quantitative values for the relative uncertainties in all mass bins for the lowest redshift bin since these ultimately set the requirements on the precision.

3.3 Systematic errors

So far, our analysis did not include any sources of bias. However, given the expected small statistical uncertainties as estimated in the previous section (cf. Fig. 3.2 and Table 3.1), any source of systematics might become important.

In general, the simplest parametrization of systematic deviations of the observed shear γ_{obs} from the true shear γ can be written as (Heymans et al. 2006)

$$\gamma_{\text{obs}} = (1 + m)\gamma + c, \quad (3.27)$$

where m refers to the multiplicative bias and c to the additive bias (e.g. Huterer et al. 2006; Massey et al. 2013 and references therein).

The multiplicative bias can arise from a variety of different sources. For example, the shear is derived from an observed image which is a convolution of a point spread function (PSF) of finite size with the true shape of the observed object. This convolution introduces a multiplicative error. The additive bias, for example, can result from anisotropies of the PSF. We expect these to largely average out when referring to a stack of galaxy clusters which implies taking an average over many cluster–source pairs.

Since the requirement on the multiplicative bias for *Euclid* is $m < 2 \times 10^{-3}$ (Laureijs et al. 2011), we find that the statistical uncertainties are still larger and thus this source of systematic can be neglected henceforth. Therefore, the primary observational sources of bias in weak lensing can both be neglected for our subsequent analysis in which we will focus then on other possible sources of bias instead.

Table 3.2: The SN = 5 limiting (apparent) magnitudes for extended objects used in the photometric redshift estimation.

g	r	i	z	Y	J	H
24.65	24.15	24.35	23.95	23.3	23.3	23.3

Notes. These limits assume DES ground-based observations (g , r , i , z) and *Euclid* NIR observations (Y , J , H). The limiting magnitudes for extended objects are assumed to be 0.7 mag shallower than for point sources.

3.3.1 Photometric redshift bias

For all ongoing and upcoming weak lensing surveys photometric redshifts of large samples of galaxies will be available. Equations (3.10) and (3.12) show the dependence of the cluster lensing signal on redshifts of the cluster itself and all background sources or a source redshift distribution, respectively. Since it would simply require too much time to obtain spectroscopic redshifts for all galaxies in and around each cluster in these large samples of galaxy clusters, photometric redshift estimates present the only feasible alternative. However, the techniques for estimating photometric redshifts from multiband observations are not as precise as spectroscopic redshifts. They might even yield catastrophic outliers, for example, due to misinterpretations or confusion of emission or absorption features (e.g. Ly α break; cf. Jouvel et al. 2011).

This is also important for the weak lensing signal since cluster member galaxies that are scattered to higher redshifts will now be treated as source background galaxies in the measurement of the weak lensing signal. In comparison to the case of a perfect assignment of cluster members and background source galaxies the weak lensing signal will be diluted because erroneously scattered cluster members are not gravitationally sheared by the cluster. In this context another bias might arise due to cluster members being intrinsically aligned although Sifón et al. (2015) showed no evidence for this. Note that any member galaxy scattered to a redshift in the foreground of the cluster does not change the lensing signal, though, because the photometric redshift distribution will be cut for all redshifts lower than $z_{\text{cut}} = z_{\text{clus}} + 0.15$.

In order to quantify the level of contamination, we need an estimate of the number of cluster members we expect. For that reason, we adopt a Schechter-type cluster luminosity function (Schechter 1976) which follows the scaling relations with respect to cluster mass (or richness) derived from a large sample of groups and clusters from the Sloan Digital Sky Survey (SDSS) as presented in Hansen et al. (2009). For simplicity we only assume a passive redshift evolution of the luminosity function. The absolute magnitudes sampled from this cluster luminosity function are converted to apparent magnitudes which will then serve as input for an estimation of photometric redshifts for the cluster member galaxies.

In general, observed magnitudes include noise from a variety of sources, for example, errors in the background subtraction, CCD readout noise, zodiacal light, and photometric errors. However, in our simulations it is sufficient to only use fixed magnitude limits. In Table 3.2 we show the signal-to-noise (SN) limits for different bands, combining DES optical photometry (e.g. Banerji et al. 2015) and *Euclid* near-infrared (NIR) observations (Laureijs et al. 2011). The photometric redshifts are estimated from the apparent magnitudes by employing a template based photo- z code derived from BPZ (Benítez 2000). A single redshift is estimated by

finding the peak of

$$\chi^2(z) = \sum_{i,T} \frac{(\tilde{f}_i - f_i(z, T))^2}{\sigma_{f_i}^2}, \quad (3.28)$$

where the sum is taken over the different filters i and different types of spectral energy distributions (SED) T for mimicking different types of galaxies. Here \tilde{f}_i is the observed flux in filter i , σ_{f_i} is the flux error, and $f_i(z, T)$ is a model flux constructed from the template library. In the estimation of the photometric redshifts, we do not include the *Euclid* visual (VIS) band. Furthermore, no priors are included and the templates equal the ones used to generate the simulations.

This yields a catalogue of photometric redshift estimates for cluster members for which we do know the true cluster redshift by construction. We cut the catalogue by imposing a detection limit for extended objects of $m^{\text{VIS}} < 24.5$ (10σ) in apparent magnitude following the requirement for lensing sources as given in [Laureijs et al. \(2011\)](#). After having applied this cut we use the catalogue to construct a photometric redshift distribution for the cluster members, $p_{\text{clus}}(z)$, which we use to define the modified total source redshift distribution $p_{\text{mod}}^i(z)$ per radial bin i :

$$p_{\text{mod}}^i(z) \propto N_{\text{src}}^i p_{\text{src}}(z) + N_{\text{clus}}^i p_{\text{clus}}(z). \quad (3.29)$$

Here N_{src}^i denotes the total number of source galaxies per radial bin, i.e. $N_{\text{src}}^i = (1 - f_{\text{src}}^{\text{scat}}) A_{\text{fit}}^i n$. The number density of sources is again assumed to be $n = 30 \text{ arcmin}^{-2}$ and with A_{fit}^i we denote the area of an annulus defined by the borders of the radial bin. Note that the actual number of source galaxies per radial bin entering in the weak lensing analysis is again calculated as in equation (3.20) with p_{src} replaced by a properly normalized p_{mod} .

Moreover, we account for the fact that background source galaxies are also scattered into the cluster foreground by introducing $f_{\text{src}}^{\text{scat}}$, the fraction of background sources scattered into the foreground of the cluster. These additional source scatterers intensify the effect of cluster galaxies scattered into the background twofold: firstly, the number of sources per bin is lowered which increases the uncertainty of the weak lensing signal and secondly the last term of $p_{\text{mod}}^i(z)$ modified by the scattered cluster galaxies gets a higher, relative weight. We estimate $f_{\text{src}}^{\text{scat}}$ from an additionally simulated source redshift distribution employing the photometric redshift estimation algorithm described above but using now luminosity functions from [Martí et al. \(2014\)](#).

The source redshift distribution has the same functional form as in equation (3.11). We estimate the number of cluster members in the same radial bin i as

$$N_{\text{clus}}^i = f_{\text{fit}}^i N_{\text{clus}}^{\text{tot}} (\leq 2 R_{\text{vir}}), \quad (3.30)$$

where f_{fit}^i is the fraction of cluster members in the radial bin i , i.e.

$$f_{\text{fit}}^i = \frac{\int_{R_{\text{low}}^i}^{R_{\text{high}}^i} \Sigma(R) R dR}{\int_0^{2 R_{\text{vir}}} \Sigma(R) R dR}. \quad (3.31)$$

The surface mass distribution $\Sigma(R)$ is derived from the NFW-profile given in equation (3.5) (e.g. [van der Burg et al. 2014](#)). The number of cluster members is estimated by integrating the luminosity function up to the absolute magnitude corresponding to the detection limit in visual apparent magnitude m^{VIS} multiplied with the volume of a cylinder with radius $2 R_{\text{vir}}$ and height $4 R_{\text{vir}}$. Note that the calculations as presented above are slightly inconsistent with our approach of effectively fitting within squares enclosing the corresponding annulus. However,

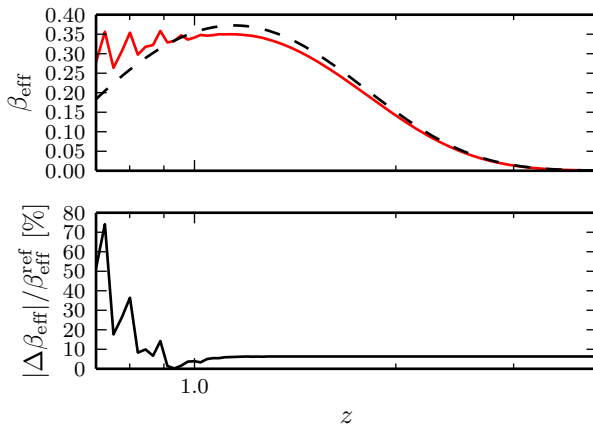


Figure 3.3: Upper panel: effective lensing efficiencies $\beta_{\text{eff}}(z)$ for the reference source background distribution (black, dashed line; cf. equation 3.11) and for a modified source redshift distribution (red, solid line; cf. equation 3.29) for a cluster of mass $M = 8.76 \times 10^{14} h^{-1} M_{\odot}$ at redshift $z_l = 0.56$ in the fitting range of the first radial bin, i.e. $0.2 R_{\text{vir}} \leq r \leq 1 R_{\text{vir}}$. The modified source redshift distribution consists only of elliptical galaxies (i.e. SED type ‘E1101’). Lower panel: relative difference between both effective lensing efficiencies.

as can be seen in Fig. 3.4, the bias decreases with increasing radius and thus this approach does not change our conclusions below.

When we fit masses, we cut and normalize $p_{\text{mod}}(z)$ over the range $z_{\text{cut}} \leq z \leq z_{\text{max}}$, where z_{max} should be formally set to infinity. We use here, however, a high enough redshift beyond which $p_{\text{mod}}(z) = 0 \forall z \geq z_{\text{max}}$. The fiducial model to which we compare in the fitting makes use of the same normalizations in $p_{\text{mod}}(z)$, but with the cluster redshift distribution $p_{\text{clus}}(z)$ set to 0.

We compare the effective lensing efficiencies (cf. equation 3.12) derived from these two distributions over the fitting range of the first radial bin between $0.2 R_{\text{vir}} \leq r \leq 1 R_{\text{vir}}$ in Fig. 3.3 for a cluster of mass $M = 8.76 \times 10^{14} h^{-1} M_{\odot}$ at redshift $z = 0.56$. The cluster redshift distribution is assumed to consist entirely of elliptical galaxies (i.e. SED type ‘E1101’) in this case. In the lower panel we show the excess in effective lensing efficiency due to an excess in the cluster redshift distribution based on misidentified photometric redshift estimates. In general, applying the foreground cut $p(z \leq z_{\text{cluster}} + 0.15) = 0$ already removes a large fraction of cluster members from the source background distribution. However, there still remains a small fraction of cluster members with wrongly assigned (higher) photometric redshifts which are then erroneously treated as members of the source redshift distribution. This affects the lensing efficiency as shown in the lower panel of Fig. 3.3. The modified lensing efficiency then leads to a bias in a weak lensing based mass derivation. Hence, we study the impact of this effect by repeating our previous weak lensing analysis by replacing the analytic expression from equation (3.11) for $p_{\text{src}}(z)$ with $p_{\text{mod}}(z)$ for two fiducial clusters with masses of $M = 0.88 \times 10^{14} h^{-1} M_{\odot}$ and $M = 8.76 \times 10^{14} h^{-1} M_{\odot}$ at 11 equidistant redshifts between $0.1875 \leq z_{\text{cluster}} \leq 0.9375$. We always include large-scale structure contributions in the error budget. Moreover, we consider two radial bins i per cluster, where the first bin spans radii in the range $0.2 R_{\text{vir}} \leq r \leq 1 R_{\text{vir}}$ and the second bin extends from $1 R_{\text{vir}}$ to $2 R_{\text{vir}}$. Typical numbers we find for the fraction of cluster members within these bins are ≈ 50 and ≈ 32 per cent, respectively. The remainder of cluster galaxies is concentrated in the very centre of the cluster, i.e. between

$$\sim 0 \leq r \leq 0.2 R_{\text{vir}}.$$

The results of this analysis are summarized in Fig. 3.4 and reveal that the impact of cluster members scattered into the lensing source sample is a minor concern for an individual cluster as indicated in the upper panels where we show the relative mass bias, b , as a function of true cluster redshift, z_{clus} . When we compare the relative uncertainties for stacks of galaxy clusters, σ/\sqrt{N} , as obtained in the previous section (cf. Fig. 3.2 and Table 3.1) with the level of expected relative bias b due to imperfect photometric redshift estimates of cluster members as shown in the lower panels of Fig. 3.4, we find that the bias is strongly dependent on the radial bin under consideration, as expected. For the first bin between $0.2 R_{\text{vir}}$ and $1 R_{\text{vir}}$ the bias can be severe for certain combinations of SED type and redshift. In the second bin between $1 R_{\text{vir}}$ to $2 R_{\text{vir}}$ the bias is always within the expected statistical uncertainties though for all SED types and redshifts but it can amount up to 40 per cent of the statistical uncertainties.

The dependence of the bias on the SED type used for the galaxy templates in the derivation of the photometric redshift estimates is exaggerated for most SED types because we always consider all members to consist of only one SED type. Galaxies with irregular SED types show the strongest bias whereas the lowest bias is found for elliptical SED types although it is then of equal strength as the statistical uncertainties. In real clusters though, the majority of member galaxies will consist of (red) elliptical galaxies with rising fractions of (blue) spiral galaxies as a function of increasing cluster redshift (Butcher–Oemler effect, [Butcher & Oemler 1984](#)). Hence, the total bias will be dominated by a combination of the individual biases of these SED types, whereas contributions from irregular galaxies, which create the strongest bias in our analysis, will be much smaller in reality. Furthermore, a mass estimate derived over the full fitting range will be less affected by this bias since such an analysis corresponds to taking the average over both radial bins. The same conclusions will also hold for a measurement of cluster density profiles so that the photometric redshift bias will be negligible in this case, too.

For high-redshift clusters most of the photometric misidentifications will be scattered to redshifts in the foreground of the cluster, especially when considering the imposed detection limits. Thus the ratio of the bias over the statistical uncertainties will flatten towards higher cluster redshifts (cf. lower panels of Fig. 3.4).

3.3.2 Miscentring bias

The position of the minimum of the cluster potential, its centre, is unknown in general. The position of the brightest cluster galaxy (BCG) or the centre of the X-ray emission can be used as a tracer for the cluster centre, but they do not have to coincide with the centre as determined by weak lensing, especially not in unrelaxed haloes. Hence, we need to consider a distribution in offsets.

For a two-dimensional offset r_s we can calculate the azimuthally averaged convergence profile $\kappa(r)$ ([Yang et al. 2006](#)):

$$\kappa(r|r_s) = \frac{1}{2\pi} \int_0^{2\pi} \kappa_{\text{NFW}} \left(\sqrt{r^2 + r_s^2 + 2rr_s \cos(\theta)} \right) d\theta, \quad (3.32)$$

where κ_{NFW} is the convergence for a spherically symmetric NFW-profile as given in equation (3.9).

Based on SDSS-like mock catalogues for the `maxBCG` BCG finder algorithm, [Johnston et al. \(2007\)](#) found that the distribution of offsets follows a two-dimensional Gaussian distribution. Although the miscentring in these mock catalogues can only be caused by misidentifications due to the algorithm by construction, we still consider their results to be sufficiently

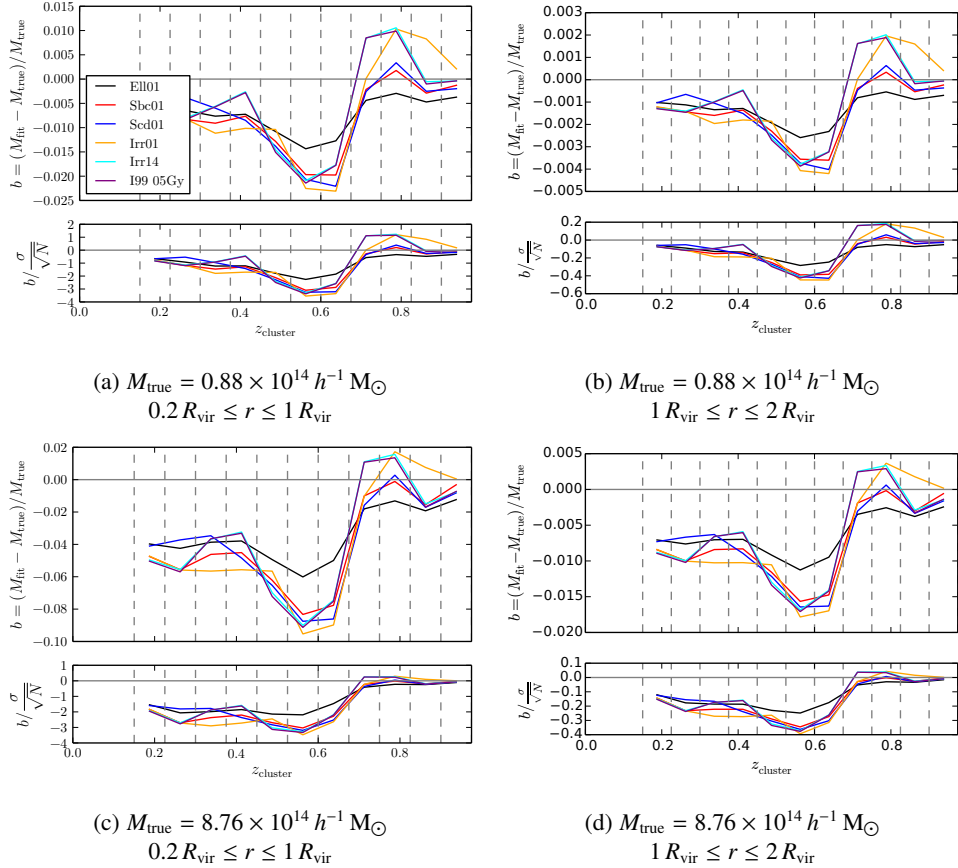


Figure 3.4: Upper panels: relative bias b due to imperfect assignment of photometric redshifts of cluster members which thus contaminate the source redshift distribution as a function of true cluster redshift z_{cluster} , SED type (i.e. ‘Ell01’ corresponding to elliptical, ‘Sbc01’ and ‘Scd01’ corresponding to spiral, and various ‘Irr’ corresponding to irregular galaxy SED templates), and cluster mass. Panels (a) and (c) show the lowest and highest mass in the first radial bin, whereas panels (b) and (d) show the corresponding masses in the second radial bin. Lower panels: comparison of the relative bias b from the upper panels with the corresponding relative uncertainties derived for a stack of galaxy clusters σ/\sqrt{N} (cf. Fig. 3.2 and Table 3.1) again as a function of cluster redshift, SED type and cluster mass. Note the different scale of the y-axis between the radial bins.

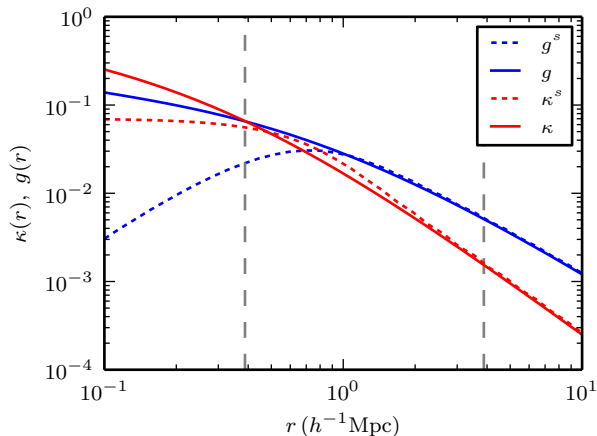


Figure 3.5: Reduced shear signals (blue) for a perfectly centred ($f = 1$) halo (solid line) of mass $M = 8.76 \times 10^{14} h^{-1} M_{\odot}$ and its maximally miscentred ($f = 0$) equivalent (dashed line) with $\sigma_s = 0.42 h^{-1} \text{Mpc}$ (see text for details). The convergence is shown in red. The vertical dashed lines indicate the region which we include for fitting in our subsequent analysis ($0.2 R_{\text{vir}} \leq r \leq 2 R_{\text{vir}}$).

good approximations since in practice one would also employ algorithms to determine miscentring offsets in samples as large as expected to be found in the *Euclid* survey. Therefore, we follow Johnston et al. (2007) by assuming a two-dimensional Gaussian distribution of offsets,

$$P(r_s) = \frac{r_s}{\sigma_s^2} \exp(-0.5(r_s/\sigma_s)^2), \quad (3.33)$$

where the effective scale length was typically found to be $\sigma_s = 0.42 h^{-1} \text{Mpc}$ independent of cluster richness. The resulting convergence for miscentred clusters is then a convolution of the above equations which yields

$$\kappa^s(r) = \int P(r_s) \kappa(r|r_s) dr_s. \quad (3.34)$$

From this convolved convergence we can derive the reduced shear g^s for a miscentred cluster and employ the lensing formalism of Section 3.2.3. The total shear signal for a stack of miscentred clusters must be weighted by the fraction f of correctly centred clusters though, i.e.

$$g^{\text{tot}} = f g + (1 - f) g^s. \quad (3.35)$$

In Fig. 3.5 we show both the reduced shear signal and the convergence of a maximally miscentred halo ($f = 0$ and $\sigma_s = 0.42 h^{-1} \text{Mpc}$) and compare it to the expected signal of a perfectly centred halo of the same mass. The effect of miscentring is to dilute the shear signal in the inner regions of the cluster. Hence ignoring this will bias masses low with a dependence on the innermost radius used while fitting.

Before considering strategies for mitigating the bias, we first examine its size further in Fig. 3.6a and Fig. 3.6b. Here, the miscentred shear signal is parametrized by the mass of the halo M and the two miscentring parameters. In Fig. 3.6a we fit a fiducial, centred cluster signal to the signal of a miscentred halo with a varying fraction of centred haloes ($0 \leq f \leq 1$) for three fiducial masses in the range $0.87 \leq M/(10^{14} h^{-1} M_{\odot}) \leq 8.76$ (dashed lines). The width of the miscentring distribution is kept fixed at $\sigma_s = 0.42 h^{-1} \text{Mpc}$. Miscentring introduces a bias

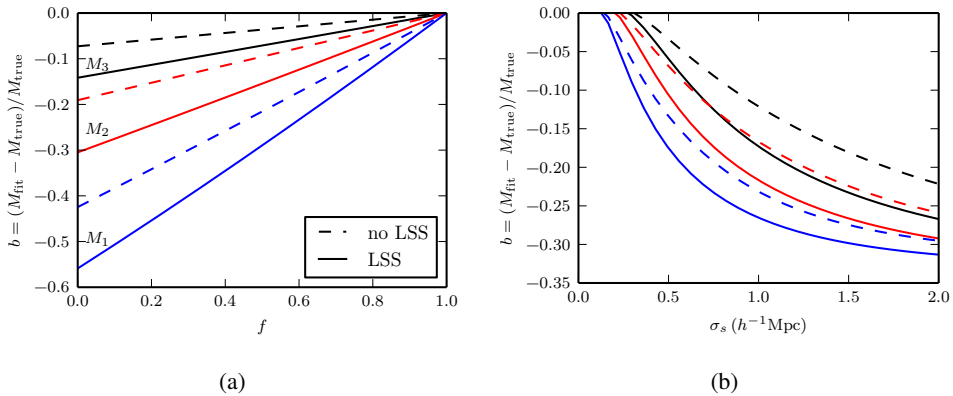


Figure 3.6: (a) Bias in halo mass introduced by miscentring as a function of the fraction of centred haloes f (for a fixed width $\sigma_s = 0.42 h^{-1}\text{Mpc}$ of the miscentring distribution) again with (solid lines) and without (dashed lines) large-scale structure contribution. The bias is shown for halo masses of $M_1 = 8.76 \times 10^{13} h^{-1}\text{M}_\odot$ (blue), $M_2 = 3.50 \times 10^{14} h^{-1}\text{M}_\odot$ (red) and $M_3 = 8.76 \times 10^{14} h^{-1}\text{M}_\odot$ (black). (b) Bias in halo mass as a function of the width σ_s of the miscentring distribution for a fixed fraction of centred haloes of $f = 0.75$ again with (solid lines) and without (dashed lines) large-scale structure contribution for the same halo masses as in (a).

Table 3.3: Requirements on the precision of the fraction of centred haloes f and the relative error $\Delta\sigma_s/\sigma_s$ of the width σ_s of the miscentring distribution.

$M_{\text{true}} (\times 10^{14} h^{-1}\text{M}_\odot)$	Δf_{max}	$\left(\frac{\Delta\sigma_s}{\sigma_s}\right)_{\text{max}} (\sigma_s = 0.42 h^{-1}\text{Mpc})$	$\left(\frac{\Delta\sigma_s}{\sigma_s}\right)_{\text{max}} (\sigma_s = 1 h^{-1}\text{Mpc})$
0.876	0.0060	0.019	0.032
3.500	0.0171	0.032	0.036
8.763	0.0747	0.088	0.064

Notes. We refer the reader to the text for details on the calculation of these requirements.

in the recovered mass and increases with decreasing fraction of centred haloes f . Furthermore, the bias is dependent on the fiducial halo mass and increases from high halo masses (of the order of $10^{15} h^{-1}\text{M}_\odot$) to low halo masses (of the order of $10^{14} h^{-1}\text{M}_\odot$). The dependence of the bias on the fiducial halo mass (for fixed σ_s) is caused by that the dilution of the shear signal due to miscentring is higher for low-mass haloes. Taking then again large-scale structure into account increases the mass bias even further (blue, solid lines) because cosmic noise reduces the relative contribution of large scales to the shear signal.

We repeat these calculations, but this time we keep the fraction of centred haloes fixed at $f = 0.75$ and leave the width of the miscentring distribution, σ_s , free to vary. The results are shown in Fig. 3.6b for the same fiducial masses. The functional behaviour is this time more complex, but again it is apparent that including large-scale structure contributions (solid lines) also increases the bias caused by miscentring.

Thus, the combined effect of large-scale structure and miscentring is to increase the uncertainties in the determination of the halo mass and to introduce a mass bias (towards lower masses). By comparing the findings of Fig. 3.6a and Fig. 3.6b to the relative uncertainties on the cluster mass as provided in Table 3.1, we conclude that for the mass estimate of a single

cluster the bias due to miscentring is negligible compared to the relative uncertainty σ . For a stacked signal with statistics such as will be provided by the *Euclid* survey, this is no longer the case, since the statistical error σ will be reduced by a factor $1/\sqrt{N}$ (cf. Table 3.1). Hence, it will be necessary to determine the miscentring parameters f and σ_s to within a few per cent in order to derive accurate mass determinations.

In order to quantify this, we calculate upper limits for the precision to within which f and the relative error on σ_s must be known such that the bias due to miscentring is smaller than the 1σ -error in mass (cf. Table 3.1). The upper bound on the precision of f is thus defined as

$$\Delta f_{\max} = \frac{\sigma}{\sqrt{N}} \left(\frac{d\Delta M}{df} \right)^{-1}. \quad (3.36)$$

Furthermore, the upper bound on the relative error $\Delta\sigma_s/\sigma_s$ of the width σ_s is given as

$$\left(\frac{\Delta\sigma_s}{\sigma_s} \right)_{\max} = \frac{\sigma}{\sqrt{N}} \left(\frac{d\Delta M}{d\sigma_s} \Big|_{\sigma_s} \right)^{-1}. \quad (3.37)$$

The values corresponding to the three fiducial masses M_{true} of Fig. 3.6b including large-scale structure contributions are provided in Table 3.3.

Next, we explore if these conclusions also hold if we marginalize over the miscentring parameters expressing our lack of knowledge about them. Note as well, that we still assume equation (3.33) to hold which in itself is an important assumption in this regard. Hence, we explore the parameter space by fitting a miscentred shear signal to the shear signal of a fiducial model with mass $M = 8.75 \times 10^{14} h^{-1} M_{\odot}$, $f = 1$ at redshift $z = 0.1875$ for different values of M , σ_s , and f . All three parameters are varied for 50 different masses in the range $2.03 \times 10^{14} h^{-1} M_{\odot} \leq M \leq 2.03 \times 10^{15} h^{-1} M_{\odot}$, 40 different values of σ_s in the range $0 \leq \sigma_s \leq 2 h^{-1} \text{Mpc}$, and 20 different values of the fraction of centred haloes in the range $0 \leq f \leq 1$, respectively.

For the fitting we adopt again the formalism of Section 3.2.3 always including large-scale structure contributions. We have repeated these calculations for a second halo with fiducial mass $M = 3.50 \times 10^{14} h^{-1} M_{\odot}$ (where we adjust the mass ranges accordingly).

In Fig. 3.7a we compare the marginalized probability distributions assuming flat priors on σ_s and f over the ranges indicated above for the two haloes with their perfect fit counterparts (cf. Fig. 3.1a). The marginalization over f and σ_s , respectively, introduces a small bias due to the truncation of the prior on σ_s at $2 h^{-1} \text{Mpc}$. However, the assumption of flat priors on both miscentring parameters is too pessimistic.

Already with current data it is possible, particularly for the most massive clusters, to derive more realistic priors for the miscentring parameters than flat ones. Based on measurements of the displacement between the BCG and the maximum of the X-ray radiation from the intracluster medium from a sample of 53 massive galaxy clusters presented in Bildfell et al. (2008), we have estimated errors on f and σ_s by bootstrapping the distribution of measured off-centre radii. We find $\Delta f = 0.04$ and $\Delta\sigma_s = 0.01 h^{-1} \text{Mpc}$ independent of the number of bootstraps once this exceeds ~ 1000 . Interpreting these errors then as widths of Gaussian priors on f and σ_s , respectively, yields qualitatively unbiased mass estimates when marginalizing over these priors instead of flat priors, as shown in Fig. 3.7b.

In the very near future a mapping of the X-ray sky will be carried out by *eROSITA* (Merloni et al. 2012) which is also aimed at detecting a large sample ($\sim 10^5$) of galaxy clusters. This sample can then be used to derive even better priors on the miscentring parameters which will mitigate the effect of the miscentring bias for *Euclid* weak-lensing cluster masses entirely. Moreover, the combination of the *eROSITA* and *Euclid* cluster surveys will also allow

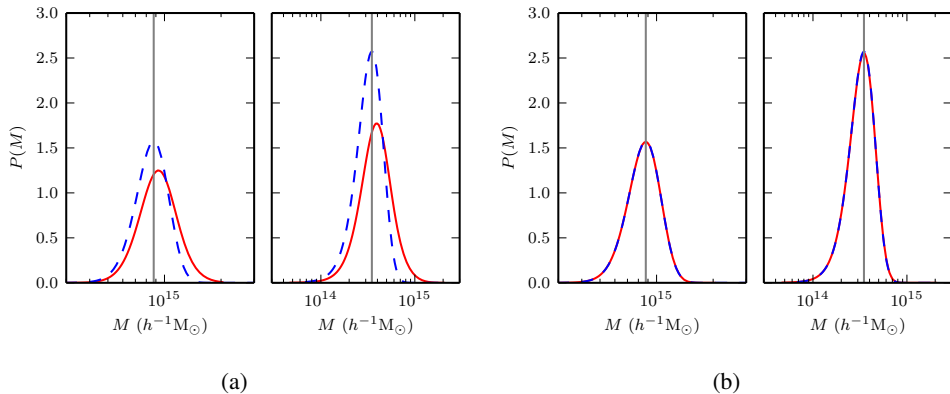


Figure 3.7: Comparison of likelihoods for two haloes of masses $M = 8.75 \times 10^{14} h^{-1} M_{\odot}$ (left) and $M = 3.50 \times 10^{14} h^{-1} M_{\odot}$ (right), respectively (blue, dashed lines) and likelihoods for the same mass haloes but marginalized over miscentring parameters σ_s and f (red, solid lines) assuming the following priors for both parameters: (a) flat priors, (b) Gaussian priors. The grey, solid line shows the fiducial mass for each halo and we always account for large-scale structure contributions in the error budget. All haloes are at redshift $z = 0.1875$.

to reduce the uncertainty on the hydrostatic mass bias between X-ray and weak-lensing mass estimates so far that determining the sum of neutrino masses will be possible with cluster counts (cf. figure 12 from [Planck Collaboration XXIV 2015a](#)).

3.4 Conclusions

We have investigated the level of statistical uncertainties and scrutinized various sources of systematic errors in the determination of masses for stacks of galaxy clusters employing weak gravitational lensing. Throughout the analysis we have been focussing on future large area surveys, in particular the *Euclid* survey, so that the predominant source of statistical uncertainty, i.e. shape noise, is as small as possible when referring to (large) stacks of galaxy clusters.

In Section 3.2 we have established the level of expected statistical uncertainties on the mass of (stacks of) galaxy clusters. We emphasize that contributions of cosmic noise must be included in realistic statistical uncertainties. However, the level of expected statistical uncertainties is very low (cf. Table 3.1 and Fig. 3.2). Thus, at this level of expected statistical precision sources of systematic errors become important which are still negligible compared to shape noise in current and ongoing surveys. Furthermore, the *Euclid* survey poses an upper limit of $m < 2 \times 10^{-3}$ ([Laureijs et al. 2011](#)) on one of the predominant biases of weak lensing, i.e. the multiplicative bias m . The other predominant bias, i.e. the additive bias, is negligible when referring explicitly to stacks of clusters due to the averaging process involved in that kind of analysis. Hence, we expanded our analysis to other sources of bias instead.

We have addressed one of these additional biases in Section 3.3.1 in which we investigated the effect on the accuracy of lensing masses when accounting for imperfect photometric redshift assignment to cluster member galaxies. Typically, a small fraction of these will be scattered to higher redshifts and thus mimic background source galaxies. This leads to a decreased weak lensing signal and thus requires the assignment of higher cluster masses during the fitting. We have shown that this bias is significant, especially for analyses using radii be-

tween $0.2 R_{\text{vir}}$ and $1 R_{\text{vir}}$. However, even including larger radii out to $2 R_{\text{vir}}$ will still require to properly account for this bias in the full analysis and we strongly recommend to study the impact of this effect further in the context of more detailed simulations.

Another source of systematic error is the effect of miscentring, i.e. the ambiguity in the choice of an observational cluster centre. In general, a displacement of the observed cluster centre and the true cluster centre leads again to a dilution of the shear signal and thus to higher mass estimates. Already with currently available data it is possible though to derive realistic priors for the miscentring parameters, so that it will be possible to mitigate this bias entirely even in the case of *Euclid* when taking complementary missions such as *eROSITA* into account.

Finally, we want to emphasize that our analysis of these additional sources of systematic errors are all based on (simple) analytic models. Eventually, these will have to be reassessed by extensive numerical simulations in order to derive more realistic bounds and quantitative estimates. Our analysis, however, is meant to point to the relative importance and order of magnitude predictions of these systematic errors in order to supply the community with a guideline for these future simulations.

Acknowledgements

We thank the anonymous referee for very detailed comments which helped to further improve this work and its presentation. FK acknowledges support from a de Sitter Fellowship of the Netherlands Organization for Scientific Research (NWO). HH and ME acknowledge support from the European Research Council under FP7 grant number 279396.

Plots in this paper were produced with PYTHON and its MATPLOTLIB (Hunter 2007). Cosmology related calculations were performed using the PYTHON package COSMOLOGY.⁷

Bibliography

- Audren B., Lesgourgues J., 2011, *J. Cosmology Astropart. Phys.*, 2011, 037
- Banerji M., et al., 2015, *MNRAS*, 446, 2523
- Bartelmann M., 1996, *A&A*, 313, 697
- Bartelmann M., Schneider P., 2001, *Phys. Rep.*, 340, 291
- Bartelmann M., Limousin M., Meneghetti M., Schmidt R., 2013, *Space Sci. Rev.*, 177, 3
- Becker M. R., Kravtsov A. V., 2011, *ApJ*, 740, 25
- Benítez N., 2000, *ApJ*, 536, 571
- Bildfell C., Hoekstra H., Babul A., Mahdavi A., 2008, *MNRAS*, 389, 1637
- Blas D., Lesgourgues J., Tram T., 2011, *J. Cosmology Astropart. Phys.*, 2011, 034
- Butcher H., Oemler Jr. A., 1984, *ApJ*, 285, 426
- Dodelson S., 2004, *Phys. Rev. D*, 70, 023008
- Duffy A. R., Schaye J., Kay S. T., Vecchia C. D., 2008, *MNRAS*, 390, L64

⁷<http://roban.github.com/CosmoLoPy/>

- Dutton A. A., Macciò A. V., 2014, *MNRAS*, 441, 3359
- Eddington A. S., 1913, *MNRAS*, 73, 359
- Eisenstein D. J., Hu W., 1999, *ApJ*, 511, 5
- Flaugher B., 2005, *Int. J. Mod. Phys. A*, 20, 3121
- Gladders M. D., Yee H. K. C., Majumdar S., Barrientos L. F., Hoekstra H., Hall P. B., Infante L., 2007, *ApJ*, 655, 128
- Hansen S. M., Sheldon E. S., Wechsler R. H., Koester B. P., 2009, *ApJ*, 699, 1333
- Heymans C., et al., 2006, *MNRAS*, 368, 1323
- Hoekstra H., 2001, *A&A*, 370, 743
- Hoekstra H., 2003, *MNRAS*, 339, 1155
- Hoekstra H., Hartlap J., Hilbert S., van Uitert E., 2011, *MNRAS*, 412, 2095
- Hoekstra H., Bartelmann M., Dahle H., Israel H., Limousin M., Meneghetti M., 2013, *Space Sci. Rev.*, 177, 75
- Hoekstra H., Herbonnet R., Muzzin A., Babul A., Mahdavi A., Viola M., Cacciato M., 2015, *MNRAS*, 449, 685
- Hu W., Kravtsov A. V., 2003, *ApJ*, 584, 702
- Hunter J. D., 2007, *Comput. Sci. Eng.*, pp 90–95
- Huterer D., Takada M., Bernstein G., Jain B., 2006, *MNRAS*, 366, 101
- Ivezic Z., et al., 2008, preprint (arXiv:0805.2366)
- Johnston D. E., et al., 2007, preprint (arXiv:0709.1159)
- Jouvel S., et al., 2011, *A&A*, 532, A25
- Laureijs R., et al., 2011, preprint (arXiv:1110.3193)
- Martí P., Miquel R., Castander F. J., Gaztañaga E., Eriksen M., Sánchez C., 2014, *MNRAS*, 442, 92
- Massey R., et al., 2013, *MNRAS*, 429, 661
- Medezinski E., et al., 2013, *ApJ*, 777, 43
- Meneghetti M., et al., 2014, *ApJ*, 797, 34
- Merloni A., et al., 2012, preprint (arXiv:1209.3114)
- Navarro J. F., Frenk C. S., White S. D. M., 1997, *ApJ*, 490, 493
- Navarro J. F., et al., 2010, *MNRAS*, 402, 21
- Oguri M., Takada M., Okabe N., Smith G. P., 2010, *MNRAS*, 405, 2215
- Planck Collaboration XVI, 2014a, *A&A*, 571, A16

Planck Collaboration XX, 2014b, *A&A*, 571, A20

Planck Collaboration XXIV, 2015a, preprint (arXiv:1502.01597)

Planck Collaboration XIII, 2015b, preprint (arXiv:1502.01589)

Press W. H., Schechter P., 1974, *ApJ*, 187, 425

Sartoris B., et al., 2015, preprint (arXiv:1505.02165)

Schechter P., 1976, *ApJ*, 203, 297

Shaw L. D., Weller J., Ostriker J. P., Bode P., 2006, *ApJ*, 646, 815

Sifón C., Hoekstra H., Cacciato M., Viola M., Köhlinger F., van der Burg R. F. J., Sand D. J., Graham M. L., 2015, *A&A*, 575, A48

Tinker J., Kravtsov A. V., Klypin A., Abazajian K., Warren M., Yepes G., Gottlöber S., Holz D. E., 2008, *ApJ*, 688, 709

Tinker J. L., Robertson B. E., Kravtsov A. V., Klypin A., Warren M. S., Yepes G., Gottlöber S., 2010, *ApJ*, 724, 878

Vafaei S., Lu T., van Waerbeke L., Semboloni E., Heymans C., Pen U.-L., 2010, *Astropart. Phys.*, 32, 340

Wright C. O., Brainerd T. G., 2000, *ApJ*, 534, 34

Yang X., Mo H. J., van den Bosch F. C., Jing Y. P., Weinmann S. M., Meneghetti M., 2006, *MNRAS*, 373, 1159

de Jong J. T. A., Kleijn G. A. V., Kuijken K. H., Valentijn E. A., Consortiums K. a. A.-W., 2012, *Exp. Astron.*, 35, 25

van der Burg R. F. J., Muzzin A., Hoekstra H., Wilson G., Lidman C., Yee H. K. C., 2014, *A&A*, 561, A79

von der Linden A., et al., 2014, *MNRAS*, 439, 2

A direct measurement of tomographic lensing power spectra from CFHTLenS

We measure the weak gravitational lensing shear power spectra and their cross-power in two photometric redshift bins from the Canada–France–Hawaii Telescope Lensing Survey (CFHTLenS). The measurements are performed directly in multipole space in terms of adjustable band powers. For the extraction of the band powers from the data we have implemented and extended a quadratic estimator, a maximum likelihood method that allows us to readily take into account irregular survey geometries, masks, and varying sampling densities. We find the 68 per cent credible intervals in the σ_8 – Ω_m plane to be marginally consistent with results from *Planck* for a simple five-parameter Λ cold dark matter (Λ CDM) model. For the projected parameter $S_8 \equiv \sigma_8(\Omega_m/0.3)^{0.5}$ we obtain a best-fitting value of $S_8 = 0.768^{+0.045}_{-0.039}$. This constraint is consistent with results from other CFHTLenS studies as well as the Dark Energy Survey. Our most conservative model, including modifications to the power spectrum due to baryon feedback and marginalization over photometric redshift errors, yields an upper limit on the total mass of three degenerate massive neutrinos of $\Sigma m_\nu < 4.53$ eV at 95 per cent credibility, while a Bayesian model comparison does not favour any model extension beyond a simple five-parameter Λ CDM model. Combining the shear likelihood with *Planck* breaks the σ_8 – Ω_m degeneracy and yields $\sigma_8 = 0.818 \pm 0.013$ and $\Omega_m = 0.300 \pm 0.011$ which is fully consistent with results from *Planck* alone.

F. Köhlinger, M. Viola, W. Valkenburg, B. Joachimi, H. Hoekstra and K. Kuijken
2016, *MNRAS*, **Volume 456**, Issue 2, pp 1508–1527

4.1 Introduction

The physical nature of the major components of current cosmological models is still unknown. Nevertheless, a simple six-parameter model including dark matter and dark energy – the Λ -dominated cold dark matter model (Λ CDM) – has been proven very successful in explaining a multitude of cosmological observations ranging from the radiation of the cosmic microwave background (CMB, e.g. [Planck Collaboration XIII 2015a](#)) to supernovae (e.g. [Riess et al. 2011](#)) and large-scale structure (LSS) probes (e.g. [Aubourg et al. 2014](#)).

The energy densities of dark matter and dark energy, at present, are very well constrained by the aforementioned observations. The next frontier is pinning down the evolution of both dark species, and observing effects from massive neutrinos. One promising probe is the growth of structure as inferred from cosmic shear: the (very) weak-lensing effect due to cosmic large-scale structure bending the light perpendicular to the line-of-sight between observer and background galaxies according to Einstein’s equivalence principle. The coherent image distortions – the shear – due to the gravitational potential of a deflector can only be measured statistically, which requires averaging over large numbers of sources. Therefore, wide-field surveys covering increasingly larger volumes on the sky are required in order to improve the precision of the measurements. An analysis of the weak-lensing signal as a function of redshift is sensitive to the growth of structure, and is thereby indirectly sensitive to the expansion rate of the Universe as well as to the clustering behaviour of various matter species: massive neutrinos, dark energy, cold dark matter, etc.

In order to constrain the dark energy equation-of-state and its possible time evolution it is hence crucial to measure the cosmic shear signal in different redshift slices ([Heymans et al. 2013](#); [Benjamin et al. 2013](#); [DES Collaboration 2015](#)) or directly in 3D ([Kitting et al. 2014](#)).

Massive neutrinos also leave their distinct physical imprints on the matter power spectrum and hence can be probed using weak lensing (e.g. [Lesgourgues & Pastor 2006](#) and references therein). Theoretically it is straightforward to study these features directly in Fourier space, i.e. in terms of shear–shear power spectra. Traditionally, lensing analyses employ real-space correlation functions for measuring cosmic shear. This introduces further complications in the comparison of observations with theory (cf. section 4.3.2 of [Planck Collaboration XIV 2015b](#)), because different scales are highly correlated. Hence, the signal at very non-linear scales requires proper modelling in order to avoid any bias in the cosmological parameters. This is generally challenging due to our limited understanding of the effect of baryons on the non-linear matter power spectrum (e.g. [Semboloni et al. 2011, 2013](#)). Therefore, in this paper we apply a method for extracting the data in multipole space and in different redshift bins in terms of band powers of the lensing power spectrum. In order to achieve this we have implemented and expanded the quadratic estimator method originally formulated in the context of weak lensing by [Hu & White \(2001\)](#). The first applications of this technique to measured shear data were presented in [Brown et al. \(2003\)](#) and [Heymans et al. \(2005\)](#) using the COMBO-17 and GEMS data sets, respectively. More recently, [Lin et al. \(2012\)](#) applied the quadratic estimator technique to shear data measured from the Sloan Digital Sky Survey (SDSS) Stripe 82. Other recent direct shear power spectrum analyses include the Dark Energy Survey (DES; [Becker et al. 2015](#)) analysis and the SDSS-FIRST cross-power spectrum analysis of [Demetroullas & Brown \(2015\)](#). All these studies did not split the power spectrum analysis into redshift bins yet and the latter two studies employed a pseudo- $C(\ell)$ power spectrum approach, the other major technique for direct power spectrum measurements. [Alsing et al. \(2015\)](#) recently presented a hierarchical inference method that also makes direct use of the shear power spectrum.

In this paper we apply our expanded tomographic version of the quadratic estimator to publicly available data from the Canada–France–Hawaii Telescope Lensing Survey (CFHTLenS;

Heymans et al. 2012). CFHTLenS is currently the statistically most constraining weak lensing data set and covers an area of about 154 deg^2 on the sky. The data include also photometric redshifts which thus allow us to carry out a tomographic analysis. As a further benefit to the state-of-the-art data, CFHTLenS has already been used before in cosmological analyses (Heymans et al. 2013; Benjamin et al. 2013; Kilbinger et al. 2013; Kitching et al. 2014) which enables us to directly cross-check our results with the literature.

The paper is structured as follows: in Section 4.2 we introduce the weak-lensing formalism in terms of power spectra. In Section 4.3 we describe the theory of the quadratic estimator approach and generalize it to include tomography. Section 4.4 provides a brief overview of the CFHTLenS data and how to perform shear measurements with it. Before presenting the extracted lensing power spectra in Section 4.6, we test and validate the method on mock data in Section 4.5. From the shear power spectra we derive cosmological parameters and discuss our results in Section 4.7. Finally we present our conclusions in Section 4.8.

4.2 Theory

The deflection of light due to mass is a consequence of Einstein’s principle of equivalence and is termed gravitational lensing. One particular case of gravitational lensing is weak lensing, the very weak but coherent image distortions of background sources due to the gradients of the gravitational potential of a deflector in the foreground.

These image distortions can only be measured in a statistical sense, given the fact that galaxies are intrinsically elliptical, by averaging over large numbers of background sources. The resulting correlations in the galaxy shapes can be used to study the evolution of all the intervening large-scale structure between the sources and the observer, in that sense the whole Universe acts as a lens. This particular form of weak lensing is called cosmic shear and studied best in terms of wide-field surveys covering increasingly more volume in the sky (cf. Kilbinger 2015 for a recent review). We intentionally skip a more basic, mathematical introduction of gravitational lensing and weak lensing in particular and refer the reader for details on that to the standard literature (e.g. Bartelmann & Schneider 2001).

A wide-field observation of the sky as part of a weak-lensing survey yields two main observables: the ellipticity of galaxies and their (photometric) redshifts. The estimates of the ellipticity components e_1 , e_2 at angular positions \mathbf{n}_i can be binned into pixels $i = 1, \dots, N_{\text{pix}}$ and (photometric) redshift bins z_μ . The averages of the measured ellipticities in each pixel are unbiased estimates of the two components of the spin-2 shear field, $\gamma_1(\mathbf{n}, z_\mu)$ and $\gamma_2(\mathbf{n}, z_\mu)$, which is sourced by the convergence field κ . In the limit of the flat-sky approximation the Fourier decomposition of this field can be expressed as

$$\gamma_1(\mathbf{n}, z_\mu) \pm i\gamma_2(\mathbf{n}, z_\mu) = \int \frac{d^2\ell}{(2\pi)^2} [\kappa(\boldsymbol{\ell}, z_\mu) \pm i\beta(\boldsymbol{\ell}, z_\mu)] W(\boldsymbol{\ell}) e^{\pm 2i\varphi_\ell} e^{i\boldsymbol{\ell}\cdot\mathbf{n}}, \quad (4.1)$$

where φ_ℓ is the angle between the two-dimensional vector $\boldsymbol{\ell}$ and the x -axis. To first order for the lensing of density perturbations the field β vanishes in the absence of any systematics. However, we still want to measure it as a systematic test and therefore include it in our notation. The Fourier transform of the pixel window function is denoted as $W(\boldsymbol{\ell})$. This function can explicitly be written out for square pixels of side length σ_{pix} in radians as

$$W(\boldsymbol{\ell}) = j_0\left(\frac{\ell_x \sigma_{\text{pix}}}{2} \cos \varphi_\ell\right) j_0\left(\frac{\ell_y \sigma_{\text{pix}}}{2} \sin \varphi_\ell\right), \quad (4.2)$$

where the zeroth-order spherical Bessel function is defined as $j_0(x) = \sin(x)/x$.

The two-point statistics of the shear field can either be expressed in real-space correlation functions or equivalently in terms of their Fourier transforms, the shear power spectra.

Following [Hu & White \(2001\)](#) and expanding the notation to also include tomographic bins we write out the shear correlations between pixels \mathbf{n}_i and \mathbf{n}_j in terms of their power spectra as:

$$\begin{aligned}\langle \gamma_{1i\mu} \gamma_{1j\nu} \rangle &= \int \frac{d^2\ell}{(2\pi)^2} \left[C_{\mu\nu}^{\text{EE}}(\ell) \cos^2 2\varphi_\ell + C_{\mu\nu}^{\text{BB}}(\ell) \sin^2 2\varphi_\ell - C_{\mu\nu}^{\text{EB}}(\ell) \sin 4\varphi_\ell \right] W^2(\ell) e^{i\ell \cdot (\mathbf{n}_i - \mathbf{n}_j)}, \\ \langle \gamma_{2i\mu} \gamma_{2j\nu} \rangle &= \int \frac{d^2\ell}{(2\pi)^2} \left[C_{\mu\nu}^{\text{EE}}(\ell) \sin^2 2\varphi_\ell + C_{\mu\nu}^{\text{BB}}(\ell) \cos^2 2\varphi_\ell + C_{\mu\nu}^{\text{EB}}(\ell) \sin 4\varphi_\ell \right] W^2(\ell) e^{i\ell \cdot (\mathbf{n}_i - \mathbf{n}_j)}, \\ \langle \gamma_{1i\mu} \gamma_{2j\nu} \rangle &= \int \frac{d^2\ell}{(2\pi)^2} \left[\frac{1}{2} (C_{\mu\nu}^{\text{EE}}(\ell) - C_{\mu\nu}^{\text{BB}}(\ell)) \sin 4\varphi_\ell + C_{\mu\nu}^{\text{EB}}(\ell) \cos 4\varphi_\ell \right] W^2(\ell) e^{i\ell \cdot (\mathbf{n}_i - \mathbf{n}_j)},\end{aligned}\quad (4.3)$$

where we have suppressed the arguments of the shear components $\gamma_a(\mathbf{n}_i, z_\mu)$ for clarity.

In the absence of systematic errors and shape noise the cosmological signal is contained in the E-modes and their power spectrum is equivalent to the convergence power spectrum, i.e. $C^{\text{EE}}(\ell) = C^{\kappa\kappa}(\ell)$ and $C^{\text{BB}}(\ell) = 0 = C^{\text{EB}}(\ell)$. Shot noise will generate equal power in E- and B-modes.

The E-mode or convergence power spectra can be predicted for a given cosmological model:

$$C_{\mu\nu}^{\text{EE}}(\ell) = \frac{9\Omega_m^2 H_0^4}{4c^4} \int_0^{\chi_H} d\chi \frac{g_\mu(\chi) g_\nu(\chi)}{a^2(\chi)} P_\delta \left(k = \frac{\ell}{f_K(\chi)}; \chi \right), \quad (4.4)$$

where χ is the radial comoving distance, χ_H the distance to the horizon, $a(\chi)$ the scale factor, $P_\delta(k; \chi)$ is the three-dimensional matter power spectrum, and the angular diameter distance is denoted as $f_K(\chi)$. Note that we use the Limber approximation ([Limber 1954](#)) in the equation above and the indices μ, ν run over the tomographic bins.

The lensing kernels $g_\mu(\chi)$ are a measure for the lensing efficiency in each tomographic bin μ and can be written as

$$g_\mu(\chi) = \int_\chi^{\chi_H} d\chi' n_\mu(\chi') \frac{f_K(\chi' - \chi)}{f_K(\chi')}, \quad (4.5)$$

where $n_\mu(\chi) d\chi = p_\mu(z) dz$ is the source redshift distribution.

4.3 Quadratic estimator

We summarize here the method originally proposed by [Hu & White \(2001\)](#) but make also extensive use of the summary provided by [Lin et al. \(2012\)](#). Furthermore, we generalize the approach to include tomographic redshift bins.

We start by assuming that the likelihood of the measured shear field in terms of band powers \mathcal{B} is Gaussian over most scales of interest for our analysis, i.e.

$$\mathcal{L} = \frac{1}{(2\pi)^N |\mathbf{C}(\mathcal{B})|^{1/2}} \exp \left[-\frac{1}{2} \mathbf{d}^T [\mathbf{C}(\mathcal{B})]^{-1} \mathbf{d} \right], \quad (4.6)$$

where \mathbf{d} denotes the data vector with components

$$d_{\mu ai} = \gamma_a(\mathbf{n}_i, z_\mu). \quad (4.7)$$

It contains the two components of the measured shear in each pixel \mathbf{n}_i per redshift bin z_μ (note that the indices are all interchangeable as long as the order is consistent throughout the

algorithm below). The full covariance matrix \mathbf{C} is the sum of the cosmological signal \mathbf{C}^{sig} and the noise $\mathbf{C}^{\text{noise}}$. The latter includes the contribution from shape and measurement errors. We use the set of equations (4.3) to build up the lensing signal correlation matrix, where we label the shear components with indices a, b , pixels with indices i, j , and redshift bins with indices μ, ν :

$$\mathbf{C}^{\text{sig}} = \langle \gamma_a(\mathbf{n}_i, z_\mu) \gamma_b(\mathbf{n}_j, z_\nu) \rangle. \quad (4.8)$$

Furthermore, the contribution of shape noise to the signals can be encoded in the matrix

$$\mathbf{C}^{\text{noise}} = \frac{\sigma_\gamma^2}{N_{i\mu}} \delta_{ij} \delta_{ab} \delta_{\mu\nu}, \quad (4.9)$$

where σ_γ denotes the root-mean-square intrinsic ellipticity per ellipticity component for all the galaxies and $N_{i\mu}$ is the effective number of galaxies per pixel i in redshift bin z_μ .¹ Thus we assume that shape noise is neither correlated between different pixels $\mathbf{n}_i, \mathbf{n}_j$, and shear components γ_a, γ_b , nor between different redshift bins z_μ, z_ν . This is a well-motivated assumption as long as the pixel noise of the detector is uncorrelated.

We approximate the angular power spectra $C_{\mu\nu}^\theta(\ell)$ with piecewise constant band powers $\mathcal{B}_{\zeta\theta\beta}(\ell)$ of type $\theta \in (\text{EE}, \text{BB}, \text{EB})$ spanning a range of multipoles ℓ within the band β . The index ζ runs only over *unique* redshift bin correlations. This enables us to write the components of the cosmic signal covariance matrix as a linear combination of these band powers:

$$C_{(\mu\nu)(ab)(ij)}^{\text{sig}} = \sum_{\zeta, \theta, \beta} \mathcal{B}_{\zeta\theta\beta} M_{\zeta(\mu\nu)} \int_{\ell \in \beta} \frac{d\ell}{2(\ell+1)} \left[w_0(\ell) I_{(ab)(ij)}^\theta + \frac{1}{2} w_4(\ell) Q_{(ab)(ij)}^\theta \right]. \quad (4.10)$$

The term in brackets in the above equation encodes the geometry of the shear field including masks and its decomposition in Fourier space. The matrices \mathbf{M}_ζ map the redshift bin indices μ, ν to the unique correlations ζ possible between those: for n_z redshift bins there are only $n_z(n_z+1)/2$ unique correlations because $z_\mu \times z_\nu = z_\nu \times z_\mu$. The explicit expressions for these matrices and the matrices \mathbf{I}^θ and \mathbf{Q}^θ are given in Appendix 4.A.

The best-fitting band powers $\mathcal{B}_{\zeta\theta\beta}$ are determined by finding the cosmic signal \mathbf{C}^{sig} which describes the measured shear data the best. For that purpose we use the Newton–Raphson method iteratively in order to find the root of $d\mathcal{L}/d\mathcal{B}_A = 0$ (Bond et al. 1998; Seljak 1998). An improved estimate for the band powers \mathcal{B}_A is found by evaluating the expression

$$\delta\mathcal{B}_A \propto \sum_B \frac{1}{2} (\mathbf{F}^{-1})_{AB} \text{Tr}[(d\mathbf{d}^T - \mathbf{C})(\mathbf{C}^{-1} \mathbf{D}_A \mathbf{C}^{-1})], \quad (4.11)$$

where we have introduced now the superindex A for a particular index combination $(\zeta\theta\beta)$. The matrices \mathbf{D}_A are derivatives of the full covariance matrix with respect to any band-power combination. We skip here a rigorous definition of \mathbf{D}_A and refer the reader to Appendix 4.A for derivations of these expressions. The elements of the Fisher matrix \mathbf{F} can be calculated as (Hu & White 2001)

$$F_{AB} = \frac{1}{2} \text{Tr}(\mathbf{C}^{-1} \mathbf{D}_A \mathbf{C}^{-1} \mathbf{D}_B). \quad (4.12)$$

In previous work (cf. Hu & White 2001; Lin et al. 2012), the inverse of the Fisher matrix was used as an estimator of the covariance between the extracted band powers. We refrain from following this approach since the inverse Fisher matrix is only an approximation of the true covariance in the Gaussian limit. Hence, we decided to estimate the covariance of the

¹The effective number of galaxies per pixel can be calculated using equation (4.17) multiplied by the area of the pixel Ω .

band powers from mock data instead. We present a detailed discussion of this approach in Section 4.5.2.

For the comparison of the measured band powers to theoretical predictions, we have to take into account that each measured band power $\mathcal{B}_A = \mathcal{B}_{\zeta\theta\beta}$ samples the power spectra with its own window function. This can be computed by noting that the expectation value of the band power, $\langle \mathcal{B}_{\zeta\theta\beta} \rangle$, is related to the power spectrum at each wave number $\mathcal{B}_{\zeta\theta}(\ell) = \ell(\ell + 1)C_{\zeta\theta}(\ell)/(2\pi)$ through the band power window function $W_{\zeta\theta\beta}(\ell)$ (Knox 1999; Lin et al. 2012), i.e.

$$\langle \mathcal{B}_{\zeta\theta\beta} \rangle = \sum_{\ell} W_{\zeta\theta\beta}(\ell) \mathcal{B}_{\zeta\theta}(\ell), \quad (4.13)$$

where the sum is calculated for integer multipoles ℓ .² The elements of the window function matrix can be derived as (Lin et al. 2012)

$$W_{\zeta\theta\beta}(\ell) = \sum_{\chi,\eta,\lambda} \frac{1}{2} (\mathbf{F}^{-1})_{(\zeta\theta\beta)(\chi\eta\lambda)} T_{\chi\eta\lambda}(\ell), \quad (4.14)$$

where \mathbf{F}^{-1} denotes the inverse of the Fisher matrix (cf. equation 4.12). The trace matrix \mathbf{T} is defined as

$$T_{\zeta\theta\beta}(\ell) = \text{Tr}(\mathbf{C}^{-1} \mathbf{D}_{\zeta\theta\beta} \mathbf{C}^{-1} \mathbf{D}_{\ell}). \quad (4.15)$$

The derivative \mathbf{D}_{ℓ} denotes the derivative of the full covariance \mathbf{C} with respect to the power at a single multipole ℓ . We write it out explicitly in Appendix 4.A (cf. equation 4.46).

The likelihood-based quadratic estimator automatically accounts for any irregularity in the survey geometry or data sampling while it still maintains an optimal weighting of the data. This is important when dealing with real data because it allows for employing sparse sampling techniques and it can deal efficiently with (heavily) masked data. The whole method and in particular its ability to deal with masks are tested extensively in Section 4.5 before we apply it to data from CFHTLenS in Section 4.6.

4.4 CFHTLenS measurements

In the following analysis we use the publicly available data³ from the lensing analysis of the Canada–France–Hawaii Legacy Survey, hereafter referred to as CFHTLenS (Heymans et al. 2012). The survey consists of four patches (W1, W2, W3, W4) covering a total area of $\approx 154 \text{ deg}^2$. Due to stellar haloes or artifacts in the images 19 per cent of the area is masked. The lensing data we use in this work are a combination of data processing with THELI (Erben et al. 2013), shear measurements with *lensfit* (Miller et al. 2013), and photometric redshift measurements with PSF-matched photometry (Hildebrandt et al. 2012). A full systematic error analysis of the shear measurements in combination with the photometric redshifts is presented in Heymans et al. (2012), with additional error analyses of the photometric redshift measurements presented in Benjamin et al. (2013). One of the main results of those extensive systematic tests was the rejection of 25 per cent of the CFHTLenS tiles (1 deg^2 each) for cosmic shear studies. In this work we only use the 75 per cent of the tiles which passed the systematic tests as outlined in Heymans et al. (2012). Note that this causes considerable large-scale masking in each patch.

²For the cosmological analysis we employ a range $80 \leq \ell \leq 2600$. The lower limit is set by the smallest multipole ℓ included in the analysis and the upper limit must include multipoles ℓ higher than the maximum ℓ used in the analysis (cf. Section 4.4).

³<http://www.cfhtlens.org/astronomers/data-store>

Photometric redshift measurements have also been extensively tested (Hildebrandt et al. 2012; Benjamin et al. 2013) and they were found reliable in the range $0.1 < Z_B < 1.3$, where Z_B is the peak of the photometric redshift posterior distribution as computed by BPZ (Benítez 2000). In our analysis we only use galaxies in this redshift range.

We compile all tiles associated to a particular CFHTLenS patch into a single shear catalogue. Coordinates in these catalogues are given in right ascension α and declination δ of a spherical coordinate system. We deproject these spherical coordinates into flat coordinates via a tangential plane projection. We centre the projection, its tangent point, on the central pointing of each patch. In order to measure shears from the ellipticity components e_1 , e_2 as measured by *lensfit*, we first divide the deprojected patch into square pixels of side length σ_{pix} . We estimate the shear components g_a per pixel at position $\mathbf{n} = (x_c, y_c)$ from the ellipticity components e_a inside that pixel:

$$g_a(x_c, y_c) = \frac{\sum_i w_i (e_{a,i} - c_{a,i})}{(1 + m) \sum_i w_i}, \quad (4.16)$$

where the index i runs over all objects inside the pixel and the index a is either 1 or 2 for the two shear and ellipticity components, respectively. The weights w are computed during the shape measurement with *lensfit* and they account both for the intrinsic shape noise and measurement errors. The subscript of the coordinates indicates that the position of the average shear is taken to be at the centre of the pixel. Note that we assume the galaxies are distributed uniformly in the shear pixels. Although this is a simplifying assumption we argue that it has only minor effects in the measurement considering the general width of the band powers. We define distances $r_{ij} = |\mathbf{n}_i - \mathbf{n}_j|$ and angles $\varphi = \arctan(\Delta y / \Delta x)$ between all pixels i, j which enter eventually in the quadratic estimator algorithm (cf. Section 4.3 and Appendix 4.A).

In each pixel we apply an average multiplicative correction $(1 + m)$ to the measured shear. This is necessary because of noise bias in shear measurements (Melchior & Viola 2012; Refregier et al. 2012; Miller et al. 2013). The multiplicative correction has been computed from a dedicated suite of image simulation mimicking CFHTLenS data (Miller et al. 2013). Moreover, we apply to each measured ellipticity an additive correction c_a which is computed from all the pass-tiles by requiring that the average ellipticity must vanish across the survey as a function of galaxy size and signal-to-noise (Heymans et al. 2012). For CFHTLenS c_1 was found to be zero but for c_2 a correction per object has to be applied (Heymans et al. 2012).

The highest multipole ℓ_{pix} up to which we want to extract band powers employing the quadratic estimator method (cf. Section 4.3) is on the one hand set by the scales we want to investigate because of expected modifications due to baryon feedback or massive neutrinos (cf. Section 4.7.1). On the other hand the simplifying assumptions of the algorithm such as Gaussianity also limit the maximum ℓ_{pix} . Hence, we only probe into the mildly non-linear regime and consider a multipole $\ell_{\text{pix}} \approx 2400$ as the maximal physical scale resolved. This corresponds to an angular scale of $0.15 = 9$ arcmin and thus sets the pixel size σ_{pix} . We keep parameters fixed throughout all CFHTLenS patches such as the side length of the shear pixels, σ_{pix} , measured intrinsic shape noise per ellipticity component, $\sigma_\gamma = 0.279$, and band power intervals. Because the sizes of the CFHTLenS patches are very different, the largest distance between shear pixels differs. Therefore, we limit our analysis to $\ell_{\text{field}} \geq 80$ (corresponding to an angular separation of pixels of about $\sim 4.5^\circ$), but note that even lower multipoles suffer from more sample variance. In summary, the physical scales for our analysis are $80 \leq \ell \leq 2300$, which corresponds to angular scales $0.15 \leq \vartheta \leq 4.5^\circ$. In total, we choose seven band-power intervals enclosing these physical scales as shown in Table 4.1 for the E-mode signal extraction. The width of each band should at least be two times as wide as ℓ_{field} in order to minimize correlations between the bands (Hu & White 2001). The band powers for the B-mode signal extraction are the same except that we omit the lowest band power. Note that the

Table 4.1: Band-power intervals.

Band No.	ℓ -range	ϑ -range	Comments
1	30–80	720–270 arcmin	(a), (b)
2	80–260	270–83 arcmin	–
3	260–450	83–48 arcmin	–
4	450–670	48–32 arcmin	–
5	670–1310	32–16.5 arcmin	–
6	1310–2300	16.5–9.4 arcmin	(a)
7	2300–5100	9.4–4.2 arcmin	(a)

Notes. (a) Not used in cosmological analysis. (b) No B-mode extracted.

The ϑ -ranges are just an indication and cannot be compared directly to ϑ -ranges used in real-space correlation function analyses due to the non-trivial functional dependence of these analyses on Bessel functions.

Table 4.2: Effective number densities.

redshift bin	W1	W2	W3	W4
$z_1: 0.50 < Z_B \leq 0.85$	3.36	2.80	3.48	3.25
$z_2: 0.85 < Z_B \leq 1.30$	2.86	2.00	2.63	2.22

Notes. Shown is the effective number density of galaxies n_{eff} (cf. equation 4.17) in arcmin^{-2} for all four CFHTLenS patches per tomographic redshift bin used in this analysis.

first band power includes scales below ℓ_{field} intentionally in order to absorb any DC offsets in the data. The last band should include multipoles above ℓ_{pix} , because the window function of square pixels has a long tail to high multipoles. In that sense the enclosing bands are designed to catch noise and therefore they are dropped in the cosmological analysis. We compute the effective number density of galaxies that is used in the lensing analysis and in the creation of mock data (cf. Section 4.5) following the definition of [Heymans et al. \(2012\)](#):

$$n_{\text{eff}} = \frac{1}{\Omega} \frac{(\sum_i w_i)^2}{\sum_i w_i^2}, \quad (4.17)$$

where Ω is the unmasked area used in the analysis and w is again the *lensfit* weight. We show all effective number densities per patch and redshift bin in Table 4.2.

Following the conclusions from [Benjamin et al. \(2013\)](#) regarding intrinsic galaxy alignments, which we discuss in more detail in Section 4.6, we define two redshift bins z_1 and z_2 in the ranges $z_1 : 0.50 < Z_B \leq 0.85$ and $z_2 : 0.85 < Z_B \leq 1.30$. These cuts are performed with respect to the peak of each galaxy’s photometric redshift distribution Z_B . For each of the two tomographic bins we compute the galaxy redshift distribution by summing the posterior photometric redshift distribution of all galaxies in the bin, weighted by the *lensfit* weight:

$$p(z) = \frac{\sum_i w_i p_i(z)}{\sum_i w_i}. \quad (4.18)$$

Table 4.3: Fiducial cosmology of the CFHTLenS Clone and the GRFs.

Ω_m	Ω_Λ	Ω_b	h	n_s	σ_8	Σm_v
0.279	0.721	0.046	0.701	0.96	0.817	0 eV

Notes. Cosmological parameters used in the creation of the CFHTLenS Clone (Heymans et al. 2012) which were also used to create the Gaussian random field (GRF) realizations.

The full galaxy redshift distribution is required in the calculation of the theoretical lensing power spectrum (cf. equation 4.5) and it is also needed in the creation of additional mock data (cf. Section 4.5).

4.5 Method validation and covariances

In order to test and validate the algorithm outlined in Section 4.3 we employ two types of mock data: first we make use of the publicly available CFHTLenS Clone⁴ (Heymans et al. 2012) and second we use Gaussian random fields (GRFs). This twofold approach is necessary since the multipole scales we employ in the cosmological analysis of Section 4.7 are not covered in the CFHTLenS Clone.

The CFHTLenS Clone is a mock galaxy catalogue that consists of 184 independent line-of-sight shear (and convergence) maps with a side length of $\approx 3^\circ.58$. These were extracted via ray-tracing through the TCS simulation suite (Harnois-Déraps et al. 2012) which was produced with the CUBEP³M N -body code (Harnois-Déraps et al. 2013). The CFHTLenS Clone is especially tailored to CFHTLenS in terms of the redshift distribution of lensing sources and the noise properties including, for example, realistic small scale masks (due to stars etc.). In addition to these small scale masks, we randomly mask out three non-overlapping tiles of $\approx 1 \text{ deg}^2$ each per shear field in order to mimic the effect of the additional ‘bad field’ masks also employed in the data. These mask typically 25 per cent of the total area of a patch (cf. Section 4.4 and Heymans et al. 2012) and their distribution over a patch does not show any systematic preferences. The input cosmology used in the creation of the CFHTLenS Clone is WMAP5-like (Komatsu et al. 2009) and summarized in Table 4.3. Eventually, we want to extract scales on the order of several degrees from the data. Kilbinger et al. (2013) showed, however, that the power on large scales is significantly underestimated in the CFHTLenS Clone.

In order to also validate the signal extraction on large scales, we created 184 Gaussian random field realizations (GRFs) of shear fields in two tomographic bins. The fields are $20 \times 20 \text{ deg}^2$ each and generated from convergence power spectra that have been computed for the same cosmology as the clone, using the measured redshift distributions of our two tomographic bins and the modified HALOFIT version of Takahashi et al. (2012) for the non-linear contributions to the matter power spectrum. Source galaxies are placed randomly in the fields with an arbitrary but high enough density of 10 arcmin^{-2} per tomographic bin, and the shears are linearly interpolated to these positions. We apply the mosaic masks of each CFHTLenS patch to all GRF realizations in turn, and also apply the patch-specific ‘bad field’ mask pattern masking about 25 per cent of the total area of a CFHTLenS patch. When we compile the actual input mock catalogues from the GRF shear fields, we also add shape noise

⁴http://vn90.phas.ubc.ca/jharno/CFHT_Mock_Public/

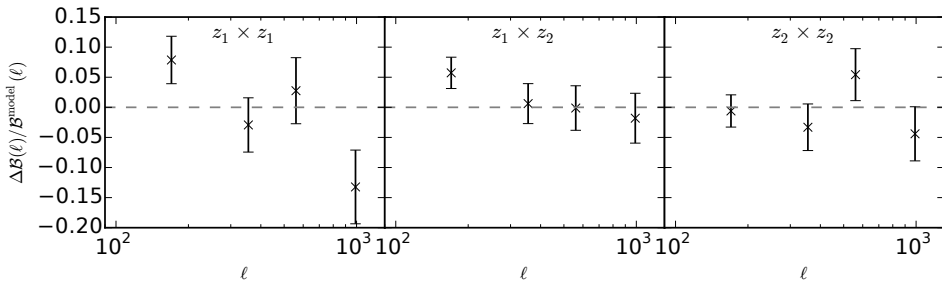


Figure 4.1: Residuals between the mean of measured E-mode band powers and predicted band powers for 184 Gaussian random field realizations of patch W3. The 1σ -error on the mean includes the scaling by $1/\sqrt{N}$ for $N = 184$ measurements. The predicted band powers use the known input cosmology (cf. Table 4.3) and take the convolution with the band window function into account. The residuals of each redshift correlation are shown from left to right.

by resampling the GRF shear from a Rayleigh distribution with width $\sigma_\gamma = 0.279$ as measured from the data. Furthermore, we randomly sample *lensfit* weights from the corresponding tomographic data catalogues such that the effective number densities (cf. equation 4.17) in the GRF mock catalogues match the ones in the data (cf. Table 4.2).

The (inverse) Fisher matrices calculated in the quadratic estimator algorithm (cf. Section 4.3) are only an approximation of the true (inverse) covariance of the extracted band powers in the Gaussian limit. In the context of a cosmological interpretation of the band powers, however, additional non-Gaussian contributions due to the non-linear evolution of the underlying matter power spectrum are expected (cf. Takada & Jain 2009). Hence, we will use our mock data also for estimating a more realistic band-power covariance matrix.

4.5.1 Signal extraction validation

The input cosmology is known for the GRFs and the Clone, and we apply a realistic CFHTLenS mask to both sets of mock data. We extract the lensing power spectrum using the quadratic estimator from the GRFs and the Clone and compare it to the input power spectrum. In Fig. 4.1 we show the residuals between the mean of the extracted band powers and the predicted band powers for the input cosmology for patch W3. The 1σ -errors on the mean include the scaling by $1/\sqrt{N}$ for $N = 184$ GRFs for each tomographic bin correlation. The binning in multipoles ℓ is the same as the one we employ in the final data extraction (cf. Section 4.4 and Table 4.1). Note that for this test we only extracted E-modes. For the calculation of the band-power predictions we take the convolution with the band window matrices (cf. equation 4.14) into account but these are computed for only one randomly drawn realization of a GRF. This is due to long run-time and we have confirmed for patch W2 that the randomly drawn band window matrix is a fair representation of the ensemble (since the noise properties of all GRFs are very similar). Fig. 4.1 demonstrates that the quadratic estimator algorithm reproduces the input signal to sufficient accuracy and precision, especially given the actual noise level of the data (cf. Fig. 4.4).

4.5.2 Band-power covariance

The extracted band powers for each of the 184 shear fields from the Clone or 184 GRFs per patch can be used to estimate the run-to-run covariance of the band powers:

$$\hat{\mathbf{C}}_{\mathcal{B}(\ell)}(A, B) = \frac{1}{A_{\text{scale}}(n_\mu - 1)} \sum_{\mu}^{n_\mu} (\mathcal{B}_A^\mu - \bar{\mathcal{B}}_A)(\mathcal{B}_B^\mu - \bar{\mathcal{B}}_B), \quad (4.19)$$

where n_μ is the total number of independent realizations per patch, $\bar{\mathcal{B}}$ is the mean of each band power per band over all realizations, \mathcal{B}^μ are the extracted band powers per realization, and A_{scale} is the scaling factor between each line-of-sight clone realization and the actual size of a CFHTLenS patch.⁵ The indices A and B denote again the previously introduced superindices and run over all bands and redshift correlations.

In order to combine the small-scale covariance estimated from the Clone and the large-scale covariance based on the GRFs, we stitch both matrices together per patch by using the GRF covariance and then replacing all values associated with a band index for which we want to use the Clone covariance. Based on the extensive analysis of the Clone and the estimation of covariances from it in Kilbinger et al. (2013), we decide to use values from the Clone covariance for multipoles $\ell \geq 670$ which corresponds to bands 5, 6, and 7 (cf. Table 4.1). Note that bands 7, 6, and 1 are not included in any cosmological data analysis though (cf. Section 4.7 and Table 4.1).

Due to noise the measured inverse covariance $\hat{\mathbf{C}}_{\mathcal{B}(\ell)}^{-1}$ is not an unbiased estimate of the true inverse covariance matrix $\mathbf{C}_{\mathcal{B}(\ell)}^{-1}$ (Hartlap et al. 2007). In order to derive an unbiased estimate of the inverse covariance we need to apply a correction derived in Kaufmann (1967) so that $\mathbf{C}_{\mathcal{B}(\ell)}^{-1} = \alpha_K \hat{\mathbf{C}}_{\mathcal{B}(\ell)}^{-1}$. Assuming a Gaussian distribution of the measured band powers $\mathcal{B}(\ell)$, this correction factor is:

$$\alpha_K = \frac{n_\mu - p - 2}{n_\mu - 1}, \quad (4.20)$$

where n_μ is the total number of independent mocks, i.e. 184 in our case, and p is the number of data points used in the analysis. In Section 4.7 we combine the data of all four CFHTLenS patches consisting of four band powers in three tomographic power spectra per patch, thus $p = 12$ for each ‘patch covariance’.

We compare the correlation matrix derived from the stitched covariance matrix with the correlation matrix based on the inverse Fisher matrix which is calculated in the quadratic estimator algorithm (cf. equation 4.12) in Fig. 4.2 for patch W3. The correlation matrices are calculated by normalizing the corresponding covariance matrix with the factor $(\mathbf{M}_{AA} \mathbf{M}_{BB})^{-1/2}$, with $\mathbf{M}_{AB} = \mathbf{C}_{\mathcal{B}(\ell)}(A, B)$ or $\mathbf{M}_{AB} = \mathbf{F}_{AB}^{-1}$. We only include E-mode bands employed later in the cosmological analysis in this comparison and find that the matrix structure in both approaches is very similar albeit with the correlation based on the Fisher estimate being smoother, as expected. Finally, we compare both approaches in terms of their variance as shown in Fig. 4.3 for each patch individually again only for E-modes used in the cosmological analysis. From this comparison we conclude that given the noise level in our data the Fisher approach still yields compatible error estimates. Nevertheless, we decide to use the stitched covariance for our subsequent analysis. This is also motivated by the fact that future surveys will yield significantly improved statistical noise levels and thus require a proper covariance estimation beyond the Fisher approach.

⁵Note that $A_{\text{scale}} = 1$ in the case of GRFs by construction. For the clones we follow (Kilbinger et al. 2013) by matching 90 per cent (due to overlapping area between the tiles) of 16 CFHTLenS tiles (minus three due to the ‘bad field’ masking also employed in the clones) into one clone field. The ratio of this number over the number of used tiles in one patch (i.e. excluding the ‘bad fields’) is then $1/A_{\text{scale}}$.

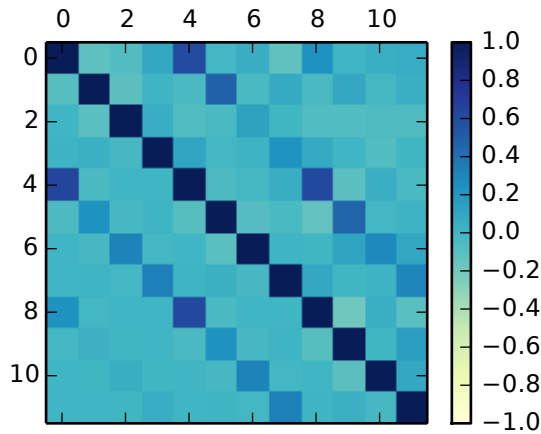


Figure 4.2: Comparison of correlation matrices for CFHTLenS patch W3: the stitched correlation matrix (upper right) is compared to the correlation matrix based on the inverse of the Fisher matrix (lower left; cf. equation 4.12). We show only tomographic E-mode bins that enter in the final cosmological likelihood analysis, i.e. bins 0–3 correspond to $80 \leq \ell \leq 1310$ in the low-redshift auto-correlation bin, bins 4–7 correspond to the same ℓ -range in the redshift cross-correlation bin, and bins 8–11 correspond to the high-redshift auto-correlation bin (cf. Tables 4.1 and 4.2).

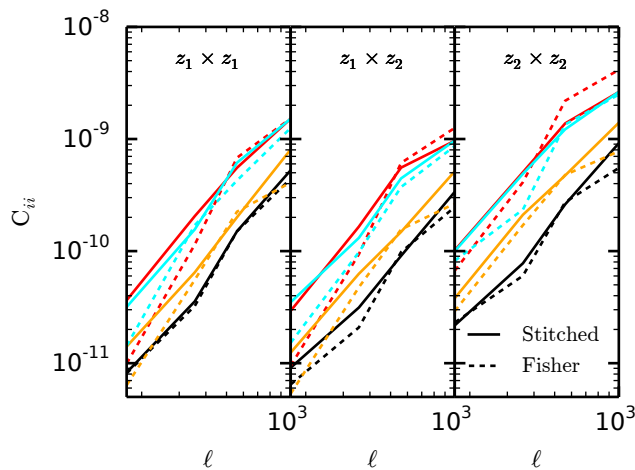


Figure 4.3: The variances calculated from the stitched covariance matrix (solid lines) and the inverse of the Fisher matrix (dashed lines) for all four CFHTLenS patches from bottom to top: W1 (black), W2 (red), W3 (orange), and W4 (cyan). From left to right we show the variances in the auto-correlation of the low-redshift bin, in the cross-correlation between the low- and the high-redshift bin, and in the auto-correlation of the high-redshift bin. We limit the ℓ -range to the one considered in the cosmological analysis.

4.5.3 Computing resources

We want to comment on the computational requirements for our tomographic quadratic estimator approach: the generalization of the method to include tomographic redshift bins is computationally demanding. The dimension of the covariance matrix defined in equation (4.8) is set by the size of the shear field (times two for the two shear components) and the pixel scale. Introducing also two redshift bins increases the number of entries in this matrix by a factor of 4. While this is still efficiently calculated in parallel for smaller patches like W2 ($\approx 22.6 \text{ deg}^2$) and W4 ($\approx 23.3 \text{ deg}^2$), it becomes demanding for patches W3 and W1 (e.g. $\text{dim}(\mathbf{C}_{W2}) = 3076^2$ versus $\text{dim}(\mathbf{C}_{W1}) = 9340^2$) even when exploiting multiprocessing and optimized libraries such as the Intel[®] Math Kernel Library (MKL⁶). Nevertheless, the data extraction including the calculation of the band window matrices takes at most a day on typical cluster machines.⁷ The computationally most demanding part in our current analysis, however, is the estimation of the covariance between the band powers. This required 184 runs on clones and 184 runs per GRF realization per patch. The total runtime for these calculations was on the order of a month on the same cluster configuration for one set of 184 realizations.

Ongoing and upcoming weak-lensing surveys come with the advantage of at least an order of magnitude increase in survey area compared to CFHTLenS and more regular survey geometries. Therefore, it will be possible to split these surveys into a statistically meaningful number of patches still containing scales up to several degrees. This will allow for estimating the patch-to-patch covariance directly from the data via resampling techniques as an alternative to estimating it from mock data alone. However, this approach limits the lowest multipole scale to the patch-size and the run-to-run covariance will be underestimated at scales close to the patch-size. Finally, the rapid advance in terms of number of cores, clock speed, and internal memory of graphics processing units (GPUs) presents a solution to the increase in complexity when extending our approach to more redshift bins, and/or more band powers, and/or larger contiguous patch sizes. The advantage of GPUs lies in their customized design to solve linear algebra problems very efficiently and massively in parallel which meets exactly the requirements of the tomographic quadratic estimator approach. We leave an update and porting to GPU programming languages for future work.

4.6 The CFHTLenS shear power spectrum

For each of the four CFHTLenS patches we extract seven E-mode and six B-mode band powers enclosing an interval of physically interesting scales of $80 \leq \ell \leq 2300$ (cf. Section 4.4 and Table 4.1). Moreover, we consider two broad mid- to high-redshift bins (cf. Table 4.2) per CFHTLenS patch in order to perform a tomographic analysis following Benjamin et al. (2013). Doing so, we attempt to decrease the expected contamination due to intrinsic galaxy alignments which is dominant at low redshifts and high multipoles ℓ . Benjamin et al. (2013) concluded that any contamination due to intrinsic alignments is at most a few per cent for each redshift bin combination. We cross-check this conclusion with state-of-the-art intrinsic alignment models constrained by recent data from Sifón et al. (2015). For the three intrinsic alignment models⁸ employed in there we do not find a significant contribution of intrinsic alignments to the cosmological signal in any of the redshift bin correlations and ℓ -scales employed in our subsequent cosmological analysis. Based on these results intrinsic alignments

⁶Version number 11.0.4

⁷24 cores @2.4 GHz, 256 GB RAM

⁸These models include intrinsic alignment due to intrinsic ellipticity correlations, i.e. II, and also intrinsic alignment due to a gravitational shear–intrinsic ellipticity correlation, i.e. GI.

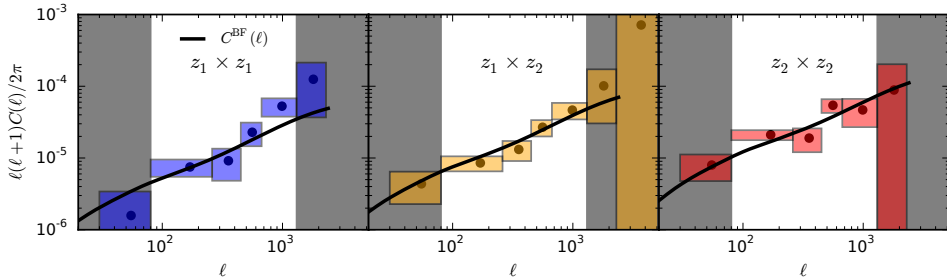


Figure 4.4: Measured E-mode band powers in tomographic bins averaged with inverse variance weights over all four CFHTLenS patches for illustrative purposes only. From left to right we show the auto-correlation signal of the low-redshift bin (blue), the cross-correlation signal between the low- and the high-redshift bin (orange), and the auto-correlation signal of the high-redshift bin (red). The low-redshift bin contains objects with redshifts in the range $0.5 < z_1 \leq 0.85$ and the high-redshift bin covers a range $0.85 < z_2 \leq 1.3$. The 1σ -errors in the signal are derived from a run-to-run covariance over 184 independent mock data fields (cf. Section 4.5.2) whereas the extent in ℓ -direction is the width of the band. Band powers in the shaded regions (grey) to the left and right of each panel are excluded from the cosmological analysis (cf. Fig. 4.5). The solid line (black) shows the power spectrum for the best-fitting five-parameter Λ CDM model derived in the subsequent analysis (cf. Section 4.7 and Table 4.4). Note, however, that the band powers are centred at the naive ℓ -bin centre and thus the convolution with the band window function is not taken into account in this plot, in contrast to the cosmological analysis. We present the E-mode signal for each individual CFHTLenS patch in Appendix 4.B.

will be ignored in the modelling of the signal in our subsequent analysis.

In Fig. 4.4 we show the extracted E-mode band powers for each tomographic bin. For illustrative purposes we combine the band powers extracted from each patch by averaging them with inverse variance weights. The errors on the signal are estimated from the stitched covariance matrix (cf. Section 4.5.2) whereas the extension of the box in ℓ -direction is just the width of the band. Only bands outside the (grey) shaded areas enter in the cosmological analysis (thus we omit explicitly the ‘noise catcher’ bands, cf. Section 4.4 and Table 4.1). Note, however, that for the cosmological likelihood analysis we do not use the averaged signals, but instead sum the likelihood of each patch as described in Section 4.7.2.

We extract E- and B-modes simultaneously. As described in Section 4.2 the cosmological signal is contained in the E-modes in the absence of systematic errors. Hence, we use the B-mode signal as a systematic cross-check and generally expect it to be zero within errors. We do not extract the EB-modes, which would hint at parity-violation in the data, because [Kitching et al. \(2014\)](#) found no evidence for EB-modes in the CFHTLenS data. Hence, we decided to only include the extraction of B-modes as a non-trivial systematic check. We show the extracted B-mode signal per tomographic bin in Fig. 4.5. For illustrative purposes we averaged the B-mode signal again with inverse variance weights over all four CFHTLenS patches. In contrast to the E-modes, the 1σ -errors on the B-modes are derived from the B-mode part of the Fisher matrix (cf. equation 4.12). This is a very conservative approach since it will generally underestimate the errorbars. The masking in the data might cause leakage of E-mode power into B-mode power. In principle, this should also be captured by the Fisher matrix but as we argued in Section 4.5.2 the Fisher matrix underestimates the E-mode error in the intermediate multipole regime due to the mildly non-Gaussian intrinsic field. This propagates into an underestimated B-mode Fisher-error when compared directly to a run-to-run B-mode error. However, that does not pose a problem as long as we can establish that the B-modes are

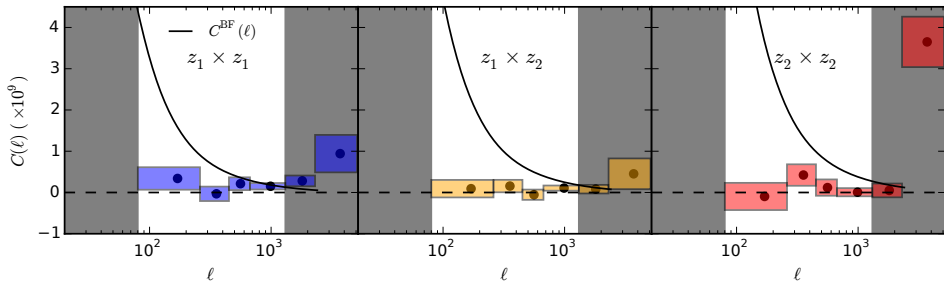


Figure 4.5: Same as Fig. 4.4 but for B-mode band powers. Note, however, the different scale (linear) and normalization used here with respect to Fig. 4.4; for reference we also plot the best-fitting E-mode power spectrum as solid line (black). We show the measured B-modes as (black) dots with 1σ -errors derived from the inverse Fisher matrix. Based on these signals we define the shaded regions (grey) to the left and right of each panel. E-mode band powers in these regions are excluded from the cosmological analysis (cf. Fig. 4.4 and see text for details). We present the B-mode signal for each individual CFHTLenS patch in Appendix 4.B.

consistent with zero using the underestimated errorbars. We assess the consistency of the B-modes with zero via a χ^2 -goodness-of-fit measure and find: $\chi_{\text{red}}^2(W1) = 1.54$, $\chi_{\text{red}}^2(W2) = 0.93$, $\chi_{\text{red}}^2(W3) = 1.07$, and $\chi_{\text{red}}^2(W4) = 0.24$ for 15 degrees of freedom, i.e. including all B-mode bands except the last one, which was designed to catch only noise due to the long tail of the window function of square pixels beyond ℓ_{pix} . However, further tests conducted on the GRF mock data show that noise from the last band leaks into the second-to-last band depending on the pixel-scale, σ_{pix} , employed. This is due to the strong oscillatory behaviour of the Fourier-transform of a real-space square pixel (cf. fig. 2 in Hu & White 2001) around ℓ_{pix} corresponding to σ_{pix} . The oscillations are amplified if the band is noise-dominated. For that reason the B-mode in the second-to-last band appears to be more significant than the B-modes in the other bands. Removing the second-to-last B-mode band power from the χ^2 -goodness-of-fit measure yields the following improved reduced χ^2 -values for 12 degrees of freedom: $\chi_{\text{red}}^2(W1) = 0.92$, $\chi_{\text{red}}^2(W2) = 0.80$, $\chi_{\text{red}}^2(W3) = 0.61$, and $\chi_{\text{red}}^2(W4) = 0.23$. Hence, we conclude that the B-modes in these remaining bands are consistent with zero. Therefore, we only use bands 2–5 in the cosmological analysis of the E-mode signal.

Following Becker et al. (2015) we define the signal-to-noise ratio, S/N , of our band-power measurements with respect to the cosmological signal in the mock data from which we estimate the covariance:

$$S/N = \frac{\mathbf{d}_{\text{meas}}^T \mathbf{C}_{\mathcal{B}(\ell)}^{-1} \mathbf{d}_{\text{mock}}}{\sqrt{\mathbf{d}_{\text{mock}}^T \mathbf{C}_{\mathcal{B}(\ell)}^{-1} \mathbf{d}_{\text{mock}}}}. \quad (4.21)$$

Considering only the band powers used in the cosmological analysis (cf. Table 4.1), we detect a cosmic shear signal in W1 at 7.1σ , in W2 at 5.5σ , in W3 at 5.7σ , and in W4 only marginally at 2.5σ . Note, however, that the above definition of S/N depends on the cosmology employed in the mocks. A discrepancy between the mock cosmology and the actual cosmology preferred by the data decreases the significance in general.

4.7 Cosmological inference

After having extracted the shear power spectrum and having derived a more robust estimate of the data covariance, we can proceed to the next step: the cosmological interpretation of the tomographic signals, employing a Bayesian framework. We estimate cosmological parameters \mathbf{p} by sampling the likelihood $\mathcal{L}(\mathbf{p})$ with a Monte Carlo Markov Chain (MCMC) method. In addition to the parameter estimation we also want to compare various model extensions to a baseline model.

The Bayesian evidence \mathcal{Z} is simply the normalization factor of the posterior over the parameters \mathbf{p} :

$$\mathcal{Z} = \int d^n \mathbf{p} \mathcal{L}(\mathbf{p}) \pi(\mathbf{p}), \quad (4.22)$$

where n denotes the dimensionality of the parameter space and $\pi(\mathbf{p})$ is the prior. Since the evidence is the average of the likelihood over the prior it automatically implements Occam's razor: a simpler theory with fewer parameters, i.e. a more compact parameter space, will have a higher evidence than a more complicated one requiring more parameters, unless the latter model explains the data significantly better. If we wish to decide now between models M_1 and M_0 , we can compare their posterior probabilities given the observed data \mathbf{D} and define the Bayes factor:

$$K_{1,0} \equiv \frac{\mathcal{Z}_1 \Pr(M_1)}{\mathcal{Z}_0 \Pr(M_0)}, \quad (4.23)$$

where $\Pr(M_1)/\Pr(M_0)$ is the a priori probability ratio for the two models, usually set to unity unless there are strong (physical) reasons to prefer one model over the other a priori. In our subsequent analysis we always assume $\Pr(M_1)/\Pr(M_0) = 1$. A Bayes factor $K_{1,0} > 1$ implies a preference of model M_1 over model M_0 . Kass & Raftery (1995) have proposed a quantitative classification scheme for the interpretation of the Bayes factor K (or equivalently $2 \ln K$).

Evaluating the usually high-dimensional integral of equation (4.22) is a challenging computational and numerical task. Here, we employ the nested sampling algorithm MULTINEST⁹ (Feroz & Hobson 2008; Feroz et al. 2009, 2013) via its PYTHON-wrapper PYMULTINEST (Buchner et al. 2014) in the framework of the cosmological likelihood sampling package MONTE PYTHON¹⁰ (Audren et al. 2012).

4.7.1 Theoretical power spectrum

In Section 4.2 we described the calculation of the tomographic lensing power spectra (cf. equation 4.4). These encode the 3D matter power spectrum smoothed by tomographic lensing kernels (cf. equation 4.5). For the calculation of the matter power spectrum, $P_\delta(k; \chi)$, we employ the Boltzmann-code CLASS¹¹ (Blas et al. 2011; Audren & Lesgourgues 2011). This already includes the non-linear corrections for which we chose to use the HALOFIT algorithm including the recalibrations by Takahashi et al. (2012). Furthermore, CLASS allows us to include (massive) neutrinos (Lesgourgues & Tram 2011). The main effect of massive neutrinos is a redshift- and scale-dependent reduction of power which also propagates into the lensing power spectra $C_{\ell, \mu\nu}^{\text{EE}}$ but is smoothed by the lensing kernels of the corresponding tomographic bins (cf. Fig. 4.6). Over the multipole range of interest massive neutrinos lower the lensing power spectrum by an almost constant factor. This introduces a degeneracy with other cosmological parameters that affect the normalization of the lensing power spectrum.

⁹Version 3.8 from <http://ccpforge.cse.rl.ac.uk/gf/project/multinest/>

¹⁰Version 2.1.4 from www.montepython.net

¹¹Version 2.4.3 from www.class-code.net

We follow [Harnois-Déraps et al. \(2015\)](#) to describe the modifications of the power spectrum due to baryon feedback:

$$b^2(k, z) \equiv \frac{P_\delta^{\text{mod}}(k, z)}{P_\delta^{\text{ref}}(k, z)}, \quad (4.24)$$

where P_δ^{mod} and P_δ^{ref} denote the power spectra with and without baryon feedback, respectively.

The baryon feedback can be computed from hydrodynamical simulations. We use in this work the fitting formula for the baryon feedback derived by [Harnois-Déraps et al. \(2015\)](#) using the Overwhelmingly Large Simulations (OWLS; [Schaye et al. 2010](#), [van Daalen et al. 2011](#)):

$$b^2(k, z) = 1 - A_{\text{bary}}(A_z e^{(B_z x - C_z)^3} - D_z x e^{E_z x}), \quad (4.25)$$

where $x = \log_{10}(k/1 \text{ Mpc}^{-1})$ and the terms A_z , B_z , C_z , D_z , and E_z are functions of the scale factor $a = 1/(1+z)$ which are also dependent on the baryonic feedback model (cf. [Harnois-Déraps et al. 2015](#) for the specific functional forms and constants). Additionally, we introduce here a general free amplitude A_{bary} which we will use as a free parameter to marginalize over while fitting for the cosmological parameters. In Fig. 4.6 we show the effect of including baryonic feedback on the matter and lensing power spectrum, respectively. In contrast to the effect of massive neutrinos baryon feedback causes a significant reduction of power in the lensing power spectrum only at high multipoles. However, this is also degenerate with the effect of massive neutrinos on these scales. Hence, a proper anchoring of the main cosmological parameters at low multipoles with high precision is paramount if one wants to break degeneracies between all these effects. Operating directly in multipole space with respect to both theory *and data* facilitates the identification of distinct features in the power spectra.

4.7.2 The shear likelihood

To compare the measured, tomographic band powers \mathcal{B}_α^i (cf. Section 4.6) to predictions $\langle \mathcal{B}_\alpha^i \rangle^{\text{model}}$ (cf. Section 4.2), we define the shear likelihood as a function of cosmological parameters \mathbf{p} :

$$-2 \ln \mathcal{L}(\mathbf{p}) = \sum_i \sum_{\alpha, \beta} d_\alpha^i(\mathbf{p}) (\mathbf{C}^{-1})_{\alpha\beta}^i d_\beta^i(\mathbf{p}), \quad (4.26)$$

where the index i runs over the four CFHTLenS patches (cf. Section 4.4) and the indices α, β run over the tomographic bins. Note that we follow all previous CFHTLenS studies in ignoring any covariance between the individual CFHTLenS patches.

The components of the data vector per patch are calculated as

$$d_\alpha^i(\mathbf{p}) = (\mathcal{B}_\alpha^i - \langle \mathcal{B}_\alpha^i(\mathbf{p}) \rangle^{\text{model}}), \quad (4.27)$$

where the predicted band powers, $\langle \mathcal{B}^i(\ell) \rangle^{\text{model}}$, depend on the cosmological parameters \mathbf{p} . They are calculated with equations (4.13) and (4.4), i.e. the band window functions are properly taken into account. The inverse of the covariance matrix \mathbf{C}^{-1} is estimated from a large suite of mock data especially tailored to CFHTLenS as described in detail in Section 4.5.2.

4.7.3 Models and discussion

In the first part of this cosmological analysis we consider the shear likelihood without further combining it with any other external cosmological probe. The lensing power spectrum is most sensitive to cosmological parameters modifying its normalization and slope. Therefore, the normalization of the primordial power spectrum, $\ln(10^{10} A_s)$, and the fraction of cold dark matter, Ω_{cdm} , are the primary parameters of interest. For an easier comparison of our results

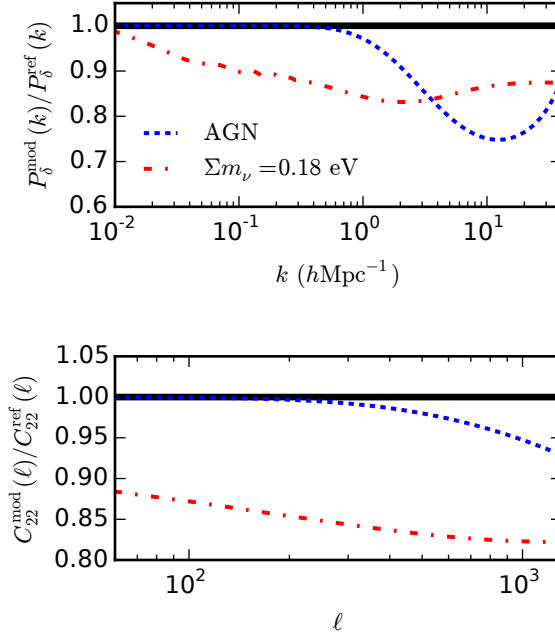


Figure 4.6: Upper panel: the ratio of modified matter power spectra over the dark matter only power spectrum. The dashed line (blue) shows the effect of the baryon feedback bias in the AGN model from OWLS (Schaye et al. 2010; van Daalen et al. 2011) using the implementation by Harnois-Déraps et al. (2015) (cf. equation 4.25). The modifications due to three degenerate massive neutrinos with total mass $\Sigma m_\nu = 0.18$ eV is demonstrated by the dash-dotted line (red). The redshift for the power spectrum calculation is $z = 1.05$ corresponding to the median redshift of the high-redshift bin used in the subsequent analysis (cf. Table 4.2). Lower panel: same as upper panel but for the lensing power spectrum of the high-redshift bin $z_2 : 0.85 < Z_B \leq 1.30$ (cf. Table 4.2).

with the literature, we also derive the root-mean-square variance of the density field smoothed with the Fourier transform of a top-hat filter on a scale $R = 8 h^{-1} \text{Mpc}$ in real-space, i.e. σ_8 , and the total fraction of matter in the Universe, Ω_m . Our baseline model to which we refer subsequently only as ‘ ΛCDM ’ includes in addition to these parameters three more free variables: the Hubble parameter h , the slope of the primordial power spectrum n_s , and the fraction of baryonic matter Ω_b . The ranges for the flat priors on these parameters are listed in Table 4.4. They follow mostly the ranges employed in the CFHTLenS studies by Benjamin et al. (2013) and Heymans et al. (2013) in order to assure a fair comparison of our results with these studies.

Data from particle physics experiments indicate that neutrinos have mass (e.g. Lesgourgues & Pastor 2006 and references therein). Hence, we follow Planck Collaboration XIII (2015a) in including already two massless and one massive neutrino with the (fixed) minimal mass of $\Sigma m_\nu = 0.06 \text{ eV}$ (assuming a normal mass hierarchy with one dominant mass eigenstate) in our baseline ΛCDM model. Moreover, we always assume a flat cosmological model.

The first extension of the baseline model is to introduce a free total mass Σm_ν for three degenerate massive neutrinos. We refer to this model as ‘ $\Lambda\text{CDM}+\nu$ ’. Since we expect the effect of massive neutrinos to be degenerate with the effect of baryonic feedback, especially at high multipoles (cf. Section 4.2 and Fig. 4.6) we investigate this effect in the model ‘ $\Lambda\text{CDM}a$ ’: here, we additionally include the fiducial baryon feedback model of equation (4.25) with $A_{\text{bary}} = 1$ for the AGN model taken from the OWLS project (Schaye et al. 2010; van Daalen et al. 2011). The degeneracy between baryonic feedback and massive neutrinos is investigated in the model $\Lambda\text{CDM}a+\nu$, where Σm_ν is free to vary but which includes the fixed fiducial baryon feedback model. We relax the assumption of a fixed baryon feedback model in the model ‘ $\Lambda\text{CDM}+A_{\text{bary}}$ ’ by allowing the amplitude of the feedback A_{bary} to vary (cf. equation 4.25). Combining the assumption of a free amplitude in the baryon feedback model and a free total mass of three degenerate massive neutrinos, Σm_ν in the model ‘ $\Lambda\text{CDM} + \nu + A_{\text{bary}}$ ’ yields a maximally degenerate model in baryonic feedback and neutrinos. In total this model consists of seven free parameters.

Moreover, we want to test the effect of a photometric redshift bias which causes a coherent shift of the photometric redshift distributions per tomographic bin (cf. equation 4.5) by Δz_μ . Hildebrandt et al. (2012) showed that the bias on photometric redshifts in CFHTLenS is $\Delta z < 0.02$ (cf. their fig. 8). However, this estimate does not account for outliers which can increase the photometric redshift bias significantly. Therefore, we make a more conservative assumption and treat the photometric redshift biases Δz_μ within a flat prior range of $-0.05 \leq \Delta z_\mu \leq 0.05$ as nuisance parameters to marginalize over. In the most complex model $\Lambda\text{CDM} + \nu + A_{\text{bary}} + \Delta z_\mu$, which we abbreviate subsequently to ‘ $\Lambda\text{CDM} + \text{all}$ ’, we include a free amplitude for the baryon feedback model, massive neutrinos and treat the photometric redshift biases Δz_μ as nuisance parameters.

All models, their prior ranges and the parameter estimates derived from the likelihood sampling are summarized in Table 4.4, where we always quote the weighted median value for each varied parameter. The errors denote the 68 per cent credible interval of the posterior distribution after marginalization over all other free parameters.

Table 4.4: Cosmological parameters from shear likelihood only.

Model	Ω_{cdm}	$\ln(10^{10}A_s)$	Ω_m	σ_8	Ω_b	n_s	h	Σm_ν (eV)	A_{bary}	Δz_1	Δz_2
Prior ranges	[0., 1.]	[0., 10.]	derived	derived	[0., 0.1]	[0.7, 1.3]	[0.4, 1.]	[0.06, 6.]	[0., 10.]	[-0.05, 0.05]	[-0.05, 0.05]
Λ CDM	$0.21^{+0.09}_{-0.15}$	$3.53^{+1.49}_{-1.52}$	$0.26^{+0.09}_{-0.15}$	$0.84^{+0.24}_{-0.23}$	$0.05^{+0.03}_{-0.03}$	$1.01^{+0.29}_{-0.23}$	$0.62^{+0.09}_{-0.22}$	$\equiv 0.06$	—	—	—
Λ CDMa	$0.21^{+0.09}_{-0.14}$	$3.50^{+1.43}_{-1.62}$	$0.25^{+0.11}_{-0.15}$	$0.85^{+0.24}_{-0.24}$	$0.05^{+0.02}_{-0.03}$	$1.00^{+0.26}_{-0.22}$	$0.64^{+0.10}_{-0.22}$	$\equiv 0.06$	$\equiv 1.$	—	—
Λ CDM + ν	$0.21^{+0.08}_{-0.13}$	$3.65^{+1.52}_{-1.44}$	$0.30^{+0.09}_{-0.14}$	$0.75^{+0.16}_{-0.15}$	$0.04^{+0.02}_{-0.03}$	$1.05^{+0.25}_{-0.28}$	$0.70^{+0.18}_{-0.16}$	$1.37^{+0.69}_{-1.31}$	—	—	—
Λ CDMa + ν	$0.21^{+0.09}_{-0.13}$	$3.69^{+1.37}_{-1.52}$	$0.29^{+0.11}_{-0.14}$	$0.76^{+0.16}_{-0.16}$	$0.04^{+0.02}_{-0.03}$	$1.05^{+0.25}_{-0.27}$	$0.71^{+0.22}_{-0.18}$	$1.34^{+0.60}_{-1.28}$	$\equiv 1.$	—	—
Λ CDM + A_{bary}	$0.21^{+0.10}_{-0.14}$	$3.62^{+1.51}_{-1.47}$	$0.26^{+0.10}_{-0.14}$	$0.85^{+0.25}_{-0.26}$	$0.05^{+0.02}_{-0.03}$	$1.00^{+0.19}_{-0.24}$	$0.60^{+0.09}_{-0.20}$	$\equiv 0.06$	$2.90^{+1.54}_{-2.90}$	—	—
Λ CDM + ν + A_{bary}	$0.22^{+0.08}_{-0.13}$	$3.69^{+1.44}_{-1.42}$	$0.30^{+0.09}_{-0.15}$	$0.76^{+0.15}_{-0.15}$	$0.04^{+0.02}_{-0.03}$	$1.06^{+0.24}_{-0.28}$	$0.69^{+0.17}_{-0.17}$	$1.29^{+0.67}_{-1.23}$	$2.51^{+1.19}_{-2.51}$	—	—
Λ CDM + Δz_μ	$0.24^{+0.10}_{-0.14}$	$3.26^{+1.28}_{-1.32}$	$0.29^{+0.10}_{-0.15}$	$0.80^{+0.21}_{-0.22}$	$0.05^{+0.03}_{-0.03}$	$0.98^{+0.19}_{-0.21}$	$0.62^{+0.10}_{-0.21}$	$\equiv 0.06$	—	$0.03^{+0.02}_{-0.01}$	$-0.02^{+0.02}_{-0.03}$
Λ CDM + all	$0.24^{+0.09}_{-0.13}$	$3.57^{+1.34}_{-1.44}$	$0.32^{+0.10}_{-0.13}$	$0.74^{+0.14}_{-0.14}$	$0.04^{+0.02}_{-0.03}$	$1.04^{+0.26}_{-0.25}$	$0.67^{+0.16}_{-0.17}$	$1.32^{+0.56}_{-1.26}$	$2.49^{+1.17}_{-2.49}$	$0.03^{+0.02}_{-0.01}$	$-0.02^{+0.02}_{-0.03}$

Notes. We quote weighted median values for each varied parameter and derive 1σ -errors using the 68 per cent credible interval of the marginalized posterior distribution.

Table 4.5: Cosmological parameters from a combined analysis of the shear and *Planck* likelihoods.

Model	Ω_{cdm}	$\ln(10^{10}A_s)$	Ω_m	σ_8	Ω_b	n_s	h	τ_{reio}	A_{Planck}
Prior ranges	[0.1, 0.4]	[2., 4.]	derived	derived	[0., 0.1]	[0.8, 1.2]	[0.5, 0.8]	[0.04, 0.12]	[90., 110.]
<i>Planck</i> (TT+lowP)	$0.263^{+0.012}_{-0.013}$	$3.093^{+0.037}_{-0.034}$	$0.313^{+0.013}_{-0.014}$	$0.830^{+0.014}_{-0.015}$	$0.049^{+0.001}_{-0.001}$	$0.966^{+0.007}_{-0.006}$	$0.674^{+0.010}_{-0.010}$	$0.079^{+0.018}_{-0.019}$	$100.04^{+0.27}_{-0.26}$
<i>Planck</i> +Shear	$0.251^{+0.010}_{-0.010}$	$3.077^{+0.037}_{-0.035}$	$0.300^{+0.011}_{-0.011}$	$0.818^{+0.013}_{-0.013}$	$0.048^{+0.001}_{-0.001}$	$0.971^{+0.006}_{-0.006}$	$0.684^{+0.008}_{-0.009}$	$0.074^{+0.020}_{-0.018}$	$100.02^{+0.27}_{-0.26}$

Notes. We quote weighted median values for each varied parameter and derive 1σ -errors using the 68 per cent credible interval of the marginalized posterior distribution. For the model *Planck* (TT+lowP) we resampled a simplified version of the original likelihood that includes only one additional nuisance parameter, A_{Planck} .

We compare the 68 and 95 per cent credible intervals for the baseline Λ CDM model and the most complex Λ CDM + all model in Fig. 4.7. Both models are marginally consistent with the 68 per cent credible interval from [Planck Collaboration XIII \(2015a, TT+lowP\)](#) and the most complex Λ CDM + all model is fully consistent with *Planck* at 95 per cent credibility. This model is very conservative because it also accounts for a possible photometric redshift bias per tomographic bin, and thus is expected to yield the largest errorbars. For this model we show marginalized 1D posteriors for every free parameter (cf. Table 4.4) and marginalized 2D contours for every parameter combination in Fig. 4.8. From this figure but also from Table 4.4 it is apparent that our parameter constraints are weaker than those derived from *Planck*. The shear data are also unable to constrain the slope of the primordial power spectrum, n_s , especially once the models also include massive neutrinos, since both parameters influence the slope of the lensing power spectrum in a similar way. Hence, the estimate on n_s is following the flat prior distribution. From our most conservative model extension, Λ CDM+all, we derive an upper limit on the total mass of three degenerate massive neutrinos at 95 per cent credibility of $\Sigma m_\nu < 4.53$ eV. In contrast, [Planck Collaboration XIII \(2015a, TT+lowP\)](#) derive an upper limit (95 per cent) on the total mass of three degenerate massive neutrinos of $\Sigma m_\nu < 0.72$ eV. Combining the primary CMB data with secondary data and/or other external probes lowers the upper limit to <0.17 eV.

In the σ_8 - Ω_m plane we can directly compare to the results from the CFHTLenS analysis by [Heymans et al. \(2013\)](#). They employed a 6-bin tomographic real-space correlation approach and in Fig. 4.9 we show the 68 per cent credible intervals for their conservative model including a marginalization over intrinsic alignments. The 68 per cent credible intervals of our baseline Λ CDM model is consistent with the one derived by [Heymans et al. \(2013\)](#). However, the contours of our model are generally broader because we use only two tomographic bins.

The shear power spectrum is most sensitive to the parameters Ω_{cdm} and $\ln(10^{10}A_s)$ or equivalently to Ω_m and σ_8 . However, as can be seen in, for example, Fig. 4.7 the relation between Ω_m and σ_8 is degenerate and what lensing can actually constrain best is the combination of both parameters in the projected quantity $\sigma_8(\Omega_m/0.3)^\alpha$. The value of α depends on the scales probed and is connected to the width of the likelihood contour. We derive it from fitting the function $\ln \sigma_8(\Omega_m) = -\alpha \ln \Omega_m + \text{const.}$ to the likelihood surface in the σ_8 - Ω_m plane. Since we find it to be consistent with ≈ 0.5 in all our models, we follow [DES Collaboration \(2015\)](#) in defining the quantity $S_8 \equiv \sigma_8(\Omega_m/0.3)^{0.5}$. We present values for this parameter combination obtained from the above shear-only likelihood sampling in Table 4.6. We compare the values of S_8 for all our models in Fig. 4.10, where we also show the constraint on that parameter combination by [Planck Collaboration XIII \(2015a, TT+lowP\)](#). For this combination all our tested models are consistent with each other. However, all models are in mild tension with the constraint on S_8 derived from *Planck* (TT+lowP).

Moreover, we present in Fig. 4.10 the constraints on S_8 of other lensing studies. In particular, we compare to the recent constraint from [DES Collaboration \(2015, ‘Fiducial DES SV cosmic shear’\)](#). This study employed a real-space correlation function approach in three tomographic bins. We find our constraints to be consistent with theirs which is mainly due to the large errorbars of the measurement on S_8 from the Dark Energy Survey (DES). In addition to their own results [DES Collaboration \(2015\)](#) also resampled the likelihoods of the CFHTLenS studies from [Kilbinger et al. \(2013\)](#) and [Heymans et al. \(2013\)](#) and derived constraints on S_8 . We show these constraints also in Fig. 4.10. [Kilbinger et al. \(2013\)](#) employed a non-tomographic real-space correlation function approach and their constraint in Fig. 4.10 employs ‘all scales’ out to large angular scales $\vartheta \approx 350$ arcmin. The constraint from [Heymans et al. \(2013\)](#) in Fig. 4.10 uses only the ‘original conservative scales’. Our results are consistent with both these studies, as was already the case for [Heymans et al. \(2013\)](#) in the full σ_8 - Ω_m

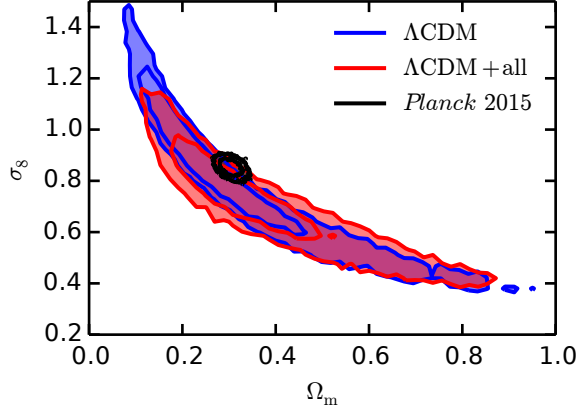


Figure 4.7: Shown are 68 and 95 per cent credible intervals (blue, inner and outer contour, respectively) for our baseline Λ CDM model where Ω_m , σ_8 , h , n_s , and Ω_b are free to vary. Additionally shown are the 68 and 95 per cent credible intervals (red, respectively) for our most complex model Λ CDM+all where also the total mass of neutrinos Σm_ν , the amplitude for the Baryon feedback model A_{bary} , and a systematic photometric redshift bias per tomographic bin Δz_μ are free to vary. We marginalize over all other free parameters. Finally, we plot the 68 and 95 per cent credible intervals derived from [Planck Collaboration XIII \(2015a, TT+lowP\)](#).

Table 4.6: Constraints on S_8 and $\sigma_8(\Omega_m/0.3)^\alpha$.

Model	$S_8 \equiv \sigma_8(\Omega_m/0.3)^{0.5}$	Mean error on S_8	$\sigma_8(\Omega_m/0.3)^\alpha$	α
Shear likelihood only				
Λ CDM	$0.768^{+0.045}_{-0.039}$	0.042	$0.762^{+0.044}_{-0.038}$	0.538
Λ CDMa	$0.770^{+0.047}_{-0.039}$	0.043	$0.765^{+0.044}_{-0.038}$	0.533
Λ CDM + ν	$0.737^{+0.057}_{-0.054}$	0.056	$0.737^{+0.057}_{-0.055}$	0.479
Λ CDMa + ν	$0.741^{+0.055}_{-0.047}$	0.051	$0.741^{+0.056}_{-0.046}$	0.465
Λ CDM + A_{bary}	$0.777^{+0.048}_{-0.040}$	0.044	$0.773^{+0.046}_{-0.040}$	0.531
Λ CDM + ν + A_{bary}	$0.748^{+0.055}_{-0.049}$	0.052	$0.748^{+0.054}_{-0.050}$	0.479
Λ CDM + Δz_μ	$0.771^{+0.050}_{-0.039}$	0.045	$0.767^{+0.045}_{-0.037}$	0.555
Λ CDM + all	$0.755^{+0.059}_{-0.059}$	0.059	$0.755^{+0.059}_{-0.059}$	0.491

Notes. We quote median values for the constraints on $S_8 \equiv \sigma_8(\Omega_m/0.3)^{0.5}$ and $\sigma_8(\Omega_m/0.3)^\alpha$. The errors denote the 68 per cent credible interval derived from the marginalized posterior distribution.

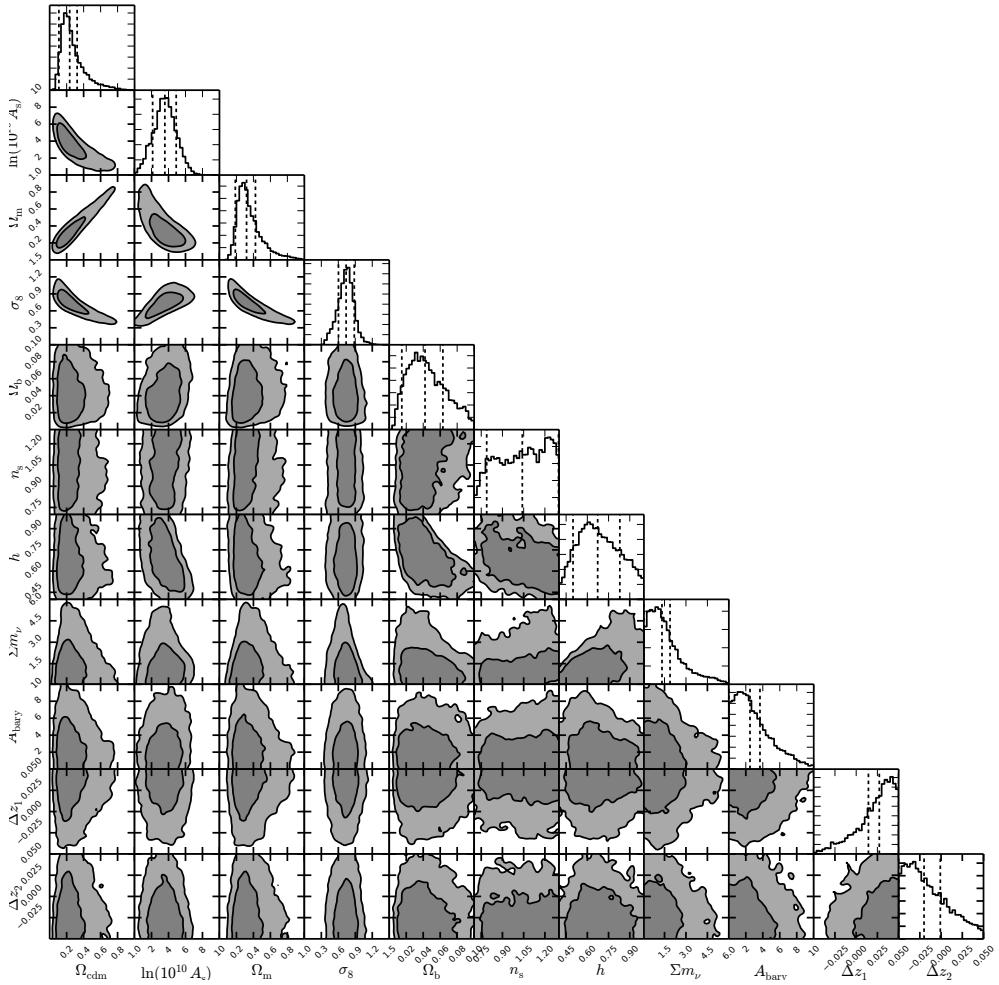


Figure 4.8: Shown are all parameter constraints from sampling the likelihood of model Λ CDM+all. The dashed lines in the marginalized 1D posteriors denote the weighted median and the 68 per cent credible interval (cf. Table 4.4). The contours in each 2D likelihood contour subplot are 68 and 95 per cent credible intervals smoothed with a Gaussian.

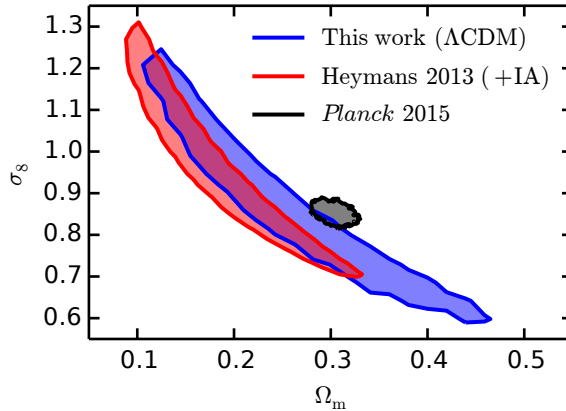


Figure 4.9: We show the 68 per cent credible interval (blue) for our baseline Λ CDM model. Additionally shown is the 68 per cent credible interval for the 6-bin tomographic real-space analysis from [Heymans et al. \(2013\)](#), cf. also their fig. 4) where intrinsic alignments are marginalized over (red). Finally, we plot the 68 per cent credible interval from [Planck Collaboration XIII \(2015a\)](#), TT+lowP).

plane (cf. Fig. 4.9).

For the comparison of our results to other CFHTLenS studies and the originally published constraints from [Kilbinger et al. \(2013\)](#) and [Heymans et al. \(2013\)](#) we have to resort to the parameter combination $\sigma_8(\Omega_m/0.3)^\alpha$. The exponent α is in general quite similar between the quoted lensing studies but not the same, which the reader should bear in mind when looking at Fig. 4.11. For completeness, we show again the constraints on that parameter combination from [Heymans et al. \(2013\)](#) and [Kilbinger et al. \(2013\)](#). [Kitching et al. \(2014\)](#) employed a 3D lensing approach which allows for control over the k -scales included in the analysis. However, their constraint on $\sigma_8(\Omega_m/0.3)^\alpha$ for which we quote the value including large scales, i.e. $k \leq 5 \text{ hMpc}^{-1}$, yields by far the largest errorbars due to which their constraint is consistent with all other CFHTLenS studies and also consistent with the *Planck* constraint. The analysis by [Benjamin et al. \(2013\)](#) is the most similar to the one presented here: although their analysis employed a real-space correlation function approach and did not include scales as large as the ones used here, the two redshift bins in their tomographic analysis are exactly the same ones employed in this analysis. The constraints are also consistent with each other and especially our Λ CDM model also yields comparable errorbars.

In summary, all models are consistent with each other mainly due to increasing errorbars for increasingly more free parameters. For the comparison of our analysis to other cosmic shear studies we derived a constraint on the projected parameters S_8 or $\sigma_8(\Omega_m/0.3)^\alpha$. In general, we find consistency in these projected parameters with all other CFHTLenS studies and DES. Employing the Bayesian model comparison framework, we can decide which of the tested models describes the shear data best: in Table 4.7 we present the natural logarithms of the evidence for each model. Comparing these models in terms of their Bayes factor K with respect to the simplest models Λ CDM or Λ CDMa, we find no evidence for any of the tested extensions except for a very weak preference of the model Λ CDM+ Δz_μ over our baseline model which is according to the interpretation scheme of [Kass & Raftery \(1995\)](#) ‘not worth more than a bare mention’.

Hence, we conclude that the extracted band powers of the tomographic shear power spectra

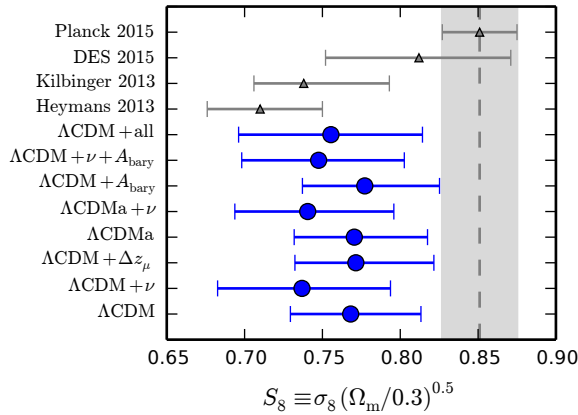


Figure 4.10: Shown are 1σ -constraints on the parameter combination $S_8 \equiv \sigma_8 (\Omega_m/0.3)^{0.5}$ for all of our tested models (cf. Tables 4.4 and 4.6). We compare them to constraints from other lensing analyses and to the constraint from [Planck Collaboration XIII \(2015a, TT+lowP\)](#). Note that for [Heymans et al. \(2013\)](#) and [Kilbinger et al. \(2013\)](#) we quote the values derived in [DES Collaboration \(2015\)](#) for the ‘original conservative scales’ and for ‘all scales’, respectively. ‘DES 2015’ refers to the fiducial result from [DES Collaboration \(2015, ‘Fiducial DES SV cosmic shear’\)](#).

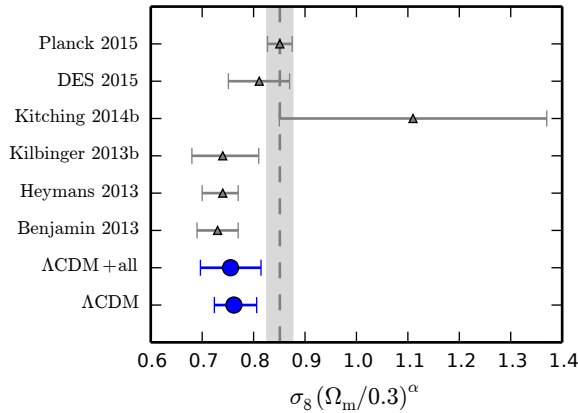


Figure 4.11: Shown are 1σ -constraints on the parameter combination $\sigma_8 (\Omega_m/0.3)^\alpha$ for our Λ CDM and Λ CDM+all models (cf. Table 4.4). We compare them to constraints from other lensing analyses and to the constraint from [Planck Collaboration XIII \(2015a, TT+lowP\)](#). Note that for [Heymans et al. \(2013\)](#) we quote the value derived by marginalising over intrinsic alignments. For [Kilbinger et al. \(2013\)](#) and [Kitching et al. \(2014\)](#) we cite values including the largest scales in their analyses.

Table 4.7: Evidences from shear likelihood only.

Model	$\ln \mathcal{Z}$	$2 \ln K$ ($K \equiv \mathcal{Z}_i / \mathcal{Z}_{\Lambda\text{CDM}}$)	Interpretation
ΛCDM	-40.96 ± 0.06	0	–
ΛCDM_a	-41.07 ± 0.06	-0.22	Support for ΛCDM
$\Lambda\text{CDM} + \nu$	-41.63 ± 0.07	-1.34	Support for ΛCDM
$\Lambda\text{CDM}_a + \nu$	-41.83 ± 0.07	-1.74	Support for ΛCDM
$\Lambda\text{CDM} + A_{\text{bary}}$	-41.66 ± 0.06	-1.40	Support for ΛCDM
$\Lambda\text{CDM} + \nu + A_{\text{bary}}$	-42.48 ± 0.07	-3.04	Support for ΛCDM
$\Lambda\text{CDM} + \Delta z_{\mu}$	-40.75 ± 0.07	0.42	Preference over ΛCDM ‘not worth more than a bare mention’
$\Lambda\text{CDM} + \text{all}$	-42.19 ± 0.07	-2.46	Support for ΛCDM

Notes. For each model we calculate the global log-evidence, $\ln \mathcal{Z}$, and compare all evidences in terms of the Bayes factor K (or equivalently $2 \ln K$) to the baseline ΛCDM model. The interpretation of the Bayes factor is following the scheme proposed by [Kass & Raftery \(1995\)](#).

measured over a range $80 \leq \ell \leq 1310$ are described sufficiently well within their errors by a standard five-parameter ΛCDM model.

Finally, we combine our shear likelihood with the most recent data and likelihood release¹² from [Planck Collaboration XIII \(2015a\)](#) in order to break the degeneracy between the parameters Ω_{m} and σ_8 . In particular we employ the *Planck* primary CMB temperature data (TT) from high multipoles ℓ in combination with the *Planck* low multipole polarization data (lowP). Due to long run-time we chose to use the PLIK HIGHL-LITE likelihood code which requires only to marginalize over one nuisance parameter, A_{Planck} . The Bayesian model comparison showed no evidence for any model extension beyond a baseline ΛCDM model for describing the shear likelihood. This implies that we would essentially reproduce *Planck*-only results if we were to add parameters for which there is no evidence. Hence, we consider only six cosmological parameters and one nuisance parameter for the combined ‘*Planck*+Shear’ model: Ω_{cdm} , $\ln(10^{10} A_{\text{s}})$, h , Ω_{b} , n_{s} , τ_{reio} , and A_{Planck} . Again we assume one dominant neutrino mass eigenstate in the normal hierarchy with $\Sigma m_{\nu} = 0.06 \text{ eV}$ and a flat cosmology. In comparison to our shear-only likelihood analysis we chose to use narrower prior ranges for most parameters (cf. Table 4.5). Due to the reduced set of nuisance parameters with respect to the original *Planck* analysis, we also resample the *Planck* likelihood for the seven parameter baseline model so that comparisons of likelihood contours are fair.

Prior ranges and parameter constraints for the resampled *Planck* likelihood and the combination of *Planck*+Shear are presented in Table 4.5. Fig. 4.12 demonstrates that combining the shear likelihood with the *Planck* likelihood yields improved constraints on σ_8 and Ω_{m} and breaks the degeneracy between the two parameters. The 68 and 95 per cent credible intervals are largely overlapping and show marginal consistency between the two data sets as already observed above. We find the constraints $\sigma_8 = 0.818 \pm 0.013$ and $\Omega_{\text{m}} = 0.300 \pm 0.011$ which are consistent with the constraints from the resampled *Planck*-only likelihood (cf. Table 4.5).

4.8 Conclusions

In this work we generalized the original quadratic estimator approach by [Hu & White \(2001\)](#) to include tomographic bins. We validated the method and its extension to tomographic bins by applying it to mock data tailored to the survey specifications of CFHTLenS. In particular we made use of the official CFHTLenS Clone but produced also our own sets of Gaussian

¹²PLC-2.0 from <http://pla.esac.esa.int/pla/>

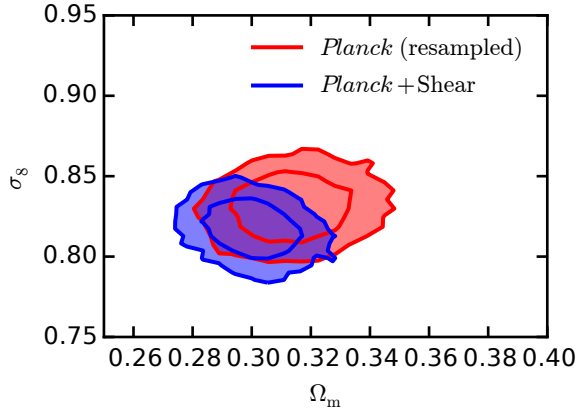


Figure 4.12: We show 68 and 95 per cent credible intervals (red, inner and outer contour, respectively) derived from sampling only the *Planck* likelihood (TT+lowP) with the simplified model consisting of six cosmological parameters and only one nuisance parameter (cf. Table 4.5). We combine the *Planck* likelihood then with the shear likelihood and sample from the combined likelihood for the same simplified model and derive 68 and 95 per cent credible intervals (blue, inner and outer contour, respectively).

random field realizations in order to test the performance for the larger scales used in our analysis. We also used the 184 independent shear catalogues from the CFHTLenS Clone and our GRFs to derive a run-to-run covariance. We applied the method to public shear data from CFHTLenS in two tomographic bins to extract band powers of the lensing power spectrum.

We use the extracted band powers and the run-to-run covariance estimated from our suite of mock data in order to sample the shear likelihood. The sampling is performed in a Bayesian framework. We derive constraints on cosmological parameters as well as the Bayesian evidence for each model. In addition to the five baseline cosmological parameters, our most conservative model extension includes a free total mass of three degenerate massive neutrinos, a free amplitude for the baryon feedback model of the matter power spectrum and photometric redshift biases to marginalize over. For this model we derive an upper limit on the total mass of three degenerate massive neutrinos of $\Sigma m_\nu < 4.53$ eV at 95 per cent credibility. Based on the analysis of the shear likelihood we find no evidence for any of the tested model extensions though: a standard, five parameter Λ CDM model is sufficient to describe the lensing power spectrum band powers measured over a range of $80 \leq \ell \leq 1310$ in two tomographic bins. The main parameters constrained by the lensing power spectra are σ_8 and Ω_m and we find the 68 percent credible intervals in this parameter plane to be marginally consistent both with [Planck Collaboration XIII \(2015a\)](#) and the CFHTLenS analysis by [Heymans et al. \(2013\)](#). Because the constraints on σ_8 and Ω_m are degenerate, we combine both parameters into the projected parameter $S_8 \equiv \sigma_8(\Omega_m/0.3)^{0.5}$. For the baseline Λ CDM model we obtain a best-fitting value of $S_8 = 0.768^{+0.045}_{-0.039}$. Marginalization over a photometric redshift bias per tomographic bin increases the errorbars on S_8 by ≈ 7 per cent. Furthermore, we compare our constraints on cosmological parameters with other CFHTLenS studies and the recent result from DES and we find general agreement. Combining the shear likelihood with the *Planck* likelihood (TT+lowP) and sampling a simple six-parameter Λ CDM model breaks the degeneracy between Ω_m and σ_8 and yields the constraints $\Omega_m = 0.300 \pm 0.011$ and $\sigma_8 = 0.818 \pm 0.013$. These constraints are consistent with the ones derived from resampling

the *Planck*-only likelihood and the errorbars decrease by ≈ 19 per cent for Ω_m and ≈ 10 per cent for σ_8 .

Data from larger weak-lensing surveys such as the Kilo-Degree Survey¹³ (de Jong et al. 2013, 2015; Kuijken et al. 2015), the Subaru Hyper SuprimeCam lensing survey,¹⁴ and the DES¹⁵ (Flaugher 2005; Jarvis et al. 2015; Becker et al. 2015) are building up right now, and these surveys will reach full coverage in the next years. This development will culminate in the surveys carried out by the Large Synoptic Survey Telescope¹⁶ (Ivezic et al. 2008) and the spaceborne *Euclid*¹⁷ survey (Laureijs et al. 2011). Given these surveys, we consider our analysis also as a proof of concept in preparation for the order(s) of magnitude increase in survey area, which also implies a significant reduction in statistical uncertainties.

Acknowledgements

The authors would like to thank the anonymous referee for her/his insightful comments that helped to further improve this work and its presentation.

FK would like to thank B. Audren, C. Heymans, W. Hu, J. Lesgourgues, M. Takada, and J. Torrado for fruitful discussions, technical expertise, and comments which helped to improve this work.

FK acknowledges support from a de Sitter Fellowship of the Netherlands Organization for Scientific Research (NWO) under grant number 022.003.013.

MV and HH acknowledge support from the European Research Council under FP7 grant number 279396. MV also acknowledges support from the Netherlands Organization for Scientific Research (NWO) through grants 614.001.103.

BJ acknowledges support by an STFC Ernest Rutherford Fellowship, grant reference ST/J004421/1.

The authors would like to thank the whole CFHTLenS team for their tremendous efforts and especially for their decision to make all data products available to the public.

Special thanks are due to C. Heymans for making her original likelihood data available to the authors.

Plots in this paper were prepared with PYTHON, its MATPLOTLIB package (Hunter 2007), and our customized version of TRIANGLE.PY (Foreman-Mackey et al. 2014).

This work is based on observations obtained with MegaPrime/MegaCam, a joint project of CFHT and CEA/IRFU, at the Canada-France-Hawaii Telescope (CFHT) which is operated by the National Research Council (NRC) of Canada, the Institut National des Sciences de l'Univers of the Centre National de la Recherche Scientifique (CNRS) of France, and the University of Hawaii. This research used the facilities of the Canadian Astronomy Data Centre operated by the National Research Council of Canada with the support of the Canadian Space Agency. CFHTLenS data processing was made possible thanks to significant computing support from the NSERC Research Tools and Instruments grant program.

Computations for the N -body simulations were performed on the TCS supercomputer at the SciNet HPC Consortium. SciNet is funded by: the Canada Foundation for Innovation under the auspices of Compute Canada; the Government of Ontario; Ontario Research Fund – Research Excellence; and the University of Toronto.

¹³kids.strw.leidenuniv.nl

¹⁴www.naoj.org/Projects/HSC/

¹⁵www.darkenergysurvey.org

¹⁶www.lsst.org

¹⁷www.euclid-ec.org

Bibliography

- Alsing J., Heavens A., Jaffe A. H., Kiessling A., Wandelt B., Hoffmann T., 2015, preprint (arXiv:1505.07840)
- Aubourg E., et al., 2014, preprint (arXiv:1411.1074)
- Audren B., Lesgourgues J., 2011, *J. Cosmology Astropart. Phys.*, 2011, 037
- Audren B., Lesgourgues J., Benabed K., Prunet S., 2012, preprint (arXiv:1210.7183)
- Bartelmann M., Schneider P., 2001, *Phys. Rep.*, 340, 291
- Becker M. R., et al., 2015, preprint (arXiv:1507.05598)
- Benítez N., 2000, *ApJ*, 536, 571
- Benjamin J., et al., 2013, *MNRAS*, 431, 1547
- Blas D., Lesgourgues J., Tram T., 2011, *J. Cosmology Astropart. Phys.*, 2011, 034
- Bond J. R., Jaffe A. H., Knox L., 1998, *Phys. Rev. D*, 57, 2117
- Brown M. L., Taylor A. N., Bacon D. J., Gray M. E., Dye S., Meisenheimer K., Wolf C., 2003, *MNRAS*, 341, 100
- Buchner J., et al., 2014, *A&A*, 564, A125
- DES Collaboration, 2015, preprint (arXiv:1507.05552)
- Demetroullas C., Brown M. L., 2015, preprint (arXiv:1507.05977)
- Erben T., et al., 2013, *MNRAS*, 433, 2545
- Feroz F., Hobson M. P., 2008, *MNRAS*, 384, 449
- Feroz F., Hobson M. P., Bridges M., 2009, *MNRAS*, 398, 1601
- Feroz F., Hobson M. P., Cameron E., Pettitt A. N., 2013, preprint (arXiv:1306.2144)
- Flaugher B., 2005, *Int. J. Mod. Phys. A*, 20, 3121
- Foreman-Mackey D., Price-Whelan A., Ryan G., Emily Smith M., Barbary K., Hogg D. W., Brewer B. J., 2014, triangle.py v0.1.1, doi:10.5281/zenodo.11020, <http://dx.doi.org/10.5281/zenodo.11020>
- Harnois-Déraps J., Vafaei S., Waerbeke L. V., 2012, *MNRAS*, 426, 1262
- Harnois-Déraps J., Pen U.-L., Iliev I. T., Merz H., Emberson J. D., Desjacques V., 2013, *MNRAS*, 436, 540
- Harnois-Déraps J., Waerbeke L. v., Viola M., Heymans C., 2015, *MNRAS*, 450, 1212
- Hartlap J., Simon P., Schneider P., 2007, *A&A*, 464, 399
- Heymans C., et al., 2005, *MNRAS*, 361, 160
- Heymans C., et al., 2012, *MNRAS*, 427, 146

- Heymans C., et al., 2013, [MNRAS](#), 432, 2433
- Hildebrandt H., et al., 2012, [MNRAS](#), 421, 2355
- Hu W., White M., 2001, [ApJ](#), 554, 67
- Hunter J. D., 2007, *Comput. Sci. Eng.*, 9, 90
- Ivezic Z., et al., 2008, preprint (arXiv:0805.2366)
- Jarvis M., et al., 2015, preprint (arXiv:1507.05603)
- Kass R. E., Raftery A. E., 1995, [Journal of the American Statistical Association](#), 90, 773
- Kaufmann G. M., 1967, Report No. 6710, Some Bayesian Moment Formulae. Centre for Operations Research and Econometrics, Catholic University of Louvain, Heverlee
- Kilbinger M., 2015, [Rep. Prog. Phys.](#), 78, 086901
- Kilbinger M., et al., 2013, [MNRAS](#), 430, 2200
- Kitching T. D., et al., 2014, [MNRAS](#), 442, 1326
- Knox L., 1999, [Phys. Rev. D](#), 60, 103
- Komatsu E., et al., 2009, [ApJS](#), 180, 330
- Kuijken K., et al., 2015, [MNRAS](#), 454, 3500
- Laureijs R., et al., 2011, preprint (arXiv:1110.3193),
- Lesgourgues J., Pastor S., 2006, [Phys. Rep.](#), 429, 307
- Lesgourgues J., Tram T., 2011, [J. Cosmology Astropart. Phys.](#), 2011, 032
- Limber D. N., 1954, [ApJ](#), 119, 655
- Lin H., et al., 2012, [ApJ](#), 761, 15
- Melchior P., Viola M., 2012, [MNRAS](#), 424, 2757
- Miller L., et al., 2013, [MNRAS](#), 429, 2858
- Planck Collaboration XIII, 2015a, preprint (arXiv:1502.01589)
- Planck Collaboration XIV, 2015b, preprint (arXiv:1502.01590)
- Refregier A., Kacprzak T., Amara A., Bridle S., Rowe B., 2012, [MNRAS](#), 425, 1951
- Riess A. G., et al., 2011, [ApJ](#), 730, 119
- Schaye J., et al., 2010, [MNRAS](#), 402, 1536
- Seljak U., 1998, [ApJ](#), 506, 64
- Semboloni E., Hoekstra H., Schaye J., van Daalen M. P., McCarthy I. G., 2011, [MNRAS](#), 417, 2020
- Semboloni E., Hoekstra H., Schaye J., 2013, [MNRAS](#), 434, 148

Sifón C., Hoekstra H., Cacciato M., Viola M., Köhlinger F., van der Burg R. F. J., Sand D. J., Graham M. L., 2015, *A&A*, 575, A48

Takada M., Jain B., 2009, *MNRAS*, 395, 2065

Takahashi R., Sato M., Nishimichi T., Taruya A., Oguri M., 2012, *ApJ*, 761, 152

de Jong J. T. A., Verdoes Kleijn G. A., Kuijken K. H., Valentijn E. A., 2013, *Exp. Astron.*, 35, 25

de Jong J. T. A., et al., 2015, *A&A*, 582, A62

van Daalen M. P., Schaye J., Booth C. M., Dalla Vecchia C., 2011, *MNRAS*, 415, 3649

4.A Indices and derivatives

In Section 4.3 we described the generalization of the quadratic estimator to include tomographic bins. This requires a great amount of indices in a strict notation. For brevity we switched rather quickly to a set of superindices and we also refrained from showing the explicit forms of certain matrices. Here, we give now the explicit forms of these matrices and we also calculate the derivatives used, for example, in equations (4.11) or (4.15) in index notation.

First, we start with specifying the components of the vector \mathcal{B} which contains all band powers β of type θ for each *unique* redshift bin correlation ζ as $\mathcal{B}_{\zeta\theta\beta}$. Note that the total number of unique correlations between n_z redshift bins is $n_{\text{corr}} = n_z(n_z + 1)/2$, because all cross-correlations contain the same information by construction. Likewise we define the components of the tensor \mathbf{G} which encodes all geometric information of the field depending on the band power β , the band type θ and the redshift bin correlation ζ as

$$G_{\zeta\theta\beta(\mu\nu)(ab)(ij)} \equiv M_{\zeta(\mu\nu)} \int_{\ell_{\min}(\beta)}^{\ell_{\max}(\beta)} \frac{d\ell}{2(\ell + 1)} \left[w_0(\ell) I_{(ab)(ij)}^\theta + \frac{1}{2} w_4(\ell) Q_{(ab)(ij)}^\theta \right]. \quad (4.28)$$

We also note here that each realization of \mathbf{G} for a given band power β of type θ and correlation ζ can be represented as a matrix $\mathbf{G}_{\zeta\theta\beta}$. We can write out the matrices \mathbf{I}^θ and \mathbf{Q}^θ for the EE-, BB-, and EB-band powers as (Hu & White 2001)

$$\mathbf{I}^{\text{EE}} = \begin{pmatrix} J_0 + c_4 J_4 & s_4 J_4 \\ s_4 J_4 & J_0 - c_4 J_4 \end{pmatrix}, \quad (4.29)$$

$$\mathbf{I}^{\text{BB}} = \begin{pmatrix} J_0 - c_4 J_4 & -s_4 J_4 \\ -s_4 J_4 & J_0 + c_4 J_4 \end{pmatrix}, \quad (4.30)$$

$$\mathbf{I}^{\text{EB}} = \begin{pmatrix} -2s_4 J_4 & 2c_4 J_4 \\ 2c_4 J_4 & 2s_4 J_4 \end{pmatrix}, \quad (4.31)$$

and

$$\mathbf{Q}^{\text{EE}} = \begin{pmatrix} J_0 + 2c_4 J_4 + c_8 J_8 & s_8 J_8 \\ s_8 J_8 & -J_0 + 2c_4 J_4 - c_8 J_8 \end{pmatrix}, \quad (4.32)$$

$$\mathbf{Q}^{\text{BB}} = \begin{pmatrix} -J_0 + 2c_4 J_4 - c_8 J_8 & -s_8 J_8 \\ -s_8 J_8 & J_0 + 2c_4 J_4 + c_8 J_8 \end{pmatrix}, \quad (4.33)$$

$$\mathbf{Q}^{\text{EB}} = \begin{pmatrix} -2s_8 J_8 & 2J_0 + 2c_8 J_8 \\ 2J_0 + 2c_8 J_8 & 2s_8 J_8 \end{pmatrix}. \quad (4.34)$$

In these equations we suppressed the argument of the Bessel functions J_n which in each case is the product ℓr_{ij} , where $r_{ij} = |\mathbf{n}_i - \mathbf{n}_j|$ is the distance between pixels i, j (cf. Section 4.4). Moreover, we employ the shorthand notations $c_n = \cos(n\varphi)$ and $s_n = \sin(n\varphi)$, where φ is the angle between the x -axis and the distance vector \mathbf{r}_{ij} between pixels i, j (cf. Section 4.4). Note that in equation (4.33) we corrected the misprint in the original reference pointed out by Lin et al. (2012). Note also, that each block in the matrices of equations (4.29)–(4.34) defines again a matrix in the indices i, j .

The matrices \mathbf{M}_ζ in equation (4.28) map between the redshift bins and their unique correlations. In order to construct them, we start with the standard basis $\mathbf{e}_{\mu\nu}$ for $\mu \times \nu$ matrices with $\mu, \nu \in (1, \dots, n_z)$. For example, the standard basis for $n_z = 2$ can be written explicitly as:

$$\mathbf{e}_{11} = \begin{pmatrix} 1 & 0 \\ 0 & 0 \end{pmatrix}, \quad \mathbf{e}_{12} = \begin{pmatrix} 0 & 1 \\ 0 & 0 \end{pmatrix}, \quad (4.35)$$

$$\mathbf{e}_{21} = \begin{pmatrix} 0 & 0 \\ 1 & 0 \end{pmatrix}, \quad \mathbf{e}_{22} = \begin{pmatrix} 0 & 0 \\ 0 & 1 \end{pmatrix}. \quad (4.36)$$

The index pairs (μ, ν) can be trivially mapped to only one index ζ' which yields for the example above, i.e. $\mu, \nu \in (1, 2)$:

$$(1, 1) \rightarrow 1, (1, 2) \rightarrow 2, (2, 1) \rightarrow 3, (2, 2) \rightarrow 4. \quad (4.37)$$

Imposing now, however, the symmetry condition $(\mu, \nu) = (\nu, \mu)$, which guarantees that for n_z redshift bins we only consider $n_{\text{corr}} = n_z(n_z + 1)/2$ independent correlations, yields the symmetric mapping matrices:

$$\mathbf{M}_1 = \begin{pmatrix} 1 & 0 \\ 0 & 0 \end{pmatrix} = \mathbf{e}_{11}, \quad (4.38)$$

$$\mathbf{M}_2 = \begin{pmatrix} 0 & 1 \\ 1 & 0 \end{pmatrix} = \mathbf{e}_{12} + \mathbf{e}_{21}, \quad (4.39)$$

$$\mathbf{M}_3 = \begin{pmatrix} 0 & 0 \\ 0 & 1 \end{pmatrix} = \mathbf{e}_{22} \quad (4.40)$$

which implies the following mapping from (μ, ν) to ζ :

$$(1, 1) \rightarrow 1, (1, 2) = (2, 1) \rightarrow 2, (2, 2) \rightarrow 3. \quad (4.41)$$

Next we construct the signal matrix \mathbf{C}^{sig} as the sum over bands β , band types θ , and redshift-correlations ζ of the product of the band power vector $\mathcal{B}_{\zeta\theta\beta}$ with the geometry matrices $\mathbf{G}_{\beta\theta\zeta}$,

$$C_{(\mu\nu)(ab)(ij)}^{\text{sig}} = \sum_{\zeta, \theta, \beta} \mathcal{B}_{\zeta\theta\beta} G_{\zeta\theta\beta(\mu\nu)(ab)(ij)}. \quad (4.42)$$

Note that the full covariance matrix \mathbf{C} also includes contributions from the shape noise matrix $\mathbf{C}^{\text{noise}}$ (cf. equation 4.9) which is constant. Thus if we wish to take the derivative of the full covariance matrix with respect to every possible band-power combination $B_{(\mu\nu)(\beta\theta)}$, this constant noise term vanishes and we are left with

$$\frac{\partial C_{(\mu\nu)(ab)(ij)}}{\partial \mathcal{B}_{\zeta\theta\beta}} = \frac{\partial C_{(\mu\nu)(ab)(ij)}^{\text{sig}}}{\partial \mathcal{B}_{\zeta\theta\beta}} \quad (4.43)$$

$$\begin{aligned} &= G_{\zeta\theta\beta(\mu\nu)(ab)(ij)} \\ &\equiv \mathbf{D}_{\zeta\theta\beta} \equiv \mathbf{D}_A. \end{aligned} \quad (4.44)$$

In order to simplify our notation with respect to the Newton–Raphson algorithm we introduced in the last step the superindex A : each specific index combination $(\zeta\theta\beta)$ can be mapped to a single index A ¹⁸, i.e. we denote a specific derivative matrix now as \mathbf{D}_A instead of $\mathbf{D}_{\zeta\theta\beta}$. Hence the components of the generalized Fisher matrix \mathbf{F} can be written as

$$F_{AB} = \frac{1}{2} \text{Tr}(\mathbf{C}^{-1} \mathbf{D}_A \mathbf{C}^{-1} \mathbf{D}_B). \quad (4.45)$$

All other equations employed in the Newton–Raphson algorithm still hold with respect to this new set of superindices (A, B) .

Finally, it only remains to write out explicitly the derivatives of the full covariance matrix \mathbf{C} with respect to the power at an integer multipole ℓ . This is required for the calculation of the window function matrix (cf. equation 4.14) in which the derivatives \mathbf{D}_ℓ enter in computing the trace matrix \mathbf{T} (cf. equation 4.15):

$$\begin{aligned} \frac{\partial C_{(\mu\nu)(ab)(ij)}}{\partial \mathcal{B}(\ell)} &= \sum_{\zeta, \theta} \frac{M_{\zeta(\mu\nu)}}{2(\ell+1)} \left[w_0(\ell) I_{(ab)(ij)}^\theta + \frac{1}{2} w_4(\ell) Q_{(ab)(ij)}^\theta \right] \\ &\equiv D_{(\mu\nu)(ab)(ij)}(\ell) \equiv \mathbf{D}_\ell, \end{aligned} \quad (4.46)$$

where we have used that

$$C_{(\mu\nu)(ab)(ij)}^{\text{sig}} = \sum_{\zeta, \theta, \ell} \mathcal{B}_{\zeta\theta}(\ell) \frac{M_{\zeta(\mu\nu)}}{2(\ell+1)} \left[w_0(\ell) I_{(ab)(ij)}^\theta + \frac{1}{2} w_4(\ell) Q_{(ab)(ij)}^\theta \right].$$

4.B Additional figures

In the following figures we show the extracted E- and B-modes for each CFHTLenS patch individually. Note that these E-mode signals enter directly in the likelihood sampling whereas the combined signal presented in Fig. 4.4 serves just for illustrative purposes.

¹⁸For example, consider again two redshift bins, i.e. $\zeta \in (1, 2, 3)$, from which we wish to extract four band powers, i.e. $\beta \in (1, 2, 3, 4)$, of a single band type $\text{EE} \hat{=} \theta = 0$. Then we can map each unique combination of $\zeta\theta\beta$ to an integer $A \in (0, \dots, 12)$.

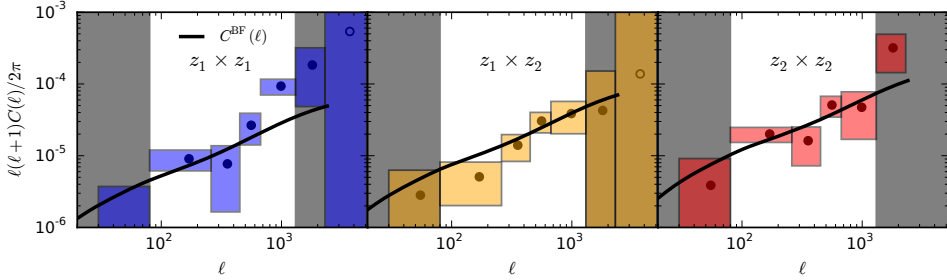


Figure 4.13: Measured E-mode band powers in tomographic bins for the CFHTLenS patch W1. From left to right we show the auto-correlation signal of the low-redshift bin (blue), the cross-correlation signal between the low- and the high-redshift bin (orange), and the auto-correlation signal of the high-redshift bin (red). The low-redshift bin contains objects with redshifts in the range $0.5 < z_1 \leq 0.85$ and the high-redshift bin covers a range $0.85 < z_2 \leq 1.3$. The 1σ -errors in the signal are derived from a run-to-run covariance over 184 independent mock data fields (cf. Section 4.5.2) whereas the extent in ℓ -direction is the width of the band. Band powers in the shaded regions (grey) to the left and right of each panel are excluded from the cosmological analysis (cf. Fig. 4.5). The solid line (black) shows the power spectrum for the best-fitting five-parameter Λ CDM model derived in the subsequent analysis (cf. Section 4.7 and Table 4.4). Note, however, that the band powers are centred at the naive ℓ -bin centre and thus the convolution with the band window function is not taken into account in this plot, in contrast to the cosmological analysis.

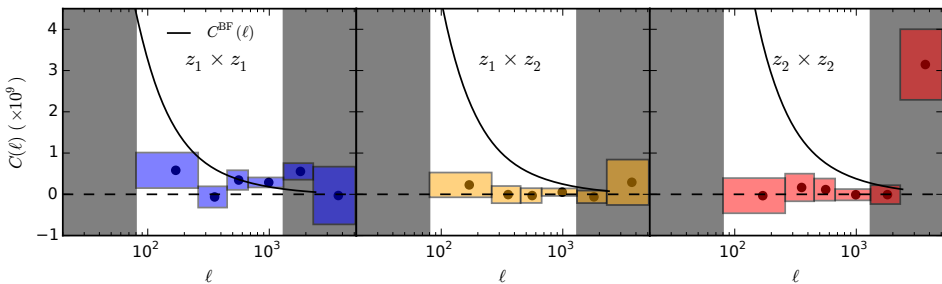


Figure 4.14: Same as Fig. 4.13 but for B-mode band powers. Note, however, the different scale (linear) and normalization used here with respect to Fig. 4.13; for reference we also plot the best-fitting E-mode power spectrum as solid line (black). We show the measured B-modes as (black) dots with 1σ -errors derived from the inverse Fisher matrix. Based on these signals we define the shaded regions (grey) to the left and right of each panel (cf. Section 4.6 for details). E-mode band powers in these regions are excluded from the cosmological analysis (cf. Fig. 4.4).

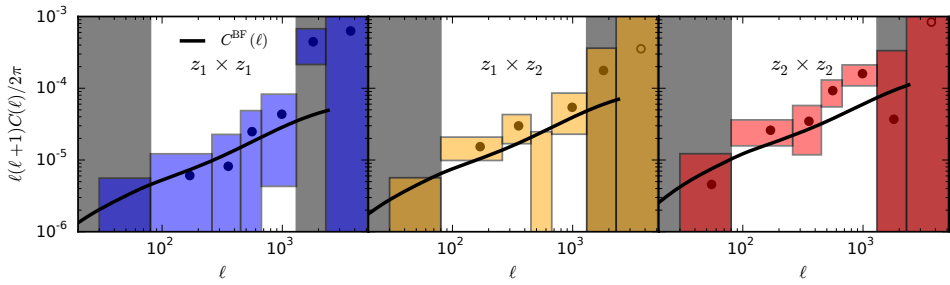


Figure 4.15: Same as Fig. 4.13 but for CFHTLenS patch W2. Open symbols denote negative values plotted with 1σ -errors centred on the absolute value.

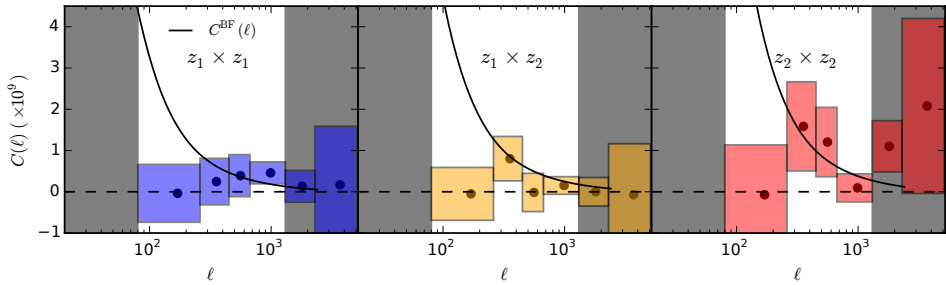


Figure 4.16: Same as Fig. 4.14 but for CFHTLenS patch W2. Open symbols denote negative values plotted with 1σ -errors centred on the absolute value.

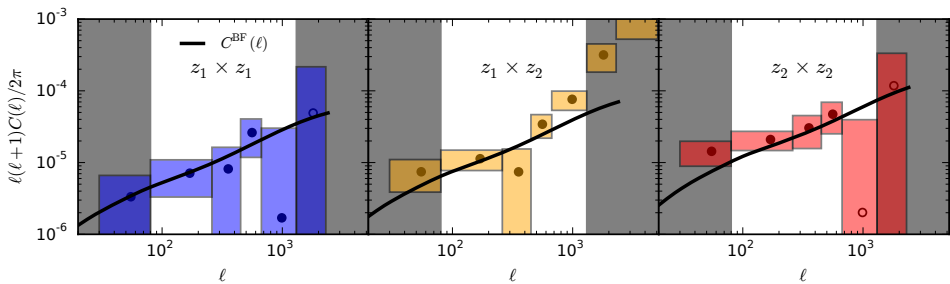


Figure 4.17: Same as Fig. 4.13 but for CFHTLenS patch W3. Open symbols denote negative values plotted with 1σ -errors centred on the absolute value.

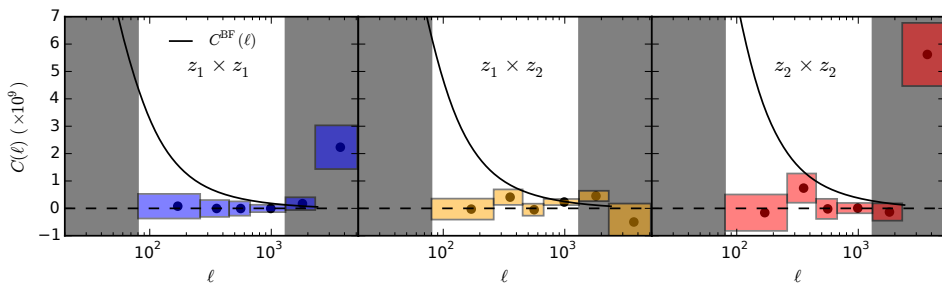


Figure 4.18: Same as Fig. 4.14 but for CFHTLenS patch W3. Open symbols denote negative values plotted with 1σ -errors centred on the absolute value.

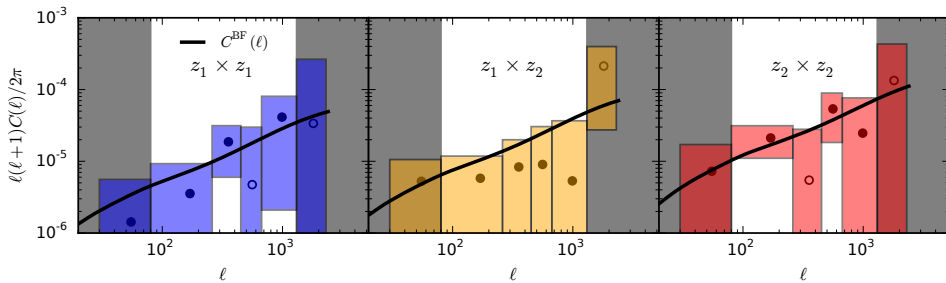


Figure 4.19: Same as Fig. 4.13 but for CFHTLenS patch W4. Open symbols denote negative values plotted with 1σ -errors centred on the absolute value.

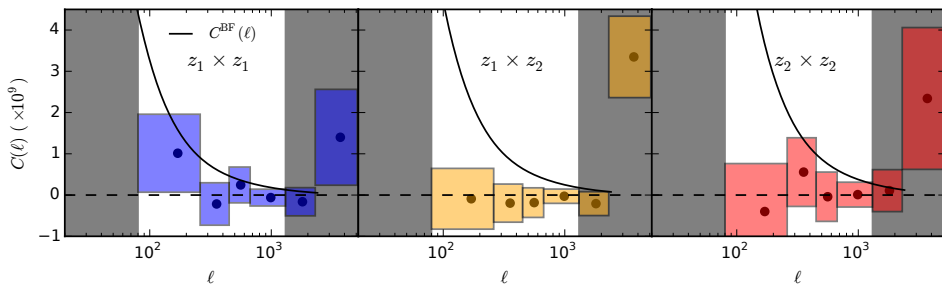


Figure 4.20: Same as Fig. 4.14 but for CFHTLenS patch W4. Open symbols denote negative values plotted with 1σ -errors centred on the absolute value.

KiDS-450: The tomographic weak lensing power spectrum and constraints on neutrinos and cosmological parameters

We present measurements of the weak gravitational lensing shear power spectrum based on $\approx 450 \text{ deg}^2$ of imaging data from the Kilo-Degree Survey (KiDS). We employ a direct quadratic estimator in two redshift bins and extract band powers of the redshift auto-correlation spectra and cross-correlation spectrum in the multipole range $76 \leq \ell \leq 1310$. The cosmological interpretation of the measured shear power spectra is performed in a Bayesian framework assuming a flat Λ cold dark matter model, while accounting for small residual uncertainties in the shear calibration, intrinsic alignments, and baryon feedback. This yields the constraint on the parameter combination $S_8 \equiv \sigma_8 \sqrt{\Omega_m/0.3} = 0.742 \pm 0.057$. This result is in tension at 1.8σ with the constraint from *Planck* based on measurements of the cosmic microwave background radiation. For the extension of the fiducial model with a free total mass of three degenerate massive neutrinos we derive the upper limit $\Sigma m_\nu < 3.46 \text{ eV}$ at 95 per cent credibility from the lensing data only. However, a Bayesian model comparison does not yield any evidence for extending the baseline model with a free total neutrino mass.

F. Köhlinger and the KiDS Collaboration

5.1 Introduction

The current cosmological concordance model successfully describes observations spanning a wide range in cosmic volume from the cosmic microwave background (CMB) power spectrum (e.g. [Planck Collaboration XIII 2015a](#)), the Hubble diagram based on supernovae of type IA (SNIa; e.g. [Riess et al. 2016](#)), big bang nucleosynthesis (BBN; e.g. [Fields & Olive 2006](#)), to the distance scales inferred from baryon acoustic oscillations imprinted in the large-scale clustering of galaxies (BAO; e.g. [BOSS Collaboration 2015](#)). Based on Einstein’s theory of general relativity and the application of the Copernican principle to the whole Universe, the Λ -dominated cold dark matter (Λ CDM) model requires in its simplest form only a handful of parameters to fit all current observational data. However, the physical nature of two of these parameters, dark matter and dark energy, is still unknown, although their energy densities at present are very well constrained by observations. Within current limits dark energy can still be interpreted in terms of the cosmological constant Λ , but any observed deviation from a constant value will have profound consequences that might eventually even lead to a revision of our theory of gravity. The cosmological concordance model is also naturally linked to the standard model of particle physics and the discovery of the constituents of dark matter will make its revision inevitable. However, experiments have already shown another shortcoming of the standard model: the experimental discovery of neutrino oscillations ([Super-Kamiokande Collaboration 1998](#); [SNO Collaboration 2001, 2002](#)) indicates that neutrinos possess mass, which is in direct contradiction to its fiducial predictions.

Massive neutrinos affect the growth of cosmological large-scale structure (e.g. [Lesgourgues & Pastor 2006](#) and references therein for a review) and hence a measurement of the growth of large-scale structure yields a constraint on the total mass over all neutrino species (e.g. [Palanque-Delabrouille et al. 2015](#)) which is an important complementary constraint to particle physics experiments.

Cosmic shear, i.e. the weak gravitational lensing due to all intervening cosmic large-scale structure between an observer and all sources along the line-of-sight, presents a viable tool to study the evolution of the dark species. However, the tiny coherent image distortions, the shear, of background sources caused by the bending of their emitted light perpendicular to the line-of-sight of a foreground mass need to be studied in statistically large samples. Hence, wide-field surveys covering increasingly more volume in the sky are the current and future strategy for improving the precision of the measurements. Data from large weak-lensing surveys such as the Kilo-Degree Survey (KiDS;¹ [de Jong et al. 2013, 2015](#); [Kuijken et al. 2015](#)), the Subaru Hyper SuprimeCam lensing survey², and the Dark Energy Survey (DES;³ [Jarvis et al. 2015](#)) are currently building up. These surveys are expected to reach coverage on the order of (several) 1000 deg² within the next few years, which presents an order of magnitude increase compared to currently available survey data ([Erben et al. 2013](#); [Kuijken et al. 2015](#); [Jarvis et al. 2015](#)). Eventually, close to all-sky surveys will be carried out over the next decade by the ground based Large Synoptic Survey Telescope⁴ ([Ivezic et al. 2008](#)) and the spaceborne *Euclid*⁵ satellite ([Laureijs et al. 2011](#)) and the *Wide Field Infrared Survey Telescope*.⁶

The cosmic shear signal as a function of redshift is sensitive to the growth of structure and the geometry of the Universe and studying its redshift dependence allows us to infer the

¹kids.strw.leidenuniv.nl

²www.naoj.org/Projects/HSC/

³www.darkenergysurvey.org

⁴www.lsst.org

⁵www.euclid-ec.org

⁶wfirst.gsfc.nasa.gov

expansion rate as well as the clustering behaviour of cosmic species such as cold dark matter, massive neutrinos, and dark energy.

There are several approaches to measure cosmic shear; the most common one to date is based on the two-point statistics of real-space correlation functions (e.g. [Kilbinger 2015](#) for a recent review). The redshift dependence is either considered by performing the cosmic shear measurement in tomographic redshift slices (e.g. [Benjamin et al. 2013](#), [Heymans et al. 2013](#), [Becker et al. 2015](#)) or by employing redshift-dependent spherical Bessel functions ([Kitching et al. 2014](#)). An alternative and mathematically equivalent approach is to switch to Fourier space and measure the power spectrum of cosmic shear instead. One particular advantage of direct shear power spectrum estimators over correlation-function measurements is that the power spectrum measurements are significantly less correlated on all scales. This is very important for the clean study of scale-dependent signatures such as, for example, those caused by massive neutrinos. In addition, proper modelling is needed on non-linear scales in order to avoid any bias in the cosmological parameters. This, however, is complicated because of the feedback effects of baryon physics on the matter power spectrum of which we still have an insufficient understanding ([Semboloni et al. 2011, 2013](#)). Direct power spectrum estimators have already been applied to data, the quadratic estimator for example to the COMBO-17 dataset ([Brown et al. 2003](#)) and the GEMS dataset ([Heymans et al. 2005](#)). In a more recent study [Lin et al. \(2012\)](#) applied a quadratic estimator and a direct pseudo- $C(\ell)$ estimator based on [Hikage et al. \(2011\)](#) to data from the SDSS Stripe 82. However, the direct power spectrum estimators in these studies did not employ a tomographic approach. This was done for the first time in **Chapter 4**, where we extended the quadratic estimator formalism to include redshift bins and applied it to shear catalogues from the lensing analysis of the Canada–France–Hawaii Telescope Legacy Survey (CFHTLenS; [Erben et al. 2013](#), [Heymans et al. 2012](#), [Hildebrandt et al. 2012](#)).

Previous results from a six bin tomographic correlation-function analysis of CFHTLenS ([Heymans et al. 2013](#)) and a re-analysis by [Joudaki et al. \(2016\)](#) incorporating new knowledge regarding systematic errors in the photometric redshift distributions ([Choi et al. 2015](#)) found cosmological parameter constraints to be in tension with CMB based results from [Planck Collaboration XIII \(2015a\)](#). However, our quadratic estimator re-analysis of CFHTLenS from **Chapter 4** using only two tomographic bins at higher redshifts and incorporating larger angular scales, did not reveal any tension with results from *Planck*, which can be attributed though to increased errorbars due to the more conservative analysis. Similarly, results from a correlation-function analysis from DES ([DES Collaboration 2015](#)) are not in tension with *Planck* either. However, due to the small area coverage of the science verification data their errorbars are significantly larger compared to results from CFHTLenS.

Results from other low-redshift probes measuring the growth rate such as galaxy cluster counts (e.g. [Planck Collaboration XXIV 2015b](#), [de Haan et al. 2016](#)) or redshift space distortions (e.g. [Beutler et al. 2014](#), [Samushia et al. 2014](#), [Gil-Marín et al. 2016](#)) consistently find a lower amplitude of fluctuations (parametrized as σ_8 , the root-mean-square variance in spheres of $8 h^{-1} \text{Mpc}$) at a given matter density (Ω_m) with respect to results from *Planck*. Hence, there are also claims in the literature (e.g. [Spergel et al. 2015](#), [Addison et al. 2016](#), [Riess et al. 2016](#)) that systematic errors that are yet unaccounted for in the *Planck* analysis might be the reason for the observed tension.

An intermediate data release from the ongoing KiDS covering an area of about 450 deg^2 presents an independent dataset to re-evaluate whether or not cosmic shear results are in tension with *Planck*. The imaging data are taken with a combination of camera and telescope designed to yield among the best shear data quality attainable from the ground and the setup is different from the one employed for CFHTLenS. Latest results from a 4-bin tomographic

correlation-function analysis employing these data (Hildebrandt et al. 2016) are in tension with results from *Planck*, but agree well with results from other low-redshift probes. At the moment it is yet too premature to decide whether the tension between *Planck* and low-redshift probes is due to internal systematics that are yet unaccounted for in each probe (e.g. for low-redshift probes the proper modelling of the matter power spectrum at very non-linear scales is a concern) or if the tension is due to new physics implying that the current cosmological concordance model is incomplete and requires physical parameter extensions (e.g. Di Valentino et al. 2015).

In this paper we follow the fiducial analysis by Hildebrandt et al. (2016) closely but use the tomographic quadratic estimator instead to measure the cosmic shear power spectrum directly from the data over the same redshift range, using two tomographic bins. This presents an important cross-check of the robustness of the results derived with two independent data analysis pipelines and estimators employing the same shear catalogues. Moreover, we explore model extensions beyond Λ CDM which might alleviate or even strengthen the tension assuming that all systematic errors are properly accounted for.

The paper is organized as follows: in Section 5.2 we summarize the theory for cosmic shear power spectra and in Section 5.3 we present the quadratic estimator algorithm. Section 5.4 introduces the KiDS-450 dataset and the most important properties of the lensing source sample. In Section 5.5 we describe the calibrations applied to the measured shear signal. Section 5.6 summarizes the details of the employed covariance matrix of the data. In Section 5.7 we present the measured cosmic shear power spectra and show a qualitative comparison to correlation-function measurements. The cosmological interpretation of the cosmic shear power spectra is discussed in Section 5.8 before we summarize all results and conclude in Section 5.9.

5.2 Theory

A consequence of Einstein's principle of equivalence is the deflection of light due to mass. We call this gravitational lensing and in this paper we will specifically work in the framework of weak gravitational lensing. It is called weak because the gradient of the gravitational potential of a deflecting foreground mass only induces very weak but coherent distortions of background sources. The measurement of the image distortions is only possible in a statistical sense and requires to average over large samples of background galaxies due to the broad distribution of intrinsic ellipticities of galaxies. The very weak-lensing effect of all intervening mass between an observer and all sources along the line-of-sight is called cosmic shear. The resulting correlations of galaxy shapes can be used to study the evolution of the large-scale structure and therefore cosmic shear becomes an increasingly valuable tool for cosmology especially in the current era of large surveys (cf. Kilbinger 2015 for a recent review). For details on the theoretical foundations of (weak) gravitational lensing we refer the reader to the standard literature (e.g. Bartelmann & Schneider 2001).

The main observables in a weak-lensing survey are the shapes and (photometric) redshifts of galaxies. The measured galaxy shapes in terms of ellipticity components e_1, e_2 at angular positions \mathbf{n}_i are binned into pixels $i = 1, \dots, N_{\text{pix}}$ and (photometric) redshift bins z_μ . Averaging then the ellipticities in each pixel yields estimates of the components of the spin-2 shear field, $\gamma_1(\mathbf{n}, z_\mu)$ and $\gamma_2(\mathbf{n}, z_\mu)$. Its Fourier decomposition can be written in the flat-sky limit as

$$\gamma_1(\mathbf{n}, z_\mu) \pm i\gamma_2(\mathbf{n}, z_\mu) = \int \frac{d^2\ell}{(2\pi)^2} \left[\kappa(\boldsymbol{\ell}, z_\mu) \pm i\beta(\boldsymbol{\ell}, z_\mu) \right] \mathbf{W}(\boldsymbol{\ell}) e^{\pm 2i\varphi_\ell} e^{i\boldsymbol{\ell} \cdot \mathbf{n}}, \quad (5.1)$$

with φ_ℓ denoting the angle between the two-dimensional vector $\boldsymbol{\ell}$ and the x -axis. For the lens-

ing by density perturbations the convergence field κ contains all the cosmological information and the field β usually vanishes in the absence of systematics. In the subsequent analysis we will still extract it and treat it as a check for residual systematics in the data.

The Fourier transform of the pixel window function, $W(\ell)$, can be written out as

$$W(\ell) = j_0\left(\frac{\ell_x \sigma_{\text{pix}}}{2} \cos \varphi_\ell\right) j_0\left(\frac{\ell_y \sigma_{\text{pix}}}{2} \sin \varphi_\ell\right), \quad (5.2)$$

where $j_0(x) = \sin(x)/x$ is the zeroth-order spherical Bessel function and σ_{pix} is the side length of a square pixel in radians.

The shear correlations between pixels \mathbf{n}_i and \mathbf{n}_j and tomographic bins μ and ν can be expressed in terms of their power spectra and they define the shear-signal correlation matrix (Hu & White 2001):

$$\mathbf{C}^{\text{sig}} = \langle \gamma_a(\mathbf{n}_i, z_\mu) \gamma_b(\mathbf{n}_j, z_\nu) \rangle, \quad (5.3)$$

with components

$$\begin{aligned} \langle \gamma_{1i\mu} \gamma_{1j\nu} \rangle &= \int \frac{d^2\ell}{(2\pi)^2} \left[C_{\mu\nu}^{\text{EE}}(\ell) \cos^2 2\varphi_\ell + C_{\mu\nu}^{\text{BB}}(\ell) \sin^2 2\varphi_\ell - C_{\mu\nu}^{\text{EB}}(\ell) \sin 4\varphi_\ell \right] W^2(\ell) e^{i\ell \cdot (\mathbf{n}_i - \mathbf{n}_j)}, \\ \langle \gamma_{2i\mu} \gamma_{2j\nu} \rangle &= \int \frac{d^2\ell}{(2\pi)^2} \left[C_{\mu\nu}^{\text{EE}}(\ell) \sin^2 2\varphi_\ell + C_{\mu\nu}^{\text{BB}}(\ell) \cos^2 2\varphi_\ell + C_{\mu\nu}^{\text{EB}}(\ell) \sin 4\varphi_\ell \right] W^2(\ell) e^{i\ell \cdot (\mathbf{n}_i - \mathbf{n}_j)}, \\ \langle \gamma_{1i\mu} \gamma_{2j\nu} \rangle &= \int \frac{d^2\ell}{(2\pi)^2} \left[\frac{1}{2} (C_{\mu\nu}^{\text{EE}}(\ell) - C_{\mu\nu}^{\text{BB}}(\ell)) \sin 4\varphi_\ell + C_{\mu\nu}^{\text{EB}}(\ell) \cos 4\varphi_\ell \right] W^2(\ell) e^{i\ell \cdot (\mathbf{n}_i - \mathbf{n}_j)}. \end{aligned} \quad (5.4)$$

In the equations above we introduced the decomposition of the shear field into curl-free and curl components, i.e. E- and B-modes, respectively. In the absence of systematic errors and shape noise, the cosmological signal is contained in the E-modes and their power spectrum is equivalent to the convergence power spectrum, i.e. $C^{\text{EE}}(\ell) = C^{\kappa\kappa}(\ell)$ and $C^{\text{BB}}(\ell) = 0$. Shot noise will generate equal power in E- and B-modes. The cross-power between E- and B-modes, $C^{\text{EB}}(\ell)$, is expected to be zero because of the parity invariance of the shear field.

The theoretical prediction for the convergence power spectrum per redshift-bin correlation μ, ν can be calculated in the Limber approximation (Limber 1954) as

$$C_{\mu\nu}^{\text{EE}}(\ell) = \int_0^{\chi_{\text{H}}} d\chi \frac{q_\mu(\chi) q_\nu(\chi)}{f_{\text{K}}^2(\chi)} P_\delta\left(k = \frac{\ell}{f_{\text{K}}(\chi)}; \chi\right), \quad (5.5)$$

which depends on the radial comoving distance χ , the distance to the horizon χ_{H} , the angular diameter distance $f_{\text{K}}(\chi)$, and the three-dimensional matter power spectrum $P_\delta(k; \chi)$.

The weight functions $q_\mu(\chi)$ depend on the lensing kernels and hence they are a measure for the lensing efficiency in each tomographic bin μ :

$$q_\mu(\chi) = \frac{3\Omega_{\text{m}} H_0^2}{2c^2} \frac{f_{\text{K}}(\chi)}{a(\chi)} \int_\chi^{\chi_{\text{H}}} d\chi' n_\mu(\chi') \frac{f_{\text{K}}(\chi' - \chi)}{f_{\text{K}}(\chi')}, \quad (5.6)$$

where $a(\chi)$ is the scale factor and the source redshift distribution is denoted as $n_\mu(\chi) d\chi = n_\mu(z) dz$. It is normalized such that $\int d\chi n_\mu(\chi) = 1$.

5.3 Quadratic estimator

There are two main techniques to extract the shear power spectrum directly from the data: one is based on a maximum-likelihood technique and employs a quadratic estimator (Bond et al.

1998; Seljak 1998; Hu & White 2001), whereas the other approach uses a pseudo spectrum (also pseudo- $C(\ell)$; Hikage et al. 2011). Moreover, there are pseudo- $C(\ell)$ methods that are based on correlation-function measurements (e.g. Becker et al. 2015). These present a hybrid approach and do not directly estimate the power spectrum from the shear data.

Here we summarize the quadratic estimator algorithm applied to cosmic shear including its extension to tomographic bins. For that we follow the original literature (Hu & White 2001; Lin et al. 2012) and the description in **Chapter 4**.

The likelihood of the measured shear field in terms of band powers \mathcal{B} is assumed to be Gaussian over most scales of interest for our analysis, i.e.

$$\mathcal{L} = \frac{1}{(2\pi)^N |\mathbf{C}(\mathcal{B})|^{1/2}} \exp \left[-\frac{1}{2} \mathbf{d}^T [\mathbf{C}(\mathcal{B})]^{-1} \mathbf{d} \right]. \quad (5.7)$$

The data vector \mathbf{d} with components

$$d_{\mu ai} = \gamma_a(\mathbf{n}_i, z_\mu) \quad (5.8)$$

contains both components of the measured shear γ_a per pixel \mathbf{n}_i for each redshift bin z_μ . The covariance matrix \mathbf{C} is written as the sum of the cosmological signal \mathbf{C}^{sig} (cf. equation 5.3) and the noise $\mathbf{C}^{\text{noise}}$.

As long as the pixel noise of the detector is uncorrelated, the noise matrix can be assumed to be diagonal, i.e. shape noise is neither correlated between different pixels $\mathbf{n}_i, \mathbf{n}_j$ and shear components γ_a, γ_b , nor between different redshift bins z_μ, z_ν :

$$\mathbf{C}^{\text{noise}} = \frac{\sigma_e^2}{N_{i\mu}} \delta_{ij} \delta_{ab} \delta_{\mu\nu}, \quad (5.9)$$

where σ_e denotes the root-mean-square intrinsic ellipticity per ellipticity component for all the galaxies and $N_{i\mu}$ is the effective number of galaxies per pixel i in redshift bin z_μ .⁷

As noted above we approximate the angular power spectra $C_{\mu\nu}^\vartheta(\ell)$ with piecewise constant band powers $\mathcal{B}_{\zeta\vartheta\beta}(\ell)$ of type $\vartheta \in (\text{EE}, \text{BB}, \text{EB})$ that span a range of multipoles ℓ within the band β . Note that the index ζ runs only over *unique* redshift bin correlations: for n_z redshift bins there are only $n_z(n_z + 1)/2$ unique correlations because $z_\mu \times z_\nu = z_\nu \times z_\mu$. Hence, the components of the cosmic signal covariance matrix can be decomposed into a linear combination of these band powers:

$$\mathbf{C}_{(\mu\nu)(ab)(ij)}^{\text{sig}} = \sum_{\zeta, \vartheta, \beta} \mathcal{B}_{\zeta\vartheta\beta} M_{\zeta(\mu\nu)} \int_{\ell \in \beta} \frac{d\ell}{2(\ell + 1)} \left[w_0(\ell) I_{(ab)(ij)}^\vartheta + \frac{1}{2} w_4(\ell) Q_{(ab)(ij)}^\vartheta \right]. \quad (5.10)$$

The geometry of the shear field, including its Fourier-space decomposition and masks, is encoded in the above expression written in square brackets. The matrices \mathbf{M}_ζ are required for mapping the redshift-bin indices μ, ν to the unique correlations ζ possible between those. Explicit expressions for these matrices and the matrices \mathbf{I}^ϑ and \mathbf{Q}^ϑ can be found in Appendix 4.A.

In order to find the best-fitting band powers $\mathcal{B}_{\zeta\vartheta\beta}$ and the cosmic signal \mathbf{C}^{sig} that describes the measured shear data the best, we employ a Newton–Raphson optimization. The algorithm finds the root of $d\mathcal{L}/d\mathcal{B}_A = 0$ (Bond et al. 1998; Seljak 1998), i.e. its maximum-likelihood solution, by iteratively stepping through the expression $\mathcal{B}_{i+1} = \mathcal{B}_i + \delta\mathcal{B}$ in which $\delta\mathcal{B}$ is calculated in each step as

$$\delta\mathcal{B}_A \propto \sum_B \frac{1}{2} (\mathbf{F}^{-1})_{AB} \text{Tr}[(\mathbf{d}\mathbf{d}^T - \mathbf{C})(\mathbf{C}^{-1} \mathbf{D}_A \mathbf{C}^{-1})]. \quad (5.11)$$

⁷The effective number of galaxies per pixel can be calculated using equation (5.17) multiplied by the area of the pixel Ω .

In the following we simplify our notation by introducing the superindex A for a particular combination of indices $(\zeta\vartheta\beta)$. The matrices \mathbf{D}_A are derivatives of the full covariance matrix with respect to any band-power combination. A rigorous definition of \mathbf{D}_A can again be found in Appendix 4.A. The elements of the Fisher matrix \mathbf{F} can be calculated as

$$F_{AB} = \frac{1}{2} \text{Tr}(\mathbf{C}^{-1} \mathbf{D}_A \mathbf{C}^{-1} \mathbf{D}_B). \quad (5.12)$$

An important point for the subsequent cosmological analysis is the estimation of the band-power covariance. The inverse of the Fisher matrix was used in previous work (cf. [Hu & White 2001](#); [Lin et al. 2012](#)) as an approximation of the true covariance. This, however, holds only in the Gaussian limit. In this analysis we use a covariance matrix based on an analytical calculation, which is discussed in more detail in Section 5.6.

For that calculation, but also for a proper comparison of theory to data in the subsequent cosmological analysis, we also have to take into account that each measured band power $\mathcal{B}_A = \mathcal{B}_{\zeta\vartheta\beta}$ samples the corresponding power spectrum with its own window function. For a general estimator we can relate the expectation value of the measured band power, $\langle \mathcal{B}_{\zeta\vartheta\beta} \rangle$, to the power spectrum at integer multipole through the band-power window function $W_{A(\zeta\vartheta)}(\ell)$ (cf. [Knox 1999](#); [Lin et al. 2012](#)), i.e.

$$\langle \mathcal{B}_{\zeta\vartheta\beta} \rangle = \sum_{\ell} W_{(\zeta\vartheta\beta)(\zeta\vartheta)}(\ell) \mathcal{B}_{\zeta\vartheta}(\ell), \quad (5.13)$$

where $W_{(\zeta\vartheta\beta)(\zeta\vartheta)}(\ell)$ denotes the elements of the block diagonal of $W_{A(\zeta\vartheta)}(\ell)$ (A is again a superindex for single indices over the band types, unique redshift correlations and bands). The sum is calculated for integer multipoles ℓ in the range $10 \leq \ell \leq 3000$ since the cosmological analysis is intended to use multipoles in the range $76 \leq \ell \leq 2300$ (cf. Section 5.4). Therefore, the lowest multipole for the summation should extend slightly below $\ell_{\text{field}} = 76$ and the highest multipole should include multipoles beyond $\ell = 2300$ in order to capture the full behaviour of the band window function below and above the lowest and highest bands, respectively.

The elements of the window function matrix can be derived as (cf. [Lin et al. 2012](#))

$$W_{A(\zeta\vartheta)}(\ell) = \sum_B \frac{1}{2} (\mathbf{F}^{-1})_{AB} T_{B(\zeta\vartheta)}(\ell), \quad (5.14)$$

where \mathbf{F}^{-1} denotes the inverse of the Fisher matrix (cf. equation 5.12). The trace matrix \mathbf{T} is defined as

$$T_{A(\zeta\vartheta)}(\ell) = \text{Tr}[\mathbf{C}^{-1} \mathbf{D}_A \mathbf{C}^{-1} \mathbf{D}_{\zeta\vartheta}(\ell)]. \quad (5.15)$$

The derivative $\mathbf{D}_{\zeta\vartheta}(\ell)$ denotes the derivative of the full covariance \mathbf{C} with respect to the power at a single multipole ℓ (per band type ϑ and unique redshift correlation ζ). We write it out explicitly in Appendix 5.A (cf. equation 5.32).⁸

5.4 KiDS-450 measurements

In the following analysis we use the KiDS-450 dataset and only provide a concise summary of it here. For full details we refer the reader to [Hildebrandt et al. \(2016\)](#) and references therein.

⁸Note that the definition of $\mathbf{D}_{\zeta\vartheta}(\ell)$ has changed with respect to the one presented in [Chapter 4](#). This is due to the fact that in the previous analysis we only needed the EE to EE part of the band window matrix for convolving the cosmological signal prediction with it. The approach of an analytical covariance, however, requires us to calculate the full band window matrix with all possible cross-terms, which is now fully accounted for by the new notation presented here in this paper.

KiDS is an ongoing ESO optical survey which will eventually cover 1500 deg^2 in four bands (u , g , r , and i). It is carried out using the OmegaCAM CCD mosaic camera mounted at the Cassegrain focus of the VLT Survey Telescope (VST). The combination of camera and telescope was specifically designed for weak-lensing studies and hence results in small camera shear and an almost round and well-behaved point spread function (PSF). The data processing pipeline from individual exposures in multiple colours to photometric redshift estimates employs the ASTRO-WISE system (Valentijn et al. 2007; Begeman et al. 2013). For the lensing-specific data reduction of the r -band images THELI (Erben et al. 2005, 2009, 2013; Schirmer 2013) is used. Finally, the galaxy shapes are measured from the THELI-processed data with a new version of *lensfit* described in Fenech Conti et al. (2016). The full description of the pipeline for previous data releases of KiDS (DR1/2) is documented in de Jong et al. (2015) and Kuijken et al. (2015). All subsequent improvements applied to the data processing for KiDS-450 are summarized in Hildebrandt et al. (2016). The *lensfit*-specific updates including a description of the extensive image simulations for shear calibrations at the sub-percent level are documented in Fenech Conti et al. (2016).

The interpretation of the cosmic shear signal also requires accurate and precise redshift distributions, $n(z)$ (cf. equation 5.6). For the estimation of photometric redshifts the code BPZ (Benítez 2000) is used following the description in Hildebrandt et al. (2012). In previous KiDS and CFHTLenS analyses the stacked $n(z)$ based on the redshift probability distributions of individual galaxies, $P(z)$, as estimated by BPZ was used for that purpose. However, the output of photometric redshift estimation codes such as BPZ is biased at a level that is intolerable for current and especially future cosmic shear studies (cf. Newman et al. 2015; Choi et al. 2015 for a discussion).

Therefore, Hildebrandt et al. (2016) employ a weighted direct calibration (‘DIR’) of photometric redshifts with spectroscopic redshifts. This calibration method employs several spectroscopic redshift catalogues from surveys overlapping with KiDS, which are described in detail in Hildebrandt et al. (2016). In practice, spectroscopic redshift catalogues are neither complete nor a representative sub-sample of the photometric redshift catalogues currently used in cosmic shear studies. In order to alleviate these practical shortcomings the photometric redshift distributions and the spectroscopic redshift distributions are re-weighted in a multi-dimensional magnitude space, so that the volume density of objects in this magnitude space matches between photometric and spectroscopic catalogues (Lima et al. 2008). The direct calibration is further cross-checked with two additional methods and found to yield robust and precise estimates of the photometric redshift distribution of the galaxy source sample (cf. Hildebrandt et al. 2016 for details).

The fiducial KiDS-450 dataset consists of 454 individual $\approx 1 \text{ deg}^2$ tiles (cf. fig. 1 from Hildebrandt et al. 2016). The median seeing is 0.66 arcsec and no r -band image has a seeing larger than 0.96 arcsec. Since the observations prioritized increasing the overlap with the spectroscopic GAMA survey (Driver et al. 2011) the tiles are grouped into five patches (and corresponding catalogues) covering an area of $\approx 450 \text{ deg}^2$ in total. Due to stellar haloes or artefacts in the images the total area of KiDS-450 is reduced to an effective area usable for lensing of about 360 deg^2 . Since the catalogue for an individual KiDS patch does not only consist of one contiguous (GAMA) field but also contains long stripes (e.g. 1 deg by several degrees) or individual tiles due to the pointing strategy, we exclude these disconnected tiles from our analysis, which amounts to a reduction in effective area by $\approx 36 \text{ deg}^2$ compared to Hildebrandt et al. (2016). Moreover, the individual patches are quite large resulting in long run-times for the signal extraction. Therefore, we split each individual KiDS patch further into two or three subpatches yielding 13 subpatches in total with an effective area of 323.9 deg^2 . Each subpatch contains a comparable number of individual tiles and the splitting into subpatches was

performed along borders that do not split individual tiles, because a single tile represents the smallest data unit for systematic checks and further quality control tests.

The coordinates in the catalogues are given in a spherical coordinate system measured in right ascension α and declination δ . Before we pixelize each subpatch into shear pixels, we first deproject the spherical coordinates into flat coordinates using a tangential plane projection (also known as gnomonic projection). The central point for the projection of each subpatch, i.e. its tangent point, is calculated as the intersection point of the two great circles spanned by the coordinates of the edges of the subpatch.

The shear components g_a per pixel at position $\mathbf{n} = (x_c, y_c)$ are estimated from the ellipticity components e_a inside that pixel:

$$g_a(x_c, y_c) = \frac{\sum_i w_i e_{a,i}}{\sum_i w_i}, \quad (5.16)$$

where the index a labels the two shear and ellipticity components, respectively, and the index i runs over all objects inside the pixel. The ellipticity components e_a and the corresponding weights w are computed during the shape measurement with *lensfit* and they account both for the intrinsic shape noise and measurement errors.

For the position of the average shear we take the centre of the pixel (hence the subscript ‘c’ in the coordinates). Considering the general width of our multipole band powers it is justified to assume that the galaxies are uniformly distributed in each shear pixel. Finally, we define distances $r_{ij} = |\mathbf{n}_i - \mathbf{n}_j|$ and angles $\varphi = \arctan(\Delta y/\Delta x)$ between shear pixels i, j which enter in the quadratic estimator algorithm (cf. Section 5.3).

The lowest scale of the multipole band powers that we extract is in general set by the largest separation θ_{\max} possible between two shear pixels in each subpatch. In a square-field that would correspond to the diagonal separation of the pixels in the corners of the patch. However, this would yield only two independent realizations of the corresponding multipole ℓ_{\min} . Hence, defining the lowest physical multipole ℓ_{field} as corresponding to the distance between two pixels on opposite sides of the patch ensures that there exist many independent realizations of that multipole so that a measurement thereof is statistically meaningful. In general, the subpatches used in this analysis are not square but rectangular and hence we follow the conservative approach of defining ℓ_{field} corresponding to the shorter side length of the rectangle. Choosing then the shortest side length among all 13 subpatches yields $\ell_{\text{field}} = 76$ corresponding to a distance $\theta \approx 4^\circ.74$. The lowest multipole over all subpatches is $\ell_{\min} = 34$ corresponding to a distance $\theta \approx 10^\circ.5$ but we set the lower border of the first band power even lower to $\ell = 10$. That is because the quadratic estimator approach allows us to account for any leftover DC offset, i.e. a non-zero mean amplitude, in the signal by including even lower multipoles than ℓ_{\min} in the first band power (cf. Section 5.5). The highest multipole ℓ_{\max} available for the data analysis is set by the side length of the shear pixels. The total number of shear pixels in the analysis is also a critical parameter for the run-time of the algorithm because it sets together with the number of unique redshift correlations and the duality of the shear components the dimensionality of the fundamental covariance matrix (cf. equation 5.3). Moreover, Gaussianity is one of the assumptions behind the quadratic estimator which naturally limits the highest multipole to the mildly non-linear regime (cf. [Hu & White 2001](#)). Hence, we set $\sigma_{\text{pix}} = 0.14$ corresponding to a maximum multipole $\ell_{\text{pix}} = 2571$. However, the borders of the last band should extend to at least $2\ell_{\text{pix}} \approx 5150$ due to the increasingly oscillatory behaviour of the pixel window function (cf. equation 5.2) close to and beyond ℓ_{pix} . The width of all intermediate bands should be at least $2\ell_{\text{field}}$ in order to minimize the correlations between them (cf. [Hu & White 2001](#)). Given all these constraints we extract in total seven E-mode band powers over the range $10 \leq \ell \leq 5150$. However, for the

Table 5.1: Band-power intervals.

Band No.	ℓ -range	θ -range	Comments
1	10–75	2160.0–288.0 arcmin	(a), (b)
2	76–220	284.2–98.2 arcmin	–
3	221–420	98.0–51.4 arcmin	–
4	421–670	51.3–32.2 arcmin	–
5	671–1310	32.2–16.5 arcmin	–
6	1311–2300	16.5–9.4 arcmin	(a)
7	2301–5150	9.4–4.2 arcmin	(a)

Notes. (a) Not used in cosmological analysis. (b) No B-mode extracted.

The θ -ranges are just an indication and cannot be compared directly to θ -ranges used in real-space correlation function analyses due to the non-trivial functional dependence of these analyses on Bessel functions (cf. Section 5.7.1).

Table 5.2: Properties of the galaxy source sample.

redshift bin	z_{median}	N	n_{eff}	σ_e
$z_1: 0.10 < z_B \leq 0.45$	0.41	5 923 897	3.63 arcmin ⁻²	0.2895
$z_2: 0.45 < z_B \leq 0.90$	0.70	6 603 721	3.89 arcmin ⁻²	0.2848

Notes. The median redshift z_{median} , the total number of objects N , the effective number density of galaxies n_{eff} (cf. equation 5.17), and the dispersion of the intrinsic ellipticity distribution σ_e per redshift bin for the KiDS-450 dataset used in our analysis.

cosmological analysis we will drop the first and last band powers due to their potential noise-contamination which reduces the physical multipole range to $76 \leq \ell \leq 2300$. In addition to the E-modes we extract six B-mode band powers. Their multipole ranges coincide with the ranges of the E-mode bands 2–7 (due to the expected strong signal in the first E-mode band power a potential B-mode contamination is negligible). All ranges are summarized in Table 5.1 where we also indicate the corresponding angular scales. Note, however, that the naïve conversion from multipole to angular scales is insufficient for a proper comparison to correlation function results. An outline of how to compare both approaches properly is given in Section 5.7.1.

We calculate the effective number density of galaxies used in the lensing analysis following Heymans et al. (2012) as

$$n_{\text{eff}} = \frac{1}{\Omega} \frac{(\sum_i w_i)^2}{\sum_i w_i^2}, \quad (5.17)$$

where w is the *lensfit* weight and the unmasked area is denoted as Ω . In Table 5.2 we list the effective number densities per KiDS patch and redshift bin. Note that there exist also alternative definitions for n_{eff} but the one used here has the practical advantage that it can be used directly to set the source number density in the creation of mock data.

In order to compare results later on to Hildebrandt et al. (2016) we only use sources in the range $0.10 < z_B \leq 0.90$, where z_B is the Bayesian point estimate of the photometric redshifts.

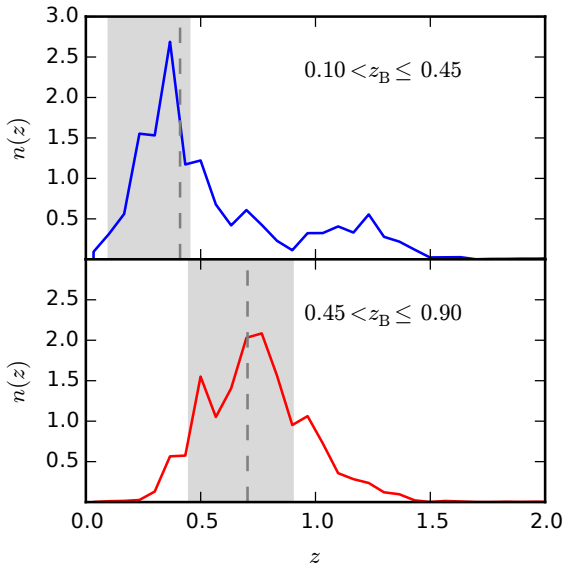


Figure 5.1: The normalized redshift distributions for the two tomographic bins employed in this study and estimated from the weighted direct calibration scheme (‘DIR’) presented in Hildebrandt et al. (2016). The dashed (grey) vertical lines mark the median redshift per bin (cf. Table 5.2) and the (grey) shaded regions indicate the target redshift selection by cutting on the Bayesian point estimate for photometric redshifts z_B .

We divide this range further into two broad tomographic bins z_1 : $0.10 < z_B \leq 0.45$ and z_2 : $0.45 < z_B \leq 0.90$ with similar effective number densities (cf. Table 5.2 and Fig. 5.1). Note that z_B is only used as a convenient quantity to define tomographic bins but does not enter anywhere else in the analysis. The limitation to only two redshift bins is due to run-time since the dimension of the fundamental covariance matrix (cf. equation 5.3) depends very strongly on the number of unique redshift correlations as noted already earlier.

5.5 Multiplicative bias correction and sensitivity to large-scale additive bias

The observed shear γ_{obs} , measured as a weighted average of galaxy ellipticities, is generally a biased estimator of the true shear γ . The bias is commonly parametrized as (Heymans et al. 2006)

$$\gamma_{\text{obs}} = (1 + m)\gamma + c, \quad (5.18)$$

where m and c refer to the multiplicative bias and additive bias, respectively.

The multiplicative bias is mainly caused by the effect of pixel noise in the measurements of galaxy ellipticities (Melchior & Viola 2012; Refregier et al. 2012; Miller et al. 2013), but it can also arise if the model used to describe the galaxy profile is incorrect, or if stars are misclassified as galaxies. The latter two effects are generally subdominant compared to the noise bias. We quantify the amplitude of the multiplicative bias in the KiDS data by means of a dedicated suite of image simulations (Fenech Conti et al. 2016). We closely follow the

procedure described in Hildebrandt et al. (2016) and we derive a multiplicative correction for each tomographic bin, i.e. $m_{z_1}^{\text{fid}} = -0.013 \pm 0.010$ and $m_{z_2}^{\text{fid}} = -0.012 \pm 0.010$. The errorbars account both for statistical uncertainties and systematic errors due to small differences between data and simulations. In our likelihood analysis we apply the multiplicative correction to the measured shear power spectrum and in order to marginalize over the uncertainties on the m -correction we propagate them into the likelihood analysis. As the errors on the $m_{z_i}^{\text{fid}}$ are fully correlated (Hildebrandt et al. 2016) we only need to include one free nuisance parameter. We vary m_{z_1} very conservatively within a 2σ tophat prior centred on its fiducial value in each step i of the likelihood estimation. The value for m_{z_2} is then fixed through the relation $m_{z_2}^i = m_{z_2}^{\text{fid}} + \Delta m^i$ with $\Delta m^i = m_{z_1}^i - m_{z_1}^{\text{fid}}$.

Additive biases are mainly caused by a residual PSF ellipticity in the shape of galaxies (e.g. Hoekstra 2004; van Uitert & Schneider 2016). More generally, any effect causing a preferential alignment of shapes in the galaxy source sample will create an additive bias. For example, in an early stage of the KiDS-450 data processing a small fraction of asteroids ended up in the galaxy source sample. This resulted in strongly aligned shape measurements with very high signal-to-noise causing a substantial c -term (cf. appendix D4 in Hildebrandt et al. 2016). This example also demonstrates that a potential c -term correction can only be derived empirically from the data: it is impossible to include every source for an additive bias in image simulations.

Here we demonstrate how the quadratic estimator can naturally deal with a residual additive shear in the data. This is a clear advantage over correlation function measurements, where the residual additive shear needs to be properly quantified and subtracted from the data, usually hampering the ability of measuring the cosmic shear signal at large angular separations.

If sufficiently low multipoles are included in the extraction of the first multipole band of the shear power spectrum band powers, this band accounts for any residual DC offset in the data such as the effect of a global c -term. For a clean demonstration of this feature, we employ Gaussian random fields (GRFs) with realistic CFHTLenS survey properties (e.g. masking, noise level; cf. Chapter 4 for details). The GRFs were readily available and for this demonstration the differences in survey properties are negligible. We extract E- and B-modes simultaneously from four GRFs that match the W1, W2, W3, and W4 fields from CFHTLenS in size and shape. The measurements are performed in two broad redshift bins but we use the same multipole binning and shear pixel size σ_{pix} as used in the analysis of the KiDS-450 data (cf. Table 5.1). In a first step we extract a reference signal from the GRFs to which no additional global c -term was added. In a second step we apply a global additive term of $c = 2 \times 10^{-3}$ to both ellipticity components and re-extract the shear power spectra. In Fig. 5.2 we show the residuals between these two signals for all tomographic and multipole bins. As expected, only the first multipole bin is affected substantially by the global c -term, but all remaining bands are essentially unaffected. Hence, removing the first multipole bin from a subsequent cosmological analysis replaces a sophisticated global c -correction at reasonable computational costs.

5.6 Covariance

An important ingredient for an accurate and precise inference of cosmological parameters from the measured band powers is the covariance matrix. There are several approaches to estimate the covariance matrix: the brute-force approach of extracting it directly from a statistically significant number (to reduce numerical noise) of mock catalogues, an analytical calculation or, as a special feature of the quadratic estimator, the inverse of the Fisher matrix. Of course, each method has its specific advantages and disadvantages. The brute-force ap-

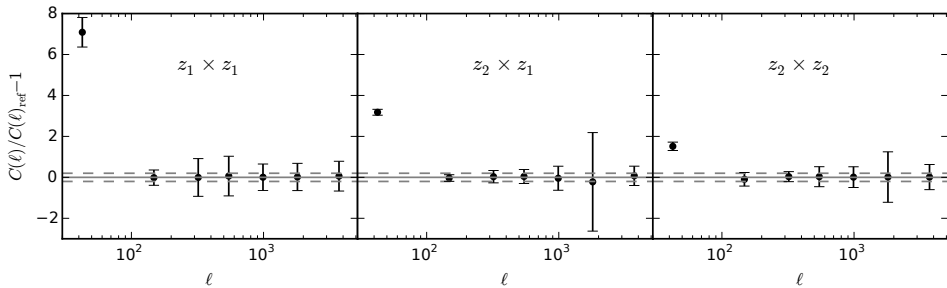


Figure 5.2: The residuals between a shear power spectrum extracted from reference Gaussian random fields (GRFs) and the one extracted from GRFs where a global c -term of $c = 2 \times 10^{-3}$ was applied to both ellipticity components. From left to right the unique correlations of the two redshift bins are shown. The GRFs were created to match the four fields of CFHTLenS in area, shape, noise properties, and redshift range (i.e. z_1 : $0.50 < z_B \leq 0.85$ and z_2 : $0.85 < z_B \leq 1.30$). The signal extraction, however, employs the multipole binning that is also used in the subsequent KiDS data analysis and extends to multipoles significantly below the one set by the field size. The globally applied c -term only affects the band power estimate of the first multipole bin but has no effect on the remaining bands. Hence, removing the first band power from a subsequent cosmological analysis is sufficient to account for a leftover global c -term in the data. The 1σ errorbars are based on the Fisher matrices and the horizontal dashed (grey) lines indicate ± 20 per cent margins.

proach requires significant amounts of additional run-time, both for the creation of the mocks and the signal extraction. This can become a severe issue especially if the signal extraction is also computationally demanding, as is the case for the (tomographic) quadratic estimator. Moreover, if the mocks are based on N -body simulations the particle resolution and box size of these set fundamental limits for the scales that are available for a covariance estimation and to which level of accuracy and precision that is possible. In contrast, the Fisher matrix is computationally the cheapest estimate of a covariance matrix since it comes at no additional computational costs. However, it is only an accurate representation of the true covariance in the Gaussian limit and hence the errors for the non-linear scales will be underestimated. Moreover, the largest scale for a Fisher matrix based covariance is limited to the size of the patch. Therefore, the errors for scales corresponding to the patch size will also be underestimated. A possible solution to the shortcomings of the previous two approaches is the calculation of an analytical covariance matrix. This approach is computationally much less demanding than the brute-force approach and does not suffer from the scale-dependent limitations of the previous two approaches. Moreover, the non-Gaussian contributions at small scales can also be properly calculated. Hence, we follow the fiducial approach of [Hildebrandt et al. \(2016\)](#) and adopt their method for computing the analytical covariance (except for the final integration to correlation functions). The model for the analytical covariance consists of the following three components:

- (i) a disconnected part that includes the Gaussian contribution to shape-noise, sample variance, and a mixed noise-sample variance term,
- (ii) a non-Gaussian contribution from in-survey modes originating from the connected matter-trispectrum, and
- (iii) a contribution from the coupling of in-survey and super-survey modes.

All cosmology dependent calculations employ a *WMAP9* cosmology ([Hinshaw et al. 2013](#)) and a detailed description of the full model will be presented in [Joachimi et al.](#) (in prepara-

tion).

We calculate the analytical covariance matrix $\mathbf{C}_{(\zeta\vartheta)(\gamma\phi)}(\ell, \ell')$ at integer multipoles ℓ, ℓ' over the range $10 \leq \ell, \ell' \leq 3000$ ⁹ where the index pairs ζ, γ and ϑ, ϕ label the unique redshift correlations and band types (EE and BB), respectively. Note that the EE to BB and vice versa the BB to EE part of this matrix is zero, i.e. there is no power leakage for an ideal estimator. Finally, we create the analytical covariance matrix of the measured band powers by convolving $\mathbf{C}_{(\zeta\vartheta)(\gamma\phi)}(\ell, \ell')$ with the full band window matrix:

$$\mathbf{C}_{AB} = \widetilde{\mathbf{W}}_{A\zeta\vartheta}(\ell) \mathbf{C}_{(\zeta\vartheta)(\gamma\phi)}(\ell, \ell') (\widetilde{\mathbf{W}}^T)_{B\gamma\phi}(\ell'), \quad (5.19)$$

where the superindices A, B run over the band powers, their types (i.e. EE and BB), and the unique redshift correlations. $\widetilde{\mathbf{W}}$ is the band window matrix defined in equation (5.14) multiplied with the normalization for band powers, i.e. $\ell(\ell+1)/(2\pi)$. Note that the convolution with the band window matrix propagates all properties of the quadratic estimator into the band power covariance.

5.7 The KiDS-450 shear power spectrum

For each of the 13 subpatches of the five KiDS fields we extract the weak-lensing power spectrum in band powers spanning the multipole range $10 \leq \ell \leq 5150$ (cf. Section 5.4 and Table 5.1). The measurement is performed in two redshift bins in the ranges $z_1: 0.10 < z \leq 0.45$ and $z_2: 0.45 < z \leq 0.90$ (cf. Table 5.2). This yields in total two auto-correlation spectra and one unique cross-correlation spectrum per subpatch. In the subsequent analysis we combine all spectra by weighting each spectrum with the effective area of the subpatch. This weighting is optimal in the sense that the effective area is proportional to the number of galaxy pairs per patch and the number of pairs sets the shape-noise variance of the measurements. We present the resulting seven E-mode band powers in Fig. 5.3. The errors on the signal are estimated from the analytical covariance (cf. Section 5.6), which includes contributions from shape noise, cosmic variance, and super-sample variance. The extension along the multipole axis indicates the width of the band. The signal is plotted at the naïve centre of the band whereas for the subsequent likelihood analysis we take the window functions of the bands into account (cf. equation 5.13). Only the bands between the (grey) shaded areas enter in the cosmological analysis. We exclude the first band as it contains by construction multipoles that extend below the lowest physical multipole (i.e. $\ell_{\text{field}} \approx 76$) in order to account for any remaining DC offset in the data (such as an additive global c -term, cf. Section 5.5). The last band at the highest multipoles is also excluded as it is designed to sum up the oscillating part of the pixel window function at high multipoles.

We simultaneously extract E- and B-modes. As noted in Section 5.2 the cosmological signal is contained entirely in the E-modes in the absence of systematics. Hence, the B-mode signal is used as a test for residual systematics in the data. We show the effective area weighted six B-mode band powers in Fig. 5.4. The B-mode errors are derived from the B-mode part of the inverse Fisher matrix as described in **Chapter 4**. We do not use the B-mode errors derived from the analytical covariance since they currently do not account for survey-boundary effects and therefore are underestimated.

In order to use the B-mode band powers as an independent test for residual systematics, we have to confirm that there is no significant leakage of power from E-modes to B-modes.

⁹This range is matching the range over which we later perform the summation when we convolve the theoretical signal predictions with the band window functions.

From a previous analysis (Lin et al. 2012) we do not expect the quadratic estimator to induce power leakage from E- to B-modes. However, if the shape noise is misestimated we might expect some power leakage for the highest multipole band powers. We investigate this using the band window functions derived from the full band window function matrix (cf. equation 5.14), which is also computed as an average over all subpatches with effective area weights. In Fig. 5.5 we show (red points) the convolution of a fiducial cosmological E-mode signal (employing the same *WMAP9* cosmology used for the calculation of the analytical covariance) for the low-redshift auto-correlation with the corresponding band window functions of all possible cross-terms (e.g. EE, $z_1 \times z_1$ to BB, $z_2 \times z_2$). The fiducial E-mode signal is plotted as the solid black line and the errorbars are derived from the analytical covariance. Additionally, we show a second set of errorbars in grey. These indicate the amplitude of the Fisher matrix based B-mode errors. We expect the signal to appear only in the leftmost panel depicting the auto-contribution (i.e. from EE, $z_1 \times z_1$ to EE, $z_1 \times z_1$). Indeed, the cross-term contributions are order(s) of magnitude lower than the E-mode band powers and well within the statistical B-mode errors. Hence, there is no significant power leakage from E- to B-modes which would introduce a detectable spurious B-mode signal.

Hence, the significance of the measured B-modes can now be used to assess whether or not there are residual systematics in the data. Qualitatively this is shown in Fig. 5.4. We test the hypothesis that the B-modes in the first five bands are consistent with zero by means of a χ^2 -goodness-of-fit measure. This yields a reduced χ^2 of $\chi^2_{\text{red}} = 1.06$ for 14 degrees of freedom. We conclude that the B-modes are consistent with zero over the multipole range used in the cosmological analysis.

In passing we note that Fig. 5.5 shows that the estimates of the fiducial E-mode power spectrum with the band window functions for bands 6 and 7 are biased low and high, respectively. This is visible in the auto-contribution (EE, $z_1 \times z_1$) to (EE, $z_1 \times z_1$), i.e. the leftmost panel. Therefore, we decide to conservatively remove band 6 from the subsequent cosmological analysis, which reduces the available multipole range to $76 \leq \ell \leq 1310$.

5.7.1 Qualitative comparison to correlation functions

Most cosmic shear studies to date employ real-space correlation functions (e.g. Heymans et al. 2013; Becker et al. 2015; Hildebrandt et al. 2016) because they are conceptually easy and fast to compute. In contrast to direct power spectrum estimates, correlation functions measured at a given angular separation sum up contributions over a wide range of multipoles. Due to this mode-mixing it is non-trivial to compare angular scales to multipole ranges, as well as to cleanly separate linear and non-linear scales.

As an example we qualitatively compare here correlation function measurements based on the angular scales presented in Hildebrandt et al. (2016) to the direct power spectrum measurements employing the quadratic estimator. For that purpose we calculate a fiducial shear power spectrum (cf. equation 5.5) employing a *Planck* cosmology (Planck Collaboration XIII 2015a) and the redshift distributions derived for our two tomographic bins. A correlation-function based estimator such as ξ_{\pm} is related to the shear power spectrum $C_{\mu\nu}(\ell)$ through

$$\xi_{\pm}^{\mu,\nu}(\theta) = \frac{1}{2\pi} \int d\ell \ell C_{\mu\nu}(\ell) J_{0,4}(\ell\theta) \equiv \int d\ell I_{\xi_{\pm}}(\ell\theta), \quad (5.20)$$

where θ is the angular distance between pairs of galaxies and $J_{0,4}$ is the zeroth- (for ξ_+) or fourth-order (for ξ_-) Bessel function of the first kind. In contrast, the quadratic estimator (QE) convolves the theoretical shear power spectrum with its band window matrix $W_A(\ell)$ (cf.

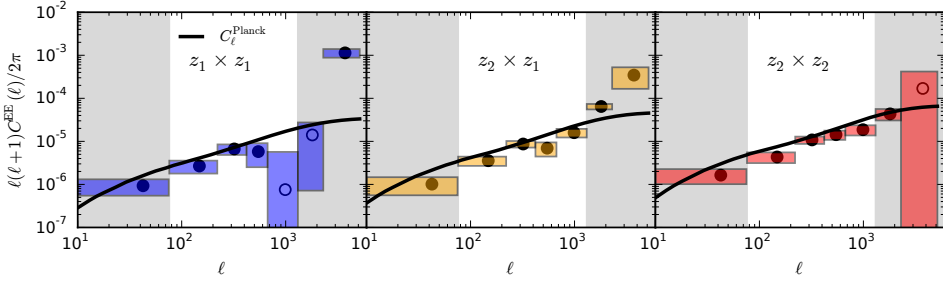


Figure 5.3: Measured E-mode band powers in tomographic bins averaged with the effective area per patch over all 13 KiDS-450 subpatches. From left to right we show the auto-correlation signal of the low-redshift bin (blue), the cross-correlation signal between the low and the high-redshift bin (orange), and the auto-correlation signal of the high-redshift bin (red). Note that negative band powers are shown at their absolute value with an open symbol. The low-redshift bin contains objects with redshifts in the range $0.10 < z_1 \leq 0.45$ and the high-redshift bin covers a range $0.45 < z_2 \leq 0.90$. The 1σ -errors in the signal are derived from the analytical covariance convolved with the averaged band window matrix (cf. Section 5.6) whereas the extension in ℓ -direction is the width of the band. Band powers in the shaded regions (grey) to the left and right of each panel are excluded from the cosmological analysis (see text for details). The solid line (black) shows the power spectrum for the cosmological model from (Planck Collaboration XIII 2015a). Note, however, that the band powers are centred at the naïve ℓ -bin centre and thus the convolution with the band window function is not taken into account in this plot, in contrast to the cosmological analysis.

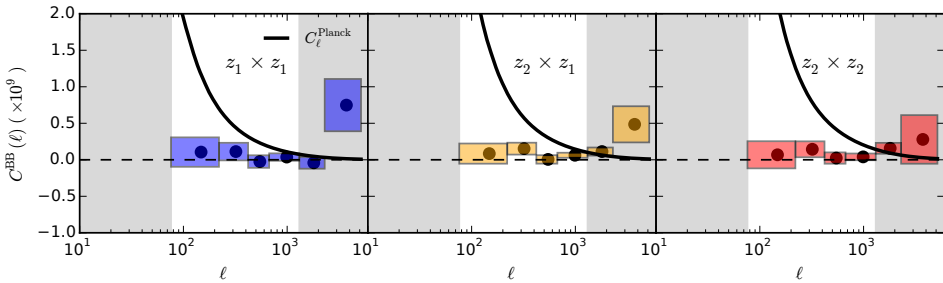


Figure 5.4: Same as Fig. 5.3 but for B-mode band powers. Note, however, the different scale (linear) and normalization used here with respect to Fig. 5.3; for reference we also plot a (Planck Collaboration XIII 2015a) based E-mode power spectrum as solid line (black). We show the measured B-modes as (black) dots with 1σ -errors derived from the averaged shape-noise contribution to the analytical covariance convolved with the B-mode part of the averaged band window matrix.

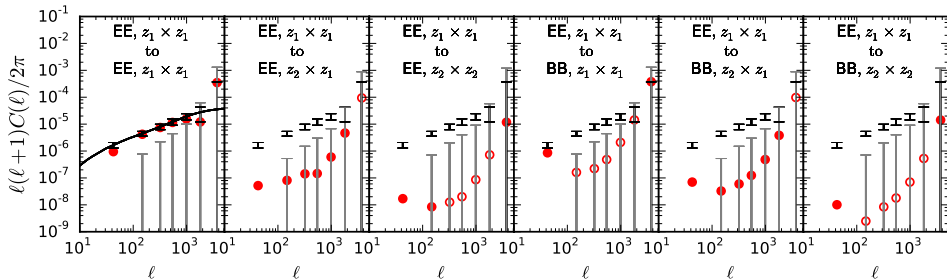


Figure 5.5: The contribution of a fiducial cosmological E-mode signal (solid, black line) for the low-redshift auto-correlation (i.e. $z_1 \times z_1$) convolved with the corresponding band window functions (red points) of all possible cross-combinations. The first panel from the left depicts the auto-contribution from (EE, $z_1 \times z_1$) to (EE, $z_1 \times z_1$). The grey errorbars show the statistical uncertainties associated with the B-modes. Open symbols denote negative values plotted at their absolute value. The corresponding plots for the remaining (EE, $z_2 \times z_1$) and (EE, $z_2 \times z_2$) cross-combinations are shown in Appendix 5.B.

equation 5.14):

$$\mathcal{B}_A = \sum_{\ell} \frac{\ell(\ell+1)}{2\pi} W_A(\ell) C_A(\ell) \equiv \sum_{\ell} I_{QE}(\ell), \quad (5.21)$$

where the superindex A runs again over all multipole bands and unique redshift correlations. The convolved power spectra as a function of multipoles defined at the right-hand sides of both equations are shown in Fig. 5.6 for the lowest redshift bin. In the upper panel we indicate the borders of the bands used in our cosmological analysis (grey dashed lines; cf. Table 5.1). In the two bottom panels we show the lower and upper limits of our power spectrum analysis. For the calculation of $I_{\xi_{\pm}}(\ell\theta)$ we use the central values of the θ_{\pm} -intervals from the cosmic shear analysis of Hildebrandt et al. (2016). Fig. 5.6 shows that the ξ_+ -measurements are highly correlated and anchored at very low multipoles, whereas the ξ_- -measurements show a high degree of mode-mixing. In contrast, the quadratic estimator measurements of the power spectrum are much more cleanly separated and the degree of mode-mixing is much lower. We also note that correlation-function measurements get contributions from lower multipoles than $\ell < 76$ as well as multipoles larger than $\ell > 1310$, which in contrast do not contribute to the signal in our power spectrum analysis. Most of the cosmological information is contained in high multipoles and although the correlation-function measurements extend further into the high multipole regime, the contributions from these scales are non-negligible only for angular scales $\theta < 3$ arcmin. Hence, we do not expect significant differences in the precision of cosmological parameters between both approaches. However, the interpretation of the correlation-function signal at these scales requires accurate knowledge of the non-linear part of the matter power spectrum at high wavenumbers k .

5.8 Cosmological inference

The cosmological interpretation of the measured tomographic band powers \mathcal{B}_{α} derived in Section 5.7 is done in a Bayesian framework. For the estimation of cosmological parameters \mathbf{p} we sample the shear likelihood

$$-2 \ln \mathcal{L}(\mathbf{p}) = \sum_{\alpha, \beta} d_{\alpha}(\mathbf{p})(\mathbf{C}^{-1})_{\alpha\beta} d_{\beta}(\mathbf{p}), \quad (5.22)$$

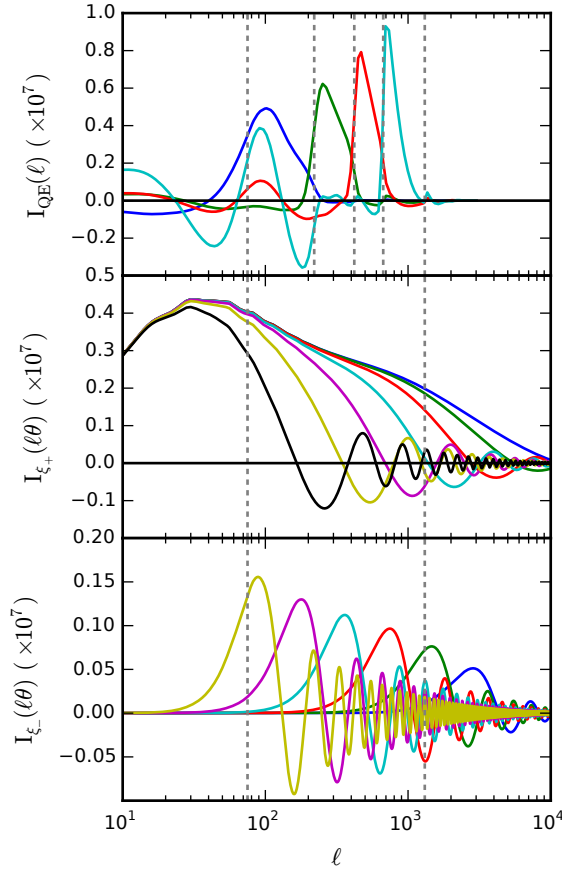


Figure 5.6: Top panel: measurement of a fiducial shear power spectrum using the quadratic estimator (cf. equation 5.21) in five band powers between $76 \leq \ell \leq 1310$. The borders of the bands are indicated by the vertical dashed (grey) lines. Mid panel: measurement of the same fiducial shear power spectrum using the ξ_+ -statistics for correlation functions (cf. equation 5.20) in an angular range $0.7 \text{ arcmin} \leq \theta_+^{\text{cen}} \leq 50 \text{ arcmin}$. Bottom panel: measurements of the same fiducial shear power spectrum using the ξ_- -statistics for correlation functions (cf. equation 5.20) in an angular range $6 \text{ arcmin} \leq \theta_-^{\text{en}} \leq 200 \text{ arcmin}$.

where the indices α, β run over the tomographic bins. The covariance matrix \mathbf{C} is the one calculated in Section 5.6 but employing only its E-mode part. The components of the data vector are calculated as

$$d_\alpha(\mathbf{p}) = (\mathcal{B}_\alpha - \langle \mathcal{B}_\alpha(\mathbf{p}) \rangle^{\text{model}}), \quad (5.23)$$

where the dependence on cosmological parameters enters only in the calculation of the predicted E-mode band powers, $\langle \mathcal{B}^i(\ell) \rangle^{\text{model}}$ (cf. equations 5.13 and 5.5).

In addition to sampling the likelihood for the derivation of cosmological parameter constraints, we also intend to compare various model extensions to a baseline model in terms of the Bayes factor which is based on the evidences of the models. The Bayesian evidence \mathcal{Z} is the normalization of the posterior over the parameters \mathbf{p} (and usually ignored if one is only interested in parameter constraints). In that sense, however, it can also be interpreted as the average of the likelihood over the prior

$$\mathcal{Z} = \int d^n \mathbf{p} \mathcal{L}(\mathbf{p}) \pi(\mathbf{p}), \quad (5.24)$$

where $\pi(\mathbf{p})$ is the prior and n is the dimension of the parameter space. Hence, the Bayesian evidence naturally implements Occam's razor: a simpler theory with fewer parameters, i.e. a more compact parameter space, will result in a higher evidence compared to a theory that requires more parameters, unless the latter explains the data significantly better.

Based on the evidences for models M_1 and M_0 and the a priori probability ratio for the two models, $\text{Pr}(M_1)/\text{Pr}(M_0)$, the Bayes factor is defined as

$$K_{1,0} \equiv \frac{\mathcal{Z}_1 \text{Pr}(M_1)}{\mathcal{Z}_0 \text{Pr}(M_0)}, \quad (5.25)$$

and can be used to make a decision between models M_1 and M_0 because $K_{1,0} > 1$ implies, for example, a preference of model M_1 over model M_0 . Usually, $\text{Pr}(M_1)/\text{Pr}(M_0) = 1$ unless there are strong (physical) reasons to prefer one model over the other *a priori* which is not the case in our subsequent analysis. Furthermore, we will use the classification scheme of Kass & Raftery (1995) for the interpretation of the Bayes factor K (or equivalently $2 \ln K$).

For an efficient evaluation of the high-dimensional integral of equation (5.24) we employ the nested sampling algorithm MULTINEST¹⁰ (Feroz & Hobson 2008; Feroz et al. 2009, 2013). Conveniently, its PYTHON-wrapper PYMULTINEST (Buchner et al. 2014) is included in the framework of the cosmological likelihood sampling package MONTE PYTHON¹¹ (Audren et al. 2013) with which we derive all cosmology-related results in this analysis.

5.8.1 Theoretical power spectrum

The calculation of the tomographic shear power spectrum $C_{\mu\nu}(\ell)$ is described in Section 5.2 and summarized by noting that it is just the projection of the 3D matter power spectrum P_δ along the line-of-sight weighted by lensing weight functions q_μ that take the lensing efficiency of each tomographic bin into account.

For the calculation of the matter power spectrum $P_\delta(k; \chi)$ in equation (5.5) we employ the Boltzmann-code CLASS¹² (Blas et al. 2011; Audren & Lesgourgues 2011). The non-linear corrections are implemented through the HALOFIT algorithm including the recalibration by Takahashi et al. (2012). Additionally, the effects of (massive) neutrinos are also implemented in

¹⁰Version 3.8 from <http://ccpforge.cse.rl.ac.uk/gf/project/multinest/>

¹¹Version 2.2.1 from https://github.com/audren/montepython_public

¹²Version 2.5.0 from https://github.com/lesgourg/class_public

CLASS following [Lesgourgues & Tram \(2011\)](#). Massive neutrinos introduce a redshift- and scale-dependent reduction of power in the matter power spectrum P_δ . However, this reduction of power also propagates into the lensing power spectra $C_{\mu\nu}(\ell)$, though smoothed by the lensing weight functions q_μ . In the multipole range considered in this analysis, we expect massive neutrinos to decrease the lensing power spectrum by an almost constant factor. Hence, the effect of massive neutrinos causes a degeneracy with cosmological parameters affecting the normalization of the lensing power spectrum.

In addition to massive neutrinos, the effect of baryon feedback is another source of a scale-dependent reduction of power, especially in the non-linear regime. Although the full physical description of baryon feedback is not established yet, hydrodynamical simulations offer one route to estimate its effect on the matter power spectrum. In general, the effect is quantified through a bias function with respect to the dark-matter only P_δ (e.g. [Semboloni et al. 2013](#); [Harnois-Déraps et al. 2015](#)):

$$b^2(k, z) \equiv \frac{P_\delta^{\text{mod}}(k, z)}{P_\delta^{\text{ref}}(k, z)}, \quad (5.26)$$

where P_δ^{mod} and P_δ^{ref} denote the power spectra with and without baryon feedback, respectively.

In this work we make use of the results obtained from the Overwhelmingly Large Simulations (OWLS; [Schaye et al. 2010](#), [van Daalen et al. 2011](#)) by implementing the fitting formula for baryon feedback derived in [Harnois-Déraps et al. \(2015\)](#):

$$b^2(k, z) = 1 - A_{\text{bary}}(A_z e^{(B_z x - C_z)^3} - D_z x e^{E_z x}), \quad (5.27)$$

where $x = \log_{10}(k/1 \text{ Mpc}^{-1})$ and the terms A_z , B_z , C_z , D_z , and E_z are functions of the scale factor $a = 1/(1+z)$. These terms also depend on the baryonic feedback model and we refer the reader to [Harnois-Déraps et al. \(2015\)](#) for the specific functional forms and constants. Additionally, we introduce a general free amplitude A_{bary} which we will use as a free parameter to marginalize over while fitting for the cosmological parameters in some models.

We demonstrate the effects of massive neutrinos and baryon feedback on the 3D matter power spectrum and the shear power spectrum (employing the KiDS-450 lensing kernel of our analysis) in Fig. 5.7. Baryon feedback causes a significant reduction of power in the high multipole regime whereas massive neutrinos lower the amplitude of the shear power spectrum over all scales by an almost constant value.

In general, the observed shear power spectrum is a biased tracer of the cosmological convergence power spectrum due to the effect of intrinsic alignments (IA):

$$C_{\mu\nu}^{\text{tot}}(\ell) = C_{\mu\nu}^{\text{GG}}(\ell) + C_{\mu\nu}^{\text{II}}(\ell) + C_{\mu\nu}^{\text{GI}}(\ell), \quad (5.28)$$

where C^{II} is the power spectrum of intrinsic ellipticity correlations between neighbouring galaxies (termed ‘II’) and C^{GI} is the power spectrum of correlations between the intrinsic ellipticities of foreground galaxies and the gravitational shear of background galaxies (termed ‘GI’). For the theoretical description of these effects we follow [Hildebrandt et al. \(2016\)](#) and employ the ‘linear non-linear’ model of intrinsic alignments ([Hirata & Seljak 2004](#); [Bridle & King 2007](#); [Joachimi et al. 2011](#)), so that we can write:

$$C_{\mu\nu}^{\text{II}}(\ell) = \int_0^{\chi_{\text{H}}} d\chi \frac{n_\mu(\chi)n_\nu(\chi)F^2(\chi)}{f_{\text{K}}^2(\chi)} P_\delta \left(k = \frac{\ell}{f_{\text{K}}(\chi)}; \chi \right), \quad (5.29)$$

$$C_{\mu\nu}^{\text{GI}}(\ell) = \int_0^{\chi_{\text{H}}} d\chi \frac{q_\nu(\chi)n_\mu(\chi) + q_\mu(\chi)n_\nu(\chi)}{f_{\text{K}}^2(\chi)} F(\chi) P_\delta \left(k = \frac{\ell}{f_{\text{K}}(\chi)}; \chi \right), \quad (5.30)$$

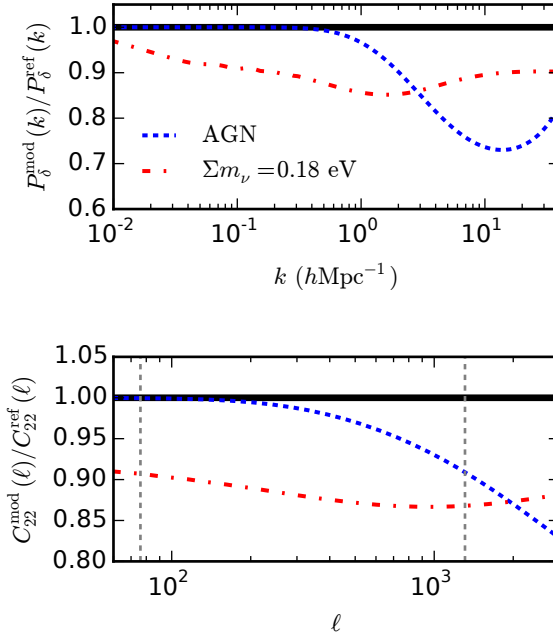


Figure 5.7: Upper panel: the ratio of modified matter power spectra over the dark matter only power spectrum. The dashed line (blue) shows the effect of the baryon feedback bias in the AGN model from OWLS (Schaye et al. 2010; van Daalen et al. 2011) using the implementation by Harnois-Déraps et al. (2015) (cf. equation 5.27 with $A_{\text{bary}} = 1$). The modifications due to three degenerate massive neutrinos with total mass $\Sigma m_{\nu} = 0.18$ eV is demonstrated by the dash-dotted line (red). The redshift for the power spectrum calculation is $z = 0.7$ corresponding to the median redshift of the high-redshift bin used in the subsequent analysis (cf. Table 5.2). Lower panel: same as upper panel but for the lensing power spectrum of the high-redshift bin $z_2 : 0.45 < z_B \leq 0.90$ (cf. Table 5.2). The vertical dashed (grey) lines mark the multipole range of the subsequent cosmological analysis (cf. Table 5.1).

with the lensing weight function $q_\mu(\chi)$ defined as in equation (5.6) and

$$F(\chi) = -A_{\text{IA}} C_1 \rho_{\text{crit}} \frac{\Omega_m}{D_+(\chi)}. \quad (5.31)$$

Here we also introduce a dimensionless amplitude A_{IA} which allows us to rescale and vary the fixed normalization $C_1 = 5 \times 10^{-14} h^{-2} \text{M}_\odot^{-1} \text{Mpc}^3$ in the subsequent likelihood analysis. The critical density of the Universe today is denoted as ρ_{crit} and $D_+(\chi)$ is the linear growth factor normalized to unity today. In general, equation (5.31) can include also a luminosity dependence and/or an additional redshift scaling. The majority of the KiDS-450 source sample consists of late-type galaxies for which no significant detection of intrinsic alignments exists to date. For massive early-type galaxies, however, a luminosity-dependent alignment signal has been measured with no indication for a redshift dependence (Joachimi et al. 2011; Singh et al. 2015). For their re-analysis of CFHTLenS, which is of similar statistical power as KiDS-450, Joudaki et al. (2016) concluded that the full flexibility of the intrinsic alignment model including either a luminosity dependence, or a redshift dependence, or both cannot be constrained sufficiently by the data. As a cross-check, we select galaxies between $20 < m_r < 24$ from COSMOS (Laigle et al. 2016) as a proxy for the KiDS sample and study their r -band luminosities. The ratio between the mean luminosities of the two tomographic bins used in this analysis is 1.03. Therefore, we can indeed neglect any luminosity dependence in the modelling of intrinsic alignments for our galaxy source sample. Hence, we follow Hildebrandt et al. (2016) and do not consider a luminosity dependence and/or additional redshift scaling. In order to facilitate the notation of equations (5.29) and (5.30) we have not introduced these additional terms in equation (5.31). Therefore, only a free amplitude A_{IA} is allowed for the modelling of intrinsic alignments in the subsequent likelihood analysis.

5.8.2 Models

The two most important parameters entering in the calculation of the shear power spectrum are Ω_m the energy density of matter in the Universe today and A_s the amplitude of the primordial power spectrum. These two quantities determine the tilt and the total amplitude of the shear power spectrum, respectively. However, simultaneous changes in these two parameters have only a subtle net effect on the shear power spectrum and lead in general to a degeneracy in these two parameters. Moreover, observationally it is easier to work instead of A_s with the quantity σ_8 which is the root-mean-square variance of the density field smoothed with the Fourier transform of a tophat filter on a scale $R = 8 h^{-1} \text{Mpc}$ in real-space. Hence, the lensing-intrinsic degeneracy is usually referred to as a degeneracy in Ω_m and σ_8 and the 2D projections of credibility intervals in this parameter plane define the lensing ‘bananas’. The extent of these degeneracy ‘bananas’ (i.e. the top and bottom of the ‘banana’) is sensitive to the choice of sampling parameters (e.g. A_s or $\ln(10^{10} A_s)$) and their prior ranges. Moreover, a principal components analysis shows that the parameter combination $\sigma_8(\Omega_m/0.3)^\alpha$, which essentially measures the width of the ‘banana’, is most robustly constrained by cosmic shear. In Fig. 5.8 we explicitly show this for two sets of priors as specified in Table 5.3. Increased priors for $\Omega_b h^2$ and h have a significant impact on the extent of the ‘banana’ along the degeneracy line in the Ω_m - σ_8 plane as shown in Fig. 5.8. However, the increased prior ranges hardly influence the constraint on the parameter combination $\sigma_8(\Omega_m/0.3)^\alpha$ for which we find $\sigma_8(\Omega_m/0.3)^\alpha = 0.709 \pm 0.037$ for the fiducial prior ranges and $\sigma_8(\Omega_m/0.3)^\alpha = 0.709 \pm 0.039$ for the increased prior ranges. Hence, we adopt the following strategy for the parameter sampling in this paper: we will sample in $\ln(10^{10} A_s)$ and $\Omega_{\text{cdm}} h^2$ and treat σ_8 and Ω_m as derived quantities in order to calculate the combined constraint $\sigma_8(\Omega_m/0.3)^\alpha$. As opposed to previous analyses we refrain

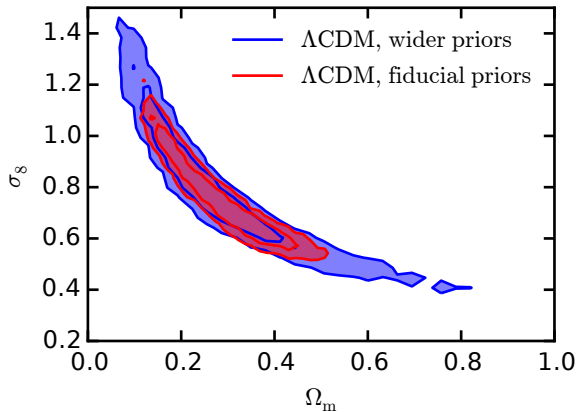


Figure 5.8: The 68 and 95 per cent credibility intervals in the Ω_m - σ_8 plane for the same baseline Λ CDM model employing two different sets of priors (cf. Table 5.3). The ‘fiducial priors’ (red contours) artificially cut the extent of the degeneracy ‘banana’ but leave its width unchanged in comparison to the ‘wider priors’ (blue contours). This results in consistent constraints on $\sigma_8(\Omega_m/0.3)^\alpha$ yielding $\sigma_8(\Omega_m/0.3)^\alpha = 0.709 \pm 0.037$ for the ‘fiducial priors’ $\sigma_8(\Omega_m/0.3)^\alpha = 0.709 \pm 0.039$ for the ‘wider priors’.

from showing any further ‘banana’-plots due to their sensitivity to priors as shown in Fig. 5.8 in order to avoid any misleading interpretations (cf. the discussions of that in Joudaki et al. 2016; Hildebrandt et al. 2016).

In addition to the parameter combination $\sigma_8(\Omega_m/0.3)^\alpha$ also the quantity $S_8 \equiv \sigma_8 \sqrt{\Omega_m/0.3}$ is used in the literature based on the observation that the exponent α is usually found to be ≈ 0.5 .

In the following likelihood analysis we assume a flat cosmological model and use the same set of parameters and priors from the analysis in Hildebrandt et al. (2016) for our fiducial model (referred to as ‘ Λ CDM’ henceforth): $\Omega_{\text{cdm}}h^2$, $\ln(10^{10}A_s)$, $\Omega_b h^2$, n_s , h . The value of the Hubble parameter today is denoted as h , $\Omega_b h^2$ is the baryonic matter density multiplied with h^2 and n_s is the exponent of the primordial power spectrum. Since data from particle physics experiments indicate that neutrinos have mass, we include two massless and one massive neutrino with a fixed minimal mass of $\Sigma m_\nu = 0.06$ eV. Moreover, we include a nuisance parameter m_{z_1} for the multiplicative correction in the first redshift bin and correlate the m -correction for the second redshift bin with it (cf. Section 5.4 for details). Since Hildebrandt et al. (2016) have shown that the uncertainty in the photometric redshift distribution is substantially smaller than the measurement errors and sampling variance on the cosmic shear signal, we do not include any nuisance parameter for the photometric redshift uncertainties. Having demonstrated the robustness of $\sigma_8(\Omega_m/0.3)^\alpha$ and S_8 under a change of priors and in the interest of run-time we choose to employ narrow priors on h and $\Omega_b h^2$. The prior range on h corresponds to the $\pm 5\sigma$ uncertainty centred on the distance-ladder constraint from Riess et al. (2016) of $h = 0.730 \pm 0.018$. Note that the corresponding prior range of $0.64 < h < 0.82$ still includes the preferred value from Planck Collaboration XIII (2015a). The prior on $\Omega_b h^2$ is based on BBN constraints listed in the 2015 update from the Particle Data Group (Olive & Particle Data Group 2014) again adopting a conservative width of $\pm 5\sigma$ such that $0.019 < \Omega_b h^2 < 0.026$.

Since we also want to constrain the total mass of massive neutrinos, we introduce as the

Table 5.3: Set of priors used for Fig. 5.8.

Parameter	fiducial priors	wider priors
$\Omega_{\text{cdm}}h^2$	[0.01, 0.99]	[0.01, 0.99]
$\ln(10^{10}A_s)$	[1.7, 5.]	[1.7, 5.]
$\Omega_b h^2$	[0.019, 0.026]	[0.001, 0.010]
n_s	[0.7, 1.3]	[0.7, 1.3]
h	[0.64, 0.82]	[0.3, 1.]
Σm_ν (eV)	$\equiv 0.06$	$\equiv 0.06$
m_{z_1}	[-0.033, 0.007]	[-0.033, 0.007]
Ω_m	derived	derived
σ_8	derived	derived

Notes. The primary cosmological and nuisance parameters for the baseline Λ CDM model for two sets of prior ranges used for Fig. 5.8. The ‘fiducial priors’ are used in the subsequent cosmological analysis.

first model extension the free parameter Σm_ν (the model is referred to as ‘ Λ CDM+ Σm_ν ’). However, as we have discussed in Section 5.8.1 there are other physical effects that we need to take into account because they might create degenerate signatures in the matter and/or shear power spectra. The first of such physical parameters is the amplitude for the intrinsic alignment model, i.e. A_{IA} . We refer to this model subsequently as ‘ Λ CDM+ A_{IA} ’. The second physical nuisance is baryon feedback and hence the model ‘ Λ CDM+ A_{bary} ’ includes the free amplitude A_{bary} . We combine both physical nuisance effects and study their combined impact on cosmological constraints in the model ‘ Λ CDM+ A_{IA} + A_{bary} ’. Finally, we combine all previous extensions into one model which we dub ‘ Λ CDM+all’ for brevity instead of showing all extensions explicitly, i.e. A_{IA} , A_{bary} , and Σm_ν .

5.8.3 Results and discussion

The resulting cosmological parameter constraints for all models and the corresponding prior ranges are summarized in Table 5.4. In order to highlight parameter degeneracies we show all possible 2D parameter projections in Fig. 5.10 in Appendix 5.B for the model Λ CDM+all. This model can be considered as the most conservative one as it includes marginalizations over several nuisance parameters (cf Section 5.8.2). For this model we derive an upper bound on the total mass for three degenerate massive neutrinos. We find $\Sigma m_\nu < 3.46$ eV at 95 per cent credibility from lensing alone. This is very similar to the constraint from our previous CFHTLenS re-analysis in **Chapter 4**. In contrast, the upper bound at 95 per cent confidence found by [Planck Collaboration XIII \(2015a, TT+lowP\)](#) is $\Sigma m_\nu < 0.72$ eV. Combining the *Planck* CMB results with measurements of the Ly α power spectrum and BAO measurements yields the very stringent upper limit of $\Sigma m_\nu < 0.14$ eV at 95 per cent confidence ([Palanque-Delabrouille et al. 2015](#)).

Table 5.4: Cosmological parameter constraints.

Model	$\Omega_{\text{cdm}}h^2$	$\ln(10^{10}A_s)$	Ω_m	σ_8	$\Omega_b h^2$	n_s	h	Σm_ν (eV)	m_{z_1}	A_{IA}	A_{bary}
Prior ranges	[0.01, 0.99]	[1.7, 5.]	derived	derived	[0.019, 0.026]	[0.7, 1.3]	[0.64, 0.82]	[0.06, 10.]	[-0.033, 0.007]	[-6., 6.]	[0., 10.]
Λ CDM no sys.	$0.13^{+0.06}_{-0.08}$	$2.60^{+0.78}_{-0.90}$	$0.29^{+0.10}_{-0.14}$	$0.72^{+0.19}_{-0.17}$	$0.022^{+0.004}_{-0.004}$	$0.93^{+0.16}_{-0.22}$	$0.74^{+0.08}_{-0.06}$	$\equiv 0.06$	–	–	–
Λ CDM	$0.14^{+0.06}_{-0.07}$	$2.61^{+0.84}_{-0.91}$	$0.29^{+0.09}_{-0.14}$	$0.72^{+0.12}_{-0.17}$	$0.023^{+0.004}_{-0.003}$	$0.93^{+0.12}_{-0.20}$	$0.74^{+0.08}_{-0.09}$	$\equiv 0.06$	$-0.007^{+0.014}_{-0.009}$	–	–
Λ CDM+ Σm_ν	$0.17^{+0.06}_{-0.09}$	$2.53^{+0.63}_{-0.83}$	$0.37^{+0.13}_{-0.11}$	$0.62^{+0.08}_{-0.11}$	$0.022^{+0.003}_{-0.004}$	$1.05^{+0.24}_{-0.16}$	$0.76^{+0.06}_{-0.05}$	$1.67^{+0.73}_{-1.61}$	$-0.008^{+0.015}_{-0.013}$	–	–
Λ CDM+ A_{IA}	$0.12^{+0.05}_{-0.07}$	$2.73^{+1.10}_{-1.03}$	$0.27^{+0.09}_{-0.12}$	$0.74^{+0.16}_{-0.18}$	$0.023^{+0.004}_{-0.003}$	$0.95^{+0.16}_{-0.19}$	$0.74^{+0.08}_{-0.07}$	$\equiv 0.06$	$-0.007^{+0.014}_{-0.010}$	$-0.22^{+1.63}_{-1.34}$	–
Λ CDM+ A_{bary}	$0.12^{+0.06}_{-0.07}$	$2.80^{+1.01}_{-1.10}$	$0.27^{+0.07}_{-0.12}$	$0.79^{+0.14}_{-0.20}$	$0.022^{+0.003}_{-0.003}$	$1.09^{+0.21}_{-0.13}$	$0.74^{+0.08}_{-0.07}$	$\equiv 0.06$	$-0.008^{+0.015}_{-0.009}$	–	$3.85^{+1.90}_{-2.94}$
Λ CDM+ A_{IA} + A_{bary}	$0.12^{+0.05}_{-0.06}$	$2.91^{+1.27}_{-1.21}$	$0.26^{+0.08}_{-0.11}$	$0.80^{+0.18}_{-0.20}$	$0.023^{+0.003}_{-0.003}$	$1.10^{+0.20}_{-0.11}$	$0.74^{+0.08}_{-0.05}$	$\equiv 0.06$	$-0.007^{+0.014}_{-0.007}$	$-0.34^{+1.51}_{-1.33}$	$4.03^{+2.31}_{-2.73}$
Λ CDM+all	$0.14^{+0.05}_{-0.07}$	$2.82^{+1.03}_{-1.12}$	$0.32^{+0.09}_{-0.12}$	$0.69^{+0.10}_{-0.15}$	$0.022^{+0.003}_{-0.003}$	$1.13^{+0.17}_{-0.13}$	$0.75^{+0.07}_{-0.05}$	$1.16^{+0.54}_{-1.10}$	$-0.007^{+0.014}_{-0.011}$	$-0.32^{+1.43}_{-1.23}$	$3.15^{+1.81}_{-3.15}$

Notes. We quote weighted median values for each varied parameter and derive 1σ -errors using the 68 per cent credible interval of the marginalized posterior distribution.

The cosmological main results for each model, i.e. $\sigma_8(\Omega_m/0.3)^\alpha$ and S_8 , are summarized in Table 5.5. We derive the exponent α from fitting the function $\ln \sigma_8(\Omega_m) = -\alpha \ln \Omega_m + \text{const.}$ to the likelihood surface in the Ω_m - σ_8 plane. Since indeed $\alpha \approx 0.5$ for all models, we compare their S_8 values in Fig. 5.9 to each other but also to constraints from other cosmic shear analyses and CMB constraints. The values we derive for each of the models in this analysis are consistent with each other and as expected introducing a free total neutrino mass is shifting S_8 to lower values. Most of our models are also consistent with previous results from CFHTLenS, where we compare in particular to a correlation-function re-analysis employing six tomographic bins and marginalization over various nuisance parameters from Joudaki et al. (2016). In addition to that, we show results from our previous quadratic estimator analysis of CFHTLenS from Chapter 4, which employed two tomographic bins at higher redshift compared to the bins used here. In that study the basic five-parameter model was also labelled ‘ Λ CDM’ but did not include a marginalization over the shear calibration uncertainties. The label ‘ Λ CDM+all’ used in that study also refers to an extension of the ‘ Λ CDM’ model with a free total neutrino mass and marginalization over baryon feedback, but does not take intrinsic alignments into account. The errors are comparable to the errors in this study, since CFHTLenS and KiDS-450 have comparable statistical power. The comparison to the KiDS-450 constraint from the correlation-function analysis with four tomographic bins (Hildebrandt et al. 2016) shows that the errorbars of that study are about 32 per cent smaller than the ones derived here. Following the discussion of Section 5.7.1 we attribute this mainly to the increased resolution along the line-of-sight for four tomographic bins, which improves the precision on the intrinsic alignment modelling. A small increase in the errorbars might also be explained by the multipole range used in this analysis compared to the effective multipole range used in Hildebrandt et al. (2016). Our results are also consistent with the result from the DES science verification (SV) correlation-function analysis (DES Collaboration 2015, ‘Fiducial DES SV cosmic shear’).

More interesting is the comparison of our results to CMB constraints including pre-*Planck* (Hinshaw et al. 2013; Calabrese et al. 2013) and *Planck* (Planck Collaboration XIII 2015a; Spergel et al. 2015) data. We find them to be most distinctively in tension with the results from Planck Collaboration XIII (2015a) at 1.8σ . We remind the reader to be cautious when quantifying tension between datasets based on parameter projections of the multi-dimensional likelihoods (cf. appendix A in MacCrann et al. 2015) which, for example, suffices to explain the mild tension in S_8 between our previous CFHTLenS results and *Planck*. However, this projection effect can certainly not explain the current tension in S_8 with *Planck*.

Finally, we want to decide which of our tested models fits the data the best. As indicated in Section 5.8 we employ for that a Bayesian model comparison framework based on evidences, their ratios, and the quantitative interpretation scheme of these by Kass & Raftery (1995). The results for the comparison of all model extensions to the baseline Λ CDM model are summarized in Table 5.6. In conclusion, none of the model extensions yields any positive evidence against the baseline Λ CDM model. Only adding a baryon feedback amplitude A_{bary} yields evidence ‘not worth more than a bare mention’ against the baseline Λ CDM model.

5.9 Conclusions

In this study we applied the quadratic estimator to state-of-the-art shear data from KiDS-450 in two redshift bins over the range $0.10 < z_B \leq 0.90$ and extracted the band powers of the auto-correlation and cross-correlation shear power spectra for multipoles in the range $76 \leq \ell \leq 1310$. The covariance matrix is based on an analytical calculation which is then convolved with the full band window matrix. We derive the parameter combination $S_8 \equiv$

Table 5.5: Constraints on S_8 and $\sigma_8(\Omega_m/0.3)^\alpha$.

Model	$S_8 \equiv \sigma_8 \sqrt{\Omega_m/0.3}$	Mean error on S_8	$\sigma_8 (\Omega_m/0.3)^\alpha$	α
Λ CDM no sys.	$0.707^{+0.041}_{-0.036}$	0.038	$0.704^{+0.038}_{-0.034}$	0.544
Λ CDM	$0.712^{+0.039}_{-0.038}$	0.039	$0.709^{+0.038}_{-0.036}$	0.543
Λ CDM+ Σm_ν	$0.696^{+0.040}_{-0.036}$	0.038	$0.692^{+0.039}_{-0.036}$	0.468
Λ CDM+ A_{IA}	$0.703^{+0.053}_{-0.044}$	0.048	$0.699^{+0.051}_{-0.043}$	0.542
Λ CDM+ A_{bary}	$0.754^{+0.047}_{-0.050}$	0.048	$0.747^{+0.044}_{-0.045}$	0.563
Λ CDM+ A_{IA} + A_{bary}	$0.742^{+0.057}_{-0.056}$	0.057	$0.734^{+0.057}_{-0.050}$	0.555
Λ CDM+all	$0.710^{+0.053}_{-0.051}$	0.052	$0.710^{+0.053}_{-0.051}$	0.501

Notes. We quote weighted mean values for the constraints on $S_8 \equiv \sigma_8 \sqrt{\Omega_m/0.3}$ and $\sigma_8(\Omega_m/0.3)^\alpha$. The errors denote the 68 per cent credible interval derived from the marginalized posterior distribution.

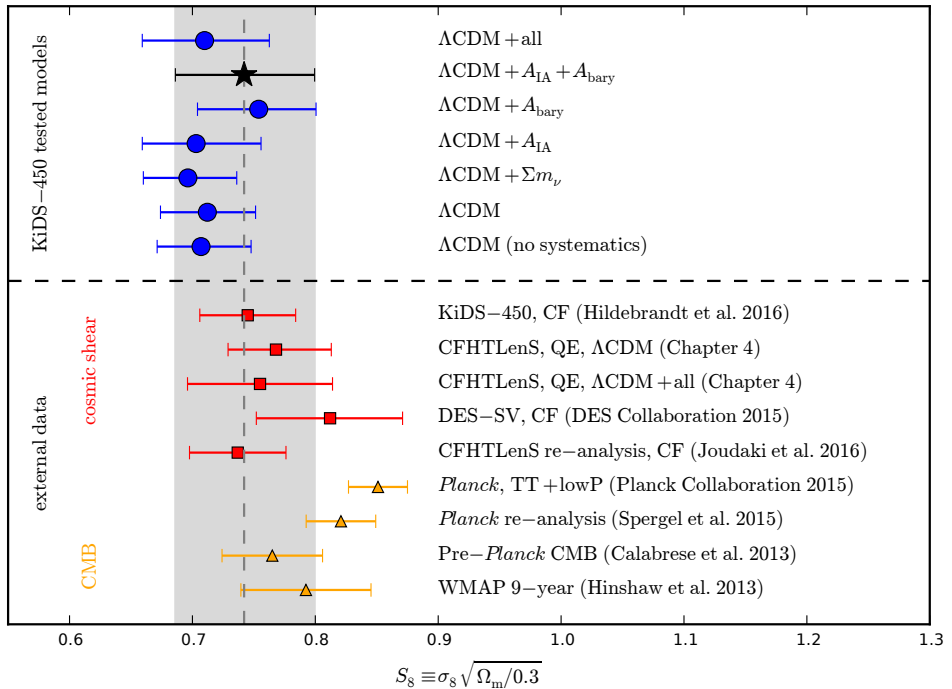


Figure 5.9: The 1σ -constraints on the parameter combination $S_8 \equiv \sigma_8 \sqrt{\Omega_m/0.3}$ for all of our tested models (cf. Tables 5.4 and 5.5). We compare them to constraints from other cosmic shear and CMB analyses. For cosmic shear analyses we indicate the type of estimator used with ‘CF’ for correlation functions and ‘QE’ for the quadratic estimator.

Table 5.6: Evidences from likelihood sampling.

Model	$\ln \mathcal{Z}$	$2 \ln K (K \equiv \mathcal{Z}_i / \mathcal{Z}_{\Lambda\text{CDM}})$	Evidence against ΛCDM
ΛCDM no sys.	-10.43 ± 0.06	–	–
ΛCDM	-10.77 ± 0.06	0	–
$\Lambda\text{CDM} + \Sigma m_\nu$	-11.24 ± 0.06	-0.94	–
$\Lambda\text{CDM} + A_{\text{IA}}$	-11.80 ± 0.06	-2.06	–
$\Lambda\text{CDM} + A_{\text{bary}}$	-10.74 ± 0.06	0.06	‘not worth more than a bare mention’
$\Lambda\text{CDM} + A_{\text{IA}} + A_{\text{bary}}$	-11.76 ± 0.06	-1.98	–
$\Lambda\text{CDM} + \text{all}$	-12.74 ± 0.07	-3.94	–

Notes. For each model we calculate the global log-evidence, $\ln \mathcal{Z}$, and compare all evidences in terms of the Bayes factor K (or equivalently $2 \ln K$) to the baseline ΛCDM model. The interpretation of the Bayes factor is following the scheme proposed by [Kass & Raftery \(1995\)](#).

$\sigma_8 \sqrt{\Omega_m/0.3}$ for a baseline ΛCDM model and several model extensions including a free total mass of neutrinos and physical nuisances such as intrinsic alignments and baryon feedback. All models also include a marginalization over the small uncertainties of the shear calibration.

A Bayesian model comparison yields no evidence against the baseline ΛCDM model for any of the extensions introduced here including a free total mass for three degenerate massive neutrinos (Σm_ν) or physical nuisances such as baryon feedback (A_{bary}) or intrinsic alignments (A_{IA}). We take the conservative approach of considering the extended model $\Lambda\text{CDM} + A_{\text{IA}} + A_{\text{bary}}$ as our fiducial model for which we find $S_8 = 0.742 \pm 0.057$. The flat five-parameter ΛCDM model without any systematics yields $S_8 = 0.707 \pm 0.038$. Thus, marginalizing over the shear calibration and the physical nuisance parameters increases the errorbars by ≈ 50 per cent.

For the model $\Lambda\text{CDM} + \text{all}$ we derive an upper limit on the total mass of three degenerate neutrinos: $\Sigma m_\nu < 3.46 \text{ eV}$ at 95 per cent credibility from lensing alone. This constraint is currently not competitive with respect to constraints derived from CMB or other large-scale structure measurements or the combination of both, but it is consistent with the constraint we derived already in our re-analysis of CFHTLenS whose statistical power is comparable to this analysis.

Most interestingly, the constraint on S_8 is in tension with the constraint from *Planck* at 1.8σ . This confirms the result from a 4-bin tomographic correlation-function analysis by [Hildebrandt et al. \(2016\)](#) with lower significance though due to the weaker S_8 constraint of our study. Moreover, the fact that this study uses less of the very non-linear scales in comparison to [Hildebrandt et al. \(2016\)](#) also disfavours insufficient modelling of these scales as a possible explanation for the discrepancy with *Planck*.

Acknowledgements

FK acknowledges support from a de Sitter Fellowship of the Netherlands Organization for Scientific Research (NWO) under grant number 022.003.013.

Based on data products from observations made with ESO Telescopes at the La Silla Paranal Observatory under programme IDs 177.A-3016, 177.A-3017 and 177.A-3018, and on data products produced by Target/OmegaCEN, INAF-OACN, INAF-OAPD and the KiDS production team, on behalf of the KiDS consortium. OmegaCEN and the KiDS production team acknowledge support by NOVA and NWO-M grants. Members of INAF-OAPD and INAF-

OACN also acknowledge the support from the Department of Physics & Astronomy of the University of Padova, and of the Department of Physics of Univ. Federico II (Naples).

Bibliography

- Addison G. E., Huang Y., Watts D. J., Bennett C. L., Halpern M., Hinshaw G., Weiland J. L., 2016, [ApJ](#), 818, 132
- Audren B., Lesgourgues J., 2011, [J. Cosmology Astropart. Phys.](#), 2011, 037
- Audren B., Lesgourgues J., Benabed K., Prunet S., 2013, [J. Cosmology Astropart. Phys.](#), 2013, 001
- BOSS Collaboration, 2015, [Phys. Rev. D](#), 92, 123516
- Bartelmann M., Schneider P., 2001, [Phys. Rep.](#), 340, 291
- Becker M. R., et al., 2015, preprint (arXiv:1507.05598)
- Begeman K., Belikov A. N., Boxhoorn D. R., Valentijn E. A., 2013, [Exp. Astron.](#), 35, 1
- Benítez N., 2000, [ApJ](#), 536, 571
- Benjamin J., et al., 2013, [MNRAS](#), 431, 1547
- Beutler F., et al., 2014, [MNRAS](#), 443, 1065
- Blas D., Lesgourgues J., Tram T., 2011, [J. Cosmology Astropart. Phys.](#), 2011, 034
- Bond J. R., Jaffe A. H., Knox L., 1998, [Phys. Rev. D](#), 57, 2117
- Bridle S., King L., 2007, [New J. Phys.](#), 9, 444
- Brown M. L., Taylor A. N., Bacon D. J., Gray M. E., Dye S., Meisenheimer K., Wolf C., 2003, [MNRAS](#), 341, 100
- Buchner J., et al., 2014, [A&A](#), 564, A125
- Calabrese E., et al., 2013, [Phys. Rev. D](#), 87, 103012
- Choi A., et al., 2015, preprint (arXiv:1512.03626)
- DES Collaboration, 2015, preprint (arXiv:1507.05552)
- Di Valentino E., Melchiorri A., Silk J., 2015, [Phys. Rev. D](#), 92, 121302
- Driver S. P., et al., 2011, [MNRAS](#), 413, 971
- Erben T., et al., 2005, [Astron. Nachr.](#), 326, 432
- Erben T., et al., 2009, [A&A](#), 493, 1197
- Erben T., et al., 2013, [MNRAS](#), 433, 2545
- Fenech Conti I., Herbonnet R., Hoekstra H., Merten J., Miller L., Viola M., 2016, preprint (arXiv:1606.05337)

- Feroz F., Hobson M. P., 2008, *MNRAS*, 384, 449
- Feroz F., Hobson M. P., Bridges M., 2009, *MNRAS*, 398, 1601
- Feroz F., Hobson M. P., Cameron E., Pettitt A. N., 2013, preprint (arXiv:1306.2144)
- Fields B. D., Olive K. A., 2006, *Nuclear Physics A*, 777, 208
- Gil-Marín H., Percival W. J., Verde L., Brownstein J. R., Chuang C.-H., Kitaura F.-S., Rodríguez-Torres S. A., Olmstead M. D., 2016, preprints (arXiv:1606.00439)
- Harnois-Déraps J., Waerbeke L. v., Viola M., Heymans C., 2015, *MNRAS*, 450, 1212
- Heymans C., et al., 2005, *MNRAS*, 361, 160
- Heymans C., et al., 2006, *MNRAS*, 368, 1323
- Heymans C., et al., 2012, *MNRAS*, 427, 146
- Heymans C., et al., 2013, *MNRAS*, 432, 2433
- Hikage C., Takada M., Hamana T., Spergel D., 2011, *MNRAS*, 412, 65
- Hildebrandt H., et al., 2012, *MNRAS*, 421, 2355
- Hildebrandt H., et al., 2016, preprint (arXiv:1606.05338)
- Hinshaw G., et al., 2013, *ApJS*, 208, 19
- Hirata C. M., Seljak U., 2004, *Phys. Rev. D*, 70, 063526
- Hoekstra H., 2004, *MNRAS*, 347, 1337
- Hu W., White M., 2001, *ApJ*, 554, 67
- Ivezic Z., et al., 2008, preprint (arXiv:0805.2366)
- Jarvis M., et al., 2015, preprint (arXiv:1507.05603)
- Joachimi B., Mandelbaum R., Abdalla F. B., Bridle S. L., 2011, *A&A*, 527, 26
- Joudaki S., et al., 2016, preprint (arXiv:1601.05786)
- Kass R. E., Raftery A. E., 1995, *J. Am. Stat. Assoc.*, 90, 773
- Kilbinger M., 2015, *Rep. Prog. Phys.*, 78, 086901
- Kitching T. D., et al., 2014, *MNRAS*, 442, 1326
- Knox L., 1999, *Phys. Rev. D*, 60, 103
- Kuijken K., et al., 2015, *MNRAS*, 454, 3500
- Laigle C., et al., 2016, *ApJS*, 224, 24
- Laureijs R., et al., 2011, preprint (arXiv:1110.3193),
- Lesgourgues J., Pastor S., 2006, *Phys. Rep.*, 429, 307
- Lesgourgues J., Tram T., 2011, *J. Cosmology Astropart. Phys.*, 2011, 032

- Lima M., Cunha C. E., Oyaizu H., Frieman J., Lin H., Sheldon E. S., 2008, *MNRAS*, 390, 118
- Limber D. N., 1954, *ApJ*, 119, 655
- Lin H., et al., 2012, *ApJ*, 761, 15
- MacCrann N., Zuntz J., Bridle S., Jain B., Becker M. R., 2015, *MNRAS*, 451, 2877
- Melchior P., Viola M., 2012, *MNRAS*, 424, 2757
- Miller L., et al., 2013, *MNRAS*, 429, 2858
- Newman J. A., et al., 2015, *Astropart. Phys.*, 63, 81
- Olive K. A., Particle Data Group 2014, *Chinese Physics C*, 38, 090001
- Palanque-Delabrouille N., et al., 2015, *J. Cosmology Astropart. Phys.*, 2015, 045
- Planck Collaboration XIII, 2015a, preprint (arXiv:1502.01589)
- Planck Collaboration XXIV, 2015b, preprint (arXiv:1502.01597)
- Refregier A., Kacprzak T., Amara A., Bridle S., Rowe B., 2012, *MNRAS*, 425, 1951
- Riess A. G., et al., 2016, preprint (arXiv:1604.01424)
- SNO Collaboration, 2001, *Phys. Rev. Lett.*, 87, 071301
- SNO Collaboration, 2002, *Phys. Rev. Lett.*, 89, 011301
- Samushia L., et al., 2014, *MNRAS*, 439, 3504
- Schaye J., et al., 2010, *MNRAS*, 402, 1536
- Schirmer M., 2013, *ApJS*, 209, 21
- Seljak U., 1998, *ApJ*, 506, 64
- Semboloni E., Hoekstra H., Schaye J., van Daalen M. P., McCarthy I. G., 2011, *MNRAS*, 417, 2020
- Semboloni E., Hoekstra H., Schaye J., 2013, *MNRAS*, 434, 148
- Singh S., Mandelbaum R., More S., 2015, *MNRAS*, 450, 2195
- Spergel D. N., Flauger R., Hložek R., 2015, *Phys. Rev. D*, 91, 023518
- Super-Kamiokande Collaboration, 1998, *Phys. Rev. Lett.*, 81, 1562
- Takahashi R., Sato M., Nishimichi T., Taruya A., Oguri M., 2012, *ApJ*, 761, 152
- Valentijn E. A., et al., 2007. eprint: arXiv:astro-ph/0702189, p. 491, <http://adsabs.harvard.edu/abs/2007ASPC..376..491V>
- de Haan T., et al., 2016, preprints (arXiv:1603.06522)
- de Jong J. T. A., Verdoes Kleijn G. A., Kuijken K. H., Valentijn E. A., 2013, *Exp. Astron.*, 35, 25

de Jong J. T. A., et al., 2015, *A&A*, 582, A62

van Daalen M. P., Schaye J., Booth C. M., Dalla Vecchia C., 2011, *MNRAS*, 415, 3649

van Uitert E., Schneider P., 2016, preprint (arXiv:1605.01056)

5.A Updated derivation of the window function matrix

The full index notation for all matrices and tensors used in the quadratic estimator algorithm can be found in Appendix 4.A. Here, we only update the notation for the derivatives of the full covariance matrix \mathbf{C} with respect to the power at an integer multipole ℓ , i.e. $\mathbf{D}_{\zeta\vartheta}(\ell)$. These are required for the calculation of the window function matrix (cf. equation 5.14) and enter explicitly in the computation of the trace matrix \mathbf{T} (cf. equation 5.15):

$$\begin{aligned} \frac{\partial C_{(\mu\nu)(ab)(ij)}}{\partial \mathcal{B}_{\zeta\vartheta}(\ell)} &= \frac{M_{\zeta(\mu\nu)}}{2(\ell+1)} \left[w_0(\ell) I_{(ab)(ij)}^\vartheta + \frac{1}{2} w_4(\ell) Q_{(ab)(ij)}^\vartheta \right] \\ &\equiv D_{(\mu\nu)(ab)(ij)(\zeta)(\vartheta)}(\ell) \equiv \mathbf{D}_{\zeta\vartheta}(\ell), \end{aligned} \quad (5.32)$$

where we have used that

$$C_{(\mu\nu)(ab)(ij)}^{\text{sig}} = \sum_{\zeta, \vartheta, \ell} \mathcal{B}_{\zeta\vartheta}(\ell) \frac{M_{\zeta(\mu\nu)}}{2(\ell+1)} \left[w_0(\ell) I_{(ab)(ij)}^\vartheta + \frac{1}{2} w_4(\ell) Q_{(ab)(ij)}^\vartheta \right].$$

5.B Additional figures

In order to highlight possible parameter degeneracies we show in Fig. 5.10 all 2D projections of the parameters used in the most extended model Λ CDM+all (cf. Section 5.8.2 and Table 5.4).

Figures 5.11 and 5.12 show the additional contributions from a fiducial cosmological E-mode signal (EE, $z_2 \times z_1$ and EE, $z_2 \times z_2$) to all possible cross-terms (cf. Section 5.7).

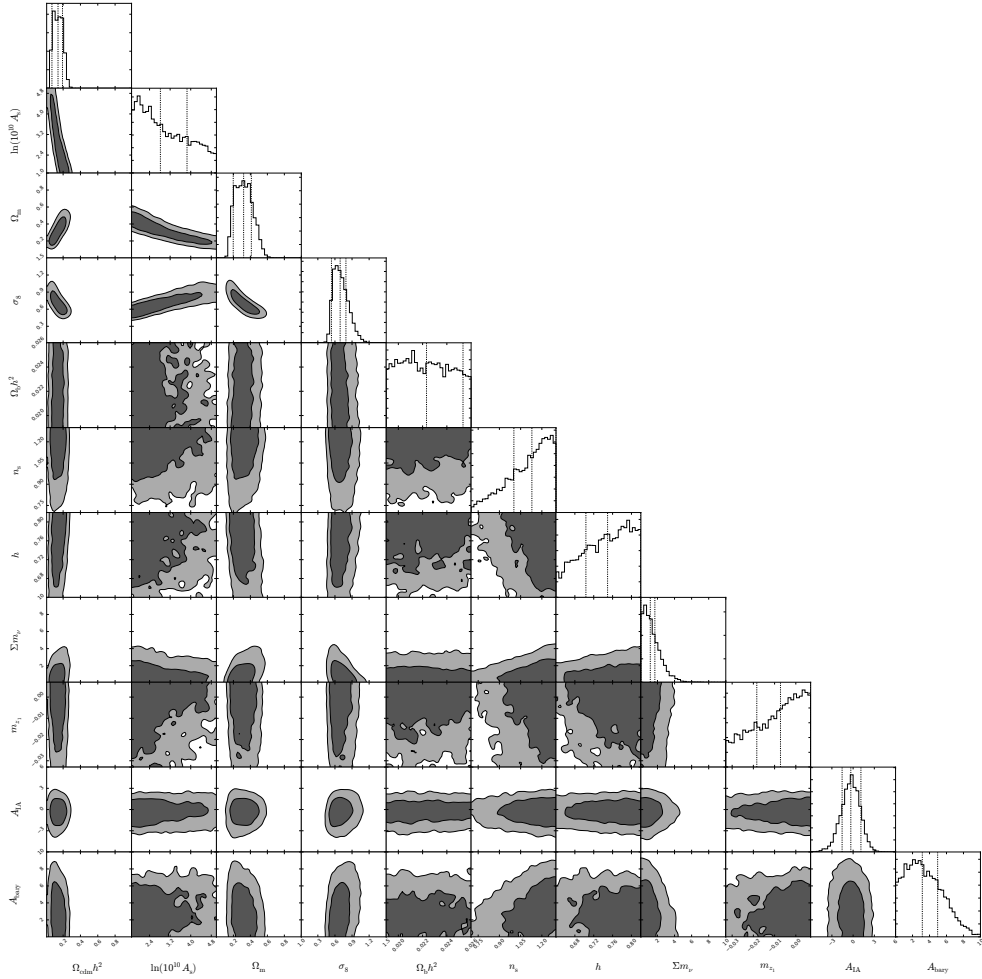


Figure 5.10: The parameter constraints derived from sampling the likelihood of model Λ CDM+all. The dashed lines in the marginalized 1D posteriors denote the weighted median and the 68 per cent credible interval (cf. Table 5.4). The contours in each 2D likelihood contour subplot are 68 and 95 per cent credible intervals smoothed with a Gaussian for illustrative purposes only.

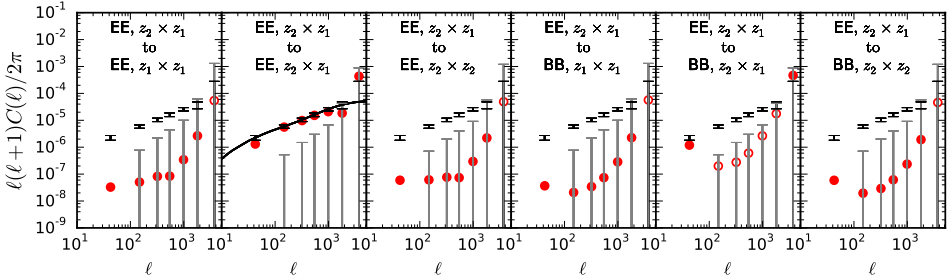


Figure 5.11: The contribution of a fiducial cosmological E-mode signal (solid, black line) for the redshift cross-correlation (i.e. $z_2 \times z_1$) convolved with the corresponding band window functions (red points) of all possible cross-combinations. The second panel from the left depicts the auto-contribution from (EE, $z_2 \times z_1$) to (EE, $z_2 \times z_1$). The grey errorbars show the statistical uncertainties associated with the B-modes. Open symbols denote negative values plotted at their absolute value.

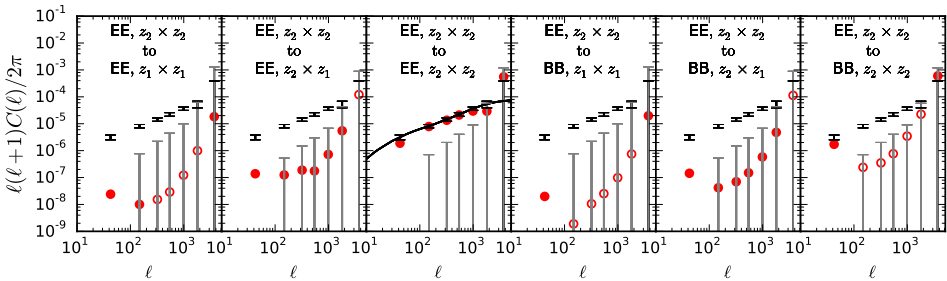


Figure 5.12: The contribution of a fiducial cosmological E-mode signal (solid, black line) for the high-redshift auto-correlation (i.e. $z_2 \times z_2$) convolved with the corresponding band window functions (red points) of all possible cross-combinations. The third panel from the left depicts the auto-contribution from (EE, $z_2 \times z_2$) to (EE, $z_2 \times z_2$). The grey errorbars show the statistical uncertainties associated with the B-modes. Open symbols denote negative values plotted at their absolute value.

6.1 Modern kosmologisch onderzoek

Het huidige kosmologische model is gebaseerd op Einstein's algemene relativiteits theorie, die de interactie beschrijft tussen materie (ofwel energie, zoals Einstein's $E = mc^2$ ons vertelt) en ruimte-tijd. Hieruit is in de laatste honderd jaar een fysisch model, het kosmologische model, opgekomen dat het ontstaan en de evolutie verklaart en het uiteindelijke lot van het universum voorspelt. Dit model beschrijft met succes een verscheidenheid aan waarnemingen met slechts een paar parameters. Desondanks, blijft een fysische verklaring voor de dominante bestanddelen, donkere materie en donkere energie, uit.

Het enige wat bekend is over donkere materie is dat het alleen door middel van zwaartekracht interactie heeft en dat het geen licht uitstraalt (vandaar de toepasselijke benaming 'donkere' materie). Echter, donkere materie speelt een belangrijke rol in de formatie van kosmologische structuren, die als een spinnenweb over het universum verspreid zijn en dus het kosmische web worden genoemd. De knopen van dit web bevatten de grootste objecten in het universum: clusters van honderden melkwegstelsels, die bij elkaar gehouden worden door hun eigen zwaartekracht. Zulke clusters van melkwegstelsels bestaan voornamelijk uit donkere materie en zijn daarom een ideaal laboratorium om de interactie tussen donkere materie en 'gewone' materie in te onderzoeken.

Een grote openbaring die uit het kosmologische model naar voren is gekomen, is dat de ruimte uitzet (alleen op kosmologische afstanden en astronomische objecten worden bijeen gehouden door hun eigen zwaartekracht). De uitdijning van het universum met de tijd betekent ook dat er een punt in het verleden is geweest waarin het universum is begonnen met uitdijen vanuit het kleinste punt. Er wordt gedacht dat deze oerknal 13,8 miljard jaar geleden heeft plaats gevonden. Het universum begon met een hoge dichtheid en temperatuur en naarmate de expansie vorderde, werd het minder dicht en koelde het af. Toen de juiste temperatuur bereikt was waarop neutrale (waterstof) atomen uit het plasma van hete subatomaire deeltjes en straling geformeerd konden worden (ongeveer 380 000 jaar na de oerknal), werd het universum transparant voor straling. Zelfs in de moderne tijd kunnen we nog de thermische straling zien die na de formatie van neutraal waterstof vrij rond kon bewegen. Deze gloed wordt de kosmische achtergrond straling genoemd. Alsmar preciezere metingen worden gedaan aan de minieme variaties in temperatuur van de kosmische achtergrond straling door satellieten in de ruimte zoals *WMAP* (engelse afkorting voor *Wilkinson Microwave Anisotropy Probe*) of *Planck*. Deze metingen geven ons de sterkste limieten voor de parameters in het kosmologische model.

Recente waarnemingen laten zien dat het universum versnelt aan het uitdijen is. Deze versnelling wordt toegeschreven aan 'donkere energie'. De benaming 'donkere energie' is voornamelijk een beschrijving van hoe wij in het duister tasten over wat dit fenomeen is. Donkere energie moet dus vooral gezien worden als een verzamelnaam voor een verscheidenheid aan theorieën die de versnelde uitdijning proberen te verklaren. Sommige van deze theorieën

hebben verstrekkende gevolgen, zoals een revisie van Einstein's theorie van de zwaartekracht. Hierdoor is de studie naar donkere energie een van de belangrijkste vragen binnen het hedendaagse kosmologische onderzoek. Hoewel we nog niet weten welke natuurkundige principes zich achter donkere energie schuilhouden, kunnen we wel de effecten van donkere energie bestuderen. Donkere materie is de drijvende kracht achter de versnelde uitdijning van het universum en de uitdijning kan zeer precies worden bestudeerd door te kijken naar de evolutie van structuren van kosmologische grootte. Bekende subatomaire deeltjes die ook de evolutie van deze enorme structuren beïnvloeden zijn neutrinos. Deze deeltjes reizen met bijna de lichtsnelheid en reageren nauwelijks door middel van de zwakke kracht (een van de vier fundamentele krachten in de natuurkunde) en de zwaartekracht. De wisselwerking tussen neutrinos en andere deeltjes is zo zwak dat op dit moment ongeveer 70 miljard neutrinos per seconde door uw duim nagel gaan. Het onderzoek dat heeft aangetoond dat neutrinos ook door middel van de zwaartekracht reageren, en dus een massa hebben, is beloond met een Nobelprijs. Het is echter niet mogelijk om met de huidige techniek met behulp van deeltjes fysica experimenten de absolute massa van neutrinos te bepalen. De sterkste aanwijzingen voor de maximale massa die neutrinos kunnen hebben, komen uit studies naar de kosmische structuren.

6.2 Zwaartekrachtslenzen

Een goede manier om de donkere materie en donkere energie in het universum te bestuderen is door middel van zwaartekrachtslenzen. Het principe van lenswerking door zwaartekracht beschrijft hoe licht vanuit een bron, zoals een sterrenstelsel, wordt afgebogen door een verzameling van massa, die zich voor de bron bevindt en de 'lens' wordt genoemd. Afhankelijk van de geometrische opstelling van de bron, de lens en de waarnemer en hoe de massa verdeeld is over de lens, kunnen zulke afbuigingen 'sterk' zijn, waardoor de bron vervormd wordt of te zien is op verschillende posities. Dit soort fenomenen worden effecten van 'sterke zwaartekrachtslenzen' genoemd en zijn alleen te zien dicht (in projectie) bij de lens. Op grotere afstand van de lens worden alleen lichte vervormingen van de bron waargenomen. Het zwakke effect van zwaartekrachtslenzen op grote afstand is een van de redenen dat een statistische aanpak nodig is om het te meten. Een andere reden is dat de intrinsieke vorm van een sterrenstelsel niet te onderscheiden is van de vervorming door de zwaartekrachtslens. We kunnen echter aannemen dat voor een grote groep van sterrenstelsels, die elk een willekeurige vorm hebben, de intrinsieke vormen uit het gemiddelde wegvallen. De enige vorm die overblijft in het gemiddelde is dan de vervorming ten gevolge van de zwaartekrachtslens. Deze aanpak wordt zwakke lenswerking door zwaartekracht genoemd.

De massa van de lens kan bepaald worden met behulp van zwakke en sterke lenswerking door zwaartekracht. Dit maakt zwaartekrachtslenzen een goede manier om kosmologisch onderzoek mee te doen. Het is namelijk de *totale massa* van donkere materie en lichtgevende materie van een lens die de vervorming veroorzaakt. Daarom is het bestuderen van de massa en massa verdeling van clusters van melkwegstelsels een uitstekende manier om limieten te zetten op de parameters van het kosmologische model. In het bijzonder is de hoeveelheid van clusters van sterrenstelsels van een gegeven massa, op een gegeven tijd, in een gegeven volume, een belangrijke kosmologische test. Deze test is echter alleen mogelijk met precieze metingen van de massa's van de clusters.

Het is niet alleen mogelijk om individuele astronomische objecten als zwaartekrachtslenzen te gebruiken. Het is ook mogelijk om het hele universum te gebruiken als zwaartekrachtslens. Licht dat door verschillende kosmische structuren reist, wordt door de zwaartekracht ervan aangetast. Door de zwakke lenswerking te bestuderen op verschillende kosmische tijd-

stippen kan de evolutie van de kosmische structuren worden bepaald. Deze tijdsevolutie kan ons weer meer vertellen over hoe donkere energie kosmische structuren beïnvloedt. De studie naar zwakke lenswerking door kosmische structuren wordt ‘cosmic shear’ in het Engels genoemd, maar we zullen het hier verder ‘kosmische lenswerking’ noemen. Op het moment worden verschillende kosmische lenswerking experimenten gedaan met observaties van grote delen van de hemel. Deze observaties van ongeveer 1000 vierkante graden zijn slechts voorlopers van toekomstige observaties van de gehele hemel.

6.3 Dit proefschrift

In dit proefschrift zullen wij toepassingen van zwakke en sterke lenswerking door zwaartekracht presenteren in de context van de kosmologie.

In **Hoofdstuk 2** bestuderen wij de massa en de massa verdeling van RX J1347.5–1445, een van de zwaarste clusters van sterrenstelsels. Daarnaast is dit cluster ook een van de helderste Röntgen straling objecten in de hemel. Dit komt door de grote hoeveelheid van ‘intra-cluster gas’, dat zo heet is dat het Röntgen licht uitzendt. De sterke lenswerking door zwaartekracht van het cluster veroorzaakt grote heldere blauwe bogen en hetzelfde achtergrondstelsel kan op verschillende posities waargenomen worden. Voor dit onderzoek gebruiken wij gearchiveerde diepe observaties gemaakt met de *Hubble Space Telescope*. Wij presenteren een gedetailleerd model van het cluster als een sterke zwaartekracht lens, dat gemaakt is met behulp van twee onafhankelijke modellerende methodes. Daarnaast meten wij het profiel van de massa verdeling van de binnenste kern van het cluster.

In **Hoofdstuk 3** bekijken wij verzamelingen van clusters van sterrenstelsels en stellen wij de vraag wat de beperkingen zijn voor zwakke lenswerking door zwaartekracht om massa’s voor verzamelingen van clusters te bepalen. Deze studie is uitgevoerd met de geplande *Euclid* missie in gedachten. Wij bepalen het niveau van de statistische onzekerheden in massa metingen voor de *Euclid* missie en bestuderen de invloed van verschillende systematische onzekerheden. Zoals eerder gezegd, zijn precieze metingen van de massa’s een belangrijk onderdeel voor het bepalen van het aantal clusters van een gegeven massa, op een gegeven kosmisch tijdstip, in een gegeven volume. Deze hoeveelheid hangt sterk af van de kosmologie. Wij bestuderen in het bijzonder het effect van het foutief bestempelen van sterrenstelsels, die bij het cluster horen, als stelsels die zich achter het cluster bevinden. Door deze cluster sterrenstelsels als bronnen in plaats van lenzen te markeren, wordt het effect van de zwakke lenswerking door zwaartekracht afgezwakt. Hierdoor zal de meting van de massa lager zijn dan de werkelijke massa. Dit effect is hevig voor gecombineerde data van clusters en moet dus worden gecorrigeerd. Een ander effect dat voor foutieve massa metingen zorgt, is het kiezen van een verkeerd centrum van het cluster van sterrenstelsels. Normaliter wordt het centrum van het cluster gekozen als de positie van het helderste sterrenstelsel in het cluster, of als de piek van de Röntgen straling. Het is echter mogelijk dat deze twee posities niet overeenkomen met het ware centrum van het cluster, waardoor de massa metingen foutief zouden kunnen zijn. Aangezien de verwachte statistische onzekerheden van *Euclid* klein zijn, is deze onzuiverheid significant. Echter zullen geplande missies, zoals de Röntgen missie *eROSITA* (engelse afkorting voor *extended ROentgen Survey with an Imaging Telescope Array*), helpen om het effect van een verkeerd centrum te verminderen.

In de laatste twee hoofdstukken nemen we de stap van de studie van clusters van sterrenstelsels naar de studie van kosmische structuren met de kosmische lenswerking. In plaats van de standaard aanpak te volgen, meten wij het signaal van de kosmische lenswerking met behulp van een mathematische transformatie techniek. Deze techniek geeft ons een beschrijving van het signaal van de kosmische lenswerking in hetzelfde kader als wordt gebruikt voor

theoretische beschrijvingen van het signaal van de kosmische lenswerking. (De theoretische voorspellingen zijn nodig om de gemeten data te vergelijken met het kosmologische model.) Een voordeel van deze techniek is dat, bijvoorbeeld, het effect van neutrinos veel gemakkelijker in dit kader beschreven kan worden. Om de limieten voor de parameters van het kosmologische model beter te kunnen bepalen, kijken wij in **Hoofdstuk 4** naar uitbreidingen van het algoritme om metingen van het signaal van de kosmische lenswerking op verschillende tijdstippen mogelijk te maken. We testen dit uitgebreide algoritme in detail met gesimuleerde data, waarna we het toepassen op vrij toegankelijke data van de zwaartekracht lens analyse van de Canada–France–Hawaii Telescope Legacy Survey (CFHTLenS).

Uiteindelijk gebruiken we in **Hoofdstuk 5** de modernste data uit de 450 vierkante graden aan observaties van een tussentijdse data verstrekking van de Kilo-Degree Survey (KiDS). Opnieuw gebruiken we ons uitgebreide algoritme om het signaal van de kosmische lenswerking te meten en de kosmologische parameters te bepalen. Onze resultaten komen niet overeen met de nieuwste metingen van de kosmische achtergrond straling door *Planck*.

Zusammenfassung

7.1 Moderne Kosmologie

Unser modernes kosmologisches Weltbild basiert auf Einsteins Allgemeiner Relativitätstheorie, welche die Wechselwirkung zwischen Masse (was nach Einsteins $E = mc^2$ gleichbedeutend ist mit Energie) und der Raumzeit beschreibt. Darauf aufbauend entstand im Verlauf der letzten Hundert Jahre ein physikalisches Modell für den Ursprung, Verlauf und das Ende des Universums, ein sogenanntes kosmologisches Modell. Für unser heutiges kosmologisches Modell benötigt man nur ein paar Parameter, um eine große Spanne von verschiedenen kosmologischen Beobachtungen sehr erfolgreich zu beschreiben. Die physikalische Grundlage für die zwei wichtigsten Parameter des kosmologischen Modells, Dunkle Materie und Dunkle Energie, ist jedoch noch ein vollkommenes Rätsel.

Zur Zeit wissen wir nur sicher, dass Dunkle Materie allein gravitativ wechselwirkt und dass sie kein Licht aussendet (von daher ist “dunkel” durchaus passend in diesem Zusammenhang). Allerdings spielt Dunkle Materie eine fundamentale Rolle in der Bildung von kosmisch großräumigen Strukturen. Diese ziehen sich wie ein Netz durchs All, deshalb spricht man in diesem Zusammenhang auch vom “kosmischen Netz”. An den Knotenpunkten dieses Netzes befinden sich die größten, durch Gravitation gebundenen Strukturen: Ansammlungen von Hunderten von Galaxien, sogenannte Galaxienhaufen. Diese bestehen hauptsächlich aus Dunkler Materie, weshalb Galaxienhaufen ideale “Testlabore” sind, um die Wechselwirkung von dunkler und gewöhnlicher Materie genau zu untersuchen.

Eine bedeutende Erkenntnis unseres heutigen kosmologischen Modells ist, dass sich der Raum ausdehnt, allerdings nur auf kosmisch großen Skalen. Durch Gravitation gebundene Objekte werden dadurch jedoch nicht “auseinander gerissen”. Wenn man die Expansion des Raumes zeitlich zurück verfolgt, gelangt man zu dem Schluss, dass es einen Anfangspunkt für die Expansion gegeben haben muss, den sogenannten Urknall. Dieser fand wohl vor ungefähr 13,8 Milliarden Jahren statt. Am Anfang war das Universum extrem dicht und heiß und dadurch, dass sich der Raum weiter ausdehnt, kühlt das All zunehmend ab und dünnt immer weiter aus. Als es dann schließlich soweit abgekühlt war, dass sich aus dem extrem heißen Teilchen- und Strahlungsplasma die ersten neutralen (Wasserstoff-)Atome bilden konnten, wurde das Universum durchsichtig für elektromagnetische Strahlung (was ungefähr 380 000 Jahre nach dem Urknall geschah). Selbst heute noch können wir die Überreste dieser Wärmestrahlung beobachten. Dieses “Nachglühen” ist die sogenannte “kosmische Hintergrundstrahlung”. Immer präzisere Messungen der winzigen Temperaturschwankungen in dieser kosmischen Hintergrundstrahlung, zum Beispiel durchgeführt mit Satellitenobservatorien wie *WMAP* (englische Abkürzung für *Wilkinson Microwave Anisotropy Probe*) oder *Planck*, liefern momentan die genauesten Werte für eine Vielzahl von kosmologischen Parametern.

Aktuelle Beobachtungen zeigen weiterhin, dass sich der Raum sogar beschleunigt ausdehnt. Die Ursache für diese beschleunigte Ausdehnung nennen wir Dunkle Energie, aller-

dings steht das “dunkel” darin eher für unser Unwissen als für eine echte physikalische Eigenschaft. Man sollte Dunkle Energie deshalb eher als abstrakten Begriff sehen, um verschiedene Theorien in einem übergeordneten Rahmen zu sammeln. Einige dieser Theorien haben weitreichende Folgen und würden sogar eine Änderung von Einsteins Allgemeiner Relativitätstheorie nach sich ziehen. Das macht das Studium der Dunklen Energie zu einem der wichtigsten Schwerpunkte in der heutigen kosmologischen Forschung. Obwohl wir nicht wissen, was genau Dunkle Energie eigentlich ist, können wir ihren Einfluss auf die beschleunigte Ausdehnung des Raumes beobachten, zum Beispiel durch das genaue Studium der Entwicklung von kosmisch großräumigen Strukturen.

Diese Entwicklung wird zudem auch noch von den uns besser bekannten Neutrinos beeinflusst. Diese Elementarteilchen bewegen sich fast mit Lichtgeschwindigkeit, interagieren aber nur sehr, sehr schwach durch die schwache subatomare Wechselwirkung (eine der vier Grundkräfte der Natur). In diesem Augenblick etwa fliegen pro Sekunde um die 70 Milliarden Neutrinos durch eine Fläche so groß wie ein Daumnagel. Dass Neutrinos gravitativ wechselwirken, wurde in nobelpreiswürdigen Teilchenphysikexperimenten herausgefunden. Diese zeigten, dass Neutrinos eine (winzige) Masse besitzen. Allerdings kann man durch Teilchenphysikexperimente zur Zeit noch nicht den absoluten Wert der Neutrinomasse messen und die derzeit genauesten Bestimmungen für die Obergrenze der Neutrinomasse erhält man durch das Studium des kosmischen Netzes.

7.2 Der Gravitationslinseneffekt

Ein sehr hilfreiches Werkzeug für das Studium von Dunkler Materie und Dunkler Energie ist der Gravitationslinseneffekt. Dieser beschreibt die Ablenkung des Lichts einer Quelle, zum Beispiel einer Galaxie, durch eine Masse im Vordergrund, die sogenannte Linse. Abhängig von der genauen geometrischen Anordnung von Quelle, Linse und Beobachter und der genauen Massenverteilung der Linse können die Lichtablenkungen so stark sein, dass extrem verformte oder sogar Mehrfachbilder derselben Quelle entstehen. Dies nennt man dann den “starken” Gravitationslinseneffekt und dieser tritt nur in kurzem (projiziertem) Abstand zur Linse auf. Weiter entfernt von der Linse kann man nur noch die Effekte von schwachen Lichtablenkungen beobachten. Das ist nur einer der Gründe dafür, warum man einen statistischen Ansatz zum Studium des schwachen Linseneffekts braucht. Der andere Grund ist, dass man die wahre, intrinsische Form einer einzelnen Galaxie und die Verformung durch den Gravitationslinseneffekt prinzipiell nicht voneinander trennen kann. Allerdings kann man annehmen, dass sich für hinreichend große Stichproben von Galaxien deren intrinsische Formen rausmitteln (da die intrinsischen Formen der Galaxien zufällig verteilt sind). Deshalb bleibt nach einer solchen Mittelung nur die durch die Gravitationslinse hervorgerufene Bildverformung übrig. Dies nennt man den “schwachen” Gravitationslinseneffekt.

Man kann sowohl mit Hilfe des starken als auch des schwachen Gravitationslinseneffektes die Masse der Linse bestimmen. Dies macht den Gravitationslinseneffekt zu einem sehr wichtigen Werkzeug für die Kosmologie, da die *Gesamtmasse* der Linse, inklusive der Dunklen Materie, die Lichtablenkungen verursacht. Daher erlaubt uns das Studium der Masse und ihrer Verteilung in Galaxienhaufen mit dem Gravitationslinseneffekt kosmologische Parameter zu bestimmen. Außerdem ist die Anzahl von Galaxienhaufen mit einer bestimmten Masse zu einer bestimmten kosmischen Zeit pro Volumen ein weiterer wichtiger kosmologischer Test, der präzise Massenbestimmungen voraussetzt.

Anstatt den starken oder schwachen Gravitationslinseneffekt nur zur Bestimmung der Masse von einzelnen Linsen, wie Galaxien oder Galaxienhaufen, zu verwenden, kann man das Universum selbst als Linse benutzen: Licht, das sich durch die kosmisch großräumigen

Strukturen ausbreitet, wird durch diese schwach abgelenkt. Durch Messung dieser schwachen Lichtablenkung zu verschiedenen kosmischen Zeiten können wir Rückschlüsse über die Entwicklung von Strukturen im kosmischen Netz ziehen. Da diese Entwicklung von der Dunklen Energie beeinflusst wird, können wir so etwas über die Eigenschaften der Dunklen Energie erfahren. Die schwache Lichtablenkung durch das kosmische Netz nennt man im Englischen “cosmic shear” (wörtlich “kosmische Scherung”), aber wir werden im Folgenden den Ausdruck “kosmischer Gravitationslinseneffekt” verwenden.

Zur Zeit werden große Himmelsdurchmusterungen durchgeführt, die schließlich mehrere Tausend Quadratgrad des Himmels umfassen werden, um den kosmischen Gravitationslinseneffekt zu messen. Diese dienen als Vorläufer für Durchmusterungen des nahezu gesamten Himmels, die noch im Verlauf des nächsten Jahrzehnts stattfinden werden.

7.3 Der Inhalt dieser Doktorarbeit

In dieser Doktorarbeit präsentieren wir Anwendungen des starken und schwachen Gravitationslinseneffekts in einem kosmologischen Kontext.

In **Kapitel 2** untersuchen wir die Masse und ihre Verteilung in einem der massereichsten Galaxienhaufen, die uns heute bekannt sind, dem Galaxienhaufen RX J1347.5–1145. Der Galaxienhaufen ist auch besonders leuchtstark im Röntgenbereich, was darauf hindeutet, dass er sehr viel heißes Gas besitzt. Dieses ist so heiß, dass es Röntgenstrahlung aussendet. Um die Masse des Galaxienhaufens zu untersuchen, benutzen wir den starken Gravitationslinseneffekt, da extrem verformte Bilder, wie zum Beispiel sogenannte helle, blaue Bogen und sogar Systeme von Mehrfachbildern um den Galaxienhaufen herum beobachtet werden können. Diese sehr detaillierten Beobachtungen wurden mit dem Weltraumteleskop *Hubble* gemacht und sind in einem Onlinearchiv frei verfügbar. Wir verwenden zwei unabhängige Modellierungsansätze um ein konsistentes und sehr detailliertes Modell des Galaxienhaufens als starke Gravitationslinse zu erstellen. Außerdem messen wir schließlich das Profil der Masse und ihre Verteilung im Kern des Galaxienhaufens.

In **Kapitel 3** wenden wir uns großen Stichproben von Galaxienhaufen zu, um zu untersuchen, was die Genauigkeit der Massenbestimmung mit Hilfe des schwachen Gravitationslinseneffektes begrenzt. Dabei konzentrieren wir uns im Besonderen auf die zukünftige Durchmusterung des fast gesamten Himmels mit dem *Euclid*-Satelliten. Wir bestimmen, wie präzise man die Masse von Stichproben von Galaxienhaufen in dieser Mission bestimmen werden kann und studieren weiter den Einfluss von mehreren systematischen Fehlerquellen auf diese Massenbestimmungen. Wie bereits zuvor erwähnt, sind diese präzisen Massenbestimmungen sehr wichtig, um die Anzahl von Galaxienhaufen einer bestimmten Masse zu einer bestimmten kosmischen Zeit pro Volumen zu messen. Diese Zahl wiederum hängt sehr stark vom kosmologischen Modell ab und erlaubt es uns deshalb kosmologische Parameter zu bestimmen. Im Besonderen untersuchen wir, welchen Effekt Galaxien des Galaxienhaufens haben, die irrtümlich als Quellen für den schwachen Gravitationslinseneffekt genommen werden, obwohl sie in Wahrheit Linsen sind. Diese “falschen” Quellen schwächen das durch den schwachen Gravitationslinseneffekt hervorgerufene Signal ab, wodurch man eine niedrigere als in Wirklichkeit vorhandene Masse misst. Für das kombinierte Signal von großen Stichproben von Galaxienhaufen ist dieser Effekt nicht zu vernachlässigen und muss sorgfältig berücksichtigt werden. Schließlich untersuchen wir noch die Auswirkung einer fehlerhaften Bestimmung des Zentrums des Galaxienhaufens auf die Massenbestimmung. Normalerweise nimmt man die Position der hellsten Galaxie im Galaxienhaufen als Zentrum oder die Position, an der die Röntgenstrahlung am höchsten ist. Diese Positionen müssen aber nicht notwendigerweise mit dem wahren Zentrum des Galaxienhaufens übereinstimmen, was dann wiederum die Mes-

sung des schwachen Gravitationslinseneffekts beeinflusst. Da wir für *Euclid* nur sehr kleine statistische Ungenauigkeiten in der Massenbestimmung erwarten, muss auch dieser systematische Effekt genau berücksichtigt werden. Komplementäre Missionen, wie zum Beispiel die geplante Himmelsdurchmusterung im Röntgenbereich durch *eROSITA* (englische Abkürzung für *extended ROentgen Survey with an Imaging Telescope Array*), werden es jedoch ermöglichen den Effekt eines falsch angenommenen Zentrums des Galaxienhaufens zu korrigieren.

In den letzten beiden Kapiteln gehen wir über das Studium von Galaxienhaufen hinaus und studieren stattdessen die Strukturen des kosmischen Netzes mit Hilfe des kosmischen Gravitationslinseneffekts. Anstatt den Standardansatz zur Messung des kosmischen Linseneffekts zu folgen, benutzen wir eine mathematische Transformationstechnik, die eine Beschreibung des Signals in derselben mathematischen Formulierung der theoretischen Vorhersagen liefert (theoretische Vorhersagen werden benötigt, um die Messungen mit dem kosmologischen Modell zu vergleichen). Ein besonderer Vorteil dieses Ansatzes ist, dass zum Beispiel die Effekte von massebehafteten Neutrinos in dieser mathematischen Formulierung klarer und eindeutiger studiert werden können. Um die Bestimmung von kosmologischen Parametern mit Hilfe dieser Technik noch genauer zu machen, erweitern wir den Algorithmus in **Kapitel 4**, sodass wir mit ihm auch Messungen des kosmischen Gravitationslinseneffekts zu unterschiedlichen kosmischen Zeiten machen können. Wir testen den erweiterten Algorithmus gründlich mit simulierten Daten, bevor wir ihn schließlich auf echte und frei zugängliche Daten der Himmelsdurchmusterung CFHTLS (englische Abkürzung für “Canada–France–Hawaii Telescope Legacy Survey”) anwenden.

Schließlich verwenden wir in **Kapitel 5** aktuellste Kataloge der Himmelsdurchmusterung KiDS (englische Abkürzung für “Kilo-Degree Survey”), die auf Beobachtungen des Himmels mit einer Fläche von ungefähr 450 Quadratgrad basieren. Mit diesen Daten messen wir wieder den kosmischen Gravitationslinseneffekt mit unserem erweiterten Algorithmus und extrahieren außerdem kosmologische Parameter. Unsere Resultate stimmen nicht mit den aktuellsten Messungen der kosmischen Hintergrundstrahlung durch *Planck* überein.

Publications

First author:

1. *A direct measurement of tomographic lensing power spectra from CFHTLenS*
F. Köhlinger, M. Viola, W. Valkenburg, B. Joachimi, H. Hoekstra and K. Kuijken
2016, Monthly Notices of the Royal Astronomical Society, Volume 456, Issue 2, pp 1508–1527 (**Chapter 4**)
2. *Statistical uncertainties and systematic errors in weak lensing mass estimates of galaxy clusters*
F. Köhlinger, H. Hoekstra and M. Eriksen
2015, Monthly Notices of the Royal Astronomical Society, Volume 453, Issue 3, pp 3107–3119 (**Chapter 3**)
3. *Strong lensing in RX J1347.5–1145.5 revisited*
F. Köhlinger and R. W. Schmidt
2014, Monthly Notices of the Royal Astronomical Society, Volume 437, Issue 2, pp 1858–1871 (**Chapter 2**)

Contributed:

1. *The first and second data releases of the Kilo-Degree Survey*
J. T. A. de Jong et al. (**incl. F. Köhlinger**)
2015, Astronomy & Astrophysics, Volume 582, p. A62
2. *Constraints on the alignment of galaxies in galaxy clusters from ~14000 spectroscopic members*
C. Sifón, H. Hoekstra, M. Cacciato, M. Viola, **F. Köhlinger** et al.
2015, Astronomy & Astrophysics, Volume 575, p. A48
3. *The Kilo-Degree Survey*
J. T. A. de Jong et al. (**incl. F. Köhlinger**)
2013, The Messenger, Volume 154, pp 44–46
4. *Infrared properties of active OB stars in the Magellanic Clouds from the Spitzer SAGE survey*
A. Z. Bonanos, D. J. Lennon, D. L. Massa, M. Sewilo, **F. Köhlinger** et al.
2011, Proceedings of the International Astronomical Union, Volume 272, pp 254–259
5. *The Infrared Properties of Massive Stars in the Magellanic Clouds*
A. Z. Bonanos, D. J. Lennon, D. L. Massa, M. Sewilo, **F. Köhlinger** et al.
2011, Bulletin de la Société Royale des Sciences de Liège, Volume 80, pp 346–350
6. *Spitzer SAGE-SMC Infrared Photometry of Massive Stars in the Small Magellanic Cloud*
A. Z. Bonanos, D. J. Lennon, **F. Köhlinger** et al.
2010, The Astronomical Journal, Volume 140, Issue 2, 416, pp 416–429

Curriculum Vitae

I was born on 8th October 1985 in Gießen, Germany, but I spent my childhood and school years in the neighbouring town of Wetzlar. There, I also attended high school with specializations in maths and history. After graduating from the ‘Goetheschule Wetzlar’ in 2005, I was recruited to accomplish nine months of military service as required by German law at the time. Consequently, I spent (too) much time in the forests of the rainy Eifel area, which strengthened my motivation to continue with university and to study physics from day to day. Therefore, after fulfilling my duty in 2006, I enrolled at Heidelberg University.

In 2009, during a six week voluntary ‘mini research’ at the ‘Astronomisches Rechen-Institut’ in Heidelberg under supervision of Dr. Robert Schmidt, I gained my first experiences with conducting (guided) research. This presented an entirely new view on physics and astronomy beyond lectures and weekly problem sets. The following ten weeks of that summer I participated in the ‘Space Astronomy Summer Program (SASP)’ hosted by the ‘Space Telescope Science Institute (STScI)’ in Baltimore in the United States. There, I conducted research on massive stars in the Small Magellanic Cloud under supervision of Dr. Daniel J. Lennon and Dr. Alceste Bonanos. In the fall of 2009, I left Heidelberg again and spent the academic year 2009/2010 following general studies in the ‘Kyoto University International Education Program (KUINEP)’ in the beautiful town of Kyoto, Japan. After my return to Heidelberg I concluded my studies with passing the final exams for the ‘Diplom’ degree. In my final year, I joined Prof. Joachim Wambsganz’s lensing group at the ‘Astronomisches Rechen-Institut’. Under his and Dr. Robert Schmidt’s supervision I wrote my ‘Diplom’ thesis on strong gravitational lensing in galaxy clusters. Already during that year I could gain my first hands-on experience as an observer at the ‘South African Astronomical Observatory (SAAO)’ in the Karoo desert.

In October 2012, I moved to the Netherlands and started my PhD research as a fellow of the ‘Leiden de Sitter Cosmology Programme’ jointly hosted by Leiden Observatory and the Lorentz Institute for Theoretical Physics at Leiden University. I decided to continue my research in gravitational lensing and started my first research project with Dr. Henk Hoekstra on weak gravitational lensing of galaxy clusters. Consequently, I also joined his and Prof. Koenderaad Kuijken’s (weak) lensing research group. Rich interactions with other group members triggered further projects changing my focus slowly but surely from galaxy clusters to cosmic shear, the ‘Kilo-Degree Survey (KiDS)’, and the study of the cosmic large-scale structure. I presented results of this work at many conferences, workshops, and seminars in Canada, Italy, Japan, the Netherlands, Switzerland, the (still) United Kingdom, and the United States. I am very grateful for having had the opportunity to participate in excellent summer/winter schools on gravitational lensing and/or cosmology in Puerto de la Cruz on Tenerife, Spain; in Varenna, Italy; and in Tokyo, Japan. Moreover, as a researcher somewhere half-way between theory and high-level data, I embraced the opportunity to expand my observational experience at the ‘Isaac Newton Telescope (INT)’ on La Palma in two observation runs during my PhD. In addition to performing research, I supervised for two semesters Bachelor students in one of the experiments of the physics laboratory course (‘Natuurkundig Onderzoek/Experimenten’) ‘organized’ by Dr. Peter Gast. Together with a fellow PhD student I also organized for about two years a biweekly journal club on cosmology in an attempt to further strengthen the ties between observational and theoretical cosmologists in Leiden.

Starting this autumn, I will continue my research as a fellow of the ‘Kavli Institute for the Physics and Mathematics of the Universe (Kavli IPMU)’ at the University of Tokyo, Japan.

Acknowledgements

*Wissen kann man mitteilen, Weisheit aber nicht.
Man kann sie finden, man kann sie leben,
man kann von ihr getragen werden,
man kann mit ihr Wunder tun,
aber sagen und lehren kann man sie nicht.*

*Knowledge can be conveyed, but not wisdom.
It can be found, it can be lived,
it is possible to be carried by it,
miracles can be performed with it,
but it cannot be expressed in words and taught.*

(Hermann Hesse, Siddhartha)

First of all, I would like to thank the citizens of the Netherlands for still funding natural sciences at a level allowing even me as a PhD student to receive a decent salary so that I never had to worry about financial aspects. This and the weather here enabled me to focus entirely on science for the last four years.

In view of recent events, I would also like to express my thanks to all people who worked so hard on making a great idea become the reality that allows me, a German citizen, to move and transit so easily between borders. Even working in the Netherlands is/was possible without having to go through a tedious visa application process. A fact I always took for granted, but recent events remind us that it really is not.

I would also like to thank all the people at Leiden Observatory who made the last four years here a smooth experience whenever I had to deal with formal requirements and/or administration in general, especially during the last few weeks of submitting this thesis. Likewise, I appreciate the great technical support, which not only provided fast and practical solutions, but also made me feel like being back in the good old 90s once in a while.

I thank all members of the ‘lensing group’ past and present for stimulating feedback on progress and interesting discussions about recent literature in our group meetings and beyond: Andrej, Berenice, Christos, Jelte, Maciej, Marcus, Margot, Martin, Elisabetta, Remco, and Vianni. Special thanks are due to Cristobál and Marco for also sharing their L^AT_EX-templates and invaluable ‘how-to-make-a-thesis’ experience with me. Thank you, Marcello, for interesting lunch discussions (especially in combination with Massimo) and all your science-related help and general support.

Thanks to former members of the Instituut–Lorentz, Jesús and Wessel, from whom I learnt a great deal about Bayesian statistics and who were always available for advice on technical or mathematical issues.

A PhD is not only dependent on your own abilities, but it is also very dependent on the people who join your group and office just by mere chance the same day your appointment starts: this thesis would have taken an entirely different route, if it would exist at all, without the support from you, Massimo. Thank you for always investing your time in quick discussions and checking of intermediate results, despite your own very busy schedule. This helped tremendously in keeping up the pace over the last four years and making things actually hap-

pen. Moreover, your knowledge and attitude towards how science should be done are inspiring and I learnt a lot from that and I hope to always be able to keep up to these standards. Your attitude towards how science actually works is both enlightening and entertaining (especially when Marcello joins in on the discussion) and helps me to keep a realistic view on ‘the game’ (or more accurately ‘the gamble’ when you take the current PhD-to-staff ratio into account...).

Another very influential aspect and as important as ‘chance encounters’ for the writing of a thesis are your collaborators or the collaboration(s) you might become a member of. In that regard I consider myself very lucky to be part of the KiDS ‘family’, which not only produces great and thorough science, but also manages to keep a nice and thriving attitude while doing that! Special thanks are due to Benjamin, Catherine, Hendrik, and Ludo for reliable delivery of critical data products, thorough feedback, and discussions during which I learnt a lot.

It was a great pleasure to share an office and beers with you, David. Discussing issues with you related to science or living in the Netherlands or life in general did not always provide a solution, but at least it showed me that I was not the only one struggling once in a while. Keep up your British humour and point of view and I wish you the best of luck for your future as a ‘legal alien’ in Europe!

Thank you, Jeroen, not only for also sharing the office with me, suffering through ‘club power’, interesting discussions about science and politics, and the de Sitter experience, but also for all your help related to ‘Dutch things’, especially in the beginning.

Although you did not share an office with me, you still dragged me along to ‘club power’ in the first place and provided great help in translating the summary to Dutch. Thank you, Ricardo, for that and the great discussions we used to have over dinner after ‘club power’. I will miss those for sure (but ‘club power’ not so much...)!

Extremely helpful in an attempt to keep the balance during the last months of writing this thesis was playing football in the least successful team I have ever participated in. Playing with you guys was nevertheless great fun and kept the thesis off my mind at least for the time we played. So, thank you, Emanuele, not only for initiating the team, but also your random ‘jokes’ turning very often into real life ‘Family guy’ moments (or is it performance art after all?!). Thank you, Clement, for sharing so many good football moments (either playing or watching) and the many beers and good discussions we had! Thanks also to all other (core) members of our football team and training partners: Andrew, Duy, François, Jit (traitor!), Pedro, Santiago, Tim, Vicente, and Victor.

The last four years would have been very boring without all the other people past and present who made coffee and lunch breaks, the traditional Friday borrels, and occasional parties so enjoyable. So, thanks to all people who contributed their valuable time also to social events here!

Vielen Dank an Robert Salewsky für die professionelle und schnelle Umsetzung meiner Coverdesign-Idee, was mir sehr viel wertvolle Zeit und Nerven gespart hat!

Unendlich dankbar bin ich meinen Eltern, Fred und Regina, und meinem Bruder Yannic für all die Unterstützung in den letzten vier Jahren, ohne die diese Arbeit hier nicht möglich gewesen wäre. Noch viel dankbarer bin ich euch hingegen dafür, dass ihr mir diesen ungewöhnlichen und nicht selbstverständlichen Weg überhaupt erst ermöglicht habt. Auch wenn er mich geographisch leider immer weiter von euch wegführt, seid ihr in meinen Gedanken immer bei mir!

Ohne den zusätzlichen Rückhalt in der weiteren Familie bestehend aus Sarah, Oma Friederike, Tante Gaby und “Tante” Karin wäre dieser Weg noch viel beschwerlicher gewesen, also auch vielen Dank an euch alle!

Gudrun, Christoph, Stefanie, Lars und Luise, euch möchte ich danken für euer herzliches

Willkommen als neuer Teil in eurer Familie. Besonders genossen habe ich die vielen schönen Wochenenden in Lippstadt gerade im vergangenen halben Jahr. Diese haben mir unter anderem gezeigt, dass es auch noch viel Erstrebenswerteres (und Anstrengenderes) im Leben gibt als das Erreichen von akademischen Würden.

Kathrin, vielen Dank, dass du auch wieder in den letzten vier, sehr arbeitsreichen Jahren voller Stress immer zu mir gehalten und mich immer unterstützt hast. Du hast mich aufgemuntert, wenn meine Laune mal wieder durch die Arbeit getrübt wurde. Außerdem hast du so selbstverständlich daran geglaubt, dass alles seinen Weg gehen wird (denn es "muss ja"), sodass Aufgeben nie wirklich eine ernsthafte Alternative war. Dass du dann auch noch zwei Jahre hier in die Nieder(schlags)lande gezogen bist, war eine unschätzbare Hilfe für mich und einfach eine sehr schöne Zeit (trotz des Wetters)! Ich freue mich jetzt riesig auf unser nächstes großes Abenteuer, diesmal zu zweit und wieder vereint in Japan!

